FLUID-STRUCTURE INTERACTION SIMULATIONS ON SKELETON-REINFORCED BIOMIMETIC FIN PROPULSION

Guangyu SHI

Declaration

I hereby declare that this thesis and all material contained herein is a record of work carried out in the Department of Naval Architecture, Ocean and Marine Engineering at the University of Strathclyde, during the period from October 2015 to April 2010. This thesis is the result of the author's original research except where otherwise indicated. It has been composed by the author and has not been previously submitted for examination, which has led to the award of a degree.

The copyright of this thesis belongs to the author under the terms of the United Kingdom Copyright Acts as qualified by University of Strathclyde Regulation 3.50. Due acknowledgement must always be made of the use of any material contained in, or derived from, this thesis.

Guangyu SHI

Signature:＿＿＿＿＿＿＿＿＿＿＿＿＿＿＿＿   Date: 23/04/2020

This is dedicated to my father in Heaven.

谨以此文奉献给我的父亲。

I would like to dedicate this thesis to my beloved wife, Qin Wang, my loving mother, grandparents and family.

谨以此文奉献给我永远挚爱的妻子王钦，我永远爱戴的母亲，爷爷奶奶和家人。

望嶽

唐·杜甫

岱宗夫如何？齊魯青未了。

造化鐘神秀，陰陽割昏曉。

蕩胸生層雲，決眥入歸鳥。

會當淩絕頂，一覽眾山小。

Mountain Tai Gazing

Du Fu (Poet of Tang Dynasty)

(Translated by Betty Tseng, 2018)

What of the Great Mountains that hither situate?

Still green everywhere are once warring states.

The creation of sky and earth gathers here heavenly splendour,

Bearing and geography determine light and shade.

My heart expands to take in layers of floating clouds,

I look out far and wide, I see birds their homeward journey make.

May I one day surmount the absolute highest,

For an outlook that miniaturize all mountains there lay.

Acknowledgements

First and foremost, I would like to thank my principal supervisor Dr Qing Xiao and my second supervisor Prof Sandy Day for their inspiring advice and kind help. Dr Xiao was always encouraging and helpful with her expertise in CFD related problems. Her efforts in supervising me with my PhD study will always be appreciated.

I would like to thank Dr Qiang Zhu from UCSD and Dr Wei Liao from Bihrle Applied Research Inc for their kind help in developing the numerical tool and sharing insights into the physical problems. Their valuable supports are much appreciated.

I would like to thank University of Strathclyde and China Scholarship Council for their financial support during my study in the UK.

I would like to thank Ms Susan Pawson and other staff in the Department of NAOME for their kind help in administrative and technical issues.

I would like to thank the technical supports from ARCHIE-WeSt HPC based at University of Strathclyde and CIRRUS HPC based at University of Edinburgh.

I would like to thank all my amazing colleagues and friends in Glasgow. They were always supportive and encouraging and the time spent with them made my life in Scotland much more enjoyable.

Finally, I am deeply indebted to my loving family for their endless love and support. I am deeply grateful to my beloved wife, Qin Wang, who always understood me and kept me company. I am also grateful to my parents-in-law for their visits and kind help in taking care of my baby. I am so blessed to have my son Isaac, who is like an angel and brightens my life.

Publications

Journal Articles:

◇ Guangyu Shi, Qing Xiao, Numerical investigation of a bio-inspired underwater robot with skeleton-reinforced undulating fins. *European Journal of Mechanics B / Fluids*, under review.

◇ Guangyu Shi, Qing Xiao and Qiang Zhu, Numerical investigation of an actively and passively controlled skeleton-reinforced caudal fin. *AIAA Journal*, under second review.

◇ Yang Luo, Qing Xiao, Guangyu Shi, Li Wen, Daoyi Chen and Guang Pan, A fluid-structure interaction solver for the study on a passively deformed fish fin with non-uniformly distributed stiffness. *Journal of Fluids and Structures*, **92**, p. 102778, 2019.

◇ Guangyu Shi, Qing Xiao and Qiang Zhu, Fluid-structure interaction modeling on a 3D ray-strengthened caudal fin. *Bioinspiration & Biomimetics*, **14**, p.036012, 2019.

Conference Papers

• Yang Luo, Qing Xiao, Guangyu Shi, Li Wen and Zhiming Yuan, A Fluid-Structure Interaction Study on a Passively Deformed Fish Fin, In *Proceedings of the 38th International Conference on Offshore Mechanics and Arctic Engineering*, Glasgow, Scotland, June 9-14, 2019. (***Attendee & Volunteer***)

• Guangyu Shi, Ruoxin Li and Qing Xiao, Bio-inspired Propulsion in Ocean Engineering: Learning from Nature. In *Proceedings of the 8th International Conference on Computational Methods in Marine Engineering*, Gothenburg, Sweden, May 13-15, 2019. (***Invited Session, Presenter***)

• Guangyu Shi, Qing Xiao and Qiang Zhu, A Study of 3D Flexible Caudal Fin for Fish Propulsion. In *Proceedings of the 36th International Conference on Offshore Mechanics and Arctic Engineering*, Trondheim, Norway, June 25-30, 2017. (***Presenter***)

Abstract

This study is inspired by the key features possessed by the fins of ray-finned fish (e.g., soft membrane supported by bony rays, anisotropic flexibility, individual actuation of fin rays, active curvature and stiffness control). A better understanding of the effects of these characteristics will provide inspirations and guidelines for the design of bio-inspired underwater locomotion systems, which are playing an increasingly important role as the growing activities in ocean engineering.

Due to the complicated structures of fish fins, it is of great challenge to numerically model such bio-membrane systems, which involve the fluid-structure interaction (FSI) between the flexible fin and the surrounding flow, and the modelling and active control of individual fin rays. It is therefore preferable to develop a compact and handy FSI solver, which allows to be tailored for specific problems, rather than using commercial software, which have no direct model capable of handling skeleton-strengthened bio-membrane systems and provides little freedom to be tailored. To elucidate the effects of the aforementioned main characteristics on the performance of biomimetic fin propulsion, a fully coupled FSI solver capable of simulating the dynamics of skeleton-reinforced bio-membranes is established in the present work. Specifically, a flow model, which solves the 3D unsteady compressible Navier-Stokes equations on an overset, multi-block, structured grid system with a finite-volume method, is coupled with a structural model, which solves a nonlinear Euler-Bernoulli beam equation with a finite-difference method, within a partitioned framework. The developed FSI solver is thoroughly validated against benchmark cases available in literature and good agreements are obtained.

Firstly, the established FSI model is applied to investigate the effects of different spanwise deformations on the propulsion performance of a simplified 3D ray-supported caudal fin. The rays are modelled as nonlinear beams. Kinematically,

the leading edge of the fin undergoes a sinusoidal sway motion while the rest part deforms passively. Our numerical results show that with specific ray stiffness distributions, certain caudal fin deformation patterns observed in real fish (e.g., the cupping deformation) can be reproduced through passive structural deformations. Among the four different stiffness distributions (uniform, cupping, W-shape and heterocercal) considered here, we find that the cupping distribution requires the least power expenditure. The uniform distribution, on the other hand, performs the best in terms of thrust generation and efficiency. The uniform stiffness distribution, *per se*, also leads to 'cupping' deformation patterns with relatively smaller phase differences between various rays.

Subsequently, the effect of active curvature control on the performance of a ray-strengthened caudal fin is examined. Kinematically, the fin is activated by a uniform sway motion at the basal ends of the rays, and distributed time-varying forces along each ray individually, which imitate effects of tendons that actively change the curvatures of the rays. The dynamics of the fin is closely associated with the exact distribution of phase lags (between the sway motion and external forces) among the rays. We find that the fin's performance can be significantly enhanced by active control when the mean phase lag is less than 90 degree. Among different deformation patterns, the cupping deformation (*C*-mode) produces the best propulsion performance. The underlying physical mechanism is found to be areas with increased pressure attributed to three-dimensional fin deformations. W-shape deformations (*W*-mode) have a similar (yet less pronounced) effect. In addition to symmetric fin deformations, asymmetric deformations such as heterocercal mode (*H*-mode) and undulation mode (*S*-mode) are reproduced in the present work. Both of which are able to generate vertical forces. Compared with the *H*-mode, the *S*-mode creates less thrust force but it significantly reduces the transverse force, making it more suitable in cases when there is no other mechanism to balance the transverse force (e.g. during the braking maneuver).

Finally, the propulsion performance of a skate-inspired underwater robot with a pair of ray-supported undulating pectoral fins is numerically investigated with the fully coupled FSI solver. Each pectoral fin is activated independently via individually distributed time-varying forces along each fin ray, which imitate effects of tendons that can actively curve the fin rays. We find that the propulsion performance of the bio-inspired robot is closely associated with the phase difference between the leading edge ray and the trailing edge ray of the pectoral fin. The results show that with a symmetrical kinematics, the highest thrust is created when the phase difference is 90 degree while the point maximizing the propulsion efficiency varies with the motion frequency. It is also found that there is a minimum frequency of generating net thrust for a specific parameter setup, which rises as the increase of phase difference. Compared with the symmetrical kinematics, the non-symmetrical kinematics generates more complicated hydrodynamic forces and moments which may be beneficial for maneuvering.

Table of Contents

Nomenclature

Roman Symbols

Δt	Physical time step
ΔV	Flow cell volume
a	Speed of sound
A_w	Width of the wake jet behind the body
A^*	Dimensionless trailing edge amplitude
c	Chord length of the body
C_D	Instantaneous drag coefficient
C_L	Instantaneous lift coefficient
C_M	Coefficient of M_Y
$\overline{C_M}$	Time-averaged C_M
C_P	Instantaneous power expenditure coefficient
$\overline{C_P}$	Time-averaged C_P
C_{pre}	Pressure coefficient
C_T	Instantaneous thrust coefficient
$\overline{C_T}$	Time-averaged C_T
C_Y	Instantaneous lateral force coefficient
$\overline{C_Y}$	Time-averaged lateral force coefficient
C_Z	Instantaneous vertical force coefficient
$\overline{C_Z}$	Time-averaged C_Z
D	Diameter of cylinder
E	Young's modulus
$\bar{E}$	Flow total energy
F_0	Magnitude of the external load
$F(t)$	Time-varying external load acting on the fin ray
$\mathbf{F}_{ex}$	Summation of all external forces acting on the thin structure
$\mathbf{F}_f$	Fluid force vector

f	Motion frequency of the body
f_r	Reduced frequency
F_X	X-component of instantaneous fluid force
F_Y	Y-component of instantaneous fluid force
F_Z	Z-component of instantaneous fluid force
h_p	Thickness of the thin structure
$h(t)$	Heave or sway motion of the body
H_{fin}	Thickness of the pectoral fin of the underwater robot
I	Second moment of inertia
K_b	Dimensionless structural bending stiffness
L_{body}	Length of the body of the underwater robot
L_{fin}	Length of the pectoral fin of the underwater robot
L_{ray}	Length of the pectoral fin ray of the underwater robot
L_p	Length of the thin structure
L_s	Spanwise length of the body
M_a	Flow Mach number
m^*	Structure to fluid mass ratio
M_Y	Instantaneous moment around y-axis and through the centre of the body
$\boldsymbol{n}$	Surface unit normal vector
p	Flow pressure
p_∞	Pressure of the incoming flow
$P(t)$	Instantaneous power expenditure
R_e	Reynolds number
S_t	Strouhal number based on the width of the wake jet
$S_{t,a}$	Strouhal number based on the excursion of the leading edge
$S_{t,d}$	Strouhal number based on the diameter of the cylinder
t	Time
T	Motion period

T_e	Flow temperature
U_∞	Incoming flow velocity
$\mathbf{U}$	Flow conservative variable vector
$\mathbf{v}$	Flow velocity vector
u	X-component of flow velocity
v	Y-component of flow velocity
w	Z-component of flow velocity
W_{body}	Width of the body of the underwater robot
W_{fin}	Width of the pectoral fin of the underwater robot
$y(t)$	Prescribed motion at the leading edge of the thin structure
y_0	Amplitude of prescribed motion

Greek Symbols

ρ	Fluid density
γ	Ratio of fluid specific heats
μ	Fluid dynamic viscosity
η	Propulsion efficiency
κ	Fluid thermal conductivity
ρ_s	Structural density
π	Ratio of circumference of a circle to its diameter
ω	Circular frequency of motion
ϕ	Phase between the leading edge motion and trailing edge motion of a heaving or swaying flexible plate
φ_i	Phase lag between leading edge sway motion and external load of the ith fin ray
φ_{diff}	Phase difference between the maximum and minimum values of φ_i
φ_{mean}	Mean value of all the φ_i
ψ	Phase lag between the sway motion and the induced yaw motion
φ_d	Phase lag between the external loads of the leading edge ray and trailing edge ray

$\theta(t)$ Pitch or yaw motion of the body

Abbreviations

2D   Two-Dimensional

3D   Three-Dimensional

ALE   Arbitrary Lagrangian-Eulerian

AOA   Angle of Attack

AUV   Autonomous Underwater Vehicle

BCF   Body Caudal Fin

CFD   Computational Fluid Dynamics

CSD   Computational Solid Dynamics

CSS   Conventional Serial Staggered

CVT   Constant Volume Tetrahedron

DES   Detached Eddy Simulation

DOF   Degree of Freedom

EPFL   Ecole Polytechnique Federale de Lausanne

FEM   Finite-Element Method

FSI   Fluid-Structure Interaction

FVM   Finite-Volume Method

GMRES   Generalized Minimal RESidual

IBM   Immersed Boundary Method

IBQN-LS   Interface Block Quasi-Newton with an approximation for the Jacobians from Least-Square models

IHC   Implicit Hole Cutting

IQN-ILS   Interface Quasi-Newton with Inverse Jacobian from a Least-Square model

JST   Jameson-Schmidt-Turkel

LES   Large Eddy Simulation

LEV   Leading Edge Vortex

LSP   Low Speed Preconditioning

MAV	Micro-Aerial Vehicle
MBD	Multi-Body Dynamics
MCYC	number of pseudo-time iteration within one physical time step
MIT	Massachusetts Institute of Technology
MPI	Message Passing Interface
NACA	National Advisory Committee for Aeronautics
NSTEP	number of time step in each motion period
OGA	Overset Grid Assembler
PIV	Particle Image Velocimetry
POD	Proper Orthogonal Decomposition
RANS	Reynolds Averaged Navier-Stokes
R.M.S	Root Mean Square
TEV	Trailing Edge Vortex
TFI	Trans-Finite Interpolation
USA	United State of America

List of Figures

List of Tables

Chapter 1   Introduction

1.1 Background

Ocean exploration and engineering has increased in the past years and with that there is also a growing need for underwater robotics that can autonomously conduct routine tasks in complicated environments [1–3]. This need not only comes from the vulnerability of humans in aqueous environments but also from the underdeveloped capacities of the currently deployed robotic systems [4]. To enhance the adaptability and performance of underwater robotics, inspirations must be sought from aquatic animals that have been diversified into almost every corner of the ocean in the past millions of years. A system is termed bioinspired if the design is derived from nature. It is called biomimicry if a system directly mimics a biological system. Such bioinspired and biomimicry systems would have applications in a wide range of civilian and military missions, e.g., water pollution monitoring, erosion monitoring, marine animal immigration monitoring, border patrol, etc. [5]. Additionally, these bioinspired underwater robotic systems have advantages of high locomotion efficiency, low noise production, high maneuverability and eco-friendliness. Therefore, it is of importance to understand the locomotion mechanisms of aquatic animals as well as to have new conceptual designs of underwater robotic systems. In this section, the classification of biological aquatic locomotion systems and the application of bioinspired locomotion systems are briefly reviewed.

1.1.1   *Classification of biological aquatic locomotion systems*

Aquatic animals rely on various mechanisms for locomotion. With different methodologies, the biological aquatic locomotion systems can be categorised in different ways. In the present thesis, we adopt an encompassing and straightforward

classification proposed by Salazar et al. [4], in which all found biological systems are divided into three main categories: fin oscillation, fin undulation and jet propulsion, as demonstrated in Figure 1-1. There are many subcategories within each main class, along with overlap between them. For example, some species may possess more complicated locomotion systems that combine several locomotion styles, such as diodontiform and tetraodontiform swimmers.
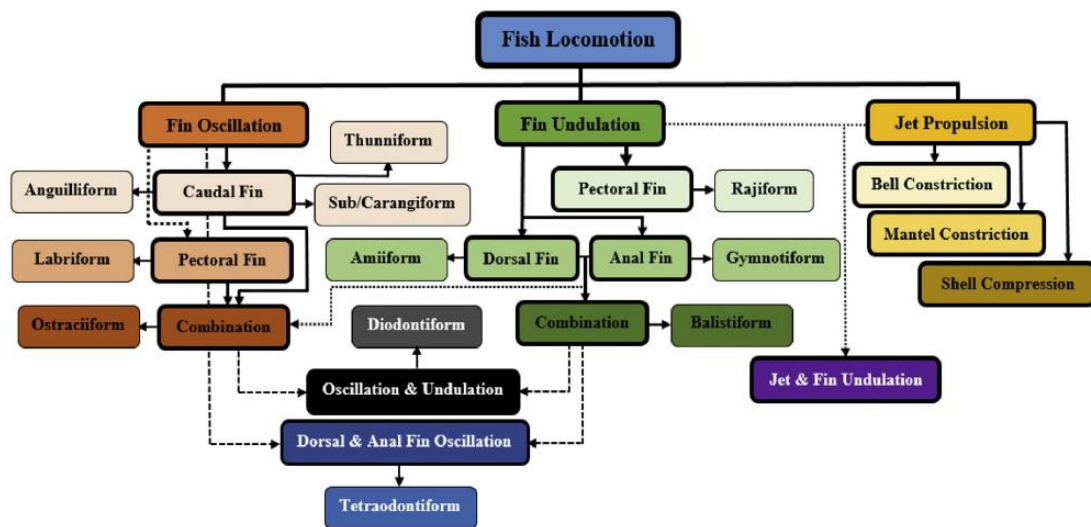
Figure 1-1 Classification of biological aquatic locomotion [4].

1.1.1.1 Fin oscillation

Fish account for a vast majority of species of marine animals and most fish species depend on their flexible body and/or fins for locomotion. Generally, fish fins can be divided into two groups, namely, median fins (including caudal fin, dorsal fin and anal fin), and paired fins (including pectoral fins and pelvic fins), as shown in Figure 1-2.

The Fin Oscillation mode includes a great variety of species that can be classified as Caudal Fin swimmer, Pectoral Fin swimmer, and Dorsal & Anal Fin swimmer, according to the main appendages used for propulsion. The Caudal Fin sub-classification is the largest among Fin Oscillation species, which is attributed to the great variety of fish species that mainly utilise caudal fin for propulsion. The

Caudal Fin swimmers generate thrust by creating a traveling wave along their flexible body. According to the degree of body undulation, Caudal Fin subcategory can further be divided into anguilliform, subcarangiform, carangiform and thunniform, as shown in Figure 1-3. In other reports, this locomotion mode is also labelled as body caudal fin (BCF) mode [3,6].
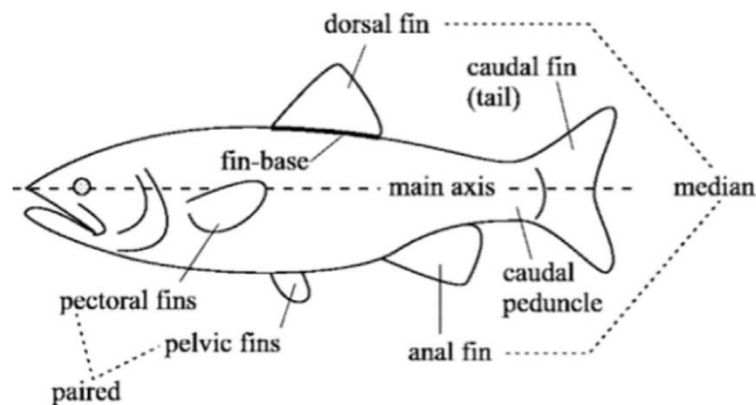
Figure 1-2 Illustration of different fins possessed by a ray-finned fish [6].
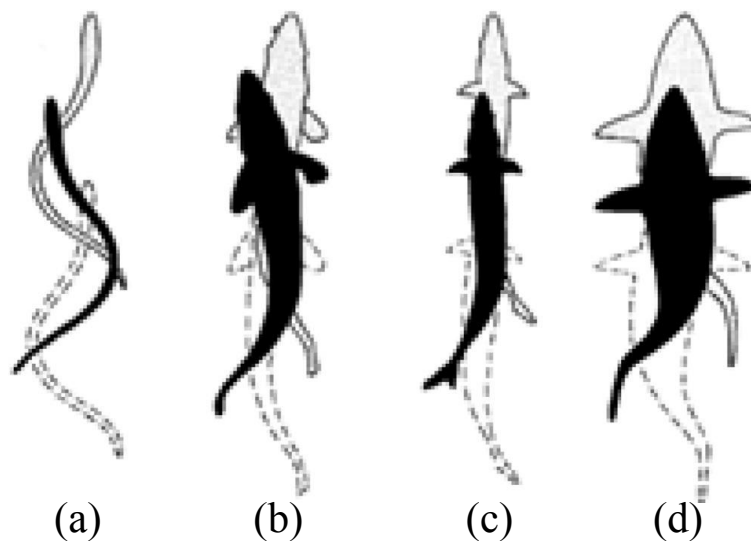
Figure 1-3 Diagrams displaying different ways to achieve tail oscillations, (a) anguilliform, (b) subcarangiform, (c) carangiform, and (d) thunniform [6].

The fish species that mainly rely on oscillating their pectoral fins for locomotion are classified as Pectoral Fin (*Labriform*) swimmer, which is the second largest group Fin Oscillation category. Labriform swimmers are usually living in reef areas where they need more agility and maneuverability. Compared with Caudal Fin swimmers,

labriform swimmers have low speed and endurance. Thus, they also use the caudal fin occasionally for relaxing the pectoral fins or bursting swimming [7]. Apart from Caudal Fin and Pectoral Fin swimmers, some fish species utilise their dorsal & anal fins (T*etraodontiform*) or combined caudal, pectoral, dorsal and anal fins (*Ostraciiform*) for locomotion. These two swimming modes are the smallest groups among Fin Oscillation category.

1.1.1.2   Fin undulation

(a)   (b)

Figure 1-4 (a) Bluespotted ribbontail ray (Rajiform) [8]. *(b) Black ghost kinfefish (Gymnotiform)* [9].

Marine animals in this category generate desired forces by creating undulatory waves along their fins. This Fin Undulation class is smaller than the Fin Oscillation category. The fish species in this class also use different fins for locomotion. For example, rajiform swimmers use their enlarged pectoral fins for propulsion (see Figure 1-4 (a)) while gymnotiform swimmers utilise their elongated undulating anal fin to create forces (see Figure 1-4 (b)). There are also species that use their elongated undulating dorsal fin (*Amiiform*) or combined undulating dorsal and anal fins (*Balistiform*) for swimming. Some species in Fin Undulation class are capable of multi-directional motion by changing the direction of the propagating wave along the fin. Besides, the rajiform swimmers are able to have null speed turns which enable them to navigate in close quarter environments.

1.1.1.3 Jet propulsion

There are two main subcategories in this classification: Bell Constriction (e.g., jellyfish, Figure 1-5 (a)) and Mantel Constriction (e.g., octopus, Figure 1-5 (b)). For Bell Constriction locomotion, the movement is produced by ejecting water, which is achieved by periodically contraction and relaxation of the muscles in the bell, leading to the periodical change of the volume of the bell. For Mantel Constriction swimmers, the propulsion is produced by filling the mantel cavity with water and expelling it out through the siphon, which not only controls the jet speed but also the moving direction.

(a)   (b)

Figure 1-5 (a) Australian box jellyfish (Bell Constriction) [10]. *(b) Juvenile octopus (Mantel Constriction)* [11].

1.1.1.4 Combined propulsion

As demonstrated in Figure 1-1, some species possess more complicated locomotion styles by combining more than one swimming modes. Figure 1-6 (a) shows a photo of spotted porcupinefish, which uses a combination of oscillating caudal, dorsal & anal fins and undulating pectoral fin. Figure 1-6 (b) illustrates a photo of common cuttlefish, which combines the mantel constriction mode and undulating fin mode. The combined swimming modes allow the animals to select the optimal swimming style according to external environments.

(a)   (b)

Figure 1-6 (a) Spotted porcupinefish (Diodontiform) [12]. *(b) Common cuttlefish (Mantel constriction and undulatory fin)* [13].

1.1.2   *Application to bio-inspired aquatic locomotion systems*

Inspired by the biological aquatic locomotion systems and aimed at having comparable efficiency and maneuverability, many different bio-inspired locomotion systems have been designed and fabricated in the past decades. These underwater robots are bio-inspired, i.e., they are not the exact duplicates of the biological systems. The real biological systems are usually complicated in terms of material properties, actuation mechanisms and control strategies. Thus it is of great difficulty to exactly mimic them. The advent of new materials and the advancement of manufacturing capabilities may shed light into the design and optimization of bio-inspired aquatic locomotion systems. In the present subsection, several typical man-made bio-inspired locomotion systems are briefly introduced.

As one of the pioneer research groups in robotic fish design, the team of Professor Triantafyllou at MIT designed and tested two generations of robotic tuna in their laboratory, as demonstrated in Figure 1-7 [14,15]. The robots they fabricated fall into the category of Fin Oscillation (*Thunniform*), which mainly uses caudal fin oscillation to generate thrust. Six servomotors were used to create the body undulation.

(a)

(b)

Figure 1-7 (a) Robotuna (Charlie I) [15] and (b) Robotuna II at MIT [14].

(a)

(b)
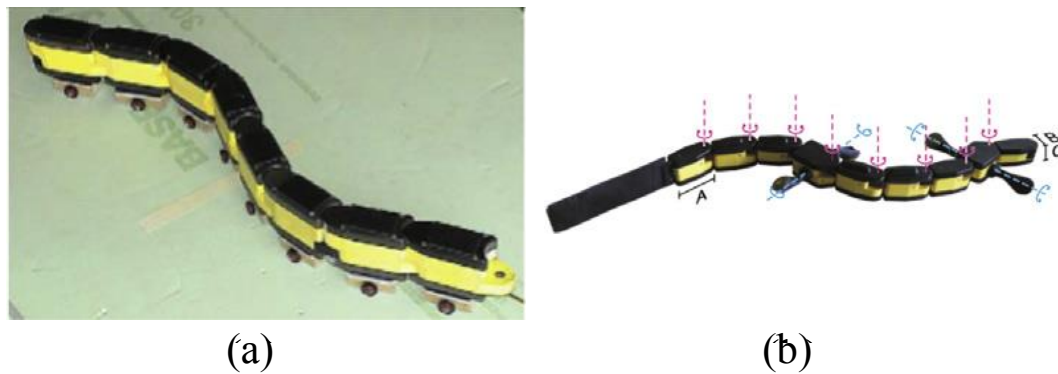
Figure 1-8 (a) Amphibot I [16]. (b) Salamandra Robotica II [17].

Figure 1-8 demonstrates two anguilliform robots designed and fabricated in Biorobotics Laboratory, Ecole Polytechnique Federale de Lausanne (EPFL), which is a leading institute in the field of bio-inspired robotics. Specifically, Figure 1-8 (a) shows an amphibious snake-like robot taking inspiration from snakes and elongate fishes such as lampreys [16]. This robot is its first generation and composed of several identical rigid elements, which have only one DOF. This robot also serves as a test-bed for novel types of adaptive controllers and investigations into the locomotion-controlling neural networks in real animals.

Research scientists in Biorobotics Laboratory, EPFL also designed and manufactured another amphibious robot called Salamandra Robotica II (Figure 1-8 (b)), which is inspired by salamanders [17]. This robot has an actuated spine composed of several

interconnected rigid elements and four legs, which enables it to perform an anguilliform swimming under water as well as walk on the ground. This robot can be used as a scientific tool to investigate the neural circuits underlying locomotion in the spinal cord of vertebrate animals.
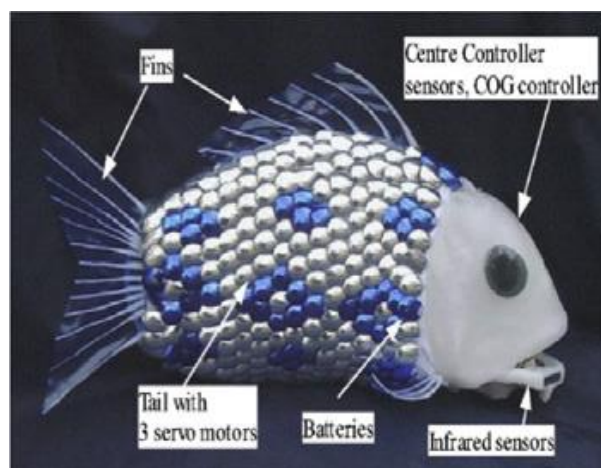
Figure 1-9 G9 fish at University of Essex [18].

A stunning fish used for pollution detection shown in Figure 1-9 was designed by the scientists in University of Essex [18]. This robotic fish has a rigid head, where stored the computers and sensors, a flexible body, which can create an undulatory motion, and several fins. The G9 robotic fish is able to swim like a real fish and navigate autonomously.

Apart from those underwater robots inspired by fishes within Fin Oscillation category, many scientists also sought inspirations from Fin Undulation swimmers. Figure 1-10 demonstrates two generations of robotic manta ray designed by the research group of Professor K. H. Low in Nanyang Technological University, Singapore. The RoMan-II robot has a rigid body and a pair of wide pectoral fins [19]. Each fin is supported by three flexible rays and each ray can be actuated individually by a brushless servomotor. This robotic manta ray can also perform diversified locomotion patterns (e.g., trilinear swimming, turning, gliding and online transition of different modes) by manipulating the two pectoral fins. RoMan-III is an improved version of RoMan-II.

The newly designed robot is more compact while maintaining the swimming speed [20].

(a)   (b)
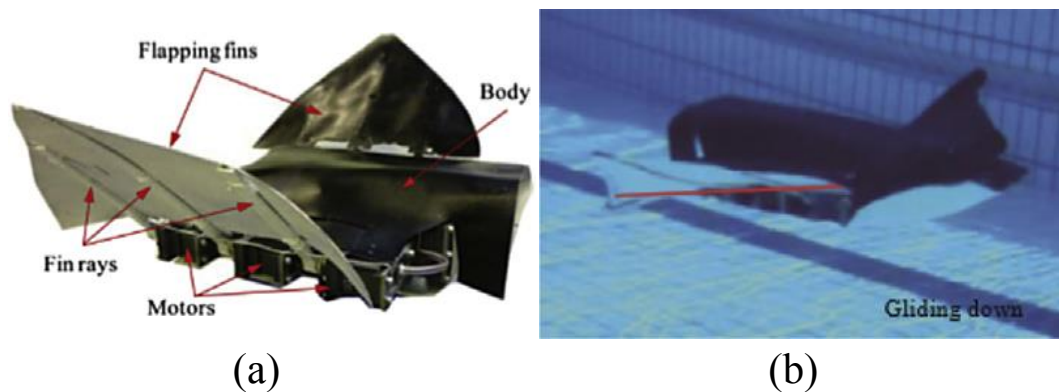
Figure 1-10 (a) Robotic manta ray (RoMan-II) [19]. *(b) Robotic manta ray (RoMan-III)* [20].

Figure 1-11 demonstrates an aquatic robot designed by researchers from Florida Atlantic University, USA [21]. This robot is inspired by black ghost knifefish, which utilises its elongated undulating anal fin for locomotion. The robotic knifefish consists of a rigid hull plus an undulatory anal fin supported by many rays. Each ray is activated independently, thus it can generate a traveling wave along the fin for propulsion by controlling the phases between different rays. This robot can easily swim backwards by reversing the direction of the propagating wave. This robot also retains a rigid body which reduces the complexity of mechanical design.

Figure 1-11 Robotic knifefish [21].
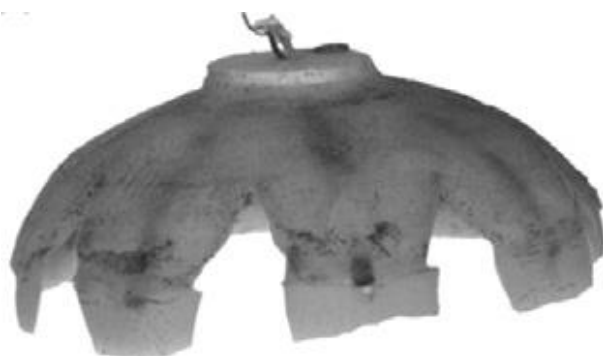
Figure 1-12 Robotic jellyfish (Robojelly) [22].

Figure 1-12 (a) shows a jellyfish-inspired underwater vehicle designed by researchers from Virginia Tech, USA [22]. The bell geometry of Robojelly is reconstructed from experimental measurement of real jellyfish and the deformation of the bell is actuated by bio-inspired shape memory alloy composite actuators, which can allow a large deformation of the bell radius at the margin as well as can retain its original profile after contraction using the elastic energy stored in the bell. The robotic jellyfish is able to generate sufficient thrust for propulsion and also achieve proficiency comparable to natural jellyfish.

Figure 1-13 demonstrates a multi-functional, multi-arm robotic swimmer inspired by octopus, featuring both manipulation and locomotion capabilities [23]. By coordinating the arm movements, this robot can achieve both forward and backward swimming, propulsion and turning.
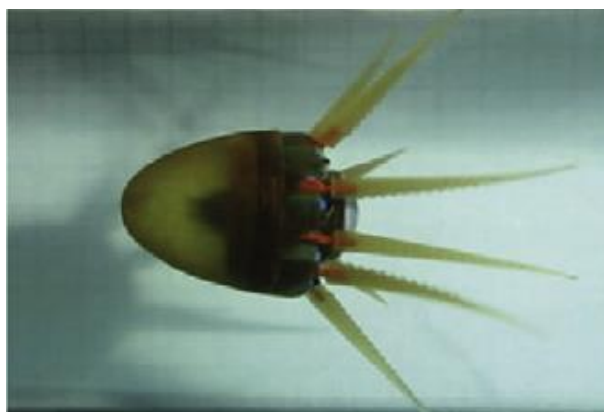
Figure 1-13 Robotic octopus [23].

1.2 Motivation and scope

1.2.1 Motivation of the present study

As the increase of ocean exploration and engineering, there is also a growing need for underwater robotics with better efficiency, maneuverability and eco-friendliness. After millions of year's evolution, aquatic animals have displayed a diversity of locomotion modes with remarkable performance (see section 1.1.1). Natural selection has ensured that the locomotion systems possessed by these marine animals, although not necessarily optimal, are highly efficient and adaptable with regard to the habitat of certain species. Therefore, these incredible biological locomotive systems have become the source of inspiration for the design of man-made underwater robotics. Although various bio-inspired underwater robots have been invented in the past decades (see section 1.1.2), our understanding for the mechanisms behind the high performance of these biological systems is still very limited. Thus, more research is needed to reveal how these mechanisms contribute to the locomotion performance.

As discussed in section 1.1.1, many fishes rely on their flexible body and multiple fins for locomotion. For some species (e.g., *Labriform* and *Rajiform* swimmers), fish fins are the primary appendages for locomotion. Therefore, fish fins play a significant role in fish locomotion. Among all the fish species, a group of species called ray-finned fish distinguish themselves from others by having uniquely designed fin architectures. Morphologically, a fin of ray-finned fish is characterised by a complicated composite structure, including a collagenous membrane, bony rays and intrinsic musculature (see Figure 2-2). The thin and soft membrane is supported by the flexible rays, and the basal ends of the rays are connected to a cartilage pad supported by the supporting bones [24]. Such a structural design is highly extensible, collapsible and deformable.

11

Structurally, a fin forms a ray-strengthened membrane system, where the Young's modulus of the collagenous membrane is much smaller than that of the supporting rays [25]. Therefore, the bending stiffness of the fin is mainly determined by those embedded rays. The non-uniform flexibility of each ray and the differences among the rigidity of different rays impart an anisotropic structural property of the fin so that it may undergo (presumably) beneficial passive deformations under hydrodynamic loads. According to previous studies, this passive flow control strategy is believed to improve the propulsion efficiency, enhance the thrust generation and reduce the lateral forces [25,26]. The benefits of anisotropic material property can also be seen from a two-dimensional study of a pectoral fin [27]. It is observed that with a strengthened leading edge, the performance of the pectoral fin can be significantly improved.

In addition to the aforementioned passive control mechanism enabled by the anisotropic material property, fish fins also possess two other important features that enable active control over their deformations. First, each fin ray can be actuated individually through the sophisticated musculature system. Second, each ray has by itself a remarkable bio-mechanical system for motion actuation. According to previous morphological studies [28–30], a fin ray is composed of a central cartilage pad surrounded by paired, segmented bony elements called hemitrichs, which are connected with short ligaments and elastic fibers (tendons) at the ends. The basal end of each ray is attached to four separate muscles. By pulling the tendons, a hemitrich can slide past the other one, creating a distributed bending moment along the length of a ray [28]. Through the embedded tendons and the unique bi-laminar design of the ray, fish is able to actively modify the curvature of the ray and change the bending stiffness of the ray itself. This characteristic is a hallmark of the bony fish, distinguishing the propulsion mechanism of these creatures from those of birds and insects [30].

The main features of the fin of ray-finned fish can be summarised as 1) anisotropic bending stiffness of the fin; 2) individual actuation of fin rays; 3) ability of actively changing the curvature of the rays. These unique characteristics enable ray-finned fish to perform multi-degree-of-freedom control over the motion and deformation of their fins. However, most previous studies of bio-inspired fin-like devices only considered the anisotropic flexibility and/or individual activation of rays. As mentioned before, ray-finned fish are capable of actively changing the curvature of the rays. However, this important feature, with a few exceptions, has not been accounted for in existing studies. The effects of these important features on the propulsion performance of fish fins remain to be fully understood.

Generally, three approaches are available to investigate the effects of these characteristics, namely, observation of live fishes, biomimetic robotic devices and numerical models. The first approach, which involves experimental observation and measurement of living fishes, has been widely used for biological studies [29,31–35]. Although experiments using live fish shed light on the kinematics and hydrodynamics of fins, the disadvantages and limitations of this approach are also obvious: for example, it is not possible to study the effect of individual traits on the performance and there is not sufficient diversity among extant species. An alternative method is to construct fin-like robotic devices [36–39]. This approach allows more freedom in alternating the parameters (e.g., geometry, material properties, and kinematics) so that the effect of each parameter can be isolated [40]. Nevertheless, this approach becomes too expensive or even infeasible when searching optimized designs within a large parameter space. With the advancement of high-performance computers and high-fidelity numerical algorithms, computational modeling has become an indispensable complement to experimental studies [41,42]. Numerical simulations can provide detailed information of the flow field as well as physical insight of the fluid-structure interactions. The advantage of examining "what if" type of questions

makes the computational modelling more appealing compared with experiments [42]. Flow solvers based on immersed boundary method (IBM) [42–46] and moving grid approaches [47–51] have been widely used for biomimetic problems. However, most numerical studies are based on either measured fish kinematics [42–44] or simplified flexible flapping foil models [45,46]. As for skeleton-strengthened fins, only a few studies using potential flow models [25,26,52,53] and 2D IBM approaches [27,54] are available so far. These studies of ray-supported fins illustrate that passive structural deformation and non-uniform stiffness distribution can enhance fin's propulsion performance.

Bearing this in mind, in this thesis we develop a fully coupled viscous flow FSI model, which captures the three main features of a real fish fin (anisotropic flexibility, individual ray activation and active curvature control), to examine the effects of each characteristic on the performance of skeleton-strengthened fins. We are also motivated by the scientific need to understand the fundamental mechanisms in fish locomotion as well as the practical applications of these biomimetic devices on unmanned underwater vehicles. The present work will be the first systematic numerical investigation on a fin-like propeller that considers both the viscous FSI and active curvature control of the fin rays.

1.2.2   Scope of the present study

Numerical modelling of ray-supported fish fins is of great challenge. As stated in Section 1.2.1, real ray-strengthened fish fins are characterised by complicated composite structures, such as collagenous membrane, bony rays with bilaminar design, intrinsic musculatures. Thus, it is not possible to exactly duplicate real fish fins numerically. From the perspective of biomimetics, it is also preferable to design simple and easily manufactured devices which capture the essential characteristics of fish fins. Therefore, some reasonable simplifications are necessary for the numerical modelling

of such structures. Fins are crucial appendages for fish swimming, especially for labriform and rajiform swimmers, which primarily rely on fins for propulsion. Therefore, the present thesis is focused on one simplified caudal fin model (see Figure 1-14) and one idealised robotic fish model with a pair of undulating pectoral fins (see Figure 1-15). The present thesis emphasises on the analysis of the propulsion performance and the fluid-structure interaction of these simplified models.

1.2.2.1 *Oscillating caudal fin*

As demonstrated in Figure 1-14, the simplified caudal fin has a rectangular shape and supported by eleven flexible rays. The caudal fin is fixed in space, i.e., it does not move forward and its leading edge undergoes a sinusoidal sway motion in *y*-direction, imitating the movement of the posterior part of the fish. The fish caudal fin usually undergoes sinusoidal sway and yaw motions according to previous experimental studies [31]. Therefore, the motion of fish caudal fin was usually simplified as sway or/and yaw motions at the leading edge [26]. Each ray can be individually actuated and its curvature can also be independently controlled. The bending stiffness can be determined individually, thus anisotropic flexibility can be easily achieved by the present model. Therefore, the present caudal fin model captures the three key features of real fish fins summarised previously (anisotropic flexibility, individual ray activation and active curvature control). The flow is uniform and considered in *x*-direction. This is equivalent to a problem that the caudal fin is moving at a constant speed along negative x-direction in calm water [55]. The effects of passive spanwise deformations (Chapter 5) as well as active curvature control (Chapter 6) on the propulsion performance of this caudal fin are studied.
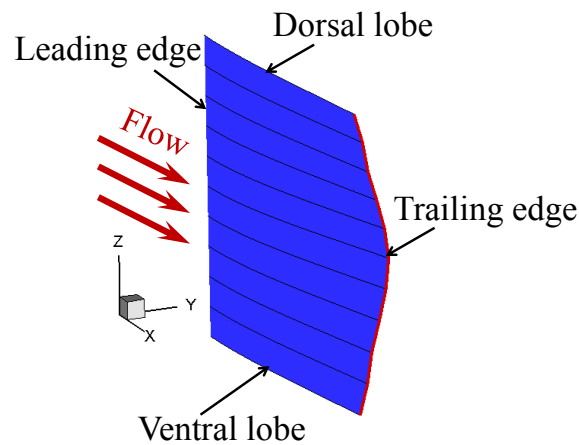
Figure 1-14 Illustration of a simplified ray-supported caudal fin model.

1.2.2.2 Undulating pectoral fin

Figure 1-15 shows an idealised robotic fish model, which is inspired by rajiform swimmers and consists of a rigid body and two flexible ray-strengthened pectoral fins. The body is simplified as a flat plate and is fixed in space. A uniform flow is coming in x-direction. Similar to the above caudal fin model, the current problem is equivalent to one that the fish model is swimming along the negative x-direction at a constant speed in calm water. The pectoral fins are supported by flexible rays and the thrust is created by generating a wave propagating in the streamwise direction. This motion characteristics is possessed by some rajiform and gymnotiform swimmers, which is often modelled as a travelling wave along the fin [21]. The hydrodynamics and propulsion performance of this fish model are investigated in Chapter 7.
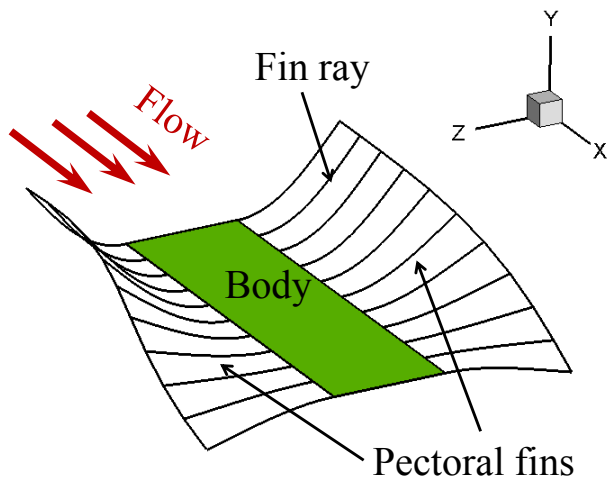
Figure 1-15 Illustration of an idealised robotic fish model.

1.2.2.3 *Difference between the oscillating and undulating motions*

For the caudal fin model in Figure 1-14, the fin rays are aligned with the incoming flow. The sway and induced yaw motion of the caudal fin produce a jet flow behind the fin and the reacting force from the jet is then reoriented in the negative x-direction, thereby generating a thrust force. Different from the rays of the caudal fin model, the rays supporting the pectoral fins are perpendicular to the incoming flow (Figure 1-15). Each ray is activated to have an effective rotation relative to the ray's basal end. By controlling the phase distribution of the rotations among the rays, the pectoral fins can produce a wave propagating along the streamwise direction. The propulsion performance of the undulating pectoral fin is closely associated with the wave number on the fin.

1.3 Objectives of this thesis

The main objective of the present thesis is to establish FSI models for some simplified bio-inspired underwater propulsive systems and investigate their propulsion performance. We are also aiming at understanding the fundamental mechanisms involved in these FSI problems and providing potential guidelines and inspirations for

the design and optimisation of bio-inspired underwater vehicles. To accomplish this goal, the following four specific tasks are targeted.

(1) A FSI solver capable of modelling bio-membrane systems should be established and validated. The novelty of this FSI solver lies in the ability of modeling the fluid-structure interaction of skeleton-reinforced membranes. The PhD candidate should make the following contributions based on the existing code: a) re-implementing a structural solver based on an old subroutine written in Fortran77; b) implementing the coupling between an in-house CFD code and the re-implemented structural solver in a partitioned framework; c) upgrading and integrating an overset grid assembler into the in-house flow solver in order to extend its capability on coping with scenarios involving complex geometries and multiple bodies with relative motion; d) validating the developed FSI solver using benchmarks and experimental data.

(2) With the aforementioned numerical tool, the effects of different spanwise deformation patterns on the performance of a simplified ray-supported caudal fin are investigated. This research is inspired by previous anatomic and morphological studies on ray-finned fish. It is revealed that fish fins have anisotropic material property and can achieve fully 3D deformations, which enables the fish generate forces in different directions.

(3) The effect of active curvature control on the performance of an idealised ray-strengthened caudal fin will be investigated. This research is motivated by the fact that the fin rays have unique bilaminar structure which enables the ray-finned fish to actively control the curvature and stiffness of their rays. Besides, each ray is actuated individually. These features allow the fish to have multiple DOF control over their fin surface.

(4) The established FSI modelling tool should be further applied to investigate the propulsion performance of a simplified underwater robot with two flexible ray-supported undulating fins, which is a more practical problem.

1.4 Outline of this thesis

This thesis is organised into eight chapters and the structure is as follows.

Chapter 1 introduced some background for the present research by providing the classification and application of bio-inspired propulsive systems as well as the motivation of the present work. The objectives and scope of the current thesis were also defined in this chapter.

A critical review of experimental and numerical studies on ray-finned fish swimming is provided in Chapter 2. The previous studies are categorised according to the research methods, specifically, experiments with live fish, experiments using robotic devices and computational models.

The governing equations and numerical methods used in the fully coupled FSI code are presented in Chapter 3. Detailed descriptions of these numerical schemes in different modules (including fluid dynamics modeling, structural dynamics analysis, fluid-structure coupling, moving mesh handling and overset grid) are provided.

Chapter 4 presents a thorough validation for the FSI solver developed in the current thesis by comparing the present results with the numerical and experimental data from literature. The flow solver is firstly validated using several 2D and 3D benchmark cases. The accuracy of the structural model is then examined by two classical problems. Finally, the coupled solver is validated by predicting the dynamic responses

of a flexible plate immersed in the wake of a square cylinder and imposed a heave motion at the leading edge.

The following three chapters are concentrated on the applications of the FSI code developed and validated in the previous two chapters. The three applications correspond to the last three minor objectives listed in subsection 1.3. In Chapter 5, the effects of various spanwise deformations on the performance of an idealised ray-supported caudal fin are investigated. In this problem, the fish caudal fin has solely passive deformations, i.e., the deformations are determined by the structural properties and the surrounding flow.

Chapter 6 continues the work presented in Chapter 5 by considering the active control of the fin rays. By individually activating each ray, different locomotion modes observed in previous experiments are reproduced and their corresponding performance is investigated. The physical mechanism behind the performance enhancement of active control is also analysed. The capability of actively changing the curvature is an important feature possessed by ray-finned fish, which has not been fully studied and its effect still remains unclear. The work presented in this chapter is the first numerical simulation attempting to investigate the effect of active control on the dynamics of ray-strengthened fins.

In Chapter 7, we further apply the FSI model to investigate the propulsion performance of an idealised underwater robotic fish, which is inspired by rajiform swimmers. The effects of motion frequency, wave length, non-symmetric kinematics of the two pectoral fins as well as Reynolds number are examined.

Finally, the conclusions of this thesis and recommendations for future research are provided in Chapter 8.

Chapter 2   Literature review

In this Chapter, experimental and numerical studies performed in the past few decades relevant to the problems studied in the present thesis, i.e., simplified ray-strengthened caudal fin model and idealised robotic fish model, are thoroughly reviewed. Generally, three main approaches are commonly used to study fish locomotion, namely, experiments with live fishes, robotic devices and computational models. Therefore, the present chapter is divided into three sections according to the aforementioned three methods. Specifically, the experimental studies using live animals are firstly reviewed in Section 2.1. The research works using robotic devices are subsequently summarised in Section 2.2. Finally, studies using computational models are reviewed in Section 2.3.

2.1 Experiments with live fish

2.1.1   *Morphology and function*

Morphologically, ray-finned fish consist of a body and various fins. Most ray-finned fish have a total of at least seven fins, which can be divided into two major groups: median fins (caudal, dorsal and anal fins) and paired fins (pectoral and pelvic fins), as demonstrated in Figure 1-2 and Figure 2-1. The shapes and positions of fish fins vary significantly among different species, as demonstrated in Figure 2-1. For example, the pectoral fins in basal ray-finned fish (e.g., S1) are located at the ventrolateral margins of the body while they are positioned more laterally on the side of the body for more derived species (e.g., S5). Besides, the orientation of the pectoral fin base in spiny-finned fish (e.g., S4 and S5) is more vertically aligned [24].

The tail of some basal ray-finned fish species is heterocercal (asymmetrical against the middle line) in shape while for more derived species, the caudal fin is homocercal (symmetrical against the middle line). But the homocercal caudal fin can also function asymmetrically to create desired lift force by generating different excursions between the dorsal lobe and ventral lobe [31].
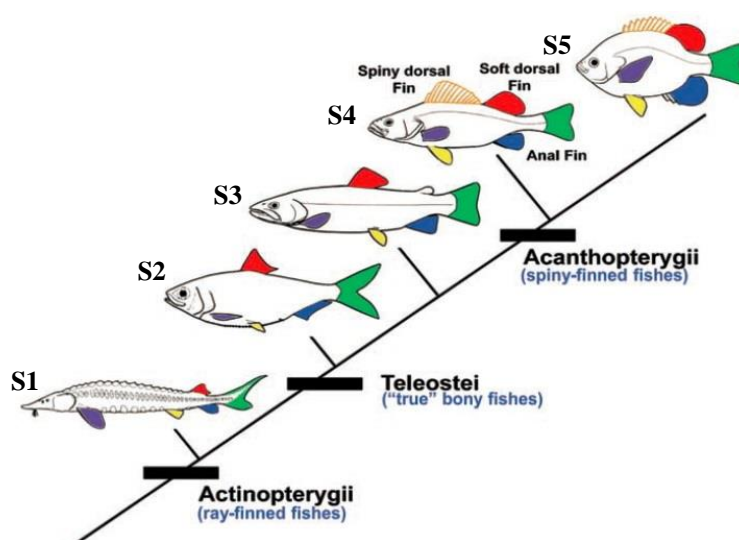
Figure 2-1 Major patterns of ray-finned fish in the evolution of the caudal fin (green), pectoral fin (purple), pelvic fin (yellow), dorsal fin (red) and anal fin (blue). Modified from [24].

Despite of the variations in shapes and positions, both median and paired fins of ray-finned fish are characterised by a collagenous membrane supported by elongated, segmented and thickened rays, and the basal ends of the rays are connected to a cartilage pad supported by the distal edges of the supporting bones, as shown in Figure 2-2 (a)–(c). For ray-finned fish, a fin ray is composed of a central cartilage pad surrounded by paired, segmented bony elements called hemitrichs, as sketched in Figure 2-2 (d), which are connected with short ligaments and elastic fibers (tendons) at the ends [28–30]. The basal end of each ray is attached to four separate muscles. By pulling the tendons, a hemitrich can slide past the other one, creating a distributed bending moment along the length of a ray (see Figure 2-2 (d)) [28]. It should be noted that the longitudinal forces provided by the tendons will cause a distributed bending

moment along the ray, which will further lead to a distributed force perpendicular to the ray. This distributed force will actively change the curvature of the ray. Therefore, this is modelled as a uniformly distributed external force along a beam in Chapter 6.
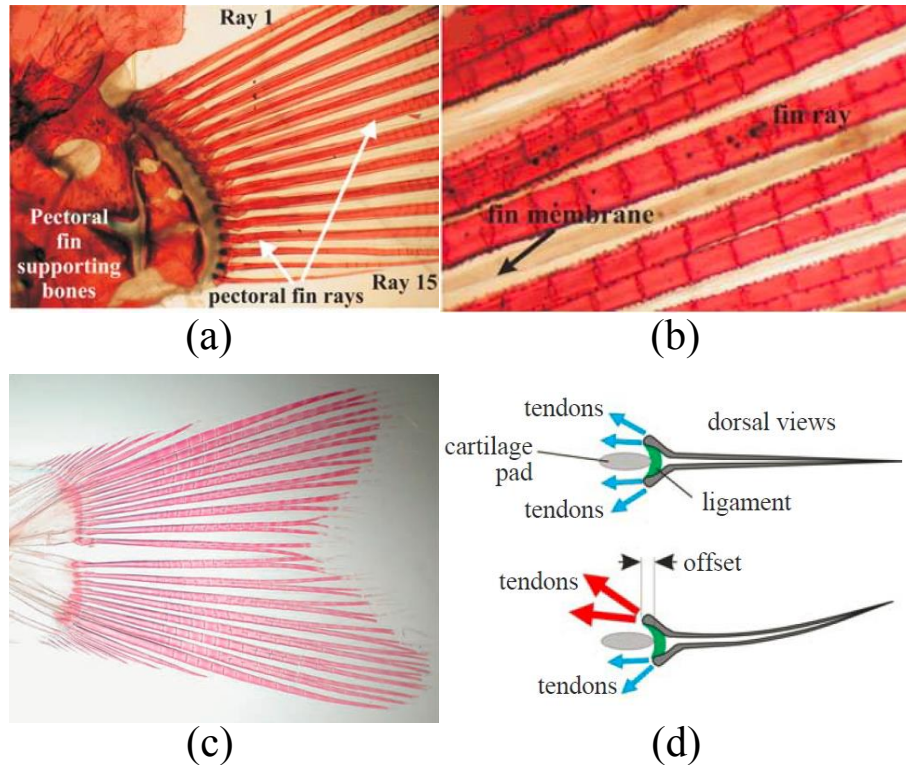
Figure 2-2 (a)Structure of a pectoral fin and the relevant skeletal supports, (b) close view of pectoral fin rays and membrane, (c) skeleton of a fish caudal fin, (d) schematic view of the bilaminar design of fin rays. Extracted from [28–30].

Generally, fish fins have two main purposes: generating force by coordinated movements and sensing for complicated locomotive tasks. The function of fins varies significantly according to the fin type and fish species. Many researchers have used the bluegill sunfish (*Lepomis macrochirus*) and rainbow trout (*Oncorhynchus mykiss*) as examples of ray-finned fish to investigate the functions of different fins. Caudal fin, as a main propeller for most fish species, is extensively studied previously ([31–35,56–59]). Early studies usually take caudal fin as an extension of fish body; however, recently functional studies reveal that caudal fin of ray-finned fish undergoes significantly 3D kinematics, which, in turn, leads to significantly 3D flow pattern and force generation [32,33]. It can create considerable lateral and lift forces

which can be used for maneuvering. Pectoral fins can be used as the primary propeller during low-speed swimming for a number of ray-finned fish species. The forces created by the pectoral fin can be reoriented by changing the attachment angle of the fin, i.e., generating forces and torques needed for maneuver behaviours such as braking, yawing, hovering and station-holding [29,60–62]. Dorsal and anal fins also play important roles in both steady and unsteady swimming by creating significant lateral and thrust forces as well as affecting the flow wake experienced by the caudal fin [33,63]. For some species (e.g., knifefish), the undulating elongated dorsal or anal fin are used as the main propellers [64,65]. The pelvic fins were believed to have very limited and mainly passive stabilizing function. However, recent studies reveal that the pelvic fins are also actively moved during many locomotion behaviours [66]. The function of a fin is also different under various locomotion behaviours. Dorsal fin is collapsed at high-speed swimming while it is actively moved during low-speed locomotion [33,67].

2.1.2 Fin kinematics

The study on the fin kinematics of ray-finned fish is mainly based on live fish experiment. The measured data can be used as input into the numerical simulations. The exact kinematics of a fin is closely associated with its function. A fin's kinematics varies significantly according to the swimming status, the type of the fin and the fish species.

2.1.2.1 Median fins

Lauder [31] experimentally measured the kinematics of two heterocercal tails (leopard shark and sturgeon) and one homocercal tail (bluegill sunfish). They found the geometrically symmetric homocercal tail of sunfish was able to function asymmetrically with larger excursion at the dorsal lobe, which created a lift force. Flammang and Lauder [35] also examined the kinematics of the caudal fin and the

motor activity of the intrinsic musculature during different locomotion behaviours using the bluegill sunfish. They found the caudal fin deformations were modulated according to various maneuvers, as shown in Figure 2-3. For example, the braking was associated with 'S'-shape deformation of the caudal fin by moving the dorsal lobe and ventral lobe in different directions. It was also found that the caudal fin muscles could be activated independently from myotomal musculature.

(a)   (b)   (c)   (d)
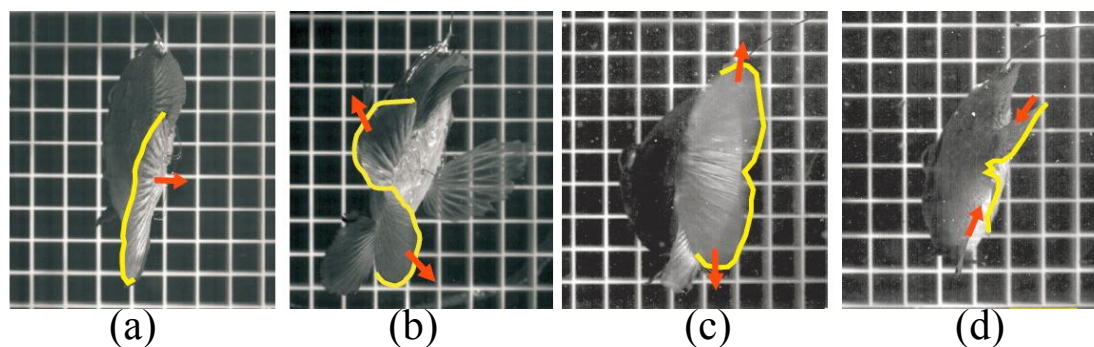
Figure 2-3 Representative examples of caudal fin shape modulation in a bluegill sunfish during different maneuvers. (a) Steady swimming at 1.2 body length per second, (b) braking, (c) kicking and (d) gliding [35]*.*

Apart from caudal fin, the kinematics of other types of fish fin was also studied by biologists. Chadwell et al. [67,68] investigated the kinematics of the dorsal and anal fins of bluegill sunfish during C-start escape response. It was found that the angular amplitudes of the rays in various positions within the fin were different, which indicated regions within the fin had different roles. They also found the fish actively bent the fin rays to resist the hydrodynamic load. Flammang and Lauder [69] studied the fin kinematics of bluegill sunfish during backward swimming. They found that the backward swimming was a multi-fin behaviour involving the coordination of the pectoral, dorsal, anal and caudal fins, rather than a simple reverse of slow forward swimming.

2.1.2.2   Paired fins

Drucker and Lauder [61] studied the function of the pectoral fin of a rainbow trout by kinematic analysis. The pectoral fin was adducted against the body when cruising at

relative higher speed, but was actively moved during a variety of maneuvering behaviours such as hovering, turning and braking. The trout was able to rotate the fin base over 30 degree in order to create desired force for maneuvering. Lauder et al. [29,62] later measured the kinematics of a pectoral fin of bluegill sunfish using high resolution digital videos. It was observed that the pectoral fin is highly flexible and subject to complicated passive and active control mechanisms, including the change of area, bending in both chordwise and spanwise directions, presence of two simultaneous leading edges by cupping the pectoral fin (Figure 2-4 (b)) and waves passing along the fin (Figure 2-4 (c)).

(a)　　　　　　　　(b)

(c)　　　　　　　　(d)
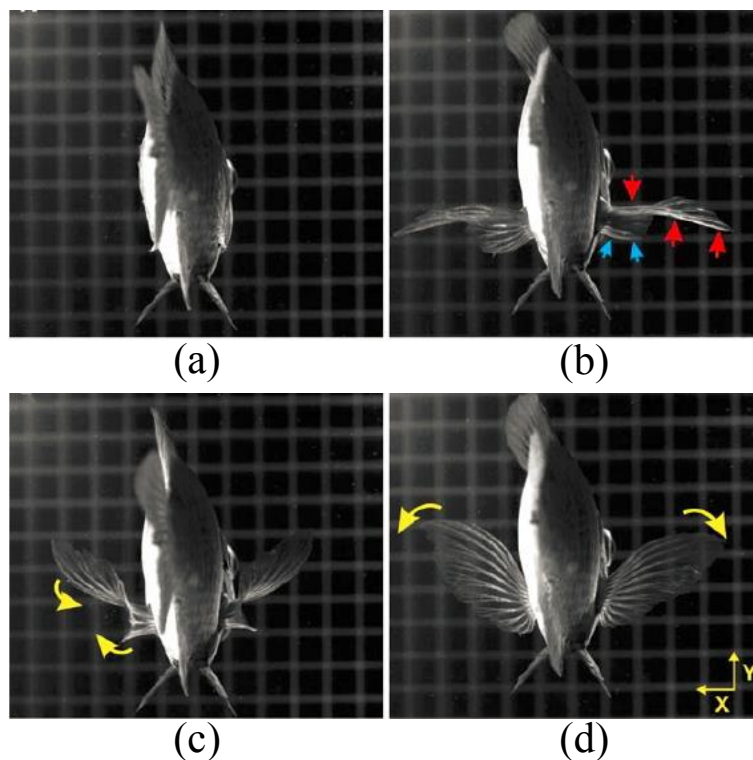
Figure 2-4 Pectoral fin kinematics in bluegill sunfish swimming at 0.5 body length per second during a single fin beat cycle. (a) Pause phase prior to the start of the fin beat cycle. (b) Middle of the fin outstroke showing the cupped configuration of the fin in which both the upper and lower fin rays move out from the body together, forming two leading edges. (c) Twisting of the fin at the transition between outstroke and return stroke. (d) Middle of the return stroke during which the fin is expanded and pulled back toward the body [29].

Different from those fish species with multiple fins (e.g., bluegill sunfish, rainbow trout), most rajiform swimmers (e.g., stingray, skate) only possess a pair of enlarged pectoral fins, which are used for both locomotion and maneuvering. In fact, most

rajiform swimmers are not ray-finned fish (*Actinopterygii*). Instead, they belong to *Elasmobranchs*, which have completely different skeleton structures compared with actinopterygii fins [70]. Due to the remarkable locomotion performance and potential applications in biomimetic underwater robots (see examples in [71,72]) of rajiform swimmers, their fin kinematics also attracts research interests from biologists. Blevins and Lauder [73] carried out a 3D analysis of the undulating motion of the pectoral fins of the freshwater stingray (Figure 2-5 (a)). As observed from Figure 2-5 (b), the wave amplitude of the pectoral fin increases both antero-posteriorly and medio-laterally, and only a relatively small region of the fin moves in large amplitudes. It was also observed that stingrays are able to produce extreme lateral curvature to resist the hydrodynamic loads, which may be related to drag reduction. Santo et al. [74] studied the effect of swimming speed on the deformation of pectoral fin in the little skate (*Leucoraja erinacea*). They found that at higher speed, the little skate can cup the pectoral fin into the flow, implying the active curvature control and fin stiffening.

(a)

(b)
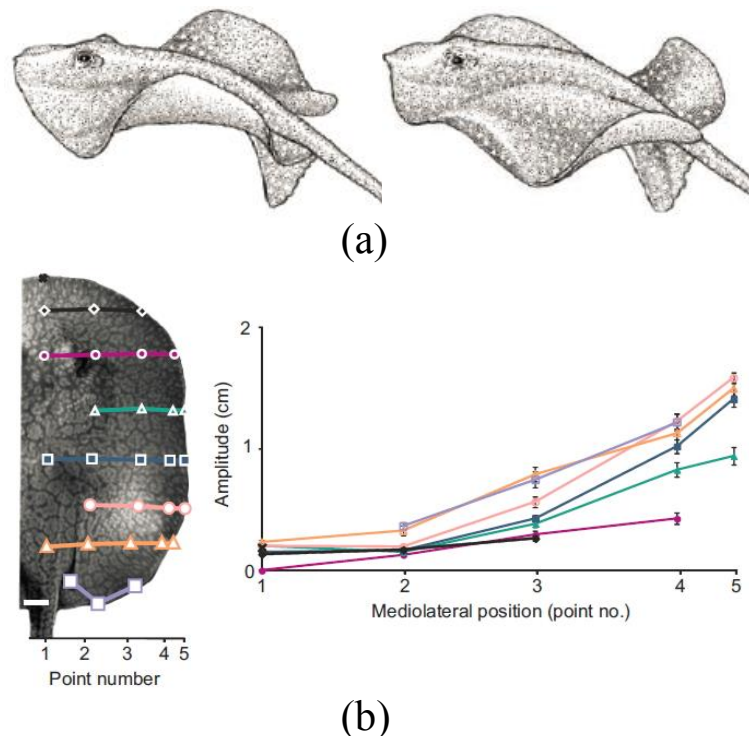
Figure 2-5 (a) Illustration of stingray swimming at 1.5 body length per second. (b) Spanwise amplitude variation along the medio-lateral axis at positions indicated on the stingray image [73].

2.1.3 *Hydrodynamics*

2.1.3.1 Median fins

Drucker and Lauder [75] investigated the hydrodynamic forces and wake structures generated by the dorsal fin of a bluegill sunfish. The dorsal fin during steady swimming (1.1 body length s^{-1}) created a reverse von Karman vortex street that contributed about 12% of total thrust. But during low-speed turning maneuvering, the force generated by the dorsal fin was mostly in lateral direction. The wake created by the dorsal fin could constructively interact with caudal fin by increasing the thrust force, as demonstrated in Figure 2-6.
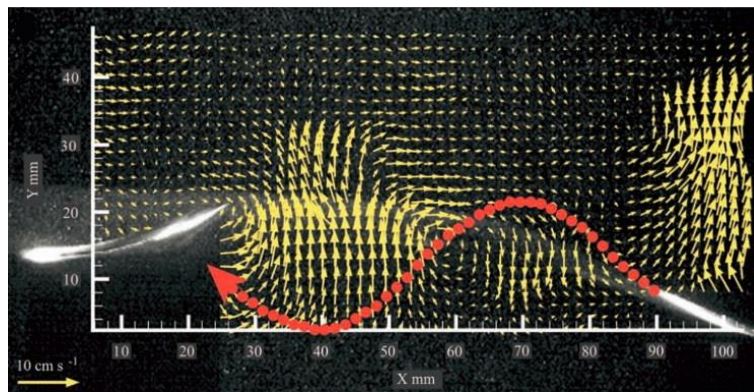
Figure 2-6 Path (red dots) taken by the tail through the wake generated by the dorsal fin (yellow arrows) [76].
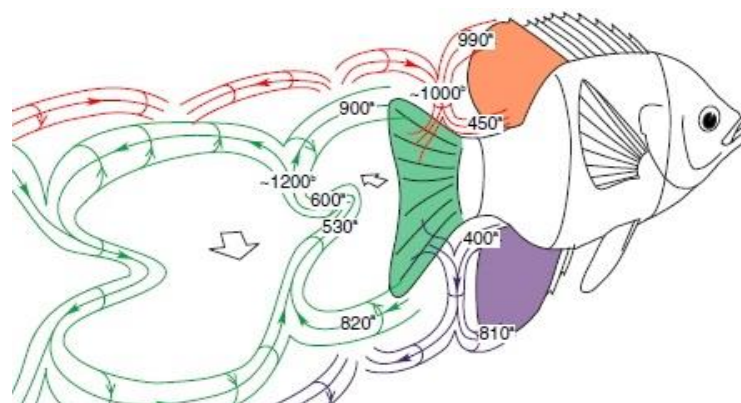
Figure 2-7 3D vortex structure for bluegill sunfish swimming at about 1.2 body length per second [33].

Tytell [32] and Tytell et al. [33] analysed the streamwise vortex structure shed by the median fins. The kinematics of these fins were fully 3D, thus it was not appropriate to be simplified as 2D motion. A hairpin vortex structure was proposed to describe the vortex wake, as shown in Figure 2-7. It was also found that the dorsal and anal fins contributed significantly to the total thrust during steady swimming.

2.1.3.2 Paired fins

With live animal experiments, Drucker and Lauder [60] measured the hydrodynamic forces and wake structures created by the pectoral fin of black surfperch (*Embiotoca jacksoni*) and bluegill sunfish (*Lepomis macrochirus*) during labriform swimming and explained why the black surfperch swam faster than similar sized bluegill sunfish. It was observed that the pectoral fin could generate either single or double vortex rings (Figure 2-8) depending on the swimming speed. They also found that black surfperch was able to generate stronger wake momentum and reorient this momentum in a direction more favourable for propulsion. In contrast, bluegill sunfish created considerably larger lateral force, which may be important for body stabilising. It was hypothesised that bluegill sunfish may have higher maneuverability and there was a hydrodynamic trade-off between swimming speed and maneuverability.
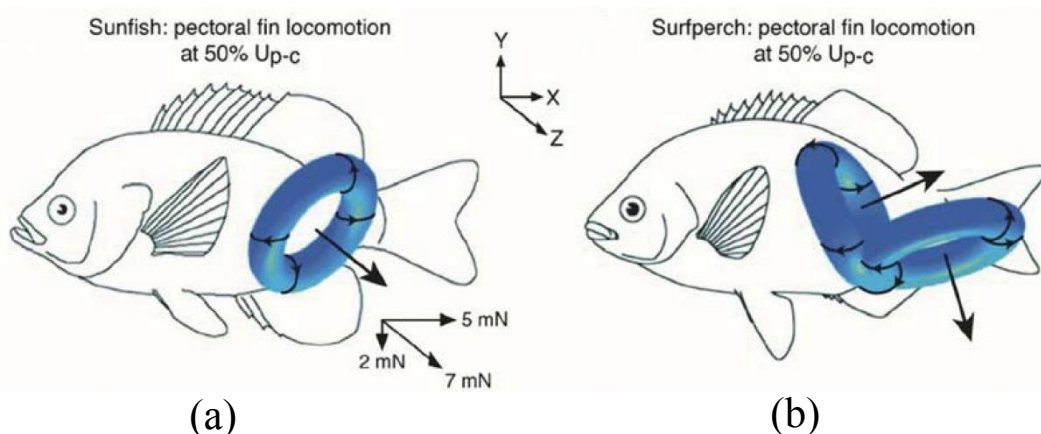
Figure 2-8 Schematic 3D representation of the pectoral fin wake at the end of the upstroke in the (a) bluegill sunfish and (b) black surfperch. Both fish are swimming at 50% of their maximal pectoral-fin swimming speed [60].
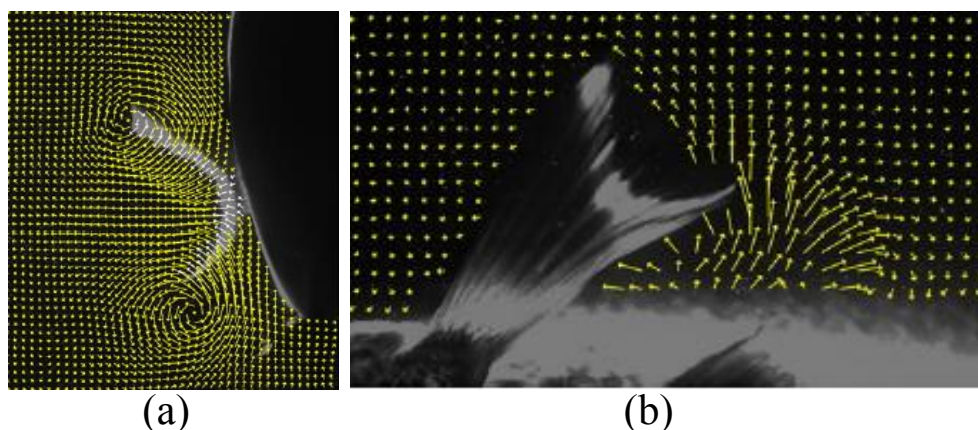
Figure 2-9 (a) Flow pattern around the sunfish pectoral fin at mid-outstroke, where the cupped shape of the fin leads to the development of two strong leading edge vortices simultaneously on both the upper and lower fin edges as the pectoral fin moves away from the body. (b) The accelerated flow resulting from fin movement away from the body, indicating that sunfish pectoral fins generate thrust both during motion away and toward the body [29,62].

Lauder et al. [29,62] studied the hydrodynamic forces and wake patterns of the pectoral fin of a bluegill sunfish. It was found that in the outstroke of the pectoral fin, dual leading edge vortices (LEVs) with opposite signs were produced due to the cupping deformation (Figure 2-9 (a)). The dual LEVs were believed to minimise the vertical body oscillation. During both outstroke and instroke, water between the pectoral fin and body was accelerated, creating thrust force (Figure 2-9 (b)). It was also found that through complicated 3D kinematics, pectoral fin was able to create net thrust throughout the whole fin beat cycle, which contrasted to the data of traditional flapping foils, where net drag force was generated during a short period of time within a motion cycle.

2.2 Experiments with robotic devices

Although experiments using live fish shed light on the kinematics and hydrodynamics of fish locomotion (see Section 2.1), the disadvantages and limitations of this approach are also obvious [8]. Primarily, it is impossible to study the effect of individual traits on the performance. Another limitation is the lack of sufficient diversity among extant species. To address these issues, an alternative method is to construct fish-like or fin-like robotic devices. This approach allows more freedom in

alternating the parameters (e.g., geometry, material properties, and kinematics) so that the effect of each parameter can be isolated [40]. Some review papers on this topic are available in [40,56,77–81].

2.2.1 *Simplified mechanical devices*

Despite the complexity of fish geometry as well as structural property, simple flexible panels have proven to be useful models for fish locomotion. These simple models are favoured because their stiffness, length and shape can be altered easily, which allow fast reconstructions and short turn-around time. Heathcote et al. [82,83] experimentally studied the propulsion performance of flexible plunging foils with different bending stiffness. They found that a certain degree of flexibility augmented both thrust and propulsion efficiency. The deformation of the flexible foil created an effective pitch motion, whose amplitude and phase angle with respect to the plunging motion played a critical role in determining the foil's performance. It was also revealed that stronger trailing edge vortices (TEVs) were associated with higher thrust generation while weaker leading edge vortices (LEVs) were corresponding to higher propulsion efficiencies. Additionally, they also found that the maximum propulsion efficiency was achieved at a pitch phase angle of 95-100 degree whereas the thrust peaked at pitch phase angles in the range of 110-120 degree at higher Strouhal numbers. This also indicated that the highest efficiency and largest thrust could not be accomplished simultaneously. Quinn et al. [84] examined the ground effect of an oscillating flexible panel. It was found that the panel was able to produce larger thrust with the existence of ground effect. The propulsion efficiency could also be increased due to the resonance swimming. The enhancements of both thrust and propulsion efficiency were attributed to the suppression of three-dimensional modes.

(a)   (b)

(c)   (d)
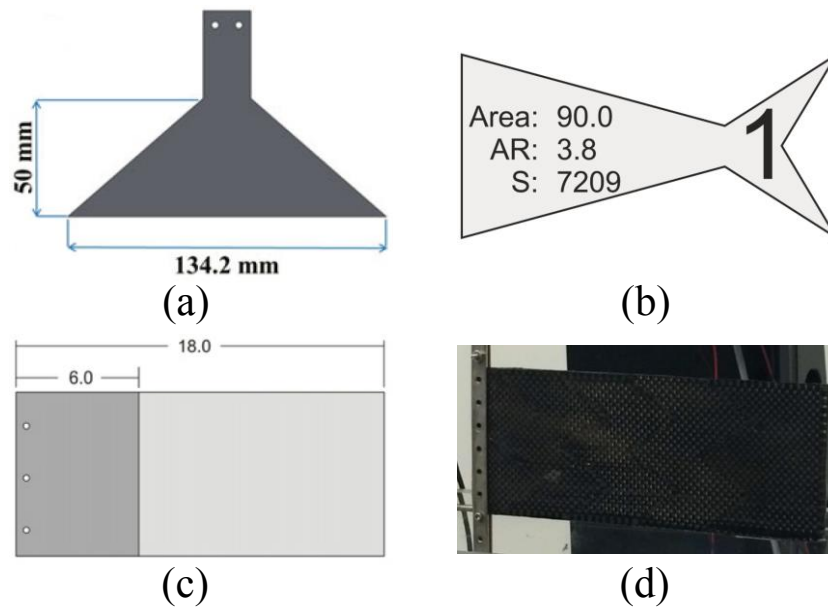
Figure 2-10 Illustrations of different simplified mechanical devices used for the study of fish locomotion. (a) Caudal fin model [36]*, (b) tuna-like tail model* [37]*, (c) fish-like foil model* [85]*, and (d) fin-like foil model* [86]*.*

Park et al. [36] experimentally examined a biomimetic caudal fin with various shapes (one of them is shown in Figure 2-10 (a)) and uniform bending stiffness to identify the optimal kinematic condition maximising the thrust generation. They concluded that the maximum thrust was achieved when the phase difference between the driving motion and the passive bending motion was close to 90 degrees. Feilich and Lauder [37] experimentally investigated the effects of caudal fin shape and stiffness on self-propelled tuna-like tail models (one of them is shown in Figure 2-10 (b)). In their experiments, four different foil shapes with three different rigidities were tested. They concluded that the foil shape and flexibility interacted in complicated ways, i.e., no single 'optimal' foil performing the best in all scenarios was found.

Considering the fact that the flexibility decreases along the fish's anterior-posterior axis, some researchers examined the effect of non-uniform bending stiffness distribution on the performance of fish-like propellers. Lucas et al. [85] fabricated four different fish-like foils, where two of them had uniform bending stiffness while the other two were with higher stiffness at the anterior regions (one of them is shown in Figure 2-10 (c)). They concluded that the combination of the non-uniformly

distributed bending stiffness and zero-degree angle of attack (AOA) pitching program resulted in higher self-propelled speed at relatively high efficiency. Kancharala & Philen [86] experimentally measured the chordwise stiffness profiles of real caudal fins. Based on the measured data, a caudal fin-like foil was fabricated and tested in water tunnel (see Figure 2-10 (d)). Improvements in thrust generation and efficiency were observed for fins with non-uniform stiffness, which were attributed to larger trailing edge amplitudes and higher curvatures.

2.2.2   *Complex mechanical devices*

(a)

(b)

(c)

(d)
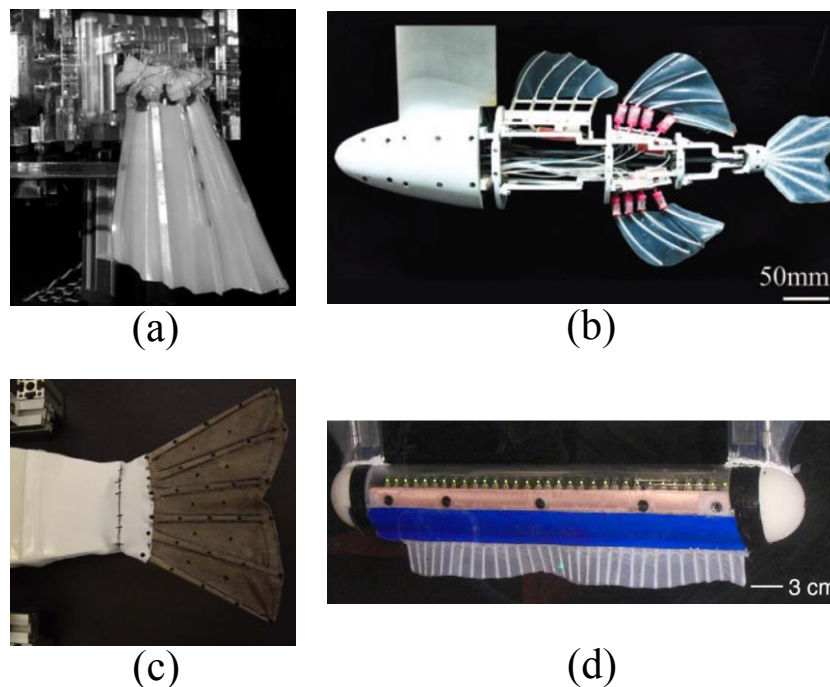
Figure 2-11 Illustrations of complex mechanical fin models. (a) Robotic pectoral fin [87], (b) robotic rainbow trout [88], (c) robotic caudal fin [38], and (d) robotic knifefish [21].

Structurally, a fin of ray-finned fish is composed of a soft membrane and supporting rays, forming a skeleton-reinforced bio-membrane system. The fish fins are able to create realistic 3D kinematics and provide multiple degree of freedoms (DOFs) for fish maneuvering, which cannot be achieved by using simple flexible panels. Therefore, some researchers are also focused on building more complicated fish-like or fin-like robotic systems, which can be used to investigate the hydrodynamics of

fish locomotion or to be the prototypes of bio-inspired underwater robots [30,64,70,89].

By fabricating robotic fin-like devices (Figure 2-11 (a)), Tangorra et al. [87,90] designed and tested a bio-robotic pectoral fin, in which the flexible, bi-laminar rays were embedded in a soft webbing material. The fin was actuated by individually controlling the nylon tendons attached to the base of each ray. Such a compliant-mechanism-based design allowed active control over the fin's deformation and motion. However, they did not compare their actively controlled robotic fin with an equivalent fin with solely passive deformation. Therefore, the effect of active control on the fin's performance remains unclear.

(a)

(b)
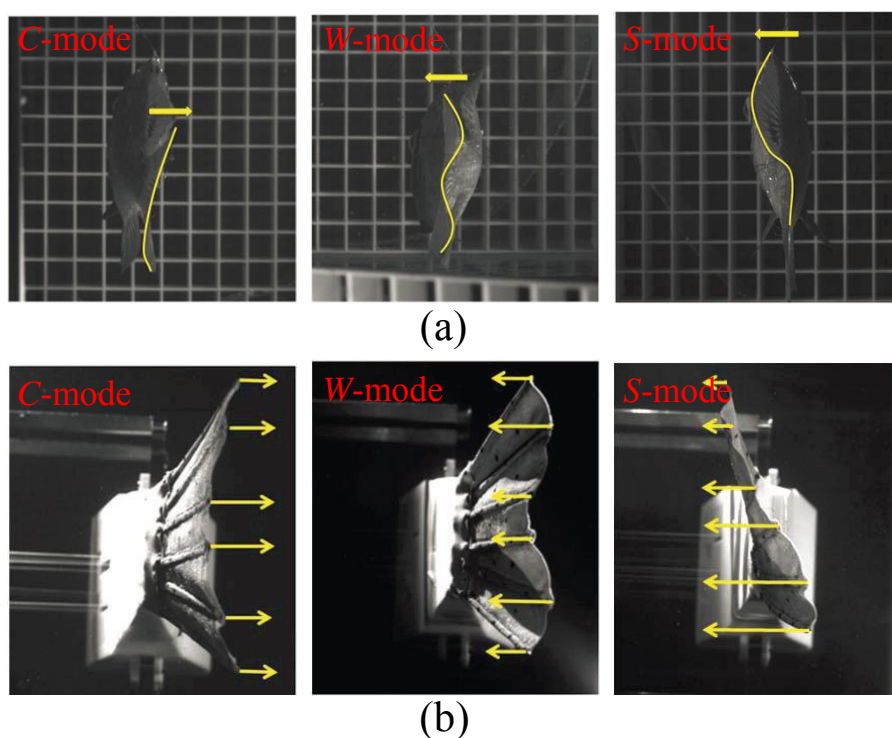
Figure 2-12 (a) Posterior views of a bluegill sunfish performing steady swimming and maneuvering motions. (b) Posterior views of the robotic caudal fin performing similar caudal fin movements. Yellow arrows indicate the direction of motion of the individual fin rays[38] .

Esposito et al. [38] constructed and tested a sophisticated robotic fin by imitating the caudal fin of bluegill sunfish (Figure 2-11 (c)). With six independently controlled and actuated rays, this robotic fin was able to produce some motions (e.g., *C*-mode: the

dorsal and ventral lobes lead the motion while the central part falls behind; *W*-mode: more than one curvature reversals can be observed; and *S*-mode: a wave-like motion exists along the spanwise direction) observed in live fish experiments (as demonstrated in Figure 2-12). They found that the cupping motion was able to create the largest thrust in most cases while the undulation motion produced lift of the same magnitude as thrust. It was also observed that larger thrust was achieved with stiffer rays at higher flapping frequency. Besides, it was suggested that different optimal values of ray stiffness exist in different scenarios.

Ren et al. [39] constructed a robotic caudal fin with individually actuated rays, whose motion was coupled with an undulatory motion of the peduncle. It was found that the propulsion performance of the mechanical caudal fin was heavily dependent on the phase between the ray's motion and peduncle's motion. Wen et al. [88] investigated the fish linear acceleration behaviour using a biomimetic robotic fish model with a spiny dorsal fin and soft dorsal, anal and caudal fins (Figure 2-11 (b)). It was found that the linear acceleration rate was enhanced by 32.5% by erecting the soft dorsal and anal fins. A decrease of lateral force was observed despite of the increase of projected body area in the lateral plane.

Shirgaonkar et al. [91] studied the hydrodynamics of ribbon fin propulsion using both a robotic ribbon fish and a computational model. The movement of the fin was idealised as a travelling sinusoidal wave. It was found that the primary thrust production mechanism was associated with the creation of a streamwise central jet. They also found that the ribbon fin was also able to create a heave force, which may be used to balance the body gravity. As the increase of the wave number along the fin, the surge force gradually surpassed the heave force, indicating a switch from oscillatory normal thrust to undulatory parallel thrust. Curet et al. [21] examined some basic properties of undulatory locomotion using a biomimetic robotic knifefish

(Figure 2-11 (d)). By systematically varying the critical parameters such as frequency, amplitude and wavelength, they recorded the forces created during different parameter combinations. They identified an optimal operational region within the kinematic parameter metrics, which was similar to those observed parameters for live black ghost kinfefish.

Liu and Curet [92] investigated the kinematics and propulsion performance of a robotic kinfefish in both fully-actuated and under-actuated states. Compared with fully-actuated case, the under-actuated fin produced less thrust but consumed significant less power as well. Both the full-actuated and under-actuated fins shared similar scale laws, i.e., linear with enclosed area and quadratic with relative velocity. Besides, it was also found that the under-actuated fin produced similar propulsion efficiency as the fully-actuated one, indicating the possibility of exploiting the passive fin motion without sacrificing the efficiency. Liu and Curet [93] studied the propulsion performance of a mechanical undulating fin with different flexible rays and aspect ratios. They found that the increase of the ray's flexibility decreases both the thrust generation and power consumption. However, the propulsion efficiency was improved by flexible rays compared with a rigid counterpart. Additionally, it was also observed that the aspect ratio had a significant effect on the performance of the undulating fin, indicating that for a given fin kinematics, there could be an optimal aspect ratio.

2.3 Computational models

From the perspective of underwater robotics design, it would be beneficial if we could explore a large parameter space to find the optimal combination. However, neither studies on live fish nor those using mechanical devices allow this. For example, the bending stiffness of the caudal fin plays a crucial role on its performance, however, we do not know if the caudal fins of live fish are at the optimal flexibility. Although

mechanical devices can be constructed with different structural properties, they are still subjected to the availability of materials. These restrictions can be circumvented in computational modeling. Moreover, numerical simulations can provide detailed information of the flow field as well as physical insight of the fluid-structure interactions. The advantage of examining "what if" type of questions makes the computational modeling more appealing compared with experiments [42]. With the advancement of high-performance computers and high-fidelity numerical algorithms, computational modeling has become an indispensable complement to experimental studies. Generally, the computational models of bio-inspired propulsive systems can be classified into flapping foil models and skeleton-reinforced fin models according their structural complexity.

2.3.1 Oscillatory foil models

(a)   (b)
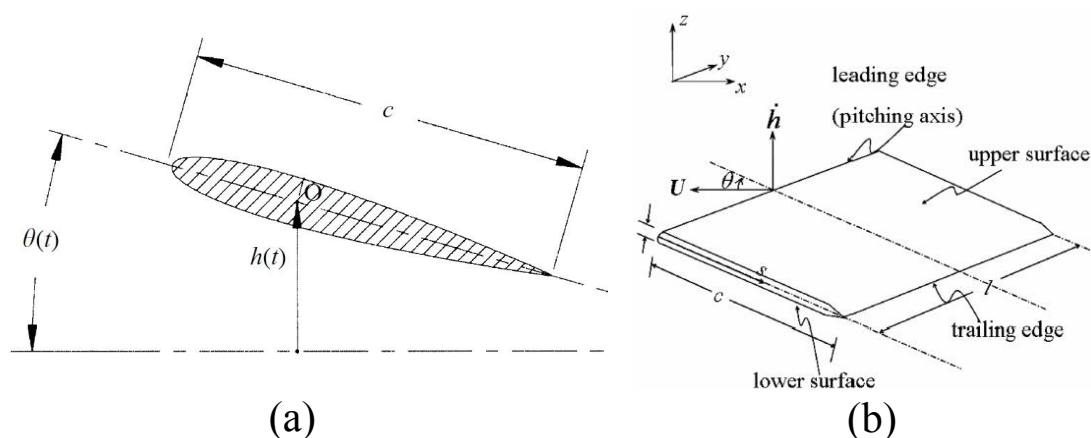
Figure 2-13 Schematic view of oscillatory foils. (a) NACA0012 foil model [94]*, and (b) flat plate model* [95]*.*

Despite of the complicated internal structure of real fish fin (see Subsection 2.1.1), it has been traditionally simplified as either rigid or flexible foils, as illustrated in Figure 2-13. The foil usually undergoes sinusoidal heave and/or pitch motion around an axis, which mimics the oscillatory motion of fish body or caudal fin. Lewin and Haj-Hariri [96] examined the thrust generation of a 2D plunging foil using a viscous flow solver. Both symmetric and asymmetric flow wake patterns were found in their study and the

maximum efficiency was achieved at an intermediate frequency. They propulsion performance was heavily dependent on the interaction (positively or negatively) between the LEVs and TEVs. Young and Lai [97] studied the mechanisms affecting the performance of a rigid foil undergoing a combined pitch and heave motion using a 2D compressible Navier-Stokes flow solver. They found the LEV shedding could significantly influence the propulsion performance. The creation and convection of the LEVs were affected by motion amplitudes, phase angle between pitching and plunging, the oscillating frequency. Therefore, the performance of an oscillating foil could not be characterised by solely the Strouhal number. Blondeaux et al. [98] numerically investigated the wake structures behind a rigid flapping foil with finite span, which imitated the tail of a carangiform swimmer. A vortex ring was shed into the wake every half a cycle and the dynamics of the vortex ring depended on the Strouhal number. Weak vortex ring interaction was observed at small Strouhal numbers while vortex ring reconnection indicating strong interaction was found at large Strouhal numbers.

Considering the structural flexibility, Zhu [95] numerically investigated the propulsion performance of a flapping foil with chordwise or spanwise flexibility. In this study, a boundary-element method based on potential flow theory was used to simulate the fluid dynamics while the flexible foil was structurally represented by a nonlinear beam model. Two different fluids (high density fluid and low density fluid) were considered. For high density fluid, where the foil's deformation was primarily determined by the fluid force, the chordwise flexibility increased the efficiency while both the thrust and efficiency were declined by the spanwise deformation. For low density fluid, where the foil's deformation was mainly affected by the inertia of the foil, it was found that chordwise deformation deteriorated both thrust and efficiency. However, spanwise deformation was able to increase the thrust without the reduction of efficiency within a small range of structural parameters.

Olivier and Dumas [99] studied the propulsion performance of a 2D flexible flapping foil at a low Reynolds number using a fluid-structure interaction model, where the fluid dynamics was resolved by OpenFOAM whilst the structural dynamics of the foil was simplified as a nonlinear beam. Both inertia-driven and pressure-driven regimes were considered in this study. It was found that for pressure-driven deformations, both thrust and efficiency could be improved by using a suitable amount of flexibility. Inertia-driven deformations, on the other hand, decreased both thrust and efficiency of the foil. However, the foil's performance could be slightly improved by introducing sustainable superharmonics into the foil's motion properly.

Dai et al. [100] numerically studied the performance of an elastic low-aspect-ratio pitching panel. The fluid dynamics was simulated by an IBM based flow solver whereas the structural dynamics was solved using a 3D FEM model. It was found that for medium flexible panels, only a 1st order bending mode was created while higher bending modes were also observed for highly flexible cases. For both rigid and flexible panels, wake transition was seen. The wake was composed of a series of interconnected horseshoe-shaped vortices at smaller Strouhal numbers while the wake topology transited into double chains of closed vortex rings. Hua et al. [46] examined the locomotion of a 2D heaving elastic plate mimicking fish swimming. The fluid field was resolved using a viscous flow solver based on an immersed boundary-lattice Boltzmann method while the elastic plate was structurally represented as a nonlinear beam. Three locomotion states were identified, namely forward, backward and irregular. The occurrence of a certain state primarily depended on the heaving amplitude and bending stiffness of the plate. An appropriate degree of flexibility was able to augment the swimming performance. Two different vortex patterns (normal and deflected wakes) were observed. Yeh and Alexeev [51] numerically studied the free swimming performance of a flexible plunging panel using a coupled FSI model,

39

where the fluid dynamics and solid dynamics were resolved using a lattice Boltzmann model and a lattice spring model respectively. It was observed that the swimming speed was maximised near the resonance frequency where larger deformations were achieved. However, the best swimming performance was found at a non-resonance frequency where the deformation pattern led to a minimum transverse movement of the panel's centre of mass.

2.3.2   *Ray-strengthened fin models*

As discussed in Section 2.1.1, the active and passive control over the bony rays embedded in the collagenous membrane enable ray-finned fish to modulate their fin shapes to obtain desired forces in different directions. This unique composite architecture of the fin has three main features: 1) anisotropic flexibility over the fin; 2) individual activation of the rays; 3) control on the ray's curvature. These features enable the fish to have multi-degree-of-freedom control over their fins, and also provide a source of inspiration for the design of bio-inspired underwater robotics.

2.3.2.1   *Fin kinematics*

Previously experimental studies of live fish [29,35,62] revealed that the fish fin kinematics is fully 3D and is achieved by complicated active and passive control mechanisms. However, with the currently available algorithms, it is extremely difficult to numerically duplicate the exact fin kinematics. Therefore, some researchers only focus on the hydrodynamics of fish fins and the CFD simulations are carried out using the experimentally measured fin kinematics as an input [42–44]. For example, Dong et al. [43] numerically investigated the hydrodynamics of the pectoral fin of bluegill sunfish during steady swimming. The kinematics was reconstructed from previous experiment using live fish [29,62] using a POD-based algorithm [101]. The raw data was obtained from two high-speed and high-resolution video cameras placed in two orthogonal perspectives (lateral and ventral). The movement of the

pectoral fin can be divided into two phases, namely abduction and adduction. The reconstructed fin deformations during abduction phase are demonstrated in Figure 2-14. It is seen that the pectoral fins of bluegill sunfish are highly flexible and exhibit complicated features: changes in area, bending in both chordwise and spanwise directions, and distinct correlated movement of the upper (dorsal) and the lower (ventral) edges.
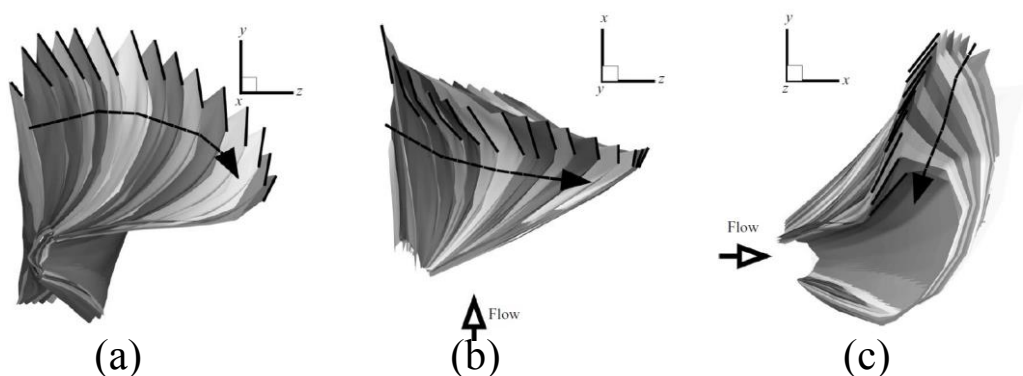
Figure 2-14 Three views of the fin motion during abduction phase. (a) Front view; (b) top view; (c) side view [43].

Although the CFD analysis using experimentally measured fin kinematics provides some insights into the hydrodynamics of fish fins, the fluid-structure interaction effect, which is an important feature of flexible fish fins, is not considered in such approaches. Therefore, some other researchers are focused on building sophisticated fin models with simplified kinematics while considering the passive fluid-structure interaction effect. Shoele and Zhu [52] built ray-supported pectoral fin model to investigate its propulsion performance. In their model, the kinematics of the pectoral fin was comprised three motions: a dorso-ventral flapping motion using the baseline as axis, an antero-posterior rowing motion of the fin rays while keeping the baseline fixed and a baseline pitching motion, as demonstrated in Figure 2-15.

41
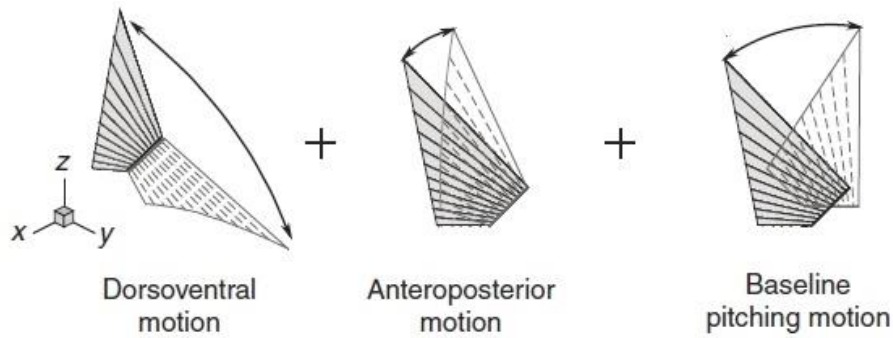
Figure 2-15 Different components of a pectoral fin kinematics [52].

Another 2D pectoral fin model during lift-based swimming was established by Shoele and Zhu [27], as shown in Figure 2-16. The fin's deformation was determined by the motion of the controlling points along the fin, which represented the locations of fin rays. The motion of the controlling points was further determined by the motion of the corresponding reference points which were connected to the controlling points via springs, which depicted the stiffness of the rays. Such a fin model allows individual actuations and non-uniform stiffness distribution of the rays.
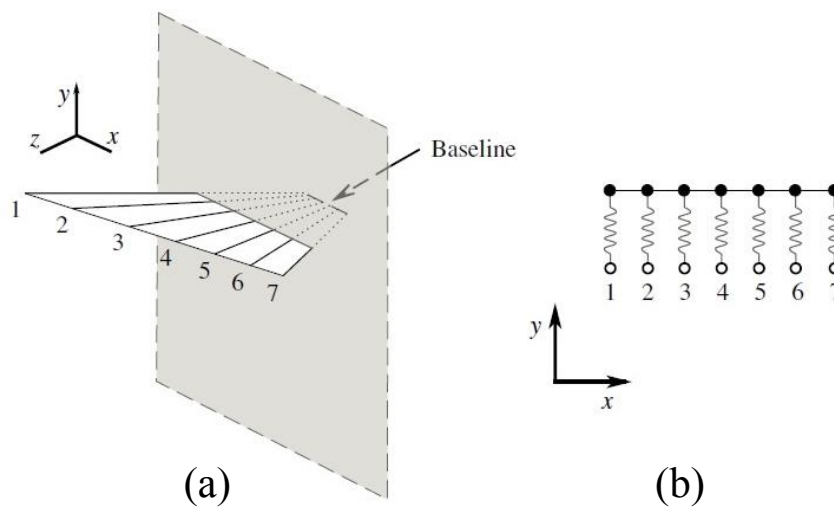
Figure 2-16 (a) Schematics of a pectoral ray fin and (b) its model system representation. The controlling points are shown as bullets, and the reference points are shown as circles [27].

As illustrated in Figure 2-17, the kinematics of fish caudal fin is usually simplified as a sway and/or yaw motion at the leading edge of the fin, which imitates the motion of the posterior part of fish body [25,53,102]. The key difference between ray-supported caudal fin and a flexible panel is that each single fin ray can be actuated individually, which enables fish to modulate the conformation of the caudal fin [35].
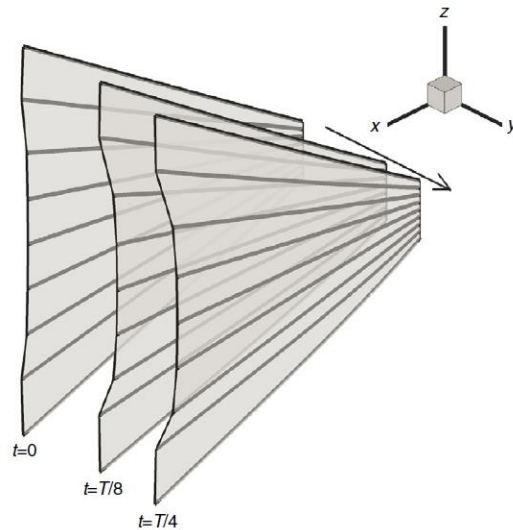
Figure 2-17 Illustrations of the caudal fin deformation within 1/4 motion period. The arrow shows the direction of sway [25].

For gymnotiform and rajiform swimmers (see Figure 1-4 and Figure 2-5 for examples), the undulatory motion of the anal fin (*Gymnotiform swimmers*) and pectoral fin (*Rajiform swimmers*) is usually idealised as travelling waves along the fin. Figure 2-18 illustrates simplified ribbon fin, which models the undulating anal fin of knifefish. The fin's performance is mainly determined by the aspect ratio of the fin, wavelength, frequency and rotation angle.
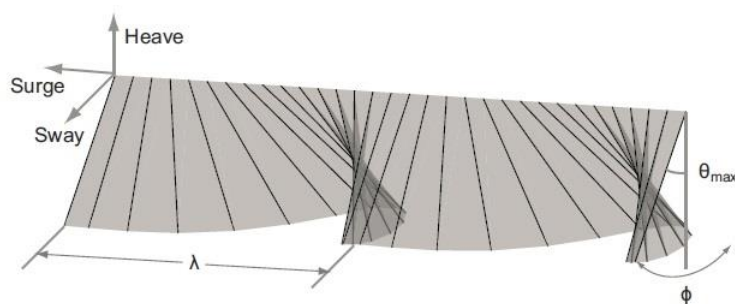
Figure 2-18 Schematic of the ribbon fin showing the wavelength (λ), angular fin amplitude (θ), and the robot body frame (surge, heave and sway) [103].

2.3.2.2 *Hydrodynamics and fluid-structure interaction*

The numerical studies on the hydrodynamics of ray-supported fish fins can be divided into two major groups according to how the kinematics of the fin is obtained. In the first group, both the geometry and the kinematics are reconstructed from experimental

measurement of live animals. Mittal et al. [42] examined the hydrodynamics of a pectoral fin with significant shape-change using an IBM flow solver. The kinematics of the pectoral fin was obtained from experimental measurements [62]. Their study shows that the pectoral fin generated net thrust throughout the entire beat cycle as demonstrated in Figure 2-19, which is consistent with experimental measurements. The flow fields from CFD and PIV are also comparable as shown in Figure 2-20. Dong et al. [43] continued the investigation of the hydrodynamics of a highly deformed pectoral fin based on the work of Mittal et al. [42]. It was found that the high propulsion performance of the pectoral fin was attributed to the complicated active and passive fin deformation. A strong, long lasting and attached tip vortex was produced during the abduction of the fin, which was responsible for the high thrust creation.
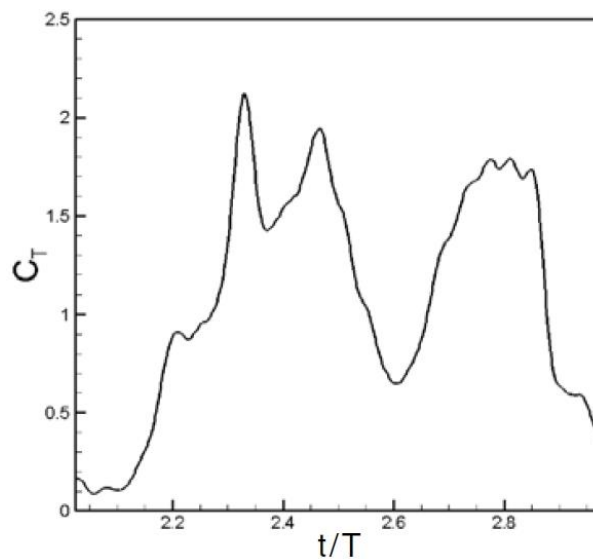
Figure 2-19 Computed temporal variation of thrust coefficient for the pectoral fin at $R_e = 1440$ [42].

<div align="center">(a)   (b)</div>
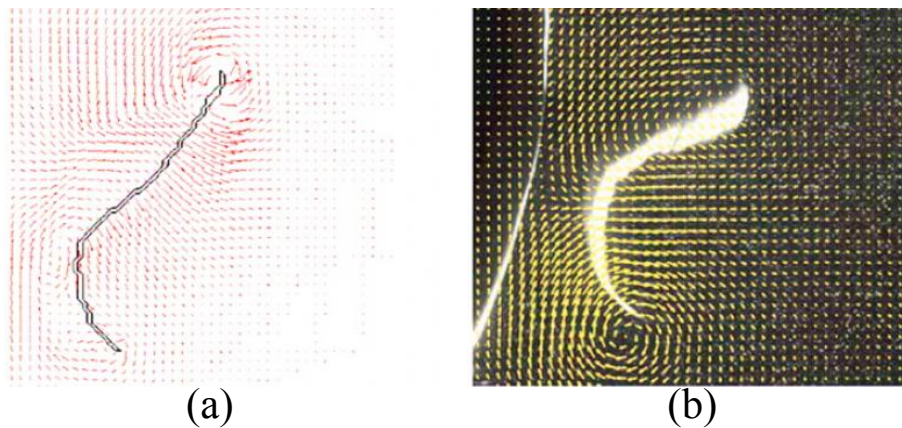
Figure 2-20 Vector plots on a streamwise plane located at 67% from the root of the fin [42], t=0.35T. (a) CFD simulation, (b) PIV measurement.

Liu et al. [44] numerically studied the hydrodynamic benefits of body-fin and fin-fin interactions using geometry and kinematic data reconstructed from live fish experiment. They found that the LEVs generated by the caudal fin, which were further strengthened by the posterior body vortices, were associated with most of the thrust generation. The median fins in the posterior region could further strengthen the posterior body vortices and caudal fin wake capture mechanism.

In the second group, researchers are using simplified models capturing some main features possessed by real fish to elucidate the effects of these characteristics. Alben et al. [28] developed a two-dimensional linear elasticity model of a bi-laminar fin ray, where the two hemitriches were represented by two identical, inextensible beams and the space between them was filled with incompressible linearly elastic material. By imposing a point force and a uniformly distributed force to the ray model, they found that tapered rays can achieve larger curvature near the tip; while for uniform rays, the curvature is localised near the base. However, the interaction with an external fluidic environment was not investigated in their study.

Shoele and Zhu [26] studied the propulsion performance of a simplified ray-supported pectoral fin during lift-based swimming. The fin was actuated by dorso-ventral

rotations of the basal ends of the rays. They found that structural flexibility could increase both the thrust and propulsion efficiency and the phase lags between different rays played a pivotal role in determining the fin's performance. With a similar numerical model, Shoele and Zhu [52] examined the propulsion performance of a ray-strengthened pectoral fin that geometrically, structurally and kinematically resembled a real fish pectoral fin during labriform swimming. The fin was activated by dorso-ventral and antero-posterior rotations of the rays as well as pitch motion of the fin base (Figure 2-15). It was found that the performance of the fin was enhanced by strengthening the leading edge ray, which decreased the effective AOA and reduced the power expenditure.

Shoele and Zhu [27] also numerically examined the propulsive performance of 2D skeleton supported pectoral fins using an IBM flow model. They concluded that the non-uniform stiffness distribution may significantly improve the performance, especially with a strengthened leading edge. This is consistent with their previous paper examining a 3D ray-supported pectoral fin using a potential flow model [52]. Shoele and Zhu [54] continued their previous work [27] by further investigating the interactions between multiple fins. Three different configurations (tandem fin, parallel fin and three-fin triangle) were considered and in all three systems, the thrust was significantly enhanced compared with single-fin system. For tandem-fin system, the largest thrust was accomplished when the global phase difference was around 180 degree. For parallel-fin case, best performance was achieved when two fins were in opposite phases and thrust increased as the distance between the two fins decreased until wake instability occurred.
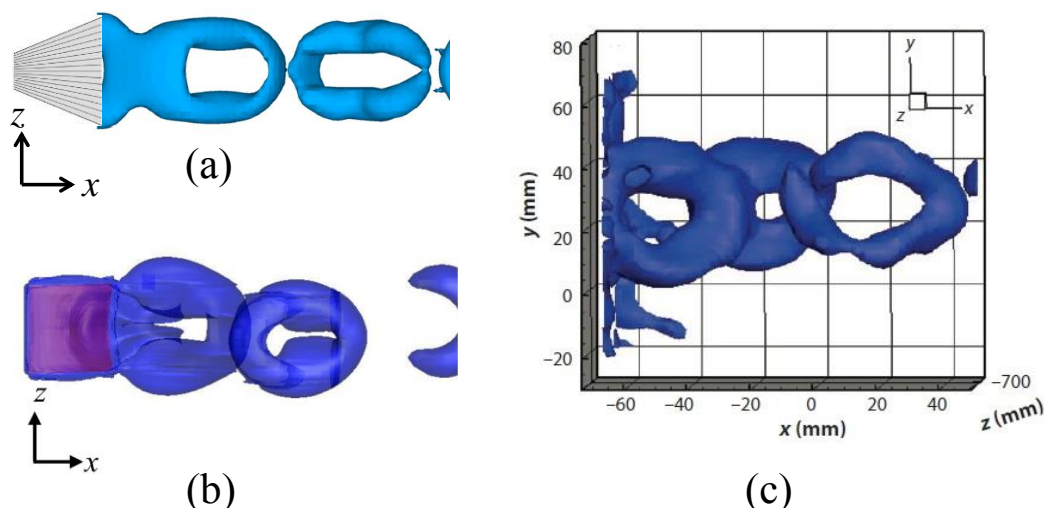
Figure 2-21 Wake structures behind a ray-supported caudal fin. (a) Potential flow model [53]. *(b) Viscous flow model* [102]. *(c) PIV result* [104].

Zhu and Shoele [25] established a FSI model to study the performance of a ray-supported caudal fin. The fin rays were represented by nonlinear beams whereas the fluid force was evaluated using a potential flow model. With individual rotation of each ray at the basal end, the fin was able to achieve both homocercal and heterocercal (*H*-mode) deformations. They concluded that, in both cases, the flexibility can enhance the propulsion performance due to the introduction of an effective yaw motion and reduction of lateral forces. Additionally, passive flexing also reduces the sensitivity of the performance to the kinematic parameters. Based on their previous work [25], Zhu and Bi [53] further investigated the effects of various spanwise stiffness distributions on the propulsion performance of a ray-supported caudal fin. Some complicated caudal fin movements were reproduced by specific spanwise stiffness distributions. Compared with uniform stiffness distribution, non-uniform distributions could further improve the fin's propulsion performance.

Shi et al. [102] developed a FSI solver for skeleton-reinforced bio-membranes by coupling a Navier-Stokes flow solver with a nonlinear Euler-Bernoulli beam model. It was then applied to investigate the propulsion performance of a 3D ray-strengthened caudal fin with various spanwise ray stiffness distributions. They found that certain

deformation patterns observed in experiment (e.g., *C*-mode, *W*-mode and *H*-mode), could be reproduced by specific ray stiffness distributions, among which the cupping distribution required the least power input while the uniform distribution performed the best in terms of thrust generation. Incidentally, the uniform stiffness distribution also caused a *C*-mode with relatively smaller phase differences between different rays. The *H*-mode, on the other hand, yielded considerable vertical force, which may play an important role in fish maneuver. Figure 2-21 demonstrates the wake structures behind a caudal fin from both computational modelling and experiment. It is seen that a linked-chain vortex structure is formed behind the fish caudal fin and numerical simulations using both potential flow model and viscous flow model can qualitatively capture this wake structure although different geometries were used. However, a Navier-Stokes flow solver is able to consider the viscous effect as well as the vortex shedding at all the edges of the fin (leading, trailing, dorsal and ventral edges), which can lead to more convincing results than inviscid flow models.

Liu et al. [105] presented an image-guided approach for inversely determining the material properties of fish fins from high-speed images. This approach was then combined with a FEM-IBM based FSI solver to examine the dynamics of a rainbow trout caudal fin. They found that the developed integrated method was able to evaluate the kinematics and hydrodynamics of fish swimming problems. However, it is known that fish fins involve both active and passive control strategies that are able to modulate the conformation of fin surface. Some conformation patterns can be reproduced by solely passive deformation while some others can only be achieved by active control [53,102].

As discussed in Subsection 2.3.2.1, the fin kinematics of gymnotiform and rajiform swimmers is usually idealised as travelling waves. Most numerical studies on the hydrodynamics of undulating fins are based on this assumption [106,107]. Curet et al.

[108] examined the mechanics of an inward counter-propagating waves (where one wave travels from the head to tail while the other wave moves from tail to head and two waves meet in the middle) using both a robotic fish model and computational fluid dynamics. They also compared the inward counter-propagating wave to other wave forms such as standing wave, unidirectional wave and outward counter-propagating wave. They found that a clear mushroom-cloud-like flow structure with an inverted jet was observed for inward counter-propagating wave, as shown in Figure 2-22 (a). With the creation of such a downward jet, the force perpendicular to the direction of swimming was significantly enhanced. This also demonstrated how fish with undulatory ribbon fin achieved fast maneuvering. Neveln et al. [103] numerically visualised the flow structures of an undulating anal fin with a high-fidelity CFD model. They found that the wake behind the undulating fin was composed of a series of linked vortex tubes, which generated a jet at an oblique angle to the fin, as illustrated in Figure 2-22 (b).

(a)

(a)

(b)

(b)
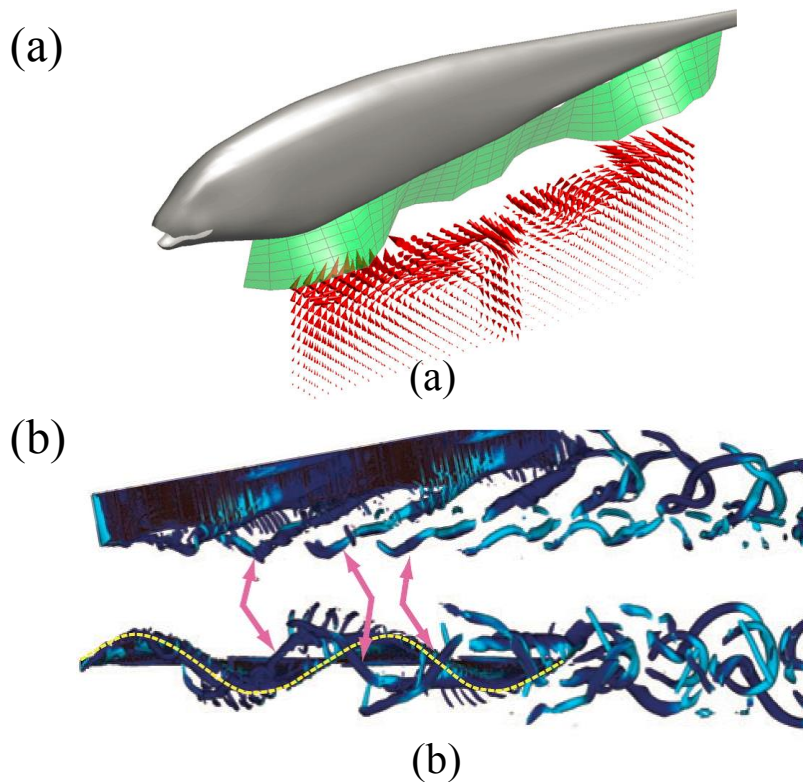
Figure 2-22 (a) Velocity vector field below the undulating fin of knifefish with counter-propagating waves [108]. *(b) 3D flow structures of an undulating anal fin* [103].

2.3.2.3 Definition and visualisation of vortical structures

Four methods are commonly used to define and visualise the wake structures in biomimetic problems:

(1) λ_2-definition

The λ_2-definition (or λ_2-criteria) was proposed by Jeong and Hussain [109], in which a vortex core is located in regions where $\lambda_2 < 0$. Here λ_2 is the second largest eigenvalue of the $\boldsymbol{S}^2 + \boldsymbol{\Omega}^2$ tensor, where $\boldsymbol{S}$ and $\boldsymbol{\Omega}$ respectively represent the symmetric and antisymmetric parts of the velocity gradient tensor. The wake structures are visualised using the iso-surface of the λ_2 value [110,111].

(2) λ_i-definition

In this definition, λ_i is the imaginary part of the complex eigenvalue of the velocity gradient tensor. This method identifies a vortical structure as the region where rotation dominates over strain [112,113]. The wake vortices can be visualised by the iso-surface of the magnitude of λ_i [42–44]

(3) Q-definition

In this definition, the Q is defined as [114,109] $Q = \frac{1}{2}(\|\boldsymbol{\Omega}\|^2 - \|\boldsymbol{S}\|^2)$, where $\boldsymbol{\Omega}$ and $\boldsymbol{S}$ are the same as those in λ_2-definition. $\|\;\;\|$ denotes Euclidean norm of a tensor. The flow structures can be visualised by the iso-surface of the Q value [47,115–117].

(4) $\|\boldsymbol{\omega}\|$-definition

Apart from the above criteria, the $\|\boldsymbol{\omega}\|$-definition is also often used to define and visualise wake structures [49–51]. Here, $\|\boldsymbol{\omega}\|$ is the magnitude of flow vorticity vector, which is defined as $\boldsymbol{\omega} = \nabla \times \boldsymbol{v}$, and $\boldsymbol{v}$ represents the velocity field. However, it should be noted that the $\|\boldsymbol{\omega}\|$-definition, though fairly successful in some flows, may misrepresents the vortices since it does not identify vortex cores in a shear flow [109].

2.3.2.4 Definition of propulsive efficiency in biomimetic systems

In most biomimetic propulsive systems, the propulsion efficiency (η) is usually defined as the ratio of the power used for propulsion ($P_{propulsion}$) to the total consumed power (P_{total}) [118]:

$$\eta = \frac{P_{propulsion}}{P_{total}}. \tag{2.1}$$

For rectilinear motion, $P_{propulsion}$ can be evaluated as

$$P_{propulsion} = \int_{t1}^{t2} F_T U_T dt. \tag{2.2}$$

where F_T and U_T are instantaneous thrust force and moving speed, t1 and t2 are the starting and ending time of swimming. For a swimmer moving at a constant speed U_1, Eq. (2.3) can be simplified as [25]

$$P_{propulsion} = \overline{F}_T U_1. \tag{2.4}$$

where $\overline{F}_T$ is time-averaged thrust force.

For a rigid oscillating body, the total consumed power can be calculated using [94]

$$P_{total} = -\int_{t1}^{t2} \left(f_Y \dot{h} + M_z \dot{\theta} \right) dt. \tag{2.5}$$

where f_Y and M_z are the total force in heaving direction and the total moment about the pitching axis. $\dot{h}$ and $\dot{\theta}$ are the instantaneous heaving and pitching velocities.

For a flexible deforming body, the total power consumption can be estimated by [27,44,47,100]

$$P_{total} = -\int_{t1}^{t2} \iint_S \boldsymbol{f}_{fluid} \cdot \boldsymbol{v}_{body} dS \, dt. \tag{2.6}$$

where $\boldsymbol{f}_{fluid}$ denotes the local fluid force and $\boldsymbol{v}_{body}$ is the local velocity of the deforming body and S is the body surface. The negative sign means the power is done by the body to the surrounding fluid.

2.4 Concluding remarks

2.4.1 *Experimental studies*

In the past decades, the experimental studies on the fins of ray-finned fish are focused on the kinematics and hydrodynamics of these fins thanks to the advancement of techniques such as particle image velocimetry (PIV) and high-speed video camera, which make it possible to visualise flow patterns, calculate wake vorticity and estimate the fluid force. The objects of the experimental studies can be either live fish or robotic devices. The experimental studies on the fin deformation and corresponding force and flow wake generations of live fish can provide the most direct physical data of fish locomotion, which have become an important source of inspiration for the design of biomimetic underwater propellers. The robotic devices are also indispensable complementary methods for the functional study of fish locomotion. However, neither live fish experiment nor robotic fish experiment allow fully parametric studies. Admittedly, parametric study and isolation of certain traits are also allowed to some extent using mechanical devices. But the parameter matrix is limited by the availability of practical materials and manufacturing techniques. On the other hand, these limitations can be circumvented by using numerical modelling, which has become an important way of investigating the fish fin propulsion problems.

2.4.2 Computational studies

The numerical modelling of ray-supported fish fins is essentially a multi-physics coupling problem, which involves unsteady viscous flow, anisotropic material property, bi-laminar designed fin rays, and muscle-tendon activation of individual rays. The interaction of fish fins with surrounding water involves shear layer separation, vortex shedding and turbulence, which are direct results of flow viscosity. Thus it is important to consider the viscous effects when simulating biomimetic flows. It is extremely challenging to consider all these features in a single numerical model. Therefore, researchers have to make assumptions to neglect or simplify some features possessed by real fish fins. In the present thesis, we emphasise on the effects of fluid-structure interaction and active curvature control of ray-strengthened fins and thus only the relevant numerical methods of fluid and structural dynamics used for skeleton-reinforced fish fins are briefly summarised in the present subsection.

2.4.2.1 Fluid dynamics

Fish swim by interacting their flexible body and fins with surrounding water. The study of the hydrodynamics of fish locomotion not only helps us understand how fish manipulate surrounding flows for swimming, but also provides useful guidelines for the design and optimisation of biomimetic underwater vehicles. In the past decades, both inviscid and viscous flow models have been used to investigate biomimetic problems.

✧ <u>Potential flow theory</u>

Under inviscid and incompressible flow assumptions, the flow velocity can be described by a velocity potential $\Phi(\boldsymbol{x}, t)$, which can be decomposed into a body velocity potential $\Phi_b(\boldsymbol{x}, t)$ and a wake velocity potential $\Phi_w(\boldsymbol{x}, t)$, each satisfying Laplace's equation. No-flux boundary condition is usually used on the body surface

and Kutta condition is usually enforced at the trailing edge. The pressure distribution along the body surface can be determined by Bernoulli's equation once the velocity potential distribution is solved. Such an inviscid flow model is computationally inexpensive, thus can provide a rapid evaluation of the hydrodynamic forces and other flow features. Examples of using such methods for biomimetic problems can be found in [26,52,53,95,119–122]. However, inviscid flow models carry inherent weaknesses when dealing with biomimetic problems where the flows are often dominated by shear layer separations and complicated vortex structures, which are direct consequences of viscous effects. Moreover, with the advance of sophisticated CFD algorithms and computational power, it is more appealing to use viscous flow models rather than inviscid ones.

◇ <u>Viscous flow models</u>

The inclusion of viscosity into the fluid dynamics immediately raises the possibility of turbulence, which should be accounted for simulations. In the past decades, various turbulence models have been developed, e.g., RANS models, DES models and LES models. However, even RANS models will significantly increase the computational cost by solving additional equations and using extra fine meshes. Table 2-1 summarises the typical Reynolds numbers of eight different fish species. It is seen that the Reynolds number ranges from $O(10^3)$ to $O(10^7)$ according to the length and speed of the fish. Admittedly, these flows in nature are turbulent, which should be accounted in numerical simulations. However, Chang et al. [47] numerically investigated the hydrodynamics of a tuna-like swimmer at three different Reynolds numbers (R_e = $7.1×10^3$, $7.1×10^4$ and $7.1×10^5$). The effects of turbulence models were studied at different motion frequencies. They found that the drag coefficient and power consumption from laminar case were almost identical to those using Spalart-Allmaras (SA) and Menter's Shear Stress Transport (SST) turbulence models at $R_e = 7.1×10^3$. The influence of turbulence became obvious at higher Reynolds numbers (R_e =

7.1×10^4 and 7.1×10^5). Besides, previous numerical studies on fish swimming also proved that the major flow features obtained at lower Reynolds numbers showed strong similarities with simulations at higher Reynolds numbers and experimental data [49,101,123]. Therefore, without much loss of the flow features, many numerical simulations of fish swimming were performed using laminar flow models at lower Reynolds numbers at the order of $O(10^3)$ where the turbulence plays insignificant effect on the fluid dynamics [42–44,50,102,115,124,125].

Table 2-1 Typical length, Strouhal number (S_t) and Reynolds number (R_e) of eight different fish species.

Species	Length (cm)	S_t	R_e
Killer whale [126,127]	473	0.28	2.6×10^7
White-sided dolphin [126,127]	221	0.24	1.3×10^7
Nurse shark [128]	220	0.41	1.8×10^6
Yellowfin tuna [129]	53	0.29	6.1×10^5
Chub mackerel [130]	21	0.25	1.6×10^5
Sockeye salmon [131]	20.4	0.31	8.0×10^4
Rainbow trout [132]	5.5	0.38	1.6×10^4
Goldfish (Eggfish) [133]	5.3	0.54	7.3×10^3

In the context of biomimetics, the numerical methods used for flow simulation can be divided into body-fitted grid method and Cartesian grid method according to the type of grid employed for CFD computation. For body-fitted grid method, both structured [48,115,134] and unstructured grids [47,50] have been used in previous studies of fish locomotion. To deal with multiple bodies with relative motion, overset grid methods based on structured or unstructured grids are also widely used for biomimetic problems [102,125,135]. For such body-fitted grid methods, an ALE methodology is

usually adopted in order to handle moving boundaries where mesh deformation or regeneration should be employed. One advantage of the body-fitted grid method is that it offers a better resolved flow boundary layer. However, the difficulties of dealing with moving boundaries have limited the body-fitted grid methods to moderate deformations. The moving boundary problem can be nicely solved by using immersed boundary methods [136,137]. Different from the body-fitted grid method, the immersed boundary method (IBM) solve the Navier-Stokes equations on a stationary Cartesian grid; therefore, no mesh deformation or regeneration is required after body motion. In IBM, the no-slip boundary condition on the body surface is enforced by modifying the flow equations in the vicinity of the boundary [138]. A number of variants are also available according to how the boundary modification is accomplished. Due to the advantages of handling complicated moving boundary problems, the IBM approach has been widely used for flow simulations of biomimetic problems [42–44,103,108,110]. However, it should be noted that for high Reynolds number problems, extremely fine grid around the body surface is needed in order to properly resolve the flow boundary layer, which may greatly increase the computational cost of IBM methodology.

2.4.2.2 Structural dynamics

The fins of ray-finned fish are composed of a thin and soft membrane supported by flexible rays. Each ray has a unique bilaminar structure, which enables fish to have active control over the fin's deformation. Such complicated architectures of fish fins make it extremely difficult or even not possible to model in every detail. Therefore, the fin rays are usually modelled as individually actuated beams rather than explicitly considering the ray's bilaminar structure in most previous studies [25,26,52,53,102]. In most numerical models, the thin and collagenous membrane is assumed to bear no bending but only provide a stretching constraint for the connected fin rays. Thus, the effect of the membrane is usually modelled as a series of linear springs connecting the

neighbouring rays. On the other hand, some researchers establish 3D FEM model for both the fin rays and the soft membrane [105].

2.4.2.3   *Numerical ray-supported biomimetic fin models*
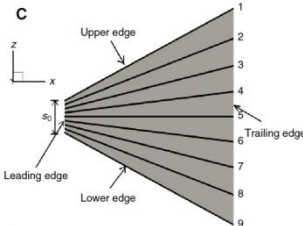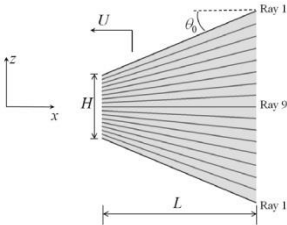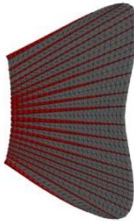
Three main features of ray-supported fish fins can be summarised from previous morphological and anatomical studies. First, fish fins are composed of a soft membrane supported by bony rays, forming skeleton-reinforced bio-membrane systems. The stiffness variation along each fin ray and the rigidity difference among the rays impart anisotropic structural flexibility of fish fins. Second, each fin ray can be actuated individually by the muscles at the ray's basal end. Third, the fin ray consists of a central bundle of collagen surrounded by small segmented bony elements called hemitrichs, forming a bi-laminar architecture. This unique design enables fish to actively control the curvature of fin rays. Table 2-2 summarises the present available computational models for ray-strengthened fish fins. Based on the critical review of previous numerical models of ray-strengthened fish fins, the following gaps in literature have been identified:

1) The majority of existing studies on ray-strengthened fish fins are experiments using live fish or fin-like robotic devices. In contrast, numerical modelling of skeleton-reinforced fish fins has received less attention.

2) Many numerical simulations of ray-supported fins use either experimentally reconstructed fin kinematics or idealised kinematics, where the hydrodynamics is emphasised while the fluid-structure interaction is not considered.

3) For fluid-structure interaction simulations of ray-supported fins, most studies use potential flow models, where the viscous effects (e.g., flow separation, vortex shedding) are neglected. Compared with inviscid flows, viscous flow models are able to produce more convincing results.

4) Most computational models of ray-supported fins only consider the first two characteristics mentioned above (anisotropic structural flexibility and individual

ray activation). However, the effect of active curvature control and the mechanisms behind the effect have not been well understood.

Therefore, the studies in the present thesis are aimed at filling these gaps listed above using a computational model of fin-like propeller considering the main features possessed by ray-supported fish fins.

Table 2-2 Summary of current numerical models of ray-strengthened fish fin

Fin Model	Description	Picture
Caudal fin Zhu & Shoele [25]	• Trapezoid shape with nine fin rays • Sinusoidal sway motion at the leading edge and individual ray yaw motion • 3D inviscid potential flow model • Nonlinear beam model for fin rays; constraints from membrane are considered as linear springs	
Caudal fin Zhu & Bi [53]	• Trapezoid shape with seventeen fin rays • Sinusoidal sway motion at the leading edge, no individual ray actuation • 3D inviscid potential flow model • Nonlinear beam model for fin rays; constraints from membrane are considered as linear springs	
Caudal fin Liu et al. [105]	• Geometry reconstructed from experimental data • Experimentally measured sway-yaw motion at the leading edge, no individual ray actuation • 3D laminar flow model based on IBM • FEM model for rays and membrane; material property determined by experimental data	

Caudal fin Shi et al. [102]	• Rectangular shape with eleven fin rays • Sinusoidal sway motion at the leading edge, no individual ray actuation • 3D laminar flow model based on overset, structured grid system • Nonlinear beam model for fin rays; constraints from membrane are considered as linear springs	
Pectoral fin Mittal et al. [42]	• Geometry reconstructed from experimental data • Experimentally measured fin deformation • 3D laminar flow model based on IBM • No structural model	
Pectoral fin Dong et al. [43]	• Geometry reconstructed from experimental data • Experimentally measured fin deformation • 3D laminar flow model based on IBM • No structural model	
Pectoral fin Shoele & Zhu [26]	• Pectoral fin-like shape with fifteen fin rays • Sinusoidal dorsal-ventral rotation at the basal end of each ray individually • 3D inviscid potential flow model • Nonlinear beam model for fin rays; constraints from membrane are considered as linear springs	
Pectoral fin Shoele & Zhu [52]	• Trapezoid shape with twelve fin rays • Sinusoidal dorsal-ventral and anterior-posterior rotation at the basal end of each ray individually • 3D inviscid potential flow model • Nonlinear beam model for fin rays; constraints from membrane are considered as linear springs	

Pectoral fin Shoele & Zhu [27]	• Single 2D pectoral fin • Sinusoidal heave motion of each reference point representing the location of a fin ray • 2D laminar flow model based on IBM • Nonlinear beam model for fin membrane	
Pectoral fin Shoele & Zhu [54]	• Multiple 2D pectoral fin • Sinusoidal heave motion of each reference point representing the location of a fin ray • 2D laminar flow model based on IBM • Nonlinear beam model for fin membrane	
Anal fin Curet et al. [108]	• Idealised rectangular anal fin • Sinusoidal travelling wave along the fin • 3D laminar flow model based on IBM	
Anal fin Neveln et al. [103]	• Idealised rectangular anal fin • Sinusoidal travelling wave along the fin • 3D laminar flow model based on IBM	

Chapter 3 Mathematical Formulations and Numerical Methods

In this chapter, the governing equations for both fluid and solid domains and the numerical schemes used to solve them are presented. Specifically, the flow and structural equations and numerical schemes are given in Section 3.1 and 3.2 respectively. The coupling procedure and data exchange method at the fluid-solid interface are provided in Section 3.3. The overset grid method and the mesh deformation algorithm are introduced in Section 3.4. Finally, the concluding remarks are given in Section 3.5.
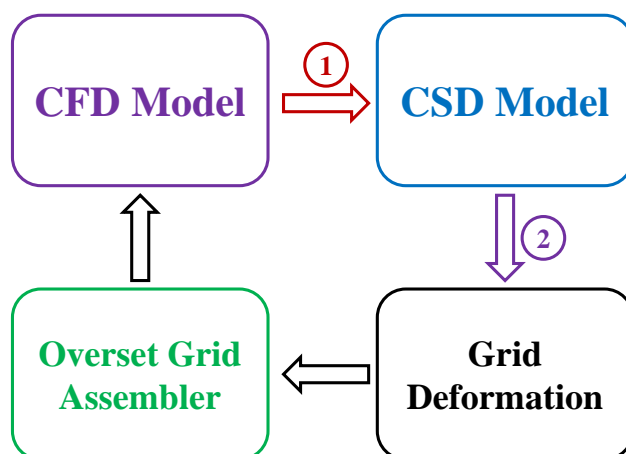
① Fluid force interpolation from CFD grid to CSD grid

② Structural displacement interpolation from CSD grid to CFD grid

Figure 3-1 Illustration of the main modules in the present FSI solver.

There are five main modules in the presently developed FSI solver, namely, a computational fluid dynamics (CFD) model, a computational structural model (CSD), an interface between the fluid and solid domains, a grid deformation module and an

overset grid assembler, as shown in Figure 3-1. In the present FSI model, the CFD model solves the compressible Navier-Stokes equations using a finite-volume method. To simulate incompressible flows using a compressible flow solver, three aspects must be carefully considered. First, the effect of compressibility should be negligible, i.e., the maximum Mach number in the computational domain should be smaller than 0.3. Second, the numerical stability and accuracy should be maintained for low flow speed calculation. This can be done by implementing low-speed preconditioning (LSP) in a compressible flow solver (see Section 3.1.5). If such a LSP method is not available, numerical tests should be conducted to find a suitable Mach number. Third, non-dimensional parameters (e.g., Reynolds number and reduced frequency) rather than absolute values should be used in calculation. By setting the same dimensionless parameters with those in other numerical simulations and experiments, the present compressible flow solver produces results with adequate accuracy (see Chapter 4 for numerical validations).

For all the modules shown in Figure 3-1, the contributions from the PhD candidate are summarised as follows:

(1) A preconditioning method was implemented in the flow solver, which enables it to deal with low speed steady flows.

(2) A nonlinear beam model was re-implemented based on an old Fortran77 subroutine, and then extended to cope with multiple structures.

(3) The flow solver and beam model were coupled in a partitioned framework.

(4) An external overset grid assembler originally developed for steady flows was upgraded and integrated into the existing code to handle unsteady moving boundary problems.

(5) A new module interpolating the fluid force to structural grid was developed, and the original module transferring structural displacement to flow mesh was upgraded to handle multiple structures.

3.1 Governing equations and numerical schemes for computational fluid dynamics

As demonstrated in Table 2-1, typical Reynolds numbers of fish swimming vary from $O(10^3)$ to $O(10^7)$. For high Reynolds number flows, turbulence models must be used to appropriately resolve the turbulence effects. However, when the Reynolds number is relatively low (e.g. below 10^3), turbulence may have insignificant effects on the flow field of biomimetic problems [47]. For these scenarios, a laminar flow model is usually adopted, see examples in [27,42–44]. As the Reynolds numbers considered in the current studies are at the order of $O(10^3)$, therefore, a laminar flow model is used in the present thesis.

3.1.1　Fluid governing equations in arbitrary Lagrangian-Eulerian frame

The continuum fluid dynamics is governed by the fundamental conservation laws, namely, mass conservation, momentum conservation and energy conservation. We assume that no sinks and sources exist in this control volume, thus the conserved quantities can only be changed by convection and diffusion effects. Furthermore, the fluid body forces such as gravity are not considered in the present work. Therefore, the flow governing equations in its integral form can be written as [139]

$$\frac{\partial}{\partial t}\iiint_V \boldsymbol{U}dV + \iint_S \boldsymbol{F}_c \cdot \boldsymbol{n}dS - \iint_S \boldsymbol{F}_d \cdot \boldsymbol{n}dS = \boldsymbol{0}, \tag{3.1}$$

where V is the flow control volume and S denotes its closed boundary surface, and $\boldsymbol{n}$ is the surface unit normal vector. In Eq. (3.1), the conservative variable vector $\boldsymbol{U}$ is defined as

$$\boldsymbol{U} = \{\rho, \rho u, \rho v, \rho w, \rho \bar{E}\}, \tag{3.2}$$

where ρ is the fluid density, u, v, w are three velocity components in Cartesian coordinate system. $\bar{E}$ is the total energy, which is defined as

$$\bar{E} = \bar{e} + \frac{u^2 + v^2 + w^2}{2},$$ (3.3)

where $\bar{e}$ is the flow internal energy.

In Eq. (3.1), $\boldsymbol{F_c}$ denotes the convective fluxes (inviscid parts), and can be written as

$$\boldsymbol{F_c} = \begin{bmatrix} \rho\tilde{u} & \rho\tilde{v} & \rho\tilde{w} \\ \rho u\tilde{u} + p & \rho u\tilde{v} & \rho u\tilde{w} \\ \rho v\tilde{u} & \rho v\tilde{v} + p & \rho v\tilde{w} \\ \rho w\tilde{u} & \rho w\tilde{v} & \rho w\tilde{w} + p \\ \rho E\tilde{u} + pu & \rho E\tilde{v} + pv & \rho E\tilde{w} + pw \end{bmatrix}.$$ (3.4)

In a traditional Eulerian description, the control volume is expected to be fixed in both space and time. However, in order to deal with moving and deforming boundaries, the control volume (shape, position and orientation) must be regarded as time dependent. Thus, the convective fluxes must be formulated in an Arbitrary Lagrangian-Eulerian (ALE) framework, where the convective fluxes through the control surface are defined relative to the motion of the control volume and are expressed in terms of relative velocity $\tilde{\boldsymbol{v}} = (\tilde{u}, \tilde{v}, \tilde{w})^T$:

$$\begin{aligned} \tilde{u} &= u - u_{grid} \\ \tilde{v} &= v - v_{grid} \\ \tilde{w} &= w - w_{grid} \end{aligned},$$ (3.5)

where $\boldsymbol{v} = (u, v, w)^T$ and $\boldsymbol{v}_{grid} = (u_{grid}, v_{grid}, w_{grid})^T$ are flow velocity and grid velocity respectively, both of which are defined in a stationary Cartesian coordinate system.

The diffusive fluxes (viscous shear stresses and thermal conduction) are given by

$$\boldsymbol{F}_d = \begin{bmatrix} 0 & 0 & 0 \\ \tau_{xx} & \tau_{xy} & \tau_{xz} \\ \tau_{yx} & \tau_{yy} & \tau_{yz} \\ \tau_{zx} & \tau_{zy} & \tau_{zz} \\ \Theta_x & \Theta_y & \Theta_z \end{bmatrix}, \tag{3.6}$$

where

$$\begin{aligned} \Theta_x &= u\tau_{xx} + v\tau_{xy} + w\tau_{xz} - q_x \\ \Theta_y &= u\tau_{yx} + v\tau_{yy} + w\tau_{yz} - q_y. \\ \Theta_z &= u\tau_{zx} + v\tau_{zy} + w\tau_{zz} - q_z \end{aligned} \tag{3.7}$$

For a Newton-Fourier fluid and using Stokes hypothesis, the shear stress tensors and heat fluxes in Eq. (3.6) and Eq. (3.7) can be defined as

$$\begin{aligned} \tau_{xx} &= 2\mu \frac{\partial u}{\partial x} - \frac{2}{3}\mu(\nabla \cdot \boldsymbol{v}) \\ \tau_{yy} &= 2\mu \frac{\partial v}{\partial y} - \frac{2}{3}\mu(\nabla \cdot \boldsymbol{v}) \\ \tau_{zz} &= 2\mu \frac{\partial w}{\partial z} - \frac{2}{3}\mu(\nabla \cdot \boldsymbol{v}) \\ \tau_{xy} &= \tau_{yx} = \mu\left(\frac{\partial u}{\partial y} + \frac{\partial v}{\partial x}\right) \\ \tau_{xz} &= \tau_{zx} = \mu\left(\frac{\partial w}{\partial x} + \frac{\partial u}{\partial z}\right), \\ \tau_{yz} &= \tau_{zy} = \mu\left(\frac{\partial v}{\partial z} + \frac{\partial w}{\partial y}\right) \\ q_x &= \kappa \frac{\partial T}{\partial x} \\ q_y &= \kappa \frac{\partial T}{\partial y} \\ q_z &= \kappa \frac{\partial T}{\partial z} \end{aligned} \tag{3.8}$$

where μ is the dynamic viscosity, κ is the thermal conductivity and T_e is the flow temperature. The total enthalpy is defined as

$$\bar{H} = \bar{h} + \frac{u^2 + v^2 + w^2}{2}. \tag{3.9}$$

For calorically perfect gas, we have the following equations:

$$\bar{e} = c_v T_e, \bar{h} = c_p T_e, c_v = \frac{R}{\gamma - 1}, c_p = \frac{\gamma R}{\gamma - 1}, \tag{3.10}$$

and equation of state:

$$p = \rho R T_e. \tag{3.11}$$

In Eq. (3.10) and Eq. (3.11), c_v and c_p are specific heats at constant volume and constant pressure respectively, γ is the ratio of specific heats and R is the specific gas constant. The viscosity coefficients for laminar flow are calculated by Sutherland's formula [139]:

$$\frac{\mu}{\mu_0} = \left(\frac{T_e}{T_{e,0}}\right)^{\frac{3}{2}} \frac{T_{e,0} + 110.4}{T_e + 110.4}, \tag{3.12}$$

where μ_0 and $T_{e,0}$ are reference viscosity and temperature respectively. Finally, the speed of sound for a perfect gas can be written as

$$a = \sqrt{\frac{\gamma p}{\rho}}, \tag{3.13}$$

and the Mach number is then defined as

$$M_a = \frac{\sqrt{u^2 + v^2 + w^2}}{a}. \tag{3.14}$$

3.1.2 Spatial discretisation: finite-volume method

The governing equations are discretised on an overset, structured, multi-block grid system using a cell-centred finite-volume method. With a structured grid method, the fluid domain is divided into an array of hexahedral cells. Each grid cell is uniquely denoted by three computational coordinates i, j, k. Within the cell (i, j, k), Eq. (3.1) can be approximated by

$$\frac{\partial}{\partial t}(U\Delta V)_{i,j,k} + G_{i,j,k} = 0, \tag{3.15}$$

where $U_{i,j,k}$ are the cell-averaged conservative variables, $V_{i,j,k}$ is the cell volume and $G_{i,j,k}$ are the net fluxes entering the control volume through all cell faces ΔS_m:

$$G_{i,j,k} = \sum_{m=1}^{6} F_m \Delta S_m \,, \tag{3.16}$$

where $F_m = F_m^c - F_m^v$ are the flux vectors on the cell faces. For a structured grid method, a cell is essentially a hexahedron composed of six cell faces. The central Jameson-Schmidt-Turkel (JST) scheme proposed by Jameson et al. [140] is implemented. The JST scheme assumes the same influence from either side of the cell face; therefore, it causes nonphysical oscillations and odd-even decoupled problems, which will be alleviated by adding artificial dissipation. In JST scheme, the fluxes through a cell face are calculated by arithmetic averaging the conservative flow variables of the two cell centres adjacent to the cell face:

$$\begin{aligned}
F_1 &= \frac{1}{2}\left(F_{i,j,k} + F_{i-1,j,k}\right) & F_2 &= \frac{1}{2}\left(F_{i,j,k} + F_{i+1,j,k}\right) \\
F_3 &= \frac{1}{2}\left(F_{i,j,k} + F_{i,j-1,k}\right) & F_4 &= \frac{1}{2}\left(F_{i,j,k} + F_{i,j+1,k}\right). \\
F_5 &= \frac{1}{2}\left(F_{i,j,k} + F_{i,j,k-1}\right) & F_6 &= \frac{1}{2}\left(F_{i,j,k} + F_{i,j,k+1}\right)
\end{aligned} \tag{3.17}$$

In order to calculate the stress tensors, the first order derivatives are defined at the cell vertices and then evaluated by Green's theorem for an auxiliary cell around the vertex [139]:

$$\frac{\partial u}{\partial \bar{x}} \approx \frac{1}{\Delta V_a} \sum_{m=1}^{6} (u n_x \Delta S)_m$$

$$\frac{\partial u}{\partial \bar{y}} \approx \frac{1}{\Delta V_a} \sum_{m=1}^{6} (u n_y \Delta S)_m , \qquad (3.18)$$

$$\frac{\partial u}{\partial \bar{z}} \approx \frac{1}{\Delta V_a} \sum_{m=1}^{6} (u n_z \Delta S)_m$$

where ΔV_a is the auxiliary cell volume, and n_x, n_y, n_z is the unit normal vector on the auxiliary cell faces.

Artificial dissipation is added in Eq. (3.16) to stabilise the numerical scheme and to eliminate the nonphysical oscillations:

$$R(U_{i,j,k}) = -G_{i,j,k} + D_{i,j,k}. \qquad (3.19)$$

Following Jameson et al. [140], $D_{i,j,k}$ is a blend of 2nd-order and 4th-order difference to provide 1st-order dissipation around shocks and 3rd-order dissipation in smooth flow regions, which can be expressed as [139]

$$D_{i,j,k} = \left(D_{i+\frac{1}{2},j,k} - D_{i-\frac{1}{2},j,k} \right)$$
$$+ \left(D_{i,j+\frac{1}{2},k} - D_{i,j-\frac{1}{2},k} \right) \qquad (3.20)$$
$$+ \left(D_{i,j,k+\frac{1}{2}} - D_{i,j,k-\frac{1}{2}} \right).$$

The artificial dissipation through the cell face $\left(i + \frac{1}{2}, j, k \right)$ is calculated as

$$D_{i+\frac{1}{2},j,k} = \widehat{\Lambda}_{I,i+\frac{1}{2},j,k} \left[\epsilon^{(2)}_{I,i+\frac{1}{2},j,k} \left(\widehat{U}_{i+1,j,k} - \widehat{U}_{i,j,k} \right) \right.$$
$$\left. - \epsilon^{(4)}_{I,i+\frac{1}{2},j,k} \left(\widehat{U}_{i+2,j,k} - 3\widehat{U}_{i+1,j,k} + 3\widehat{U}_{i+1,j,k} + \widehat{U}_{i-1,j,k} \right) \right] \qquad (3.21)$$

with $\widehat{U} = (\rho, \rho u, \rho v, \rho w, \rho E + p)^T$. The expressions for other cell faces can be formulated in a similar manner and thus are omitted here. The term $\widehat{\Lambda}_{I,i+\frac{1}{2},j,k}$ is the scaled spectral radius of the flux Jacobian matrices in *I*-direction and defined as

$$\widehat{\Lambda}_{I,i+\frac{1}{2},j,k} = \Lambda_{I,i+\frac{1}{2},j,k} \Theta_{I,i+\frac{1}{2},j,k}. \tag{3.22}$$

In Eq. (3.22), the scaling factor is written as

$$\Theta_{I,i+\frac{1}{2},j,k} = 1 + \left(\frac{\Lambda_{J,i+\frac{1}{2},j,k}}{\Lambda_{I,i+\frac{1}{2},j,k}}\right)^{\vartheta} + \left(\frac{\Lambda_{K,i+\frac{1}{2},j,k}}{\Lambda_{I,i+\frac{1}{2},j,k}}\right)^{\vartheta}, \tag{3.23}$$

where ϑ is a parameter ranging from 0 to 1, and the spectral radii read

$$\Lambda_{I,i+\frac{1}{2},j,k} = \left|\boldsymbol{v}_{i+\frac{1}{2},j,k} \cdot \Delta \boldsymbol{S}_{I,i+\frac{1}{2},j,k}\right| + a \left|\Delta \boldsymbol{S}_{I,i+\frac{1}{2},j,k}\right|$$

$$\Lambda_{J,i+\frac{1}{2},j,k} = \left|\boldsymbol{v}_{i+\frac{1}{2},j,k} \cdot \Delta \boldsymbol{S}_{J,i+\frac{1}{2},j,k}\right| + a \left|\Delta \boldsymbol{S}_{J,i+\frac{1}{2},j,k}\right| \tag{3.24}$$

$$\Lambda_{K,i+\frac{1}{2},j,k} = \left|\boldsymbol{v}_{i+\frac{1}{2},j,k} \cdot \Delta \boldsymbol{S}_{K,i+\frac{1}{2},j,k}\right| + a \left|\Delta \boldsymbol{S}_{K,i+\frac{1}{2},j,k}\right|.$$

The coefficients $\epsilon^{(2)}$ and $\epsilon^{(4)}$ in Eq. (3.21) are used to control the amount of 2nd-order and 4th-order dissipation and are calculated by

$$\epsilon^{(2)}_{I,i+\frac{1}{2},j,k} = \psi^{(2)} min\left(0.25, \tilde{\chi}_{i+\frac{1}{2},j,k}\right)$$

$$\epsilon^{(4)}_{I,i+\frac{1}{2},j,k} = \psi^{(4)} min\left(0, \psi^{(4)} - \epsilon^{(2)}_{I,i+\frac{1}{2},j,k}\right), \tag{3.25}$$

where

$$\tilde{\chi}_{i+\frac{1}{2},j,k} = max\left(\chi_{i+1,j,k}, \chi_{i,j,k}\right), \tag{3.26}$$

and

$$\chi_{i,j,k} = \frac{\left|p_{i+1,j,k} - 2p_{i,j,k} + p_{i-1,j,k}\right|}{\left|p_{i+1,j,k} + 2p_{i,j,k} + p_{i-1,j,k}\right|}. \tag{3.27}$$

and $\psi^{(2)} = 1/4$, $\psi^{(4)} = 1/256$. The coefficients $\epsilon^{(2)}$ and $\epsilon^{(4)}$ in other directions can be computed in a similar way. The 2nd-order dissipation term is used to capture shock waves, i.e., for low Mach number flows, this term ($\epsilon^{(2)}$ in Eq. (3.25)) can be turned off (setting $\psi^{(2)}$ to zero) in order to reduce the amount of artificial dissipation.

3.1.3 Temporal integration

The discretised governing Eq. (3.15) can be rearranged as

$$\frac{\partial}{\partial t}(U\Delta V)_{i,j,k} = R\big(U_{i,j,k}\big) \tag{3.28}$$

The time derivative in Eq. (3.28) is discretised using an implicit backward-difference scheme of second order accuracy

$$\frac{3(U\Delta V)^{n+1} - 4(U\Delta V)^n + (U\Delta V)^{n-1}}{2\Delta t} = R(U^{n+1}), \tag{3.29}$$

where Δt is the physical time step. It should be noted that the formulation in Eq. (3.29) has accounted for a temporal change of the cell volume ΔV. Since the flow variable U^{n+1} at the current time level is not known as a priori, an iterative approach is applied to obtain the solution for U^{n+1}. As proposed by Jameson [141], the problem can be reformulated at each time step as a steady-state problem in a pseudo time $\tilde{t}$:

$$\frac{\partial}{\partial \tilde{t}}U^{n+1} = \frac{1}{\Delta V^{n+1}}\widetilde{R}(U^{n+1}), \tag{3.30}$$

where

$$\widetilde{R}(U^{n+1}) = R(U^{n+1}) - \frac{3(U\Delta V)^{n+1} - 4(U\Delta V)^n + (U\Delta V)^{n-1}}{2\Delta t}. \tag{3.31}$$

When $\widetilde{R}(U^{n+1})$ becomes zero, the unsteady flow Eq. (3.28) will be automatically satisfied. The pseudo time $\tilde{t}$ has no physical meaning and is merely a variable for numerical iteration.

A multi-stage Runge-Kutta scheme is adopted to integrate the discretised Eq.(3.30). The *m* stages of the integration are conducted as follows:

$$
\begin{aligned}
U_{i,j,k}^{(0)} &= U_{i,j,k}^{n} \\
U_{i,j,k}^{(1)} &= U_{i,j,k}^{(0)} + \alpha_1 \frac{\Delta \tilde{t}_{i,j,k}}{\Delta V_{i,j,k}^{(n+1)}} \widetilde{R}\left(U_{i,j,k}^{(0)}\right) \\
&\cdots \\
U_{i,j,k}^{(m)} &= U_{i,j,k}^{(0)} + \alpha_m \frac{\Delta \tilde{t}_{i,j,k}}{\Delta V_{i,j,k}^{(n+1)}} \widetilde{R}\left(U_{i,j,k}^{(m-1)}\right) \\
U_{i,j,k}^{n+1} &= U_{i,j,k}^{(m)}
\end{aligned}
\qquad (3.32)
$$

where α_m are constant coefficients.

For five-stage time stepping, the coefficients are [141]

$$
\alpha_1 = \frac{1}{4}, \alpha_2 = \frac{1}{6}, \alpha_3 = \frac{3}{8}, \alpha_4 = \frac{1}{2}, \alpha_5 = 1.
\qquad (3.33)
$$

The reformulated discretised Eq. (3.30) has the form of an equivalent steady state problem. Therefore, acceleration techniques such as local time-stepping and residual smoothing, which are developed for steady-state problems, can be directly applied to the pseudo-time iteration without affecting the real-time accuracy [141]. Therefore, both acceleration techniques have been implemented in the present code. Additionally, the present CFD solver is parallelised with Message Passing Interface (MPI). More details regarding this flow solver can be found in [139,142–147].

3.1.4   *Boundary conditions*

To numerically solve the fluid governing equations, appropriate variable values must be imposed at the grid boundary. In the present code, this is achieved by using two layers of ghost cells wrapped around the grid. By specifying appropriate values to the flow variables in the ghost cells, the fluxes and derivatives at the fluid field boundaries are calculated in the same manner as interior cell faces. Here, three flow boundary conditions, namely adiabatic solid wall, far-field and symmetric plane, are presented. To better demonstrate the implementation of these boundary conditions, in the following, the variables of the ghost cells are donated as $\phi_{g,k}$ while the variables of the interior cells are donated as ϕ_k, where $k = 1$ depicts the cell is adjacent to the boundary while $k = 2$ represents the cell at the second outer layer, as shown in Figure 3-2.
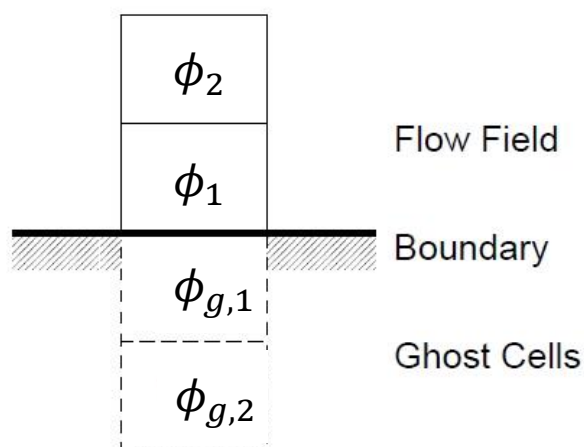
Figure 3-2 Ghost cell notations

3.1.4.1   *Adiabatic solid wall*

For viscous flow, the no-slip condition (zero flux across the wall) should be satisfied on the body surface. This is accomplished by assigning the negative velocity of the interior cells to corresponding ghost cells, i.e., the flux across the body surface is zero:

$$v_{g,1} = -v_1, \tag{3.34}$$

The temperature gradient in the direction normal to the wall should be zero to satisfy the adiabatic condition, which is achieved through:

$$\begin{aligned} \rho_{g,1} &= \rho_1 \\ \bar{E}_{g,1} &= \bar{E}_1. \\ p_{g,1} &= p_1 \end{aligned} \tag{3.35}$$

3.1.4.2 Far-field

For external compressible flows, the far-field condition at the outer boundary of the computational domain must be (approximately) nonreflective. The characteristic wave propagation is considered by using the Riemann invariants, where a quasi-one-dimensional method is applied along the normal direction of each cell. The 1-D Riemann invariants in normal direction are defined as

$$\begin{aligned} R_+ &= \boldsymbol{v}_+ \cdot \boldsymbol{n} + \frac{2a_+}{\gamma - 1} \\ R_- &= \boldsymbol{v}_- \cdot \boldsymbol{n} + \frac{2a_-}{\gamma - 1} \end{aligned} , \tag{3.36}$$

where a_+ and a_- are speed of sound corresponding to Riemann invariants R_+ and R_-.

The flow variable values at the boundary are extrapolated by those from freestream (subscript ∞) and interior cells (subscript 1). The extrapolation direction is determined by the wave propagation direction. Specifically, for subsonic inflow where the boundary normal velocity $v_{n,b} \leq 0$, and $\left| v_{n,b} \right| < a$, we have

$$\begin{aligned} \boldsymbol{v}_+ &= \boldsymbol{v}_1, & a_+ &= a_1 \\ \boldsymbol{v}_- &= \boldsymbol{v}_\infty, & a_- &= a_\infty. \end{aligned} \tag{3.37}$$

For supersonic inflow where $v_{n,b} < 0$ and $\left| v_{n,b} \right| > a$, we have

$$\begin{aligned} \boldsymbol{v}_+ = \boldsymbol{v}_\infty, \quad a_+ = a_\infty \\ \boldsymbol{v}_- = \boldsymbol{v}_\infty, \quad a_- = a_\infty. \end{aligned} \tag{3.38}$$

For subsonic outflow where $v_{n,b} \geq 0$ and $\left| v_{n,b} \right| \leq a$, we have

$$\begin{aligned} \boldsymbol{v}_+ = \boldsymbol{v}_1, \quad a_+ = a_1 \\ \boldsymbol{v}_- = \boldsymbol{v}_\infty, \quad a_- = a_\infty. \end{aligned} \tag{3.39}$$

For supersonic outflow where $v_{n,b} > 0$ and $\left| v_{n,b} \right| > a$, we have

$$\begin{aligned} \boldsymbol{v}_+ = \boldsymbol{v}_1, \quad a_+ = a_1 \\ \boldsymbol{v}_- = \boldsymbol{v}_1, \quad a_- = a_1. \end{aligned} \tag{3.40}$$

Using the Riemann invariants defined above, the boundary normal velocity $v_{n,b}$ and speed of sound a_b are then calculated as

$$\begin{aligned} v_{n,b} &= \frac{1}{2}(R_+ + R_-) \\ a_b &= \frac{\gamma - 1}{4}(R_+ + R_-) \end{aligned}. \tag{3.41}$$

Considering that the tangential velocity component is invariant in the quasi-one-dimensional method, the velocity vector at the inflow boundary ($v_{n,b} \leq 0$) is computed from the freestream values:

$$\boldsymbol{v}_b = \boldsymbol{v}_\infty + \left(v_{n,b} - \boldsymbol{v}_\infty \cdot \boldsymbol{n} \right)\boldsymbol{n}, \tag{3.42}$$

whereas the velocity vector at the outflow boundary ($v_{n,b} > 0$) is extrapolated from the first interior cell:

$$\boldsymbol{v}_b = \boldsymbol{v}_2 + \left(v_{n,b} - \boldsymbol{v}_2 \cdot \boldsymbol{n} \right)\boldsymbol{n}. \tag{3.43}$$

The density at the boundary is obtained as

$$\rho_b = \left(\frac{a_b^2}{\gamma \frac{p_b}{\rho_b^\gamma}} \right)^{\frac{1}{\gamma-1}},$$ (3.44)

where the entropy $\frac{p_b}{\rho_b^\gamma}$ at the boundary is computed from the freestream values for inflow and interior cells for outflow. With the velocity, sound speed and density known at the boundary, the pressure and total energy can be readily determined. Finally, the conservative variables in the ghost cells can be computed as

$$\boldsymbol{U}_{g,1} = 2\boldsymbol{U}_b - \boldsymbol{U}_1$$ (3.45)

where $\boldsymbol{U}_b$ is the conservative flow variable vector calculated using the flow variables with subscript b obtained above. $\boldsymbol{U}_1$ is the flow variables at the interior cells adjacent to the boundary.

3.1.4.3 *Symmetric plane*

In some cases, the flow is known or assumed to be symmetric. To reduce computational effort, only half of the computational domain is used by setting an appropriate symmetric plane. For scalar variables (density, pressure and total energy), the values of the ghost cells are assigned in a similar manner as Eq. (3.35) while for the vector variable (velocity), it is mirrored by

$$\boldsymbol{v}_{g,1} = \boldsymbol{v}_1 - 2(\boldsymbol{v}_1 \cdot \boldsymbol{n})\boldsymbol{n}.$$ (3.46)

With the variable values in the first ghost cell layer, the variable values in the second ghost cell layer can be extrapolated as:

$$\boldsymbol{U}_{g,2} = 3\boldsymbol{U}_{g,1} - 3\boldsymbol{U}_1 + \boldsymbol{U}_2$$ (3.47)

3.1.5 *Low-speed preconditioning*

Numerous time-marching schemes designed to solve the compressible Navier-Stokes equations (Eq. (3.1)) have been very successful for transonic/supersonic flows. However, the accuracy and convergence rate of these original schemes are deteriorated for very low speed flows due to the large disparity of acoustic and convective wave speeds, which leads to a very large *condition number* (defined as the ratio between the largest and smallest eigenvalues of convective flux Jacobian) [148]. Fortunately, the problems can be addressed by utilising low-speed preconditioning (LSP) methods which equalise all the eigenvalues and thus reduce the stiffness of the system of equations. This not only produces better convergence rate, but also improves solution accuracy. In the past decades, various forms of LSP methods had been developed for both Euler and Navier-Stokes equations [148–153]. These methods were then extended to solve time-dependent flows [154–156] and moving boundary problems [135,157]. Due to the modification of the path to the steady state, preconditioning techniques need to be combined with dual-time stepping method in order to retain the temporal accuracy [154–156].

Despite of the success of preconditioning methods in solving low-speed flows with compressible CFD codes, the improvements of convergence and accuracy are gained in accompany with reduced robustness [158]. The loss of robustness arises primarily from the existence of stagnation points and diffusion dominated regions. For FSI problems, the existence of moving boundary may also lead to numerical instability. One possible solution is to include some cut-off values when formulating the preconditioning matrices. However, difficulties still remain for complicated flows in the proper definition of the limiting factors. Nevertheless, with properly formulated preconditioning matrices, the LSP techniques can be greatly useful in resolving the practical problems involving mixed compressible/incompressible flows.

Strictly speaking, low-speed preconditioning method should be adopted to calculate incompressible flows using a compressible flow solver. In the present thesis, the low-speed preconditioning technique has been implemented successfully for steady-state flows (see Appendix for details). However, the current preconditioned flow solver experienced severe deterioration in accuracy when extending time-dependent flow problems (see Appendix). Further investigation and development are needed in the future. Therefore, for the biomimetic problems examined in Chapter 5 – 7, the low-speed preconditioning was not used.

To simulate incompressible flows using a compressible flow solver without preconditioning, it is necessary to ensure that the compressibility effect is negligibly small. A flow can be considered as incompressible if the Mach number is below the critical value of 0.3. In the current thesis, we choose the freestream Mach number to be $M_{a,\infty}= 0.06$, which is far below the critical value but still sufficiently large for numerical stability. Considering the problems with moving boundaries, the actual Mach number experienced by the body can be larger than $M_{a,\infty}$. To ensure the accuracy of the present flow solver, the local Mach numbers in the whole computational domain are monitored to guarantee that it is below the critical value. The present CFD code has been successfully applied to investigate various incompressible flow problems in our previous publications [134,145,147,159,160]. If not specified, all the simulations in this thesis are carried out at $M_{a,\infty}=0.06$.

3.2 Governing equations and numerical schemes for computational structural dynamics

3.2.1 Governing equations of nonlinear Euler-Bernoulli beams

For a sufficiently thin plate with length L_p and uniform thickness h_p, its configuration undergoing oscillating and deformational motions can be denoted by the instantaneous

location of its centreline. By using the thin-plate assumption ($h_p \ll L_p$), the potential energy V_p of the plate is given as [161,162]

$$V_p = \frac{1}{2} \int_0^{L_p} Eh_p \left[\left(\frac{\partial \boldsymbol{x}}{\partial s} \cdot \frac{\partial \boldsymbol{x}}{\partial s} \right)^{\frac{1}{2}} - 1 \right]^2 ds + \frac{1}{2} \int_0^{L_p} \frac{Eh_p^3}{12} \left(\frac{\partial^2 \boldsymbol{x}}{\partial s^2} \cdot \frac{\partial^2 \boldsymbol{x}}{\partial s^2} \right) ds \quad (3.48)$$

Similarly, the kinetic energy T_k is

$$T_k = \frac{1}{2} \int_0^{L_p} \rho_s h_p \frac{\partial \boldsymbol{x}}{\partial t} \cdot \frac{\partial \boldsymbol{x}}{\partial t} ds, \quad (3.49)$$

where $\boldsymbol{x} = (x, y)$ is the Cartesian coordinates of any point along the centreline, s is the Lagrange coordinate which measures the non-stretched distance from any point of the centreline to the leading edge, and ρ_s is the density of the plate, and E is the Young's modulus. Employing variational analysis, within any time interval (t_1, t_2), we can derive

$$\int_{t_1}^{t_2} dt \left[\delta(T - V) + \int_0^{L_p} \boldsymbol{F}_{ex} \cdot \boldsymbol{x} ds \right] = 0, \quad (3.50)$$

where $\boldsymbol{F}_{ex}$ is the summation of all the external forces, including the fluid forces. By substituting Eq. (3.48) and Eq. (3.49) into Eq. (3.50), and considering the fact that the equation is valid at arbitrary t_1 and t_2, we can obtain the final governing equation for the structural dynamics:

$$\rho_s h_p \frac{\partial^2 \boldsymbol{x}}{\partial t^2} + \frac{\partial^2 \boldsymbol{x}}{\partial s^2} \left(\frac{Eh_p^3}{12} \frac{\partial^2 \boldsymbol{x}}{\partial s^2} \right) - \frac{\partial}{\partial s} \left\{ Eh_p \left[1 - \left(\frac{\partial \boldsymbol{x}}{\partial s} \cdot \frac{\partial \boldsymbol{x}}{\partial s} \right)^{-\frac{1}{2}} \right] \frac{\partial \boldsymbol{x}}{\partial s} \right\}$$
$$= \boldsymbol{F}_{ex}. \quad (3.51)$$

In Eq. (3.51), the first term on the left-hand side represents the inertia effect; the second and third terms depict the elastic effects of bending and stretching, respectively; and the right-hand-side term stands for external forces (including fluid force). The hysteretic

structural damping caused by internal friction is considered using the Kelvin-Voigt model, where the Young's modulus E in Eq. (3.51) is replaced by $E(1 + \sigma\, \partial/\partial t)$, where σ denotes the magnitude of the energy dissipation.

At the ends of the beam (leading edge $s_p = 0$, trailing edge $s_p = L_p$), two boundary conditions are available. One is the boundary condition with prescribed motion, which is expressed as

$$
\begin{aligned}
\boldsymbol{x}(s_p, t) &= \boldsymbol{x}(s_p, 0) + [s_p, y(t)]^T \\
\frac{\partial \boldsymbol{x}(s_p, t)}{\partial s} &= [1, s_p]^T
\end{aligned}
\qquad .
$$
(3.52)

Another boundary condition is free boundary condition (zero stress and bending), which can be expressed as

$$
\begin{aligned}
\frac{\partial \boldsymbol{x}}{\partial s}\left(\frac{E h_p^3}{12} \frac{\partial^2 \boldsymbol{x}}{\partial s^2}\right) - E h_p \left[1 - \left(\frac{\partial \boldsymbol{x}}{\partial s} \cdot \frac{\partial \boldsymbol{x}}{\partial s}\right)^{-1/2}\right] \frac{\partial \boldsymbol{x}}{\partial s} &= \boldsymbol{0} \\
\frac{\partial^2 \boldsymbol{x}}{\partial s^2} &= \boldsymbol{0}
\end{aligned}
\qquad .
$$
(3.53)

3.2.2   *Discretisation: finite-difference method*

The nonlinear Euler-Bernoulli beam model described by Eq. (3.51) together with Eq. (3.52) and Eq. (3.53) are numerically solved by a finite difference method [162]. The plate centreline is discretised by N evenly distributed grid points $s_j\left(j = 1, \ldots, N\right)$. Let Q represents the coordinates *x, y* or their combinations, the derivatives are then written as

$$
\frac{\partial^2 Q}{\partial t^2} = \frac{2Q_j^{n+1} - 5Q_j^n + 4Q_j^{n-1} - Q_j^{n-2}}{\Delta t_s^2},
$$
(3.54)

$$\frac{\partial Q}{\partial s} = \frac{Q_{j+1}^{n+1} - Q_{j-1}^{n+1}}{2\Delta s}, \tag{3.55}$$

$$\frac{\partial^3 Q}{\partial s^3} = \frac{5Q_j^{n+1} - 18Q_{j-1}^{n+1} + 24Q_{j-2}^{n+1} - 14Q_{j-3}^{n+1} + 3Q_{j-4}^{n+1}}{2\Delta s^3}$$
$$\frac{\partial^3 Q}{\partial s^3} = \frac{-5Q_j^{n+1} + 18Q_{j+1}^{n+1} - 24Q_{j+2}^{n+1} + 14Q_{j+3}^{n+1} - 3Q_{j+4}^{n+1}}{2\Delta s^3}, \quad \text{or} \tag{3.56}$$

$$\frac{\partial^4 Q}{\partial s^4} = \frac{Q_{j+2}^{n+1} - 4Q_{j+1}^{n+1} + 6Q_j^{n+1} - 4Q_{j-1}^{n+1} + Q_{j-2}^{n+1}}{\Delta s^4}, \tag{3.57}$$

where Δt_s is the structural time step and Δs is the grid size. The resulting system of linear equations is solved by an iterative Gauss-Seidel method [161,162].

3.3 Fluid-structure coupling and interfacing

3.3.1   *Overview of fluid-structure coupling procedures*

FSI coupling procedures have been actively developed over the past decades. Generally, the coupling procedures can be categorised into two groups: monolithic method and partitioned method. Monolithic approach is able to solve the FSI problems as a whole system, thus has the advantages of robustness, rapid convergence and lager permissible time steps, especially in low solid-fluid mass ratio scenarios. This method can be achieved by two schemes: discrete monolithic scheme [163–167] and unified monolithic scheme [168–170]. In discrete monolithic schemes, the solid and fluid domains are formulated and linearized separately and then are assembled into a global linear system. In the unified schemes, however, both fields are handled at the equation level. Despite of the merits in monolithic methods, it should be noted that in some complicated applications, it is mathematically difficult or even impossible to formulate single set of equations for both domains. Moreover, the monolithic approach is more prone to have ill-conditioned linear systems, which greatly compromises its accuracy and convergence rate. [171]

In contrary, a partitioned method defines, discretises and solves each physical field independently, allowing the use of existing robust and well-established solvers in each domain. The coupling is restricted to the fluid/solid interface at which the velocity and traction continuity should be satisfied [172]. Partitioned approaches can generally be divided into explicit schemes and implicit schemes. The explicit scheme requires no subiteration within one time step, but has only first-order temporal accuracy regardless the temporal orders of the fluid and solid solvers used. A stability analysis of an explicit coupling algorithm was performed by Causin et al. [173] using a simplified FSI model in the context of elastic structures and incompressible flows. They found that the complete FSI algorithm becomes unconditionally unstable if

$$\frac{\rho_s h_p}{\rho \chi_{max}} < 1, \tag{3.58}$$

where χ_{max} is the largest eigenvalue of a discrete operator from the discretised structural equations, which is only determined by the structural geometry. From Equation (3.58), we know that when the solid/fluid density ratio becomes smaller and/or the structure becomes more slender (thinner geometry has larger χ_{max}), the complete FSI system will be more unstable. For those cases involving relatively weak fluid-solid interactions (e.g., in the scenario of higher solid/fluid density ratio), this algorithm can be used due to the satisfaction of the stability condition, although the equilibrium condition at the coupling interface is not enforced. Piperno et al. [174] develop a Conventional Serial Staggered (CSS) method to study the classical aeroelasticity problems in aeronautical engineering. This method solves the structural dynamics implicitly using the fluid loads evaluated at time step index $n + 1$ while the fluid dynamics is resolved explicitly, resulting in first-order temporal accuracy. Besides, this algorithm is also constrained by the stability condition in Equation (3.58). Despite of the loss in time-accuracy and numerical stability issue associated with the explicit partitioned approach, this method still has an advantage in saving

computational time because no coupling subiteration is required within each time step.

To recover the temporal accuracy while keeping its non-iterative manner, Piperno and Farhat [175] develop a generalised CSS procedure by introducing a structural displacement predictor. This prediction-correction approach guarantees that both the fluid and solid equations are resolved implicitly, which retains the second-order accuracy of the FSI system. Förster et al. [176] conduct a stability analysis on the prediction-correction type of sequential staggered coupling methods. They found that the explicit scheme will become more unstable if the fluid/solid density ratio is reduced and/or the time-step is smaller, which is consistent with the conclusions from Causin et al. [173]. Furthermore, they also concluded that higher order of predictors or time discretisation schemes will increase the instabilities of the FSI system.

To remedy the instability issue associated with the explicit partitioned procedure, a fully implicit scheme must be used. This can be done by introducing a subiteration loop within each time step so that the equilibrium conditions at the interface are satisfied. Before proceeding to any implicit coupling scheme which requires subiterations within each physical time step, the flow solver ($\mathcal{F}$) and the structural solver ($\mathcal{S}$) are expressed in two different formulations:

(1) fixed point formulation:

$$\begin{aligned} \boldsymbol{f} &= \mathcal{F}(\boldsymbol{x}) \\ \boldsymbol{x} &= \mathcal{S}(\boldsymbol{f})' \end{aligned}$$

(3.59)

(2) root-finding formulation:

$$\begin{aligned} \mathcal{F}(\boldsymbol{x}) - \boldsymbol{f} &= \boldsymbol{0} \\ \mathcal{S}(\boldsymbol{f}) - \boldsymbol{x} &= \boldsymbol{0}' \end{aligned}$$

(3.60)

where $\boldsymbol{x}$ is the position of the fluid-structure interface and $\boldsymbol{f}$ is the fluid load on it.

With the fixed-point formulation, the coupled system (Eq. (3.59)) can be solved with fixed-point iterations (also known as Gauss-Seidel iterations) between the flow and structure solvers, where a relaxation factor ϖ is usually used [177]. Causin et al. [173] also analyse the stability characteristics of the Gauss-Seidel coupling method using their linearised FSI model. They found that for a constant relaxation factor, this factor is required to be a smaller value if 1) the structure becomes more flexible; 2) the time-step is reduced; 3) the fluid/solid density ratio is decreased. Another stability analysis of a Gauss-Seidel coupling method is performed by Degroote et al. [178,179] using a simplified one-dimensional model. By performing a Fourier error analysis, they demonstrate that the error modes with low spatial frequencies have higher amplification factors, which means that those low wave number error modes are responsible for the unstable behaviour. They also find that a simple fixed-point iterative scheme (also known as Gauss-Seidel iterative method) is difficult to converge, even if it converges, it often requires more subiterations. Additionally, they also show that reducing the time step and increasing the structure flexibility will increase the subiterations required in fixed-point iterative method. The performance of the fixed-point scheme can be significantly improved by adding artificial compressibility to continuity equation [180,181], introducing reduced order models [182] or using dynamic relaxation parameters (e.g., Aitken relaxation scheme) [183]. The artificial compressibility is added as a source term to the continuity equation for the cells adjacent to the fluid-structure interface, which imitates the effect of structural displacement due to the fluid force and mitigates the compressibility constraint. The artificially added term disappears when the coupling converges. However, adding artificial compressibility to flow equations requires the accessibility of the source code of the flow solver and the additional modification work is nontrivial. However, the latter two approaches can be applied to black-box solvers.

The coupled equations in root-finding formulation (Eq. (3.60)) can be solved with Interface-Newton methods with Newton-Raphson iterations, where the (inverse)

Jacobian can be approximated using reduced order models [184,185]. The linear system within each Newton-Raphson iteration can also be solved using a matrix-free Krylow solver e.g., generalised minimal residual method (GMRES), with a linear combination of previous residual vectors [186,187]. The Interface-Newton methods with the Jacobian approximated with reduced order models are also referred to as quasi-Newton methods. Vierendeels et al. [182] develop a quasi-Newton method aimed at coupling black-box fluid and structural solvers. In their coupling algorithm, the Jacobians of both fluid and structural solvers are approximated by means of constructing least-squares models using fluid-structure interface information from all previous subiterations within one physical time step. In later publications of the same research group [177,188], this method is referred to as the Interface Block Quasi-Newton with an approximation for the Jacobians from Least-Squares models (IBQN-LS). Degroote et al. [177] develop a new quasi-Newton method named IQN-ILS (interface-quasi-Newton with inverse Jacobian from a least-squares model) based on the technique creating Jacobian approximation from the IBQN-LS algorithm. The key difference between the IQN-ILS and the IBQN-LS is that the inverse of the Jacobian appearing in the Newton linearisation rather than the Jacobian itself is approximated in the IQN-ILS algorithm. The performance of the IQN-ILS is compared with other partitioned algorithms (IBQN-LS, Aitken relaxation and Interface-GMRES(R)) by Degroote et al. [188]. They conclude that the IQN-ILS method has similar performance with the IBQN-LS method but better performance than Aitken relaxation and Interface-GMRES(R).

Generally, three important aspects must be considered when selecting coupling algorithms, namely, implementation complexity, computational time and numerical stability. The explicit coupling schemes (e.g., CSS algorithm with or without predictors) have the lowest complexity of implementation, the least computational expenditure, but are the most unstable. Thus, the explicit coupling methods are usually applied to problems involving weak fluid-structure interactions. For strong fluid-structure interactions, fully implicit coupling schemes must be employed in

order to ensure the numerical stability. The Gauss-Seidel iterative schemes solve the FSI problem in fixed-point formulation by alternatively calling the fluid solver and solid solver within a time step until a convergence is reached. The Gauss-Seidel methods with no or constant relaxation factors usually cannot reach a convergence, or even converged, they require more coupling iterations. These methods can be stabilised by introducing artificial compressibility, reduced order models or dynamic relaxations. However, these stabilisation methods only enhance the coupling stability, but also increase implementation complexity. Another way of achieving fully implicit coupling schemes is solving the FSI system in root-finding formulation with Interface-Newton methods. However, all these implicit schemes require subiterations within one physical time step which substantially increases the computational cost. The features of different coupling schemes are summarised in Table 3-1.

Table 3-1 Summary on the main features of different coupling algorithms

Coupling Method	Complexity	Cost	Stability
CSS	Low	Low	Low
Aitken Relaxation	Medium	High	Medium
Interface-GMRES	High	Medium	High
IBQN-LS	High	Medium	High
IQN-ILS	High	Medium	High

3.3.2   *Coupling between CFD solver and CSD solver*

In the present thesis, we are focusing on numerically studying bio-inspired propulsive systems, which are fully three-dimensional and thus require considerable computational time. The CSS method is therefore used in the current code implementation due to its simplicity and efficiency. As discussed previously, the numerical stabilities of explicit coupling algorithms (e.g., CSS method) are determined by the geometry, solid-to-fluid mass ratio and flexibility of the structure (see Eq. (3.58)), which means that the issues associated with the numerical stability of

an explicit coupling approach can be avoided by carefully selecting the parameter space.

The CSS procedure implemented in the present code has the following basic steps when marching from time step t^n to t^{n+1}:

1) Advance fluid field explicitly to time step t^{n+1} based on structural solution at t^n.

2) Collect fluid forces on the solid boundary of the fluid mesh and interpolate onto the structural mesh.

3) Advance structural solution implicitly to time step t^{n+1} based on newly obtained fluid field at t^{n+1}.

4) Transfer the structural displacement at t^{n+1} to the fluid mesh.

5) Update the entire mesh of the fluid domain.

6) Build the connectivity between different sub-grids if overset grid function is used.

The coupling procedure within one time step is also demonstrated in Figure 3-3
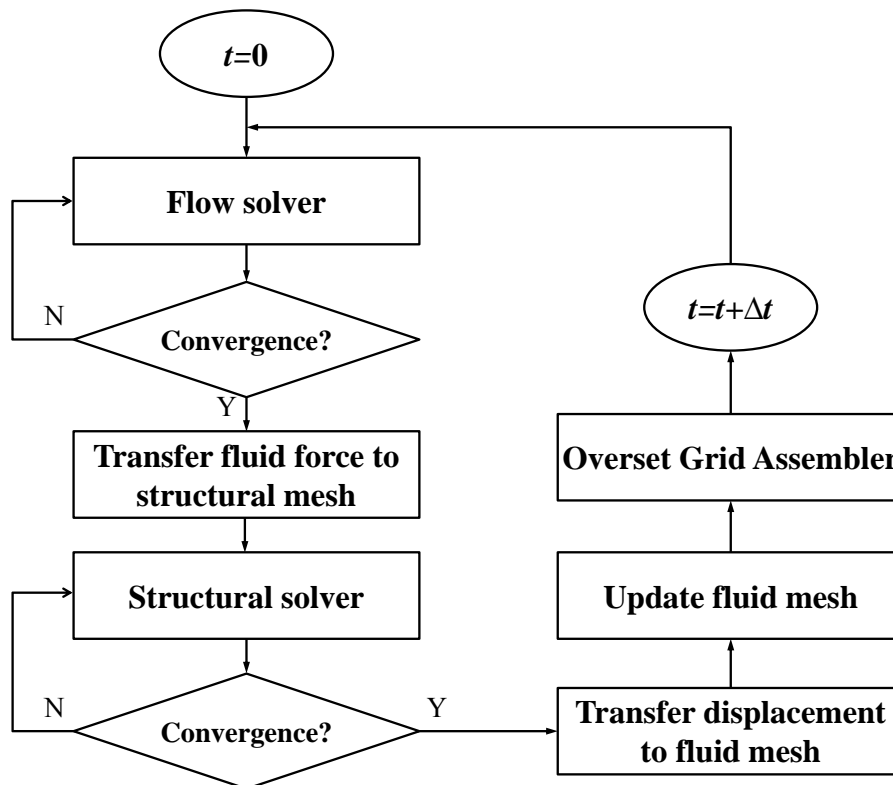
Figure 3-3 Illustration of CSS fluid-structure coupling procedure within one physical time step.

3.3.3 Fluid-structure interface

In the present FSI model, the fluid domain and the solid domain are discretised with different schemes owing to different requirements for solving the fluid and structural equations. The solution of the fluid equations requires an accurate description of the geometry of the body. However, the body is structurally represented by beams or plates for the dynamic analysis. Therefore, an interface used for data exchange between the two domains is necessary for FSI simulations.

3.3.3.1 Structural displacement transfer

Figure 3-4 (a) illustrates the non-conformal interface between the fluid and the solid grids. The geometry of the wing is accurately described by the fluid mesh while the wing's structural dynamics is analysed on a planar mesh. For a fluid-structure interface depicted in Figure 3-4 (a), an interpolation-extrapolation approach [139] needs to be employed in order to convert the displacements from the structural mesh points to the fluid mesh points on the wet boundary of the wing. This is achieved using a constant-volume tetrahedron (CVT) method proposed by Goura et al. [189]. Here, only the concept and mathematical formulation of the CVT method are introduced, more details can be found in [189,190].
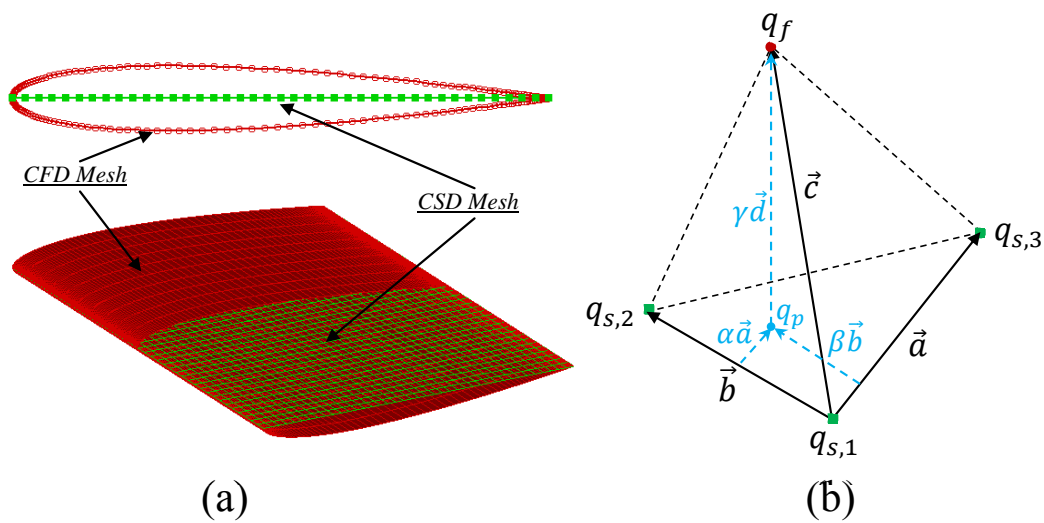
Figure 3-4 Illustrations of (a) non-conformal fluid-structure interface and (b) constant volume tetrahedron.

As shown in Figure 3-4 (b), each node q_f on the fluid grid is connected rigidly to three closest points $q_{s,i}$ on the solid plane spanning a tetrahedron. During the deforming process, the volume of the tetrahedron is assumed to be a constant. The out-of-plane distance $\|\bar{\gamma}\vec{d}\|$ thus becomes a function of the in-plane stretching of the three connected solid points. In the local coordinate system spanned by difference vectors $\vec{a}$ and $\vec{b}$ and the normal vector $\vec{d} = \vec{a} \times \vec{b}$, the position of the fluid node q_f can be described as

$$q_f - q_{s,1} = \alpha\vec{a} + \beta\vec{b} + \bar{\gamma}\vec{d}. \tag{3.61}$$

After the deformation of structural grid, the vectors $\vec{a}, \vec{b}$ and thus $\vec{d}$ are known. The parameters α and β are chosen to be constant, i.e., $\alpha = \alpha_0$ and $\beta = \beta_0$ (subscript 0 denotes the initial values). As proposed by Goura et al. [189], the parameter $\bar{\gamma}$ is defined as

$$\bar{\gamma} = \frac{\vec{d_0} \cdot \vec{d_0}}{\vec{d} \cdot \vec{d}} \bar{\gamma}_0, \tag{3.62}$$

which ensures the volume of the tetrahedron spanned by $\vec{a}, \vec{b}$ and $\vec{c}$ to be a constant. With the relation in Eq. (3.61), the displacement of the fluid node can be expressed as

$$\Delta\vec{c} = \alpha\Delta\vec{a} + \beta\Delta\vec{b} + \Delta(\bar{\gamma}\vec{d}). \tag{3.63}$$

In order to keep the conservativeness, the structural displacements need to be transformed to fluid grid linearly. However, the last term in Eq. (3.63), which involves cross-product calculation, is nonlinear. With the linearisation method of Sadeghi et al. [190], the displacement of a fluid node can be written as

$$\begin{aligned}
\Delta\vec{c} = &\left\{\alpha[I] - \tilde{\gamma}\left([I] - \frac{2}{\tilde{d}^2}[\tilde{D}]\right)[\hat{B}]\right\}\Delta\vec{a} \\
&+ \left\{\beta[I] - \tilde{\gamma}\left([I] - \frac{2}{\tilde{d}^2}[\tilde{D}]\right)[\hat{A}]\right\}\Delta\vec{b},
\end{aligned} \tag{3.64}$$

where $\tilde{d}$ is the normal vector evaluated at the linearisation point, and $\left[\widetilde{D}\right]$ is defined

by $\widetilde{D}_{i,j} = \tilde{d}_i \tilde{d}_j$. $\tilde{\gamma} \equiv \frac{\overline{\gamma}_0 d_0^2}{\tilde{d}^2}$ is an intermediate variable. The cross-product matrix $\left[\hat{A}\right]$ of

vector $\overrightarrow{a} = (a_1, a_2 a_3)^T$ is given by

$$[\hat{A}] = \begin{bmatrix} 0 & -a_3 & a_2 \\ a_3 & 0 & -a_1 \\ -a_2 & a_1 & 0 \end{bmatrix}. \tag{3.65}$$

Matrix $\left[\hat{B}\right]$ can be formulated in a similar manner.

3.3.3.2   *Fluid force interpolation*

Due to the non-conformal feature at the fluid-structure interface shown in Figure 3-4 (a), the fluid load calculated at the fluid nodes must be transferred onto the solid nodes via interpolation. The fluid force needed by the structural equation (Eq. (3.51)) is the force difference between the two sides of the structure. As demonstrated in Figure 3-4 (a), the body surface is divided by the structural mesh into two parts: the upper and lower surface. The fluid force at the upper and lower surfaces is sequentially interpolated to the CSD grid and then averaged to obtain the force difference required by the structural solver.
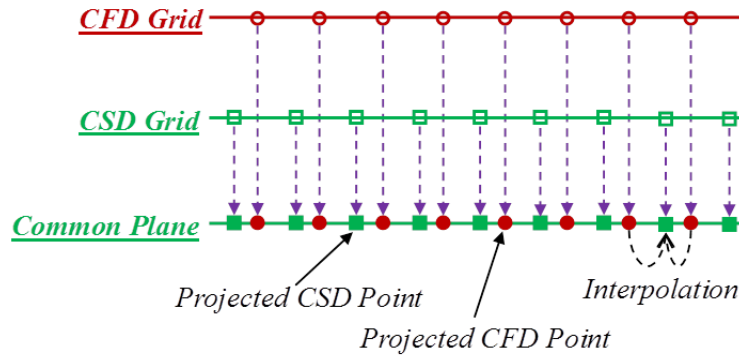
Figure 3-5 Projection of the fluid and structural points onto a common plane.

After obtaining the fluid force at the wet boundary of the body, both the fluid points at the upper/lower surface which contain the newly calculated fluid load and the structural grid points are projected onto a common plane as shown in Figure 3-5. In the present work, both the fluid and solid domains are discretised using structured

grids, i.e., the projected CFD and CSD grids are composed of quadrilaterals, as demonstrated in Figure 3-6. The fluid force value of CSD node p is interpolated from four CFD nodes a,b,c,d (which form a quadrilateral containing node p) using the following bilinear scheme.

$$f(p) = \hat{\lambda}[\hat{X}][\hat{Q}][\hat{Y}], \tag{3.66}$$

where

$$\hat{\lambda} = \frac{1}{(x_b - x_a)(y_c - y_a)},$$

$$[\hat{X}] = [x_b - x \quad x - x_a],$$

$$[\hat{Q}] = \begin{bmatrix} f(a) & f(c) \\ f(b) & f(d) \end{bmatrix}, \tag{3.67}$$

$$[\hat{Y}] = [y_c - y \quad y - y_a]^T.$$
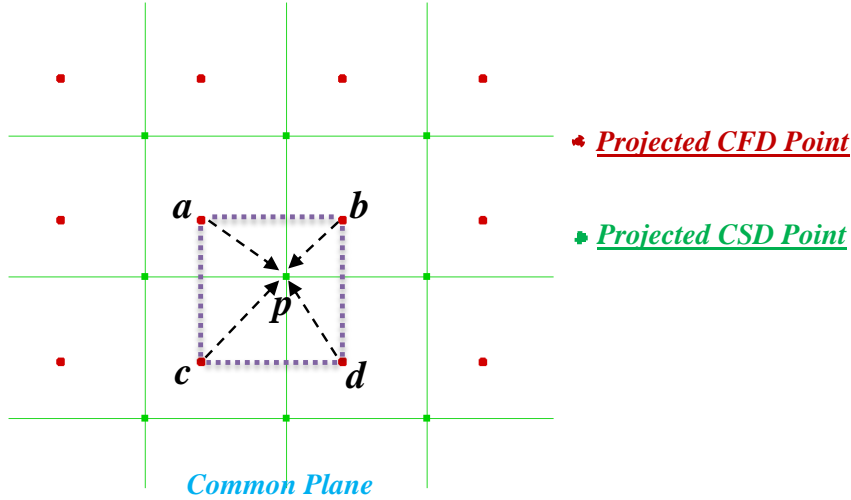
Figure 3-6 Bilinear interpolation from projected fluid nodes to projected structural nodes.

3.4 Strategy for deformable overset grids

The overset grid methodology uses a set of grids which can overlap/embed with each other to discretise the flow domain in CFD simulations. A body-fitted grid is generated for each component of the geometry without interfering each other, which greatly simplifies the overall mesh generation process. This overlapping grid method has even

stronger advantages when dealing with multiple bodies with relative motion due to the fact that the motion of a component grid will not affect the grid quality of another component. However, in order to make the overlapping grids work as one composite grid, special treatment must be done to enable the communication between each component grid (referred as sub-grid hereafter). Otherwise, one sub-grid will not feel the existence of other sub-grids. This special treatment is the process of establishing the connectivity between sub-grids, which is known as Overset Grid Assembly (OGA). Despite the advantages of overset grid on generating complicated grids and handling multiple bodies in relative motion, it does have some restrictions: firstly, meshes in the overlapping region should be in similar resolution in order to mitigate the interpolation errors. Secondly, the overlapping region must be sufficiently large to provide enough stencil points used for desired interpolation schemes. The OGA procedure can be either implemented in a stand-alone code, which requires additional work on inter-communication with the flow solver, or integrated with flow solver as a unified code. The overset grid methods used in the present thesis are introduced in Section 3.4.1 and 3.4.2.

The biomimetic problems studied here involve passive structural deformations. The CFD mesh should also be deformed accordingly. For an overset grid method with moving mesh, only the sub-grids associated with deforming bodies need to be deformed while the rest sub-grids will stay stationary. For CFD calculation on a moving grid, the Geometric Conservation Law (GCL) should be fulfilled [191]. In the present CFD solver, the discrete GCL is satisfied by using the relative flow velocity when formulating convective flux in Eq. (3.4) and accounting for the temporal change of the control volume in Eq. (3.29). No direct evidence so far has proved that the overset grid method will violate the GCL. The mesh deformation algorithm used here will be introduced in Section 3.4.3.

3.4.1   Implicit hole-cutting technique

An implicit hole-cutting (IHC) method was proposed by Lee & Baeder [192,193] in order to alleviate the complexity of explicit hole-cutting method when creating the domain connectivity. The IHC method does not require explicit definition of the hole boundary, thus it can be completely automated. However, one disadvantage of this IHC method is that it could be more computationally demanding than the explicit counterpart.

3.4.1.1 Basic donor detection steps

The IHC method is intrinsically a cell selection process based on the criterion of cell size, and the concept of 'donor' and 'receiver' is also used here. The donor cell for a receiver point on one sub-grid refers to the cell on another sub-grid containing the receiver point, as illustrated in Figure 3-7 (a). Following Liao et al. [194], the basic donor detection procedure for IHC method follows three steps

1) Low-order inside/outside cell test. The test uses a quick cross and dot product method to check if the testing point is inside or outside a cell. This test is required in every step of the donor search process.

2) High-order inside/outside cell test. Once a potential donor cell is identified in the low-order cell test, a test with higher order is triggered, which requires the calculation of the computational coordinate (ξ) of the testing point within this cell. The cell will become a candidate of the optimum donor for the current testing point if ξ converges to a value ranging from 0 to 1.

3) Cell size based donor selection. If multiple donor cells are found after the previous two steps, the one having the smallest cell volume will be selected as the optimum donor cell and used for inter-grid interpolation.
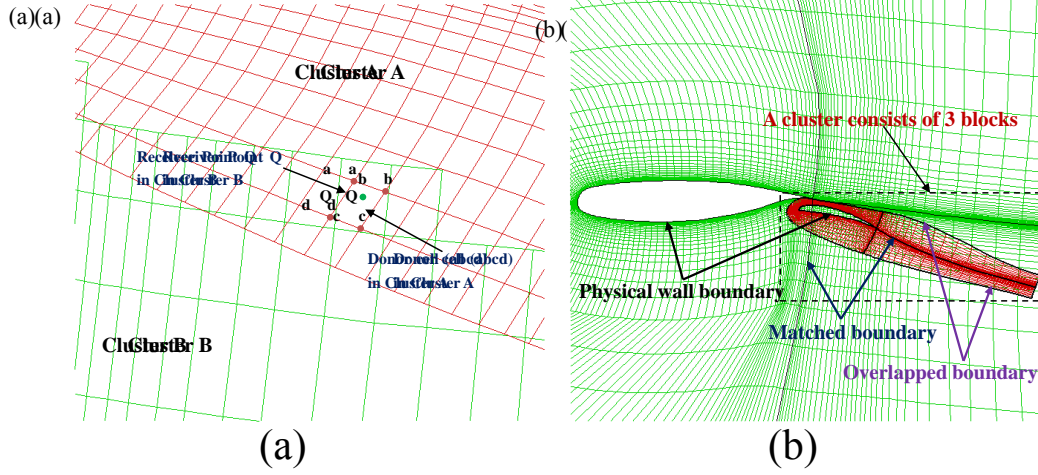
Figure 3-7 (a) Illustration of the receiver and donor in overset grid; (b) demonstration of the concept of 'cluster'.

3.4.1.2 Interpolation schemes

In the present work, the flow variables are transferred from the center points of donor cells to receiver points by a trilinear interpolation method. The eight (for 3D case) or four (for 2D case, such as a, b, c, d shown in Figure 3-7 (a)) vertices of the donor cell form the interpolation stencil points for the receiver point (such as point Q shown in Figure 3-7 (a)). With this set of stencil points, the trilinear interpolation method used in the present study can be expressed as follows:

$$Q_{\hat{\xi},\hat{\eta},\hat{\zeta}} = \sum_{i=0}^{1}\sum_{j=0}^{1}\sum_{k=0}^{1} \hat{\xi}^i\left(1-\hat{\xi}\right)^{1-i}\hat{\eta}^j(1-\hat{\eta})^{1-j}\hat{\zeta}^k\left(1-\hat{\zeta}\right)^{1-k}\tilde{Q}_{i,j,k}, \quad (3.68)$$

where $Q_{\hat{\xi},\hat{\eta},\hat{\zeta}}$ is the function value at the receiver point and $\tilde{Q}_{i,j,k}$ are the function values at the stencil points. $\left(\hat{\xi},\hat{\eta},\hat{\zeta}\right)$ are the values of computational coordinate ξ calculated via a Newton's method when establishing the domain connectivity. It should be noted that the computational coordinate ξ is not only used during the donor searching process, but also simplifies the interpolation of flow variables between different clusters in the flow solver.

3.4.2 Integrating IHC with hybrid multi-block system

3.4.2.1 Concept of 'cluster'

For a multi-block structured grid method, the entire computational domain is separated into many smaller blocks in order to reduce the complexity of mesh generation. Such a grid system consists of two different boundaries: physical boundaries (far-field, wall etc.) and matched boundaries (boundaries between different blocks in a point-to-point connection fashion). For an overset grid method, the entire computational domain is split into several sub-domains and a sub-grid (comprised of multiple blocks) is generated for each sub-domain. A sub-grid is here termed as a 'cluster', i.e., a cluster is a sub-grid composed of one or multiple blocks with matched boundaries between them. Figure 3-7 (b) shows a cluster (red coulour) consists of three blocks. The basic component of an overset, multi-block grid is 'block', and a block belongs to a 'cluster'. The inclusion of overset grid method creates a third type of boundary: overlapped boundary. Therefore, in the present overset, multi-block grid method, the block boundaries are classified into three categories: the physical boundary, matched boundary and overlapped boundary (see Figure 3-7 (b) for example). At the physical boundary, physical boundary conditions such as viscous wall boundary and far-field boundary conditions need to be applied. The matched boundary is the boundary where blocks are connected exactly by a point-to-point fashion, and the information is exchanged through two-layer of ghost cells around each block. The overlapped boundary is the non-physical outer boundary of one cluster. To ensure accurate data transfer between different clusters, the two layers of ghost cells are also included as fringe cells and join the grid connectivity.

3.4.2.2 Basic steps of establishing domain-connectivity

The IHC-based overset-grid algorithm for a multi-block grid system has the following basic steps [194]:

1) The complete geometry is separated into different components; for each component, a multi-block body-fitted grid (a cluster) is generated. A Cartesian off-body grid is also

generated at the background if necessary. Then all grid clusters are assembled into a single overset grid.

2) Generally, all the blocks in the overset grid have two overlapping relationship: overlapped or non-overlapped (far away from each other). The second step is to establish overlapping relationship and find donor cells for the boundary cell centre points (including the ghost-cell centre points) using the aforementioned donor detection procedure. After the process of searching donor cells for boundary cell centre points, the overlapping relationship between different blocks is determined. Since blocks in the same cluster are connected via matched boundaries, thus the donor cell for a boundary cell centre point in one cluster can only exist in the other clusters, and the cell centre points in the matched boundaries need not to be tested.

3) The third step is to search donor cells for interior cell centre points. After determining the overlapping relationship in the second step, the interior cell centre points only need to be tested for the overlapped block-pairs. This treatment will tremendously reduce the computational cost of testing the large number of interior cell centre points by ignoring blocks that have non-overlapping relationship. Here, the same donor detection procedure is applied to interior points.

4) For the parallel fluid solver used in the present study, the index information of all receiver points and the corresponding donor cells is stored in a preprocessed array on master node. Then all the information are reclassified and distributed to the other slave nodes. For each processor, it only requires the index information of the receiver points distributed to this processor and the corresponding donor cells.

After the aforementioned hole cutting procedure, all grid cells in the multi-block overset grid system are categorised into calculated cell and interpolated cell. If a cell fails to find the corresponding donor cell, it will be labeled as calculated cell; otherwise, it is known as interpolated cell. The fluid variables of the calculated cells will be updated normally while the values of these variables of the interpolated cells need to be

obtained from their corresponding donor cells. In the present study, the information exchange between a receiver cell and its donor cell is completed using a trilinear interpolation scheme introduced in subsection 3.4.1.2.

3.4.2.3 *Identification of points inside the body*

For IHC method, it is not required to identify the cells lying inside the body (termed as body cells), but it is important for residual estimation and flow visualization. Therefore, in the present code, the body cells are identified using the following procedure [195]:

1) After the IHC process, all cells are labeled as either calculated cell or interpolated cell. For a closed solid boundary, it is obvious that the calculated cells inside the body (body cells) are surrounded by interpolated cells. Thus, the body cells at the border of the interpolated cell region can be easily detected by checking the intersection status of one cell with the solid surface. First, the coordinates of the mid-point of the wall edge are evaluated for all wall cells.

2) If a calculated cell is adjacent to an interpolated cell, it is labelled as suspicious body cell.

3) If a wall mid-point *p* is located within a calculated cell *abcd* (as shown in Figure 3-8), this calculated cell (*abcd*) is labeled as body cell. If all wall interested cells are discovered, the rest suspicious body cells should be marked as calculated cells again.

4) If a calculated cell is adjacent to a body cell, it is then labelled as body cell. Continue this process until all calculated cells inside the body are labelled as body cell.
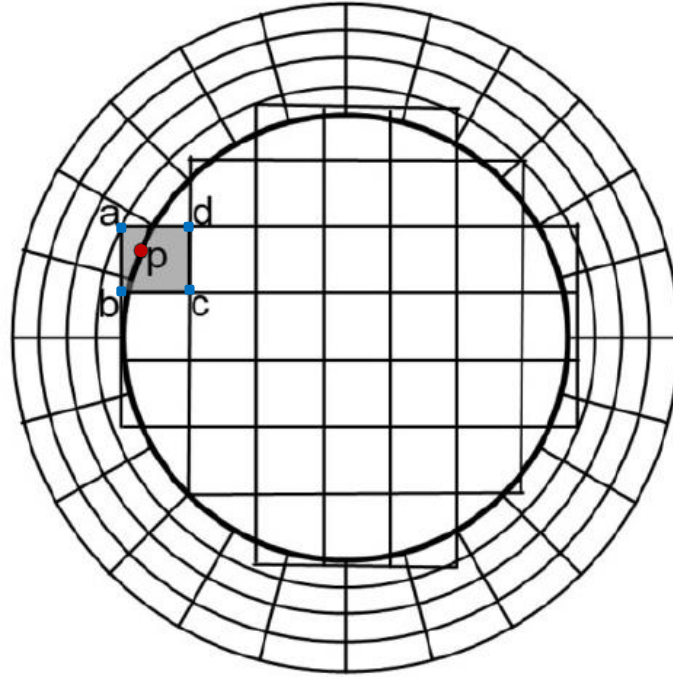
Figure 3-8 Identification of body cells, modified from [195]*.*

3.4.3   Grid deformation algorithm

For the grid system used in the present study, the geometry is divided into several components and a multi-block body-fitted grid termed 'cluster' is generated for each component. One or several Cartesian grids may also be needed as the background mesh. Only the sub-grids in the clusters involving moving/deforming bodies need to be deformed, which will avoid unnecessary movements of mesh vertices. For a cluster involving moving bodies, the grids are deformed via a fast and robust moving mesh algorithm developed by Tsai et al. [196], where all block corner points in this cluster are assumed to be connected with each other by springs whose rigidities are inversely proportional to the length of the connecting edges. With the prescribed displacements of the block corner points on the deformed surfaces, the motion of the other corner points are calculated by iteratively solving the equations of static equilibrium with a predictor-corrector process [191]. For parallel computations, the described predictor-corrector procedure is performed only on the master node. Once the coordinates of all block corner points are obtained, they will be sent to other processors, where the TFI algorithm is carried out independently [139]. After computing the new

coordinates of all grid vertices, the grid-vertex velocities are then calculated using a backward scheme [139]:

$$V_{grid} = \frac{3\overline{x}^{(n+1)} - 4\overline{x}^{(n)} + \overline{x}^{(n-1)}}{2\Delta t} \tag{3.69}$$

where $\overline{x}$ is the grid-vertex coordinate.

3.5 Concluding remarks

In this chapter, the governing equations for both fluid and solid domains and the corresponding numerical methods were introduced. Specifically, the fluid dynamics was approximated by solving the compressible Navier-Stokes equations using a finite-volume method while the structural dynamics was predicted by solving a nonlinear Euler-Bernoulli beam equation with a finite-difference method. The flow solver and structural solver were coupled in a partitioned framework using a conventional serial staggered procedure. Additionally, the flow solver was based on an overset grid system, in which the domain connectivity was created using an implicit hole cutting technique.

Chapter 4   Numerical Validations

The present CFD code based on a multiblock structured grid system and the coupling with a linear structural solver based modal analysis have been extensively validated and applied to investigate different incompressible flow problems in the previous publications of our research group [145,147,159,160,197]. In the present thesis, the CFD solver has been extended to deal with overset grids (see Chapter 3 for more information on the overset grid method) and been coupled with a nonlinear Euler-Bernoulli beam model in a partitioned framework. In this chapter, the flow solver with overset grids (Section 4.1), the nonlinear beam model (Section 4.2) and the coupled FSI solver (Section 4.3) will be validated separately.

4.1 Validation cases for flow solver

In this section, the CFD code is validated by four cases. The unsteady flows over stationary 2D and 3D cylinders are firstly simulated in Subsection 4.1.1 and 4.1.2 respectively. In order to demonstrate the capability of the present flow solver in coping with moving boundaries, the flows past an oscillating 2D cylinder and a plunging 3D wing are simulated in Subsection 4.1.3 and 4.1.4 respectively. It should be noted that the present flow solver works only on 3D mesh. For 2D simulations, two layers of mesh vertices are used in the direction of the third axis (e.g., z-axis) and symmetric boundary condition is applied to the two planes perpendicular to this axis.

4.1.1   Flow past a stationary 2D cylinder

The first case used to validate the flow solver in the present thesis is the unsteady flow past a 2D circular cylinder, as sketched in Figure 4-1 (a). This case is a benchmark case widely adopted to test the accuracy of CFD codes. The Reynolds number based

on the diameter of the cylinder D and the uniform incoming flow velocity U_∞ is $R_e =$ 185. Two different types of fluid mesh (illustrated in Figure 4-1 (b)) are used in the present simulation in order to check the accuracy of the overset grid method. For each type of fluid mesh, a fine mesh and a coarse mesh are used to demonstrate the sensitivity of the present flow solver to mesh density. Specifically, the fine and coarse overset grids consist of 78656 cells and 37600 cells respectively whist the fine and coarse multiblock meshes are composed of 80000 cells and 45696 cells respectively.
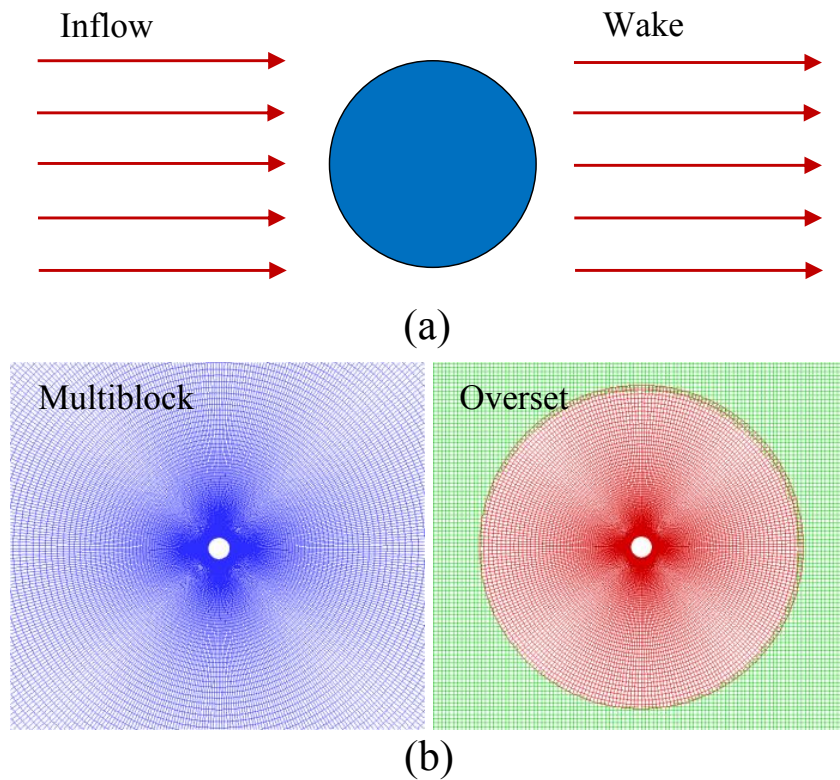
Figure 4-1 (a) Diagram of the flow past a stationary cylinder, (b) two different types of fluid mesh used in the present simulation.

Figure 4-2 demonstrates the lift and drag coefficients as a function of non-dimensional time for fine multiblock mesh, fine overset mesh and coarse overset mesh. It can be seen that both lift and drag vary periodically after a transient period. The results from meshes of different types and densities agree well with each other in both amplitude and frequency, which demonstrates that the overset grid method in the present thesis is accurate and not sensitive to the number of mesh cells if sufficiently high mesh density is used.
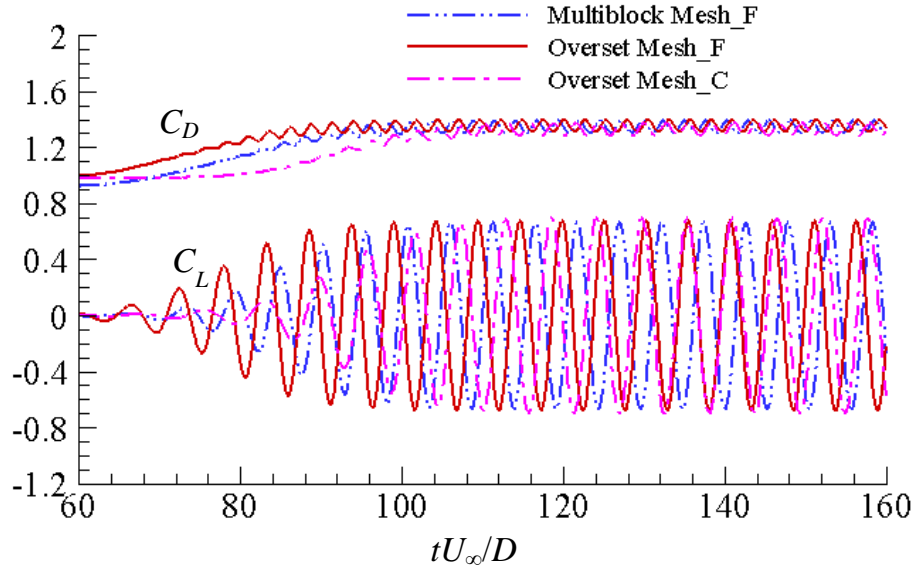
Figure 4-2 Time histories of the lift and drag coefficients obtained from different fluid meshes.

Table 4-1 Numerical and experimental results of $C_{L,r.m.s.}$, $C_{D,mean}$ and $S_{t,d}$ at R_e=185.

	$C_{L,r.m.s.}$	Error	$C_{D,mean}$	Error	$S_{t,d}$	Error
Present Case I	0.479	*8.1%*	1.351	*5.5%*	0.190	*0%*
Present Case II	0.489	*10.3%*	1.327	*3.7%*	0.183	*-3%*
Present Case III	0.473	*6.7%*	1.351	*5.5%*	0.189	*-0.5%*
Present Case IV	0.507	*14.1%*	1.347	*5.2%*	0.188	*-1%*
Numerical [198]	**0.443**	*0%*	1.287	*0.5%*	0.195	*2.6%*
Experimental [199]	-	-	**1.280**	*0%*	**0.190**	*0%*
Numerical [199]	0.422	*-4.7%*	1.310	*2.3%*	0.195	*2.6%*
Universal Strouhal [200]	-	-	-	-	0.193	*1.6%*

Case I: Overset Mesh_F, dt = 0.04D/U$_\infty$. Case II: Overset Mesh_C, dt = 0.10D/U$_\infty$. Case III: Multibock Mesh_F, dt = 0.04D/U$_\infty$. Case IV: Multiblock Mesh_C, dt = 0.10D/U$_\infty$.

The mean value of drag coefficient, the root-mean-square (r.m.s.) value of lift coefficient and the Strouhal number from the present simulation and the literature are summarised in Table 4-1. It is seen that the present results obtained from different mesh type, mesh density and time step agree well with each other. Compared with

data from the literature, the present simulation slightly overestimates the $C_{L,r.m.s.}$ and $C_{D,mean}$, but is still in a reasonable range. The Strouhal numbers predicted by the present simulation and those from literature are in good agreement. The snapshots of flow vorticity from overset grid and multiblock grid when C_L is at the maximum value are demonstrated in Figure 4-3. The formation of Von Karman vortex street behind the cylinder can be clearly observed from this figure. Besides, the vortex shedding simulated using overset grid and multiblock grid agree very well with each other.
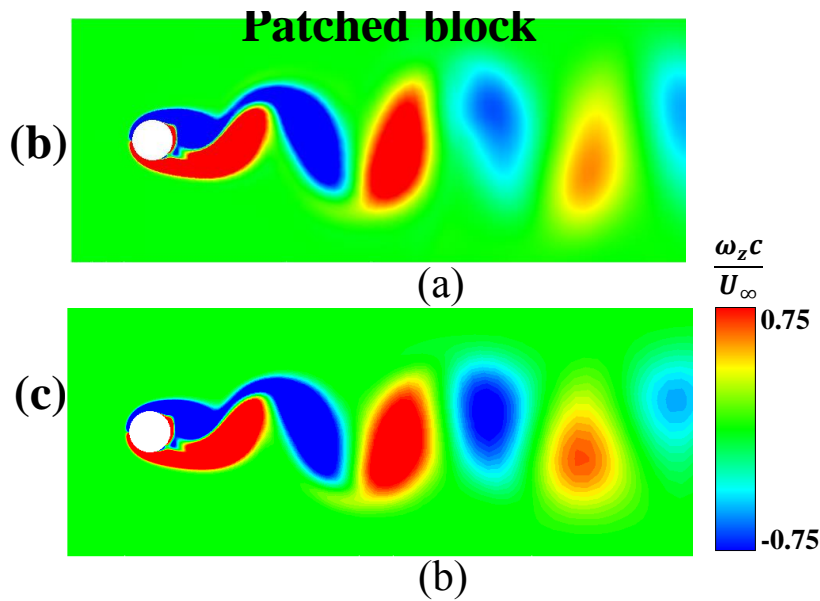
Figure 4-3 Flow vorticity from fine overset mesh (a), and fine multiblock mesh (b) when C_L reaches its peak, dt = 0.04D/U_∞.

4.1.2   *Flow past a stationary 3D cylinder*

The flow past a three-dimensional cylinder with two different aspect ratios (for Case I, L_s/D = 6.28 and for Case II, L_s/D =10.24) is simulated to demonstrate the capability of the present code in dealing with fully three-dimensional flows. The spanwise length of the cylinder is L_s. The results from the present simulations are then compared with those from the literature [201,202]. The Reynolds number based on freestream velocity U_∞ and the diameter D is Re = 300. The temporal evolutions of lift and drag coefficients at two aspect ratios are illustrated in Figure 4-4 (a) and (b). It can be seen

that the time histories of force coefficients are modulated for both cases. A similar phenomenon is also observed in [202].

(a)

(b)

(c)

(d)
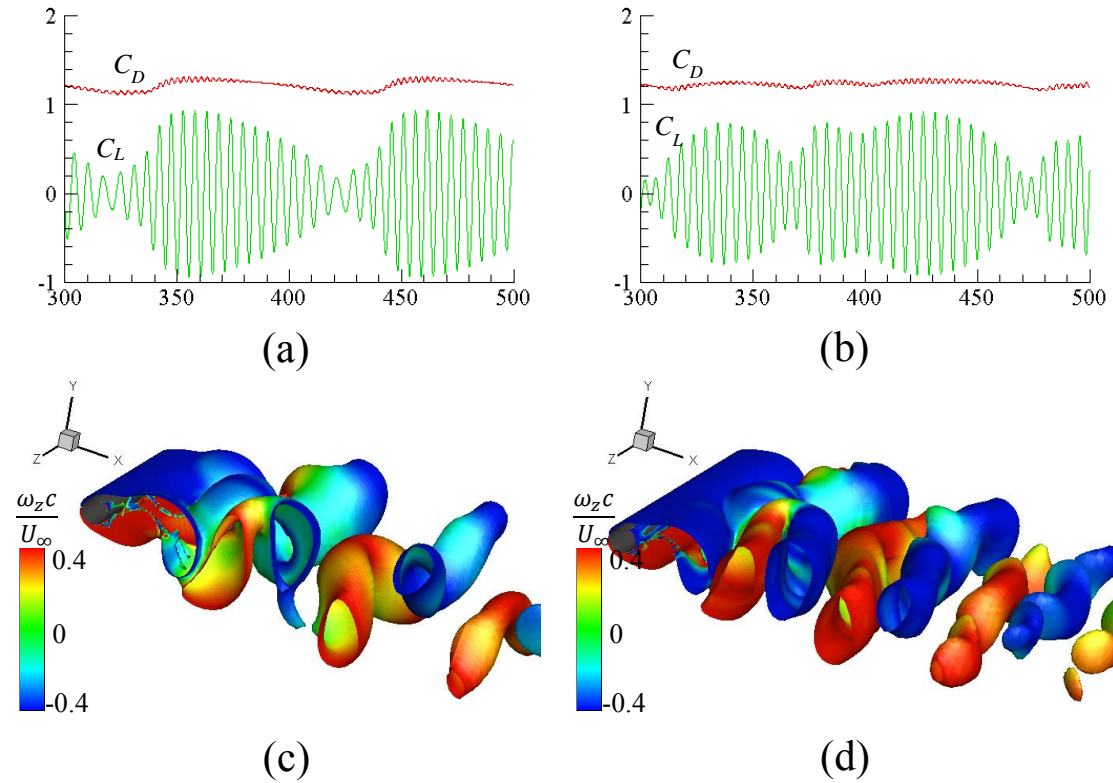
Figure 4-4 Time histories of drag and lift coefficients (a), (b) and iso-surfaces of instantaneous normalised vorticity magnitude at $\omega_{mag}=0.4$ (c), (d).   (a), (c) $L_s/D = 6.28$, and (b), (d) $L_s/D = 10.24$.

Table 4-2 Comparison of the present results with those from literature.

	L_s/D	$C_{d,mean}$	Difference	$C_{l,rms}$	Difference
Present Case I	6.28	1.217	5.2%	0.463	11.8%
Rajani et al. [201]	6.28	1.284	-	0.525	-
Present Case II	10.24	1.234	13.7%	0.466	2.9%
Constant et al. [202]	10.24	1.430	-	0.453	-

Figure 4-4 (c) and (d) demonstrate the iso-surfaces of normalised vorticity magnitude in the wake of the cylinder, from which we can see that the vortex shedding behind the cylinder is completely 3D. The mean value of drag coefficient and r.m.s. value of lift coefficient from the present simulation and the literature are summarised in Table

4-2. It can be observed that the present results agree reasonably well with the published data.

4.1.3   *Flow past an oscillating 2D cylinder*

Here we consider the vortex shedding of an oscillatory circular cylinder in uniform incoming flow. All non-dimensional variables are normalised by the cylinder diameter D, incoming flow velocity U_∞ and the fluid density ρ. Simulations are performed based on the overset grid shown in Figure 4-1 (b). The Reynolds number is R_e = 185. The cylinder undergoes a transversal oscillation which can be described as $y(t) = y_0 sin(2\pi f t)$ where y is the lateral displacement of the cylinder, y_0 and f are oscillation amplitude and frequency respectively. To compare the present results with those of Guilmineau & Queutey [198], we select y_0/D = 0.2, f/f_0 = 0.8, 0.9, 1.0, 1.1, 1.12 1.2, where f_0 is the vortex shedding frequency from a stationary cylinder at the same Reynolds number.
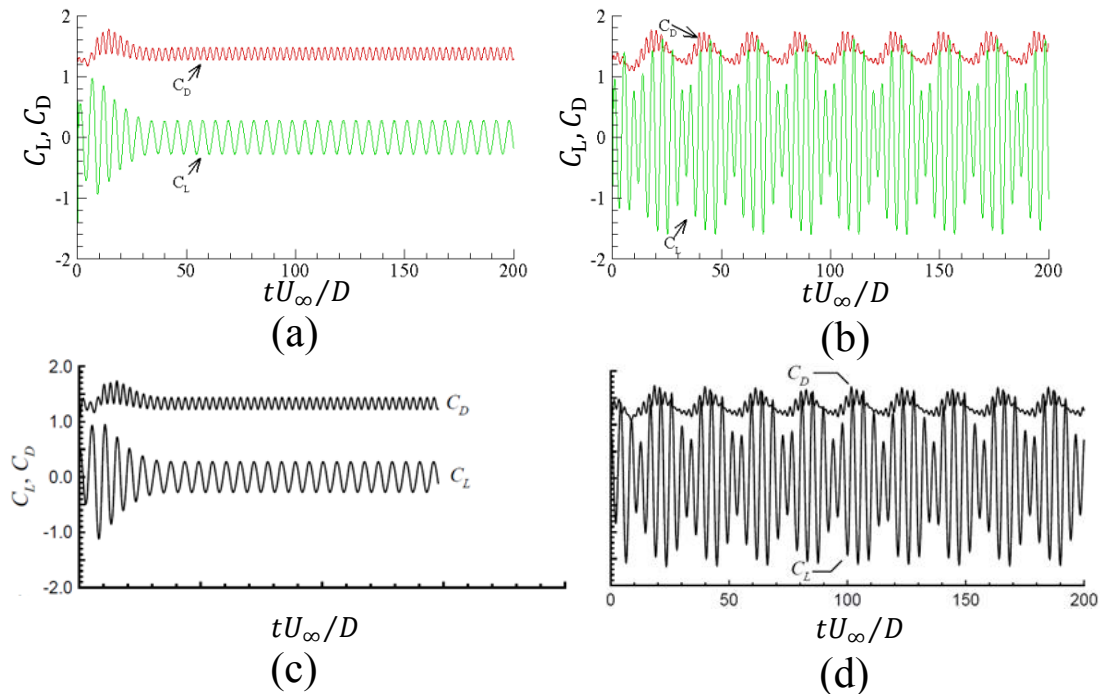
Figure 4-5 Time histories of C_L and C_D at R_e=185; (a) present simulation, f/f_0=0.9, (b) present simulation, f/f_0=1.2, (c) Guilmineau & Queutey, f/f_0=0.9, (d) Guilmineau & Queutey, f/f_0=1.2 [198].

Figure 4-5 compares the time histories of C_L and C_D from the present simulation with those from Guilmineau & Queutey [198]. For both frequency ratios, the present result shows good agreement with that from [198]. The mean value of C_D, r.m.s. values of C_D and C_L from both the present simulation and [198] are demonstrated in Figure 4-6. It is observed that for all three variables, the present data agrees very well with that from the literature.
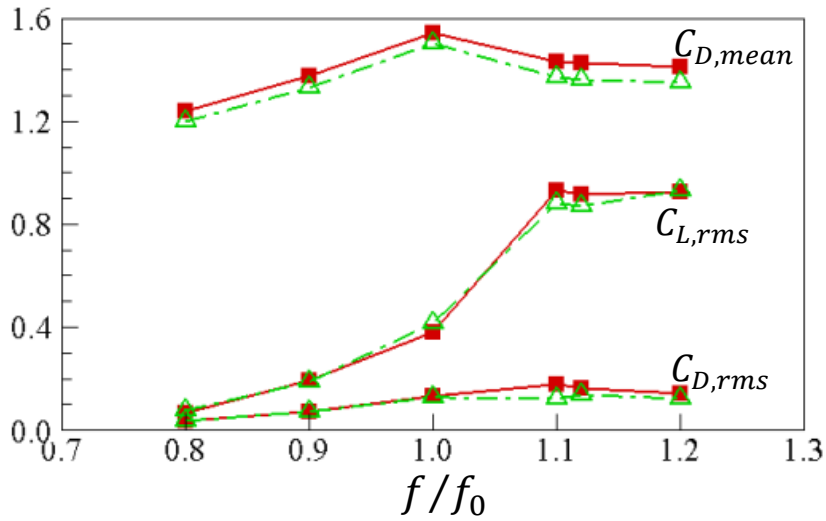
Figure 4-6 Variations of mean C_D, r.m.s. C_D and r.m.s. C_L as a function of f/f_0, red solid square is present simulation result, green empty delta is data from Guilmineau and Queutey [198].

As discussed in Subsection 3.1.3, the unsteady Navier-Stokes equation is reformulated at each time step as a steady-state problem with a pseudo time $\tilde{t}$. Instead of specifying a convergence criterion, we specify the number of iterations within each physical time step. In order to guarantee the flow is fully converged and check the sensitivity of the present CFD code to certain parameters, we carry out a parameter test in the present thesis. The parameters involved in the test are: Mach number (M_a), number of time-step in each motion period (NSTEP) and number of iteration within each physical time step (MCYC). The time histories of lift and drag coefficients obtained from different parameter combinations are demonstrated in Figure 4-7. We can observe from Figure 4-7 (a) that with the same Mach number, if sufficiently large NSTEP and MCYC values are used, the flow solver can converge to the same

solution. Similarly, Figure 4-7 (b) demonstrates that the Mach number ($M_a = 0.06$) is sufficiently low to make the compressibility effect negligible. The parameter test is quantitatively summarised in Table 4-3.
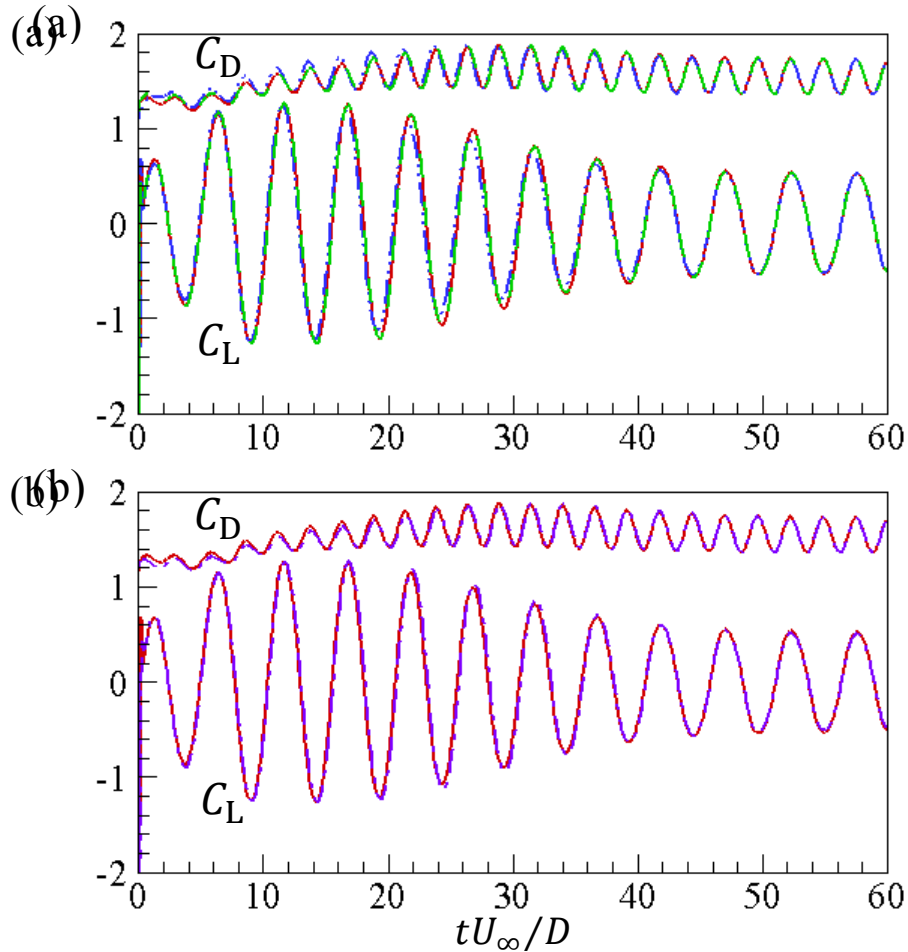
Figure 4-7 Instantaneous lift and drag coefficients obtained from the parameter test at at $R_e=185$, $f/f_0=0.9$. Red solid line: $M_a=0.06$, NSTEP=100, MCYC=100; blue dash-dot-dot line: $M_a=0.06$, NSTEP=100, MCYC=50; green dash line: $M_a=0.06$, NSTEP=200, MCYC=100; purple dash line: $M_a=0.1$, NSTEP=100, MCYC=100.

Table 4-3 Summary of parameter test on M_a, NSTEP and MCYC.

	M_a	NSTEP	MCYC	$C_{D,mean}$	$C_{D,rms}$	$C_{L,rms}$
Case I	0.06	100	50	1.544	0.129	0.377
Case II	0.06	100	100	1.544	0.129	0.378
Case III	0.06	200	100	1.542	0.129	0.380
Case IV	0.1	100	100	1.541	0.128	0.372

4.1.4   Flow past a plunging 3D wing

A three-dimensional plunging wing undergoing a plunge motion in a uniform flow is simulated and the present results are then compared with those from previous numerical [203] and experimental [204] studies. The plunge motion is described as $y(t) = y_0 \cos(2\pi f t)$, where y_0 is the plunging amplitude and f is the motion frequency. The Reynolds number based on freestream velocity U_∞ and chord length c is 30,000, the plunging amplitude $y_0 = 0.175c$ and the reduced frequency f_r ($\equiv \pi f c / U_\infty$) is 1.82. It is acknowledged that the turbulence effect may be considerable at this Reynolds number (R_e = 30,000). However, Heathcote et al. [204] used a laminar flow model to validate the force measurement in their experiment and a good agreement was achieved in their paper, which indicates the turbulence may still paly a marginal role even at the Reynolds number as high as 30,000. Therefore, a laminar flow model is chosen in the present case.
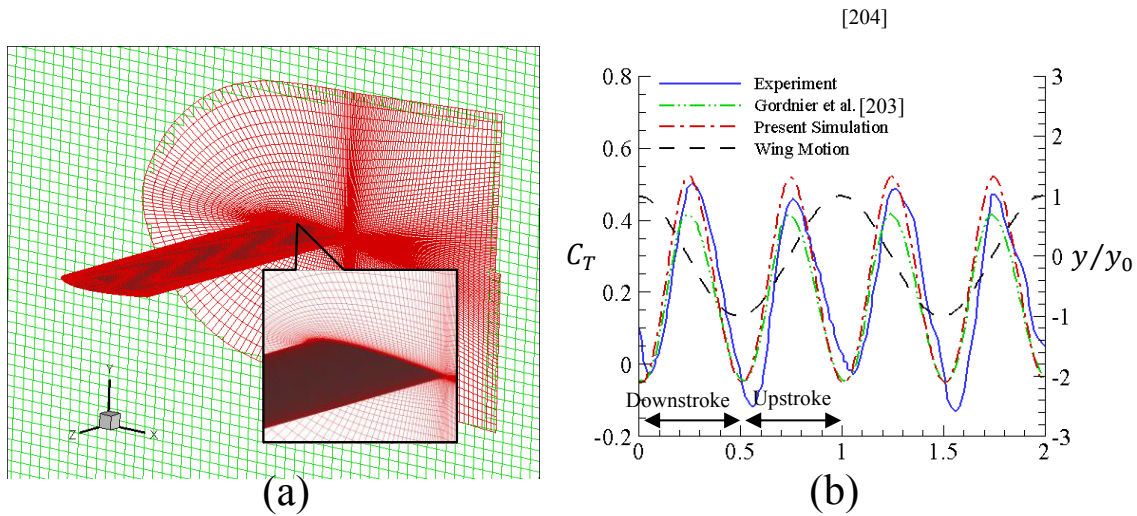
Figure 4-8 (a) Overset grid of the 3D plunging wing. (b) Experimental and numerical time histories of the thrust coefficients for the plunging wing within two flapping periods [203,204]

Figure 4-8 (a) demonstrates the overset grid used for the CFD simulation, where a body-fitted cluster is generated around the wing and a Cartesian background mesh is used to provide a far-field boundary condition. The experimental and numerical time

histories of the thrust coefficients are compared in Figure 4-8 (b). It is seen that the experimental thrust coefficient is asymmetric between the downstroke and the upstroke of the wing, while this phenomenon was not observed in the numerical simulation of the present and Gordnier et al. [203]. However, the reason for this asymmetry was not discussed in Heathcote et al. [204]. The current computed thrust peak is in good agreement with the peak during downstroke in the experiment. The flow vorticity is demonstrated in Figure 4-9, where we can observe the vortex shedding behind the wing.
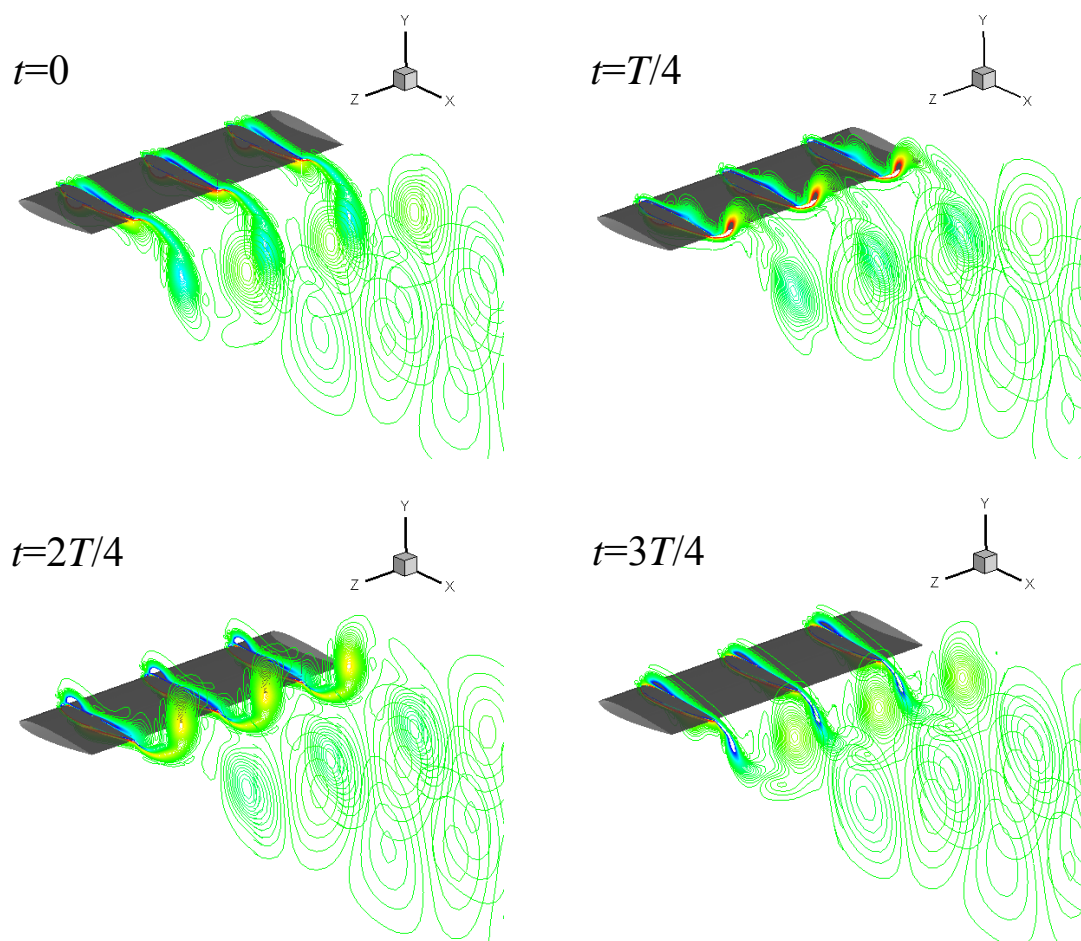
Figure 4-9 Instantaneous Z-vorticity of the plunging wing at four typical positions.

4.2 Validation cases for structural solver

4.2.1 Structural deflections of a cantilever under static loads

The structural solver is firstly validated by examining the deflections of a cantilever beam under different static external loads. Here, two different types of load are examined: concentrated load P_c at the free end (Case I) and uniformly distributed load ω_u (Case II), as sketched in Figure 4-10. The length of the cantilever is l. Theoretically, the bending deformation of the cantilever under concentrated load (Case I) can be described as

$$y = \frac{P_c x^2}{6EI}(3l - x).$$ (4.1)

For uniformly distributed load (Case II), the deformation of the cantilever can be expressed as

$$y = \frac{\omega_u x^2}{24EI}(x^2 + 6l^2 - 4lx).$$ (4.2)
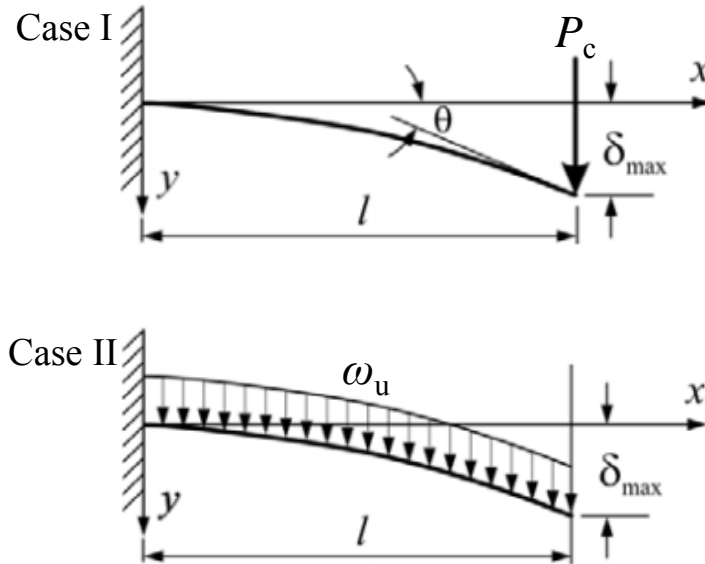
Figure 4-10 Sketch of beam deflections under static external loads [205].
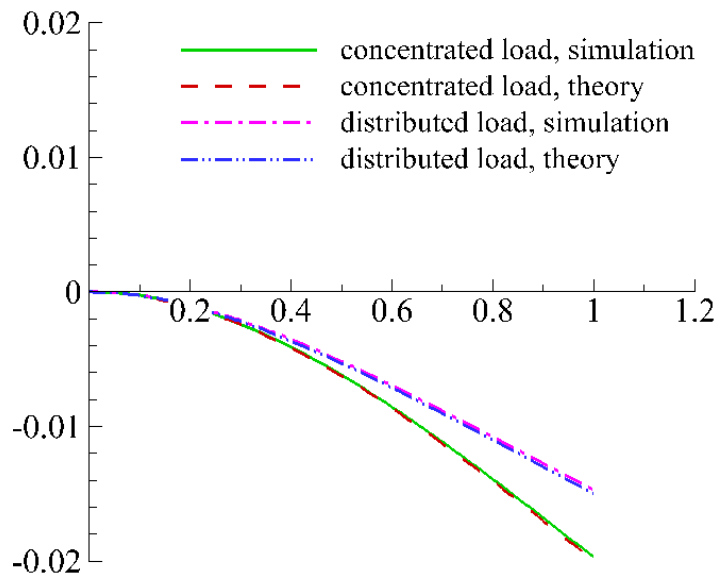
Figure 4-11 Deflections of a cantilever beam under different static loads. Theory [205].

Here, we select Young's modulus $E = 10^6$ Pa, beam length $l = 0.1$ m and beam thickness $h_p = 0.001$ m. The concentrated load is $P_c = 5\times10^{-4}$ N and the uniform load is $\omega_u = 1.0\times10^{-2}$ N/m. The present simulation results are compared with those obtained from theory in Figure 4-11, from which we can observe the present results agree very well with theory.

4.2.2   The first and second order bending modes of a cantilever

The accuracy of the present structural solver is further validated by numerically reproducing the first and second order bending modes of a cantilever via imposing a forced heave motion with small amplitude at the leading edge of the beam. The following parameters are used in this simulation: length $l = 0.1$ m, thickness $h_p = 0.001$ m, density $\rho_s = 10$ kg/m^3, Young's modulus $E = 100$ GPa, and heave amplitude $y_0 = 0.5h_p$. The natural frequencies of a cantilever can be calculated as [205]

$$\omega_i = \left(\frac{\beta_i}{l}\right)^2 \sqrt{\frac{EI}{\rho_s S}} \quad (i = 1, 2, \cdots), \tag{4.3}$$

where I is second moment of inertia, S is the cross-section area, and , $\beta_i =$ 1.875 and 4.694 for the first and second order natural frequencies respectively. The modal functions are expressed as

$$
\begin{aligned}
\phi_i(x) = cos(\beta_i x) - ch(\beta_i x) \\
+ \zeta_i[sin(\beta_i x) - sh(\beta_i x)] \ (i = 1, 2, \cdots),
\end{aligned}
\tag{4.4}
$$

where

$$\zeta_i = -\frac{cos(\beta_i l) + ch(\beta_i l)}{sin(\beta_i l) + sh(\beta_i l)} \quad (i = 1, 2, \cdots). \tag{4.5}$$

The first two bending mode shapes are shown in Figure 5.2-1 (b). It can be observed that the calculated and theoretical results agree perfectly well with each other.
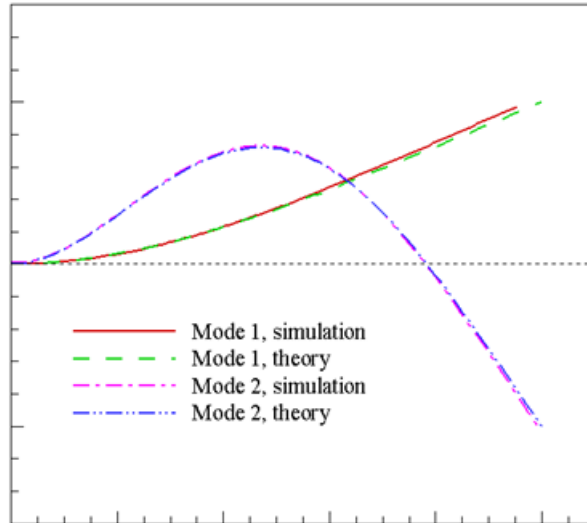
Figure 4-12 First and second order bending modes of a cantilever beam. Theory [205].

4.3 Validation cases for coupled FSI solver

4.3.1 Responses of a flexible cantilever behind a square cylinder

To validate our coupled fluid-structure interaction solver, we numerically predict the dynamics of a thin elastic cantilever placed in the wake of a stationary rigid square cylinder (as shown in Figure 4-13). This case has been widely used as validation benchmark for fluid-structure interaction solvers [206–209]. When the Reynolds number is higher than a critical value, the flow separates from the leading corners of cylinder at a constant frequency. The oscillating flow results in the oscillation of lifting force, which excites the flexible cantilever attached behind it to vibrate accordingly. The dimensionless parameters for the fluid and structure are as follows: The structure to fluid mass ratio, which is defined as $m^* \equiv \rho_s h_p / \rho L_p$, is 1.27, the non-dimensional bending stiffness of the cantilever, which is defined as $K_b \equiv EI / \rho U^2 L_p^3$, is 0.226 and the Reynolds number based on D is 332. Both the multiblock grid and the overset grid are used for fluid dynamics simulation, as shown in Figure 4-14. For overset grid, independent clusters are generated for the square body and the cantilever.
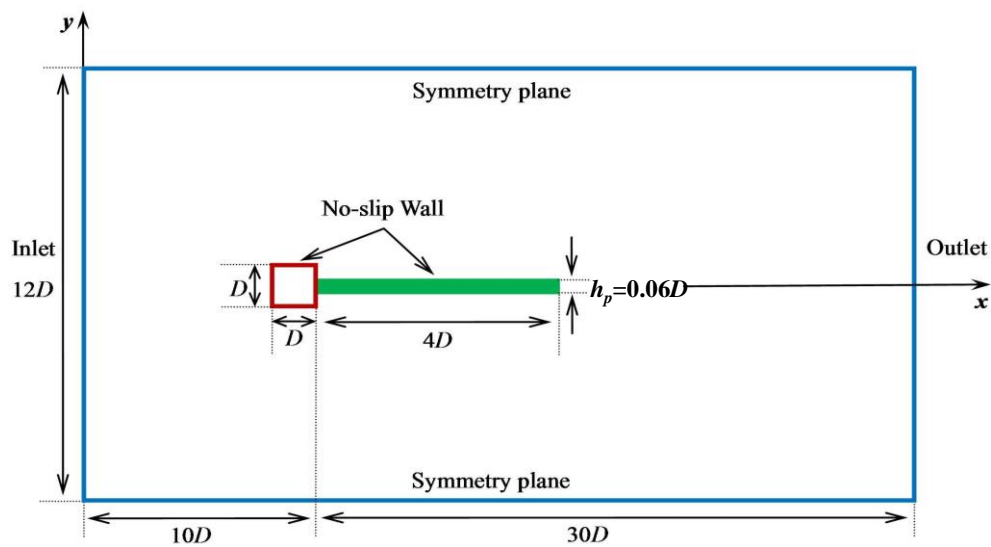
Figure 4-13 Diagram of a flexible cantilever attached behind a square cyldiner.

(a)   (b)
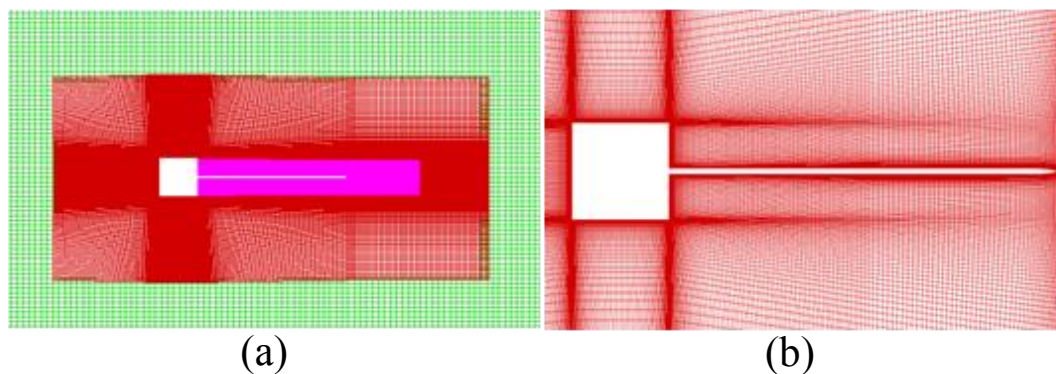
Figure 4-14 Overset grid (a) and multiblock grid (b) used for the computational fluid dynamics simulation.

The time histories of the dimensionless cantilever tip displacements obtained from both overset grid and multiblock grid are demonstrated in Figure 4-15, from which we can see that the vibration of the cantilever becomes periodic after a transient region and results from two different kinds of mesh agree well with each other in terms of oscillation amplitude and frequency. Figure 4-16 shows vorticity contours when the beam reaches the extreme positions. It is observed that flow separates at the leading corners and a clockwise vortex forms at the upper region while its counterpart forms at the lower region. These vortices travel along the vibrating cantilever and dissipate into the wake. The vortices at the trailing edge shed into the wake forming the famous Von Karman vortex street. The quantitative reduced frequency ($f_r = \pi f D / U_\infty$) and the dimensionless maximal tip displacement (d^*_{max}) are summarised in Table 4-4 along with other available data. Obviously, present results from both overset grid and multiblock grid agree well with others from the literature though the reduced frequency in the present simulation is slightly higher than the results from referred literatures [206–209]. The maximal tip displacements obtained here d^*_{max}=1.12 and 1.08 are close to those using different FSI solvers, which ranges from1.02 to 1.25.
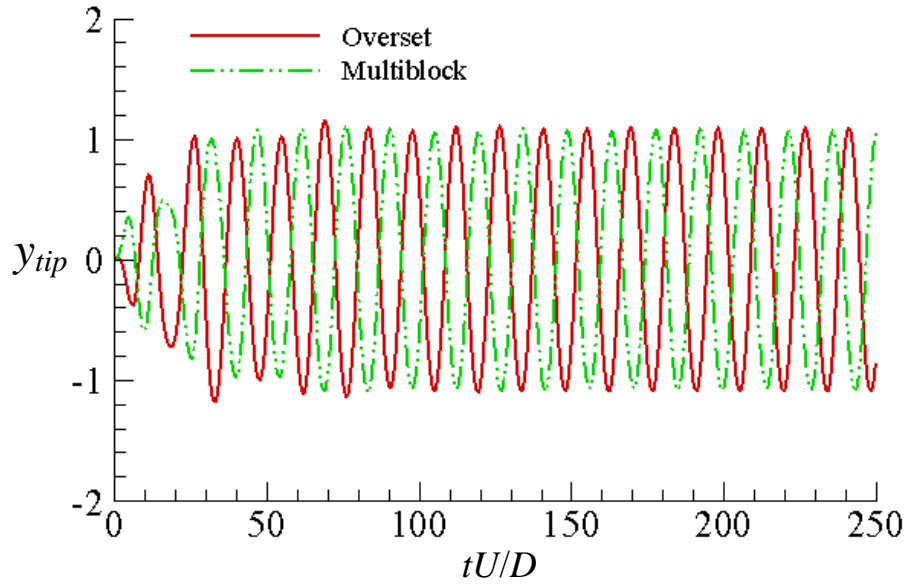
Figure 4-15 Tip displacement of the flexible cantilever.

Table 4-4 Comparison of present result with those from open literature.

Author	f_r	d^*_{max}
Matthies et al. [209]	0.192	1.18
Dettmer et al. [210]	0.185	1.25
Wood et al. [206]	0.179	1.15
Kassiotis et al. [207]	0.182	1.05
Habchi et al. [208]	0.201	1.02
Present (overset grid)	0.211	1.12
Present (multiblock grid)	0.213	1.08
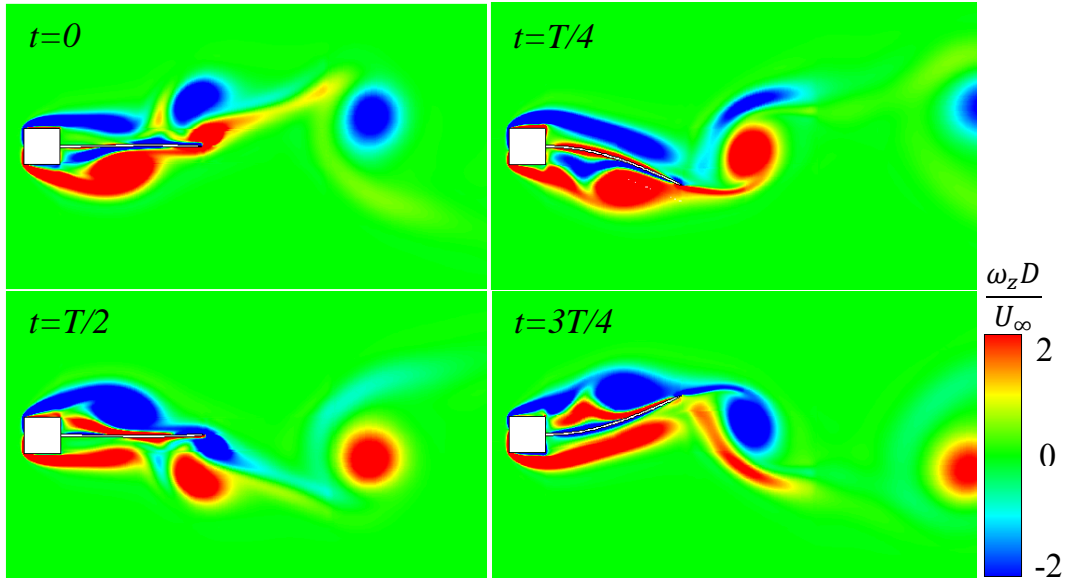
Figure 4-16 Instantaneous flow vorticity of the oscillating elastic cantilever at typical positions, overset grid.

4.3.2   Responses of a heaving flexible plate in a uniform flow

The present FSI solver is further validated against previous experiment [211], where a flexible plate is immersed in a uniform flow and imposed a heave motion at the leading edge, as schematically illustrated in Figure 4-17 (a). In the experiment, the plate has a rounded leading edge and tapered trailing edge. The chord length is c, the thickness is $h_p = 0.033c$, and the aspect ratio is unity. The dimensionless bending stiffness is $K_b = 4.2$, mass ratio $m^* = 0.3$. The Reynolds number based on the chord length and incoming flow velocity is $R_e = 6000$. The heave motion at the leading edge is prescribed as $y(t) = y_0 cos(2\pi f t)$, where $y_0 = 0.033c$ is the heaving amplitude and f is the heaving frequency. Although the experiment is three-dimensional, only two-dimensional deformations are recorded. To reduce the computational cost, in our simulation, a two-dimensional model is used. The multiblock mesh for the numerical simulation is demonstrated in Figure 4-17 (b).
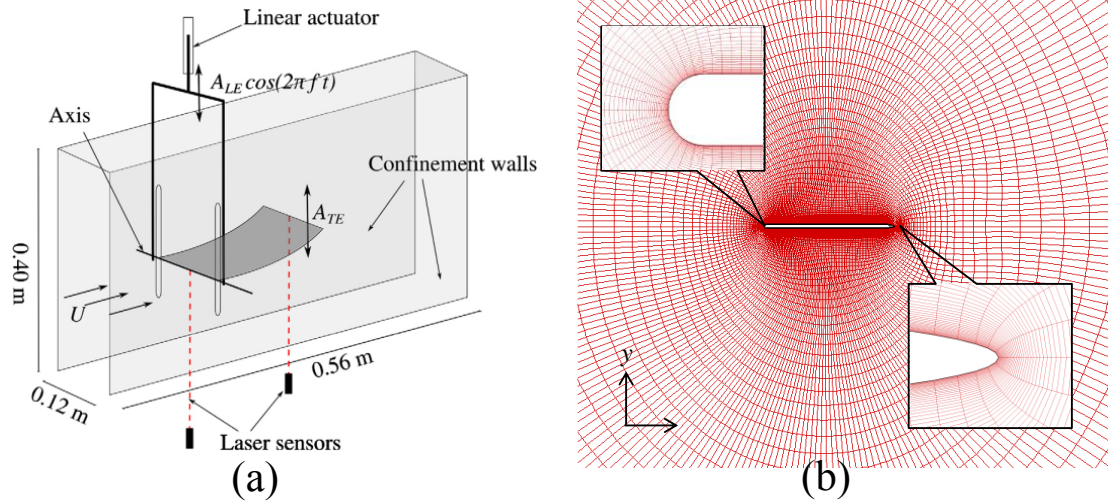
Figure 4-17 (a) Sketch of the experimental setup [211]. (b) Fluid mesh used for CFD simulation.

The dimensionless trailing edge amplitude A^* (normalised by y_0) and the phase lag (ϕ) between the leading edge motion and the trailing edge displacement as functions of reduced frequency are demonstrated in Figure 4-18. It is seen that as the increase of the motion frequency, the trailing edge amplitude reaches a peak when f_r is approximately 5.6, which is attributed to the resonance when the motion frequency is close to the natural frequency of the plate. It is observed that the present simulation successfully captures this peak value and the phase lag is also in good agreement with the experimental data.
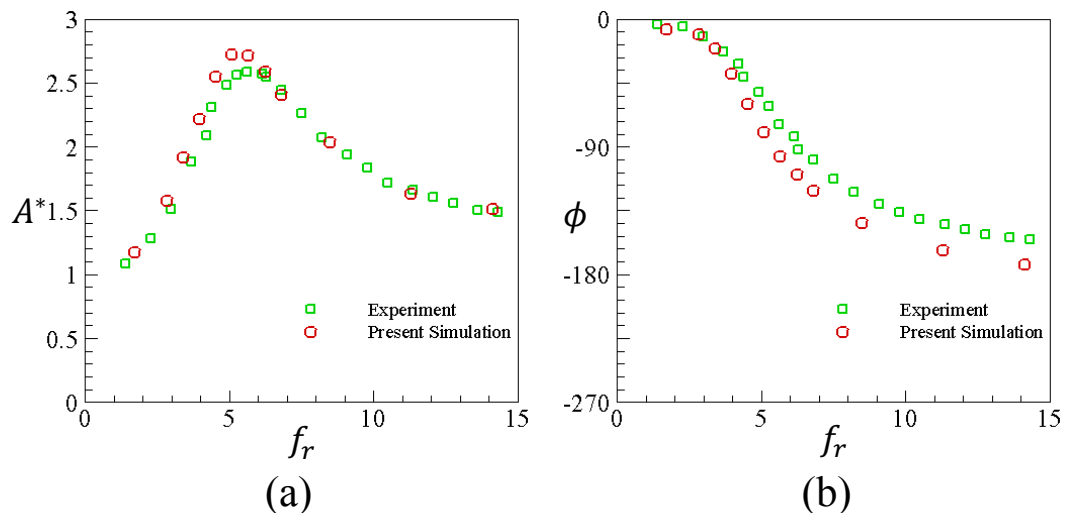
Figure 4-18 (a) Non-dimensional trailing edge amplitudes, and (b) phase lags between the leading edge motion and the trailing edge motion. Experiment [211].

(a)

(b)
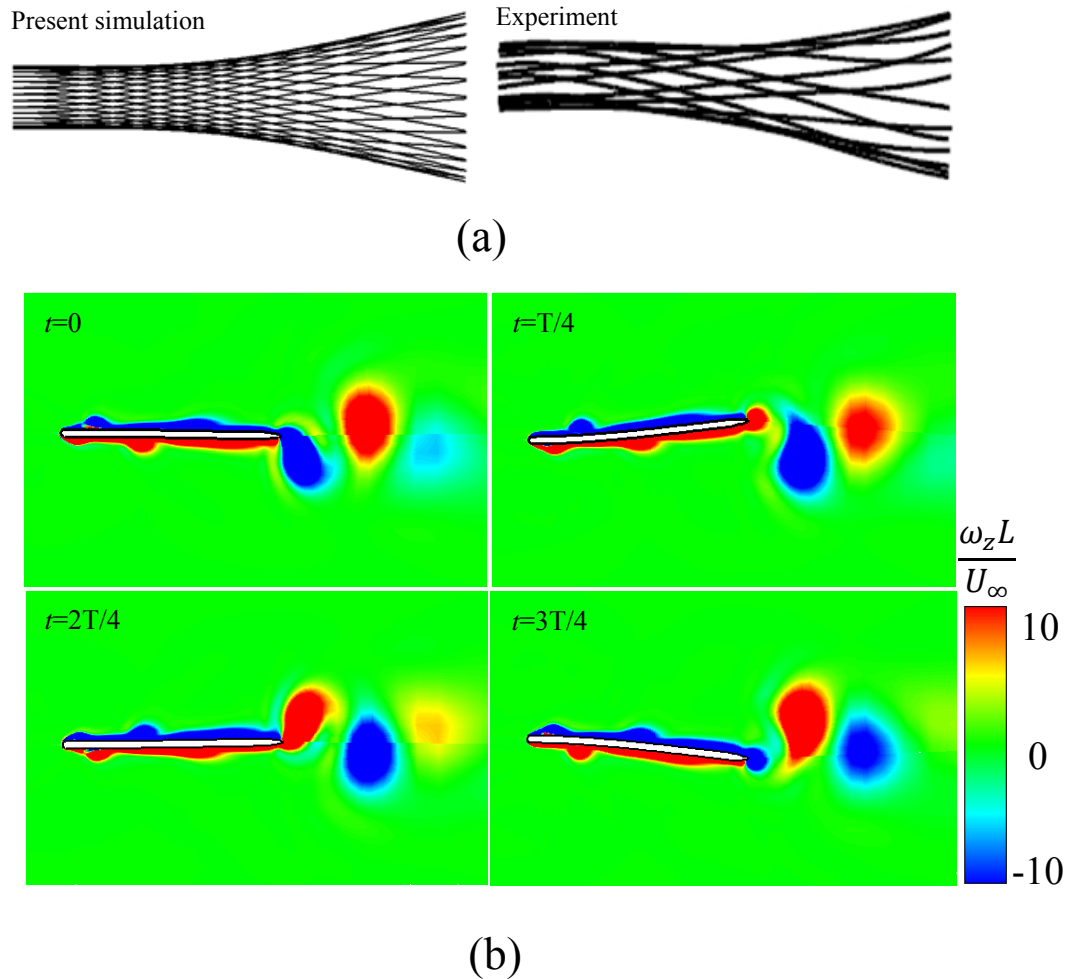
Figure 4-19 (a) Deformation patterns, f_r=5.6, and (b) flow vorticity within one motion period.

Figure 4-19 (a) shows the deformation pattern when the resonance occurs ($f_r = 5.6$). It can be seen that the present result agrees quite well with that recorded in experiment. The flow vorticity from the present simulation is demonstrated in Figure 4-19 (b), from which we can see the vortex traveling along the plate and the vortex shedding at the trailing edge, forming a reverse Von Karman vortex street.

4.4 Concluding remarks

In this chapter, the present code was validated through some benchmark and experiments. Firstly, the flow solver was validated by simulating the unsteady flows over 2D and 3D circular cylinders. The time averaged lift and drag coefficients were compared with data from literature and good agreements were obtained. To examine

the accuracy of the present CFD code in coping with moving boundary problems, the flow past an oscillating 2D circular cylinder was simulated. The present simulation results agreed well with those from literature. Additionally, the sensitivities of the present flow solver to some parameters (e.g., grid type, grid density and time step) were also checked in this chapter. It was concluded that with sufficiently dense grid and small time step, good convergence was achieved by the present CFD code. Besides, results from overset grid and multiblock grid agreed very well with each other, demonstrating the successful implementation of the overset grid function in the present code. Next, the accuracy of the structural solver used in the present thesis was examined by numerically calculating the deflection of a cantilever under static external loads, and reproducing the first and second bending modes of a cantilever. The present simulation results agreed well with the theories.

Finally, the coupled FSI code was validated by two cases. The first case involved a flexible cantilever attached to a rigid square cylinder. The flow separated from the leading corners of the square and the shedding vortices excited the flexible beam to vibrate. The oscillating amplitude and frequency of the flexible cantilever were then compared with those from literature. Good agreements were accomplished. The second case was a heaving flexible plate immersed in a uniform flow. The flexible plate experienced a resonance as the heaving frequency increases from low to high, which was also captured in the present simulation.

In summary, the validation and sensitivity studies of the present FSI solver were carried out in this chapter. It can be concluded that the present FSI solver has acceptable order of accuracy, i.e., it can be used to investigate some fluid-structure interaction problems encountered in practical applications.

Chapter 5 Effects of Spanwise Deformations on the Performance of a Ray-Strengthened Caudal Fin

5.1 Problem description

In the present study, an idealised three-dimensional fin, as shown in Figure 5-1 (a), is numerically examined. The fin is modelled as a rectangular membrane supported by evenly distributed rays. The lengths in both *x*- and *z*-directions are *c*, resulting in an aspect ratio of unity. The thickness is selected to be $h_p = 0.004c$. Kinematically, the front end (i.e. the basal end) of each ray undergoes a sinusoidal sway motion in *y*-direction, which is depicted as $y(t) = y_0 cos(2\pi f t)$, where y_0 is the sway amplitude and *f* is the motion frequency. In the present simulations, we select $y_0 = 0.5c$ and the Strouhal number based on the sway amplitude is defined as $S_{t,a} = \frac{2f y_0}{U_\infty}$. It should be noted that this definition of the Strouhal number is different from the one based on the tip excursion. This is because the displacement of the trailing edge varies along the span so that it is difficult to specify a tip excursion.

(a)

(b)
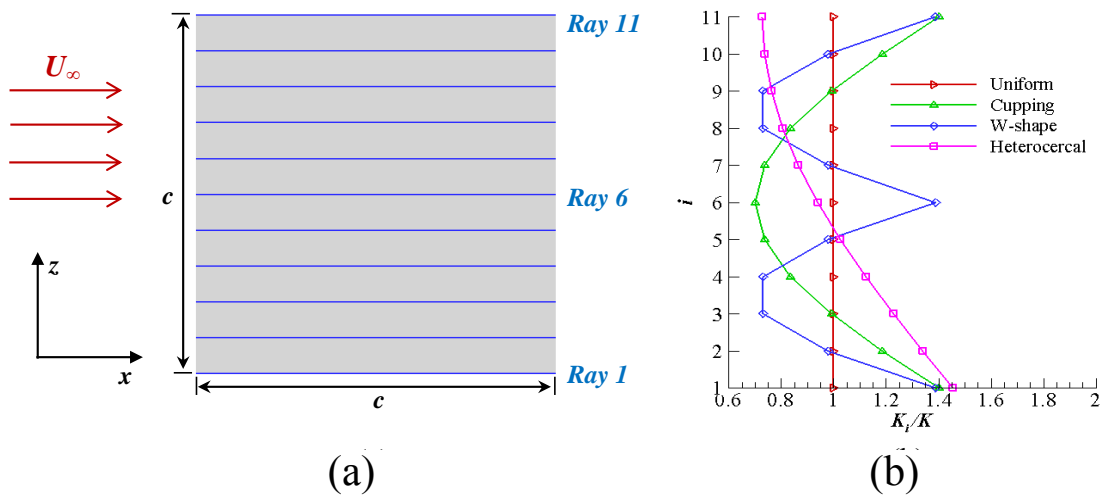
Figure 5-1 (a) Illustration of the idealised caudal fin model; (b) Stiffness of each ray (K_i) in various stiffness distributions.

119

The fin considered here has 11 evenly distributed rays (typical number in a real fish fin varies from 10 to 20, [37]) with various bending stiffness. Each ray is structurally represented by a nonlinear beam with uniform Young's modulus. The normalised bending stiffness of the ith ray is defined as $K_i = \frac{E_i I}{\rho U_\infty^2 c^3}$ ($i = 1, \cdots, N$), where $N = 11$, E_i is the Young's modulus of the ray and ρ is the fluid density [161]. In this study, we assume that the bending stiffness of the membrane itself is negligible, i.e., the rigidity of the fin is solely determined by the stiffness of the rays. However, the membrane does provide constraints upon the ray's motion, which are modelled as linear springs. Based on our numerical tests, the spring constant here is chosen to be $0.02\rho U_\infty^2 c$, i.e., the springs are soft enough to allow large spanwise deformations, yet stiff enough to prevent too much expansion of the membrane. To reduplicate various fin deformations observed in previous experiments [38] and simulations [53], four different distributions of K_i (as shown in Figure 5-1 (b)), which correspond to four different deformation patterns, are considered in the present work:

1) Uniform distribution: $K_i = K_b$.

2) Cupping distribution: $K_i = K_b Q_i/Q$, where $Q_i = 1 + \lambda\left[1 - sin\left(\frac{\pi(i-1)}{N-1}\right)\right]$.

3) W-shape distribution: $K_i = K_b Q_i/Q$, where $Q_i = 1 + \lambda\left[1 - \left|sin\left(\frac{2\pi(i-1)}{N-1}\right)\right|\right]$.

4) Heterocercal distribution: $K_i = K_b Q_i/Q$, where $Q_i = 1 + \lambda\left[1 - sin\left(\frac{\pi(i-1)}{2(N-1)}\right)\right]$.

Here K_b is a constant and measures the mean stiffness of all the rays and $Q = \frac{1}{N}\sum_{i=1}^{N} Q_i$. The parameter λ is selected to be 1, i.e., the stiffness of the least flexible ray is twice that of the most flexible one. Apart from the bending stiffness, another important parameter for this problem is the mass ratio, which is defined as $m^* \equiv \rho_s h_p/\rho c$. Here the mass ratio is selected to be $m^* = 0.2$.

The propulsion performance of the fin is characterised by the mean thrust coefficient $\overline{C_T}$, the mean power expenditure coefficient $\overline{C_P}$ and the propulsion efficiency η. Here $\overline{C_T}$ is calculated by averaging the instantaneous thrust

coefficient $C_T(t)$ over one motion period T. The thrust coefficient is defined as [83,100]

$$C_T(t) = \frac{-F_X(t)}{1/2\,\rho U_\infty^2 c^2}, \tag{5.1}$$

where $F_X(t)$ is the *x*-component of the instantaneous hydrodynamic force $\mathbf{F}_f(t)$.

Similarly, we have [83]

$$C_P(t) = \frac{P(t)}{1/2\,\rho U_\infty^3 c^2}, \tag{5.2}$$

where *P(t)* is the instantaneous power expenditure, which is evaluated as [27,54,100]

$$P(t) = -\iint_S \mathbf{F}_f(\mathbf{x},t) \cdot \mathbf{V}_{grid}(\mathbf{x},t)d\mathbf{x}, \tag{5.3}$$

where $\mathbf{V}_{grid}(\mathbf{x},t)$ is the moving velocity of the fin, which is evaluated using Eq. (3.69). The mean power expenditure coefficient $\overline{C_P}$ is then calculated by averaging power coefficient $C_P(t)$ over one motion period. We assume that the energy transferred from the fluid to the caudal fin cannot be reused, thus the negative values of $C_P(t)$ are set to be zero [100]. Therefore, the propulsion efficiency η is calculated as [83,100]

$$\eta = \frac{-\overline{F}_X U_\infty}{\overline{P}} = \frac{-\overline{F}_X(t)}{1/2\,\rho U_\infty^2 c^2} \Big/ \frac{\overline{P}(t)}{1/2\,\rho U_\infty^3 c^2} = \frac{\overline{C_T}}{\overline{C_P}}. \tag{5.4}$$

It is worthy to point out that we are not exactly duplicating the real fish caudal fin geometrically and materially. Instead, we extract some key features (ray-strengthened, anisotropic flexibility and fluid-structure interaction) possessed by real fish caudal fin, aiming at providing some useful guidelines for bio-inspired robotic fin design. Additionally, the present work is definitely not a simple repeat of Zhu and Bi [43].

Instead, we use a more sophisticated flow solver which is physically more accurate (e.g. the capturing of vorticity shedding from the leading, dorsal, and ventral edges). The present work also paves the way for future research involving active control over the curvature and stiffness of the fin rays.

5.2 Self-consistency study

In order to check the dependency of the current numerical results on the CFD mesh density and physical time step size, simulations are carried out for cupping stiffness distribution at $K_b = 1.0$ and $S_{t,a} = 0.4$. Since the near fluid field around the caudal fin has more significant effect on the fin's performance, only the mesh density of Cluster 2 (see Figure 5-2) is varied in mesh dependency test and the background mesh (Cluster 1) remains unchanged.
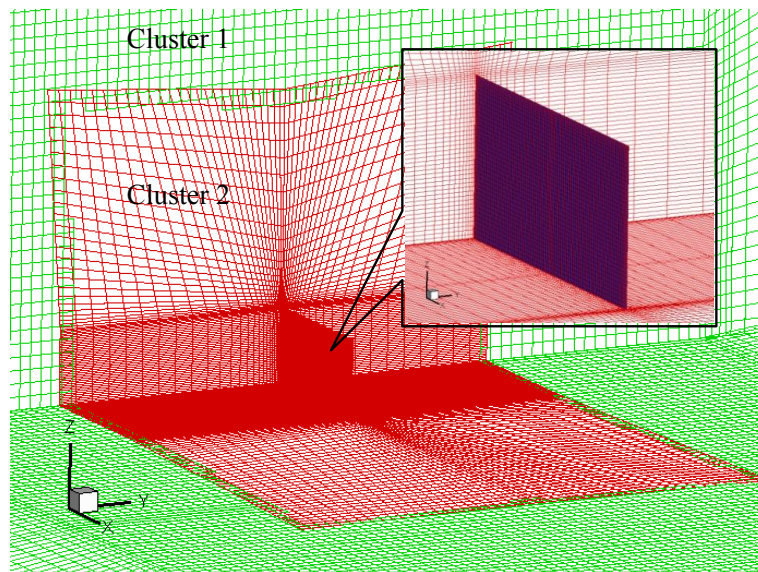
Figure 5-2 The overset grid for the fluid domain.

The computational domain of the body-fitted cluster is essentially a box. The mesh density is changed via adjusting the number of grid point along three directions. A fine mesh (MESH_F) is generated with 201×161×81 grid points in x-, y-, and z-direction respectively. Similarly, a medium mesh (MESH_M) and a coarse mesh (MESH_C) are generated with 161×141×61 grid points and 121×121×41 grid points respectively. Figure 5-3 (a) shows the instantaneous thrust coefficient within one motion period using different body-fitted meshes. It is observed that the thrust

produced by the three meshes perfectly agree with each other, indicating that MESH_M is sufficient to simulate the three-dimensional caudal fin case. With MESH_M, we then examine the sensitivity of the present CFD code to the physical time step size using three different time steps. The results are illustrated in Figure 5-3 (b), from which we find that $dt = T/200$ is sufficient to simulate the flow field around the caudal fin. The time-averaged thrust, power expenditure coefficients and the propulsion efficiency are summarised in Table 5-1. Therefore, in the following simulations, we use MESH_M and $dt = T/200$ to investigate the proposed problem.

Table 5-1 CFD mesh and time-step sensitivity test results.

	$\overline{C_T}$	$\overline{C_P}$	η
MESH_C, dt=T/200	0.545	2.980	0.183
MESH_F, dt=T/200	0.548	3.023	0.181
MESH_M, dt=T/200	0.547	3.024	0.180
MESH_M, dt=T/160	0.541	3.026	0.179
MESH_M, dt=T/240	0.545	3.023	0.180
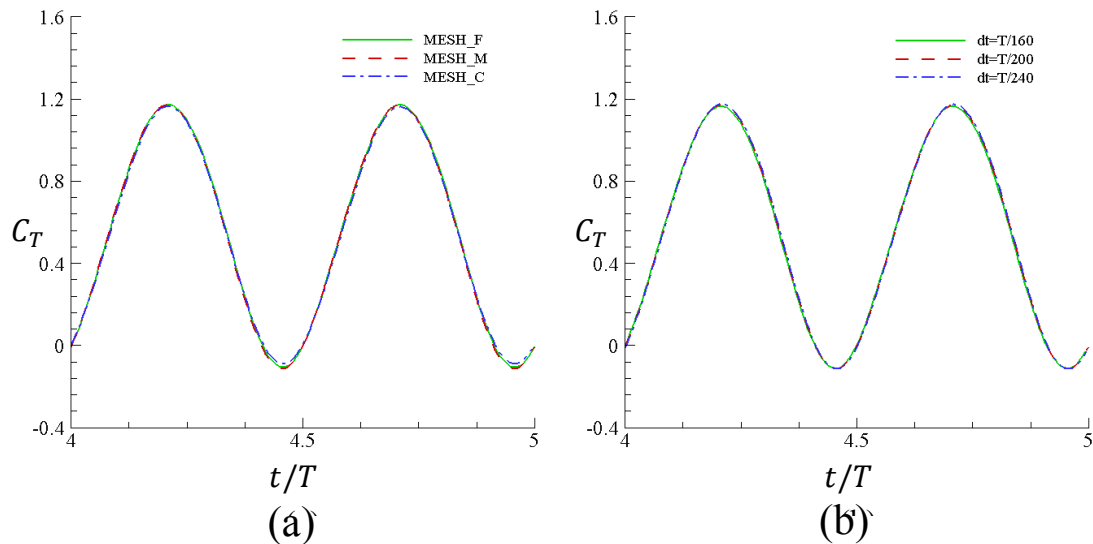
Figure 5-3 Sensitivity study of the present code to (a) mesh density, (b) physical time step. Cupping distribution, K_b=1.0, $S_{t,a}$=0.4.

5.3 Results and discussions

The three-dimensional caudal fin problem depicted in Figure 5-1 is solved using the aforementioned fluid-structure interaction solver in Chapter 3. Figure 5-4 shows the computational domain for fluid dynamics. In Figure 5-4, the fin is enlarged for clarity, which does not represent the real scale in the computational domain. The origin is located at the leading edge of Ray 1 and the flow direction is along the *x*-axis. On the fin surface, we apply the no-slip boundary condition; while for the other boundaries, the non-reflective far-field boundary condition is imposed. The Reynolds number, which governs the fluid behavior, is defined as $R_e = \frac{\rho U_\infty c}{\mu}$, where μ is the fluid dynamic viscosity, and in the present simulations we choose $R_e = 1000$. It is worth noting that in real applications, the Reynolds number could be in the order to 10^4 or higher (see Table 2-1), where the turbulence effects should be taken into consideration.
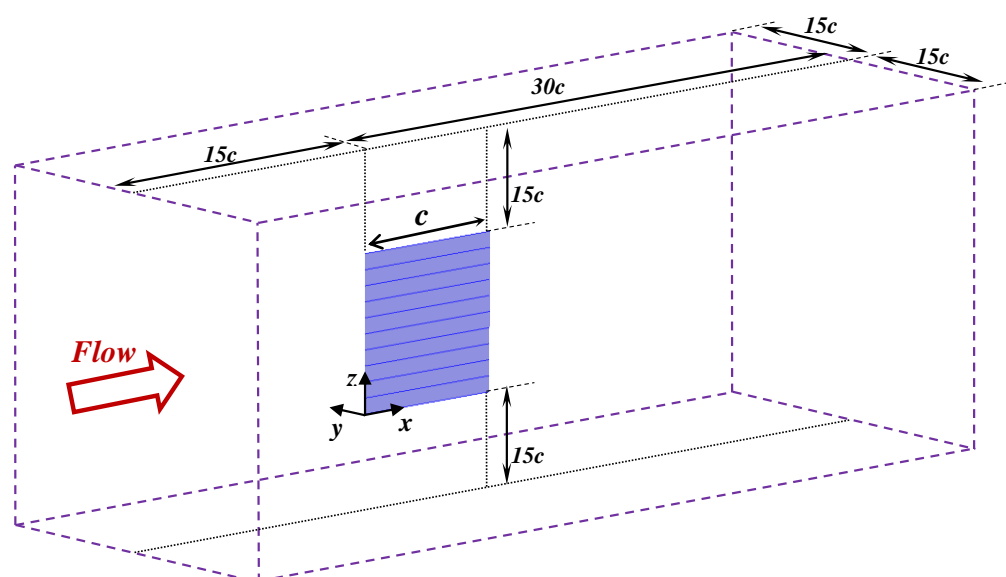
Figure 5-4 Sketch of the computational domain for 3D caudal fin simulation. The fin is not in scale with the computational domain.

5.3.1   Fin deformation

Figure 5-5 demonstrates the fin deformations within one motion period for various stiffness distributions. From the top views, we can see that the deformation patterns from different stiffness distributions are quite similar to each other, with the bending of

all the fin rays dominated by the lowest mode. However, for the deformation patterns viewed from behind, different stiffness distributions demonstrate distinctive features. Despite the fact that all the rays are identical, the fin with uniform stiffness distribution also displays spanwise deformation (Figure 5-5 (b)), which resembles a cupping deformation. This can be attributed to the non-uniformly distributed fluid forces along the span of the fin due to the finite aspect ratio and the vortices rolling up at the dorsal and ventral edges (Ray 11 and Ray 1 respectively).
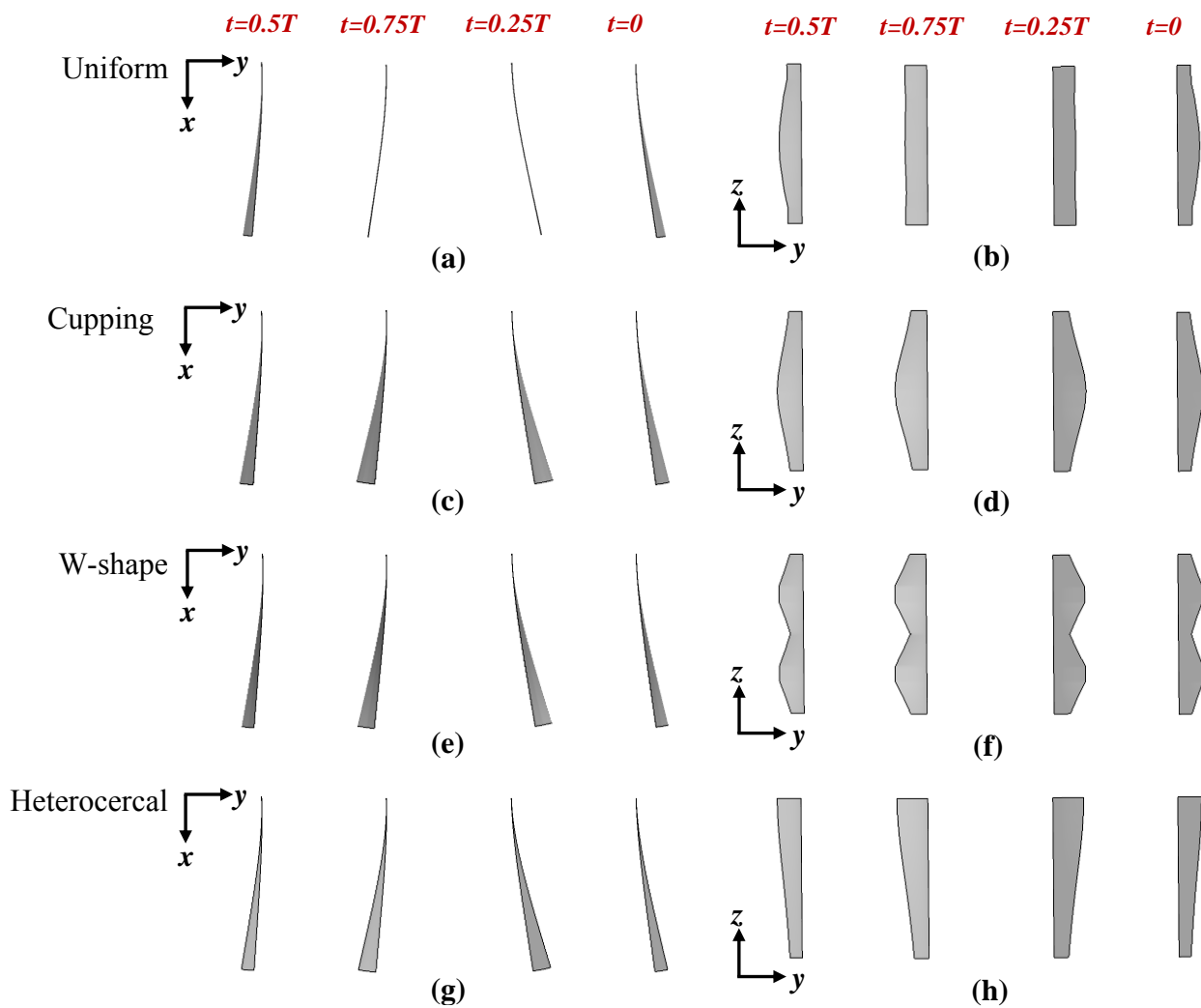
Figure 5-5 Typical fin deformations for different ray stiffness distributions viewed from the top (left column) and behind (right column); (a) (b) uniform distribution; (c) (d) cupping distribution; (e) (f) W-shape distribution; (g) (h) heterocercal distribution.

For the cupping distribution of the ray stiffness (Figure 5-5 (d)), the rays at the dorsal and ventral edges lead the sway motion while the ray in the middle (Ray 6) falls behind.

This is because the ray in the middle is softer than those at the upper and lower edges, and the hydrodynamic loading on the central part of the fin is larger than elsewhere. With the W-shape stiffness distribution, the fin deformations become more complicated, where multiple curvature reversals are generated. The heterocercal stiffness distribution generates asymmetrical deformation patterns, which distinguishes itself from the other stiffness distributions, where the deformations obtained are symmetrical with respect to the centre line (Ray 6). It should be noted that the fin deformation patterns in the present paper are achieved solely by passive ray deflections. In the experiments of Esposito et al. [38], the fin deformations were modulated by changing the phases and excursions of the fin rays, which are intrinsically different from the approach we use here.
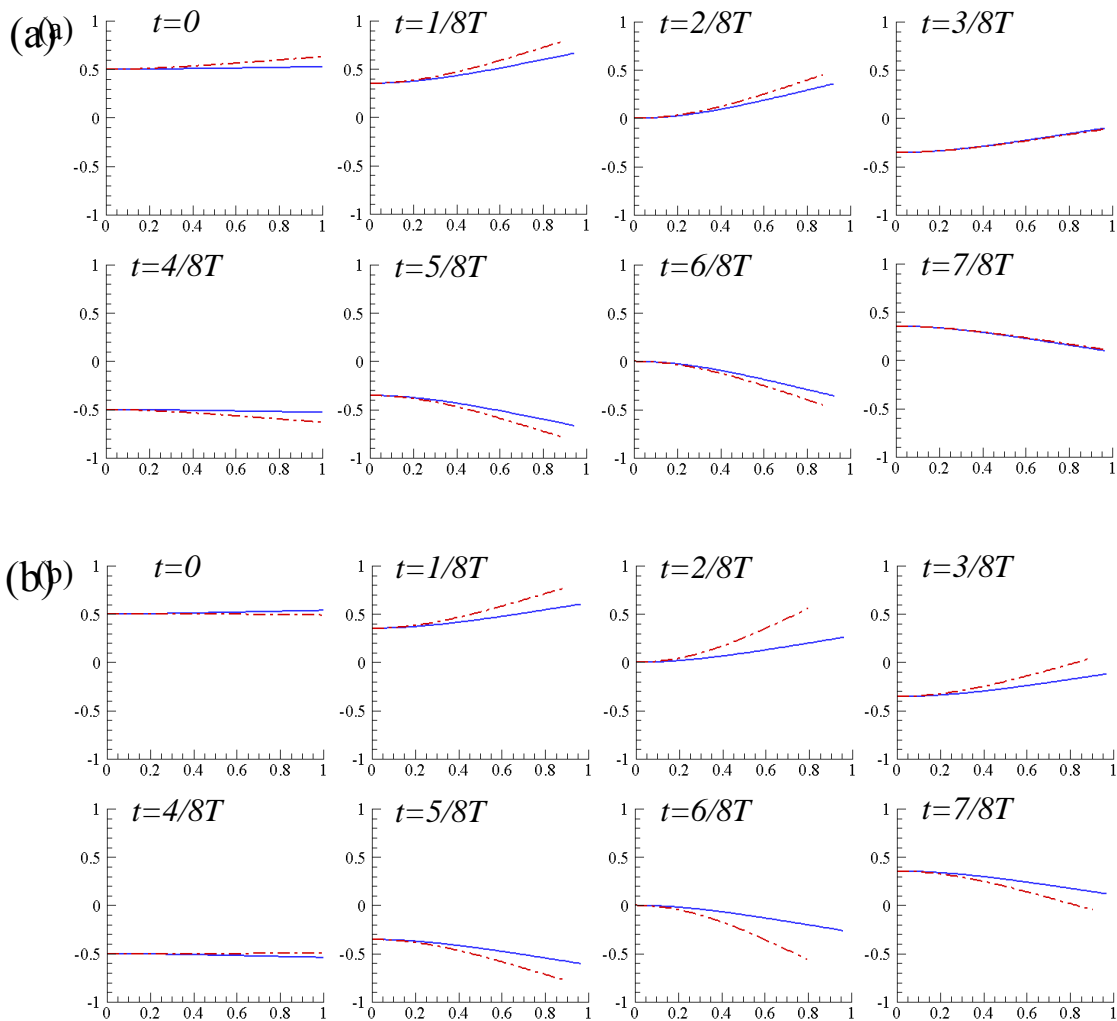
Figure 5-6 Deflections in y-direction of Ray 1 (blue solid lines) and Ray 6 (red dash-dot lines) for (a) uniform distribution and (b) cupping distribution, $S_{t,a}$=0.4, K_b=0.5.

The actual lateral deflections of Ray 1 and Ray 6 for two different stiffness distributions within one flapping period are shown in Figure 5-6. Overall, the deformation patterns from uniform and cupping distributions are similar to each other, indicating that the uniform distribution actually leads to a cupping deformation. However, for the cupping distribution, Ray 6 deforms much more significantly due to the lower bending stiffness while Ray 1 has smaller lateral deflection, which creates a higher phase lag between the two rays.
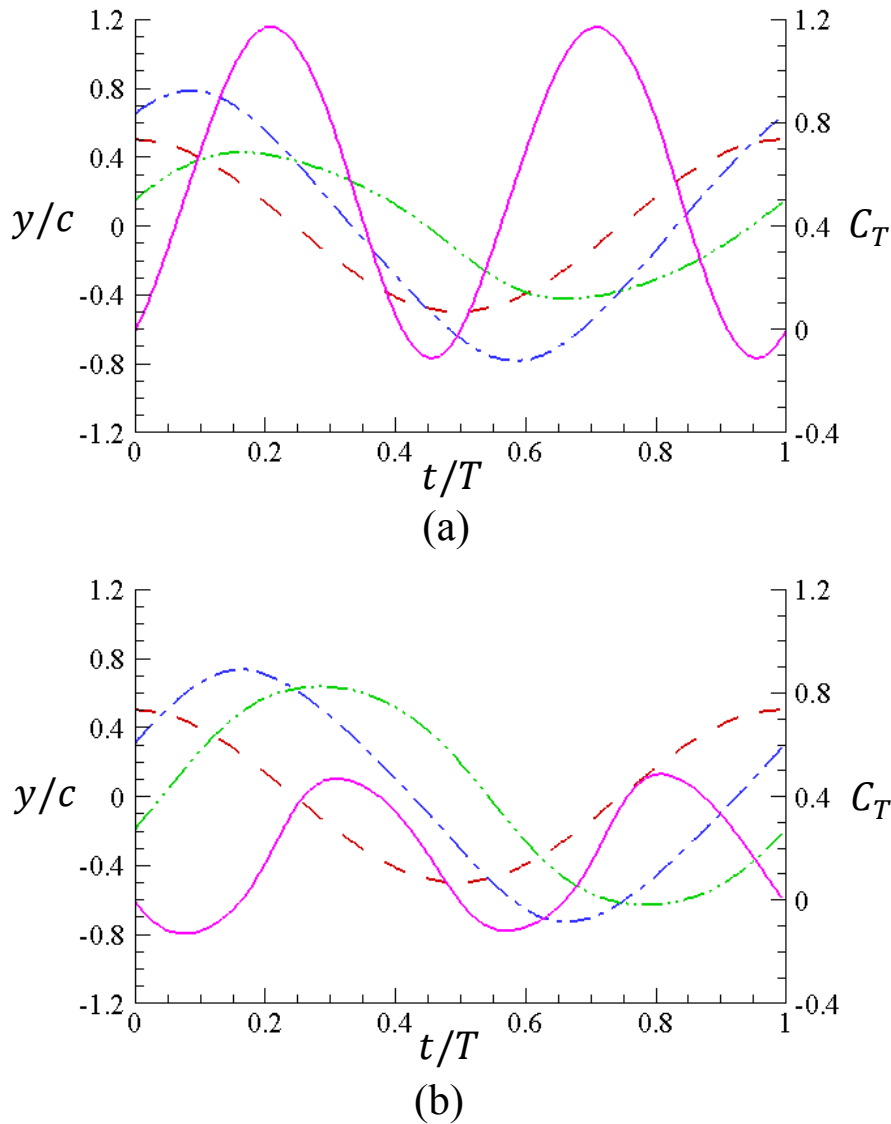
Figure 5-7 Normalised displacements of leading edge y_L/c (red dash line), trailing edge y_T/c (blue dash-dot line) and effective pitch motion $(y_T - y_L)/c$ (green dash-dot-dot line) of Ray 6, and thrust coefficient C_T (pink solid line) in cupping distribution at $S_{t,a}=0.4$; (a) $K_b=1.0$, and (b) $K_b=0.3$.

The lateral deflection of the caudal fin rays shown in Figure 5-6 essentially creates a pitch motion, which can be expressed as $(y_T - y_L)/c$, where y_T and y_L are the lateral displacement of the ray's trailing edge and leading edge respectively. Figure 5-7 demonstrates the lateral deflections of the leading edge, trailing edge and pitch motion of Ray 6, together with the thrust coefficient C_T in cupping distribution at two different values of K_b. The amplitude of the ray's trailing edge is larger than that of the leading edge due to the lateral deflection, which leads to a stronger wake and thereby enhancing the thrust generation. Another factor contributing to higher thrust is the creation of a pitch motion, which redirects the fluid forces acting on the fin surface and generates larger component in forward direction. Comparing the pitch motion curve (green dash-dot-dot line) with the C_T curve (pink solid line), we can observe that the peak value of the thrust is accomplished at the largest relative displacement (corresponding to the largest pitch angle). A closer observation and comparison of Figure 5-7 (a) and (b) reveal that the thrust generation is also greatly affected by the phase lag between the lateral motion and the pitch motion. For example, at K_b=1.0, where the largest mean thrust coefficient is achieved (see Figure 5-9), the phase lag between the lateral motion and the pitch motion is approximately 76 degrees while the phase lag at K_b=0.3, where the lowest thrust is generated, is found to be around 105 degrees, which is considered out of the optimal range [36]. We note that the phase lag maximising the thrust generation in our study deviates from the optimal value obtained experimentally by Park et al. [36]. This may be attributed that the mechanical caudal fins used by Park et al. [36] have uniform material properties; whilst in the present study, the bending stiffness is varied along the span, leading to more complicated deformation patterns. Another reason may be the effect of mass ratio. To enhance numerical stability, the mass ratio is chosen to be 0.2 in the present simulations, whereas the mass ratio used in the experiment of Park et al. is below 0.03.

5.3.2 *Force generation and propulsion efficiency of the fin*

The instantaneous thrust coefficient, lateral force coefficient and power expenditure coefficient within one flapping period for both rigid and flexible fins are shown in

Figure 5-8. The most pronounced effect of the structural flexibility is the significant increase in the peak value of C_T. This is attributed to larger flapping amplitude and effective pitching angle due to the structural deformation, which will be discussed later. Another effect of flexibility is the reduction in lateral force C_Y. This can be explained by the fact that flexibility can significantly reduce the work done to the surrounding fluid so that less energy is needed to activate the caudal fin.

Figure 5-9 shows the mean thrust coefficient $\overline{C_T}$, the mean power expenditure coefficient $\overline{C_P}$ and the propulsion efficiency η as functions of the mean bending stiffness of the rays for different distributions at $S_{t,a}$=0.4. The rigid ray case is also included for comparison. From these figures, we can see that the rigid fin cannot generate any net thrust at this Strouhal number, as the longitudinal force is mostly provided by shear stresses due to the lack of effective pitching motion. This is different from the result of Zhu & Bi [53], where finite thrust was generated by a rigid caudal fin. The difference is attributed to the fact that the fin used in our study is much thinner than the one used by Zhu & Bi ($0.004c$ vs. $0.02c$) so that the component of the pressure force in the forward direction is significantly reduced. Moreover, the current model includes viscous friction on the fin surface, which further diminishes the thrust. Within the range of bending stiffness considered here, all flexible fins have improved propulsion performance with increased thrust and efficiency. For all types of stiffness distributions, the mean thrust coefficient $\overline{C_T}$ experiences a significant increase and then a sharp decline with the increase of the flexibility, with the peak $\overline{C_T}$ values achieved at an optimal flexibility of K_b=1.0 [86]. A similar trend is seen in the propulsion efficiency, where the peaks are achieved at smaller K_b values, which vary with specific stiffness distribution profiles. Interestingly, a slight increase of the power expenditure $\overline{C_P}$ is witnessed at stiffer rays for all types of stiffness distributions. But due to the fact that $\overline{C_T}$ is increased at a larger magnitude, the efficiency still rises. As the bending stiffness becomes smaller than the optimal value, both the thrust coefficient $\overline{C_T}$ and the power expenditure coefficient $\overline{C_P}$ begin to fall, but $\overline{C_P}$ drops with a larger rate,

resulting in an increase of the propulsion efficiency. As the mean stiffness K_b further decreases, $\overline{C_T}$ decreases faster than $\overline{C_P}$, which causes a significant decline in efficiency.
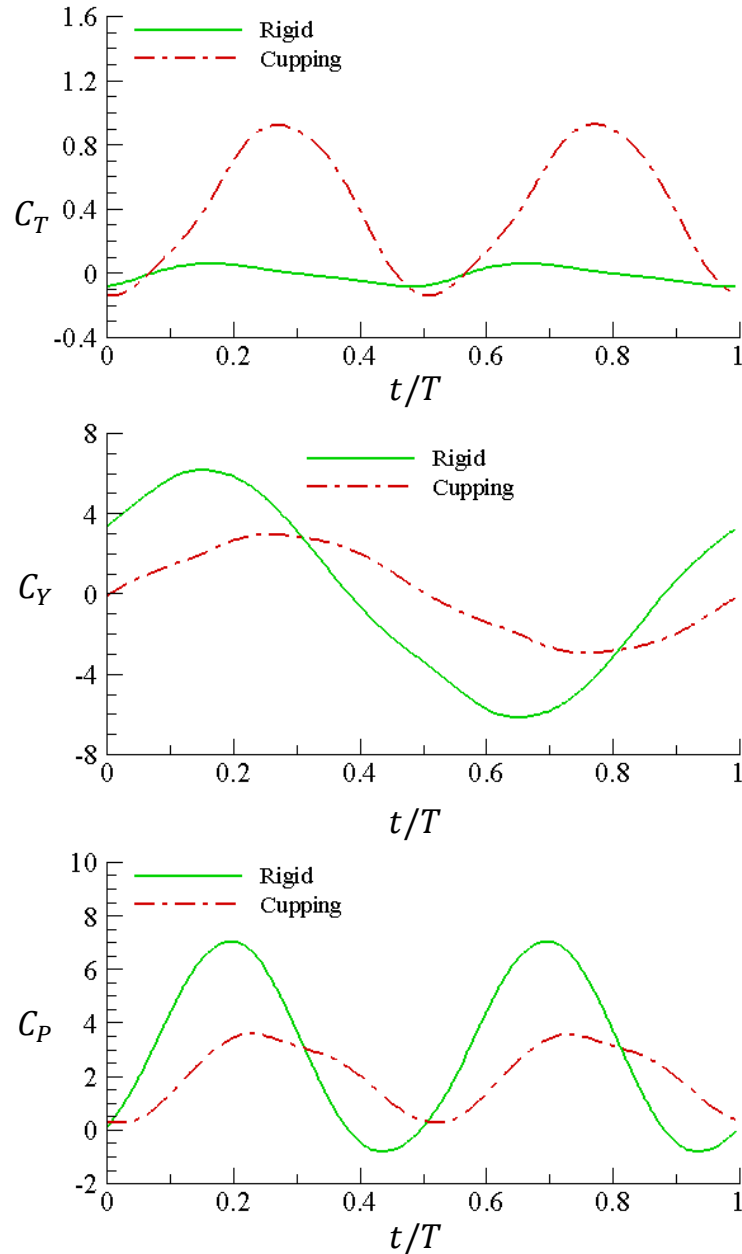
Figure 5-8 Time histories of the instantaneous thrust coefficient C_T, lateral force coefficient C_Y and power expenditure coefficient C_P over one motion period for a rigid fin and a flexible fin (cupping distribution, $K_b=0.5$) at $S_{t,a}=0.4$.

A closer inspection of Figure 5-9 reveals that when the mean bending stiffness K_b is larger than the optimal flexibility value, the differences between various stiffness distributions are marginal. The thrust forces generated by cupping and W-shape

distributions are only slightly higher than those from uniform and heterocercal distributions. However, the differences become more pronounced when the fins are more flexible, which is consistent with previous simulations [53] while contradictory with the experimental study [38], where they concluded that with more compliant fin rays, the forces generated by the robotic caudal fin are less varied. However, we note that there exists fundamental difference in terms of the mechanism used to actuate the rays and create various deformation patterns between the present work and the experiment. In our cases, all fin rays undergo the same sway motion at the basal ends and the various deformations are accomplished passively.
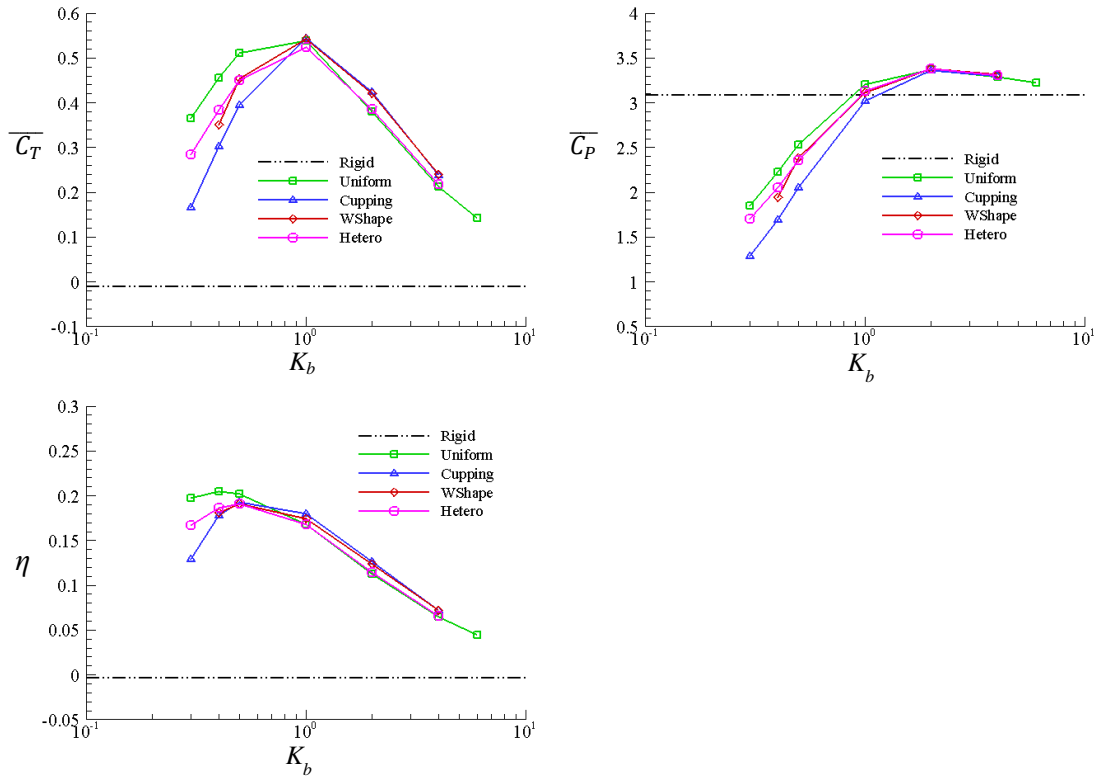
Figure 5-9 Mean thrust coefficient $\overline{C_T}$, mean power expenditure coefficient $\overline{C_P}$ and propulsion efficiency η as functions of the mean bending stiffness K_b for different fin deformations at $S_{t,a}=0.4$.

On the contrary, in the experiment, the robotic rays were activated individually, and various fin shapes were created by varying the phase lags between different rays. Generally, more flexible fin rays are more compliant to surrounding flows. For the present simulations, compliance enlarges the differences between the deflections of fin rays, thus magnifying the effect of various stiffness distributions. In the experiment, the

compliance of the robotic fin rays mitigates the effects of phase lags between them and reduces the differences between various deformation patterns.

As aforementioned, in the present study, softer caudal fins have more distinctive deformation patterns under different bending stiffness distributions. Therefore, the differences in thrust generation and efficiency between various stiffness distributions are more pronounced for fins with more flexibility, which can be observed in Figure 5-9. Specifically, for very soft caudal fins, the uniform distribution creates the largest thrust and highest propulsion efficiency, whereas the cupping distribution generates the least thrust and lowest efficiency. But cupping distribution has the lowest power expenditure coefficient. The W-shape and the heterocercal distributions only have mediocre performance. Figure 5-10 shows the same plots as Figure 5-9 at a smaller Strouhal number ($S_{t,a} = 0.3$), from which we can draw the same conclusions.
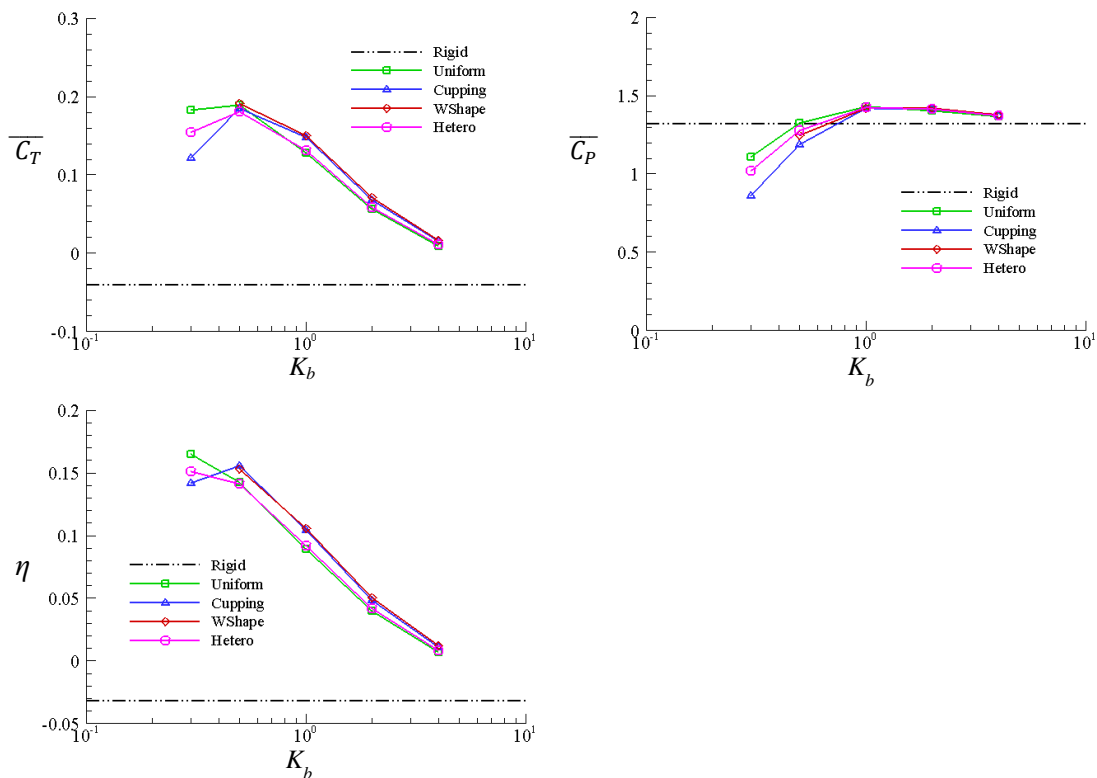
Figure 5-10 Mean thrust coefficient $\overline{C_T}$, mean power expenditure coefficient $\overline{C_P}$ and propulsion efficiency η as functions of the mean bending stiffness K_b for different fin deformations at $S_{t,a}$=0.3.

The present conclusion that the fin with uniform stiffness distribution has the best overall performance in terms of thrust generation and efficiency seems to be different

with those from previous experimental [38] and numerical [53] studies. For example, Esposito et al. [38] found that the cupping motion produced more thrust than the other motions (flat, W, undulation and rolling). However, as previously mentioned, the mechanism to actuate the fin rays in the numerical studies is different from the one in experiments. Besides, we should note that the uniform distribution in the present work does not correspond to the flat motion in the experiment. In the present paper, the uniform stiffness distribution eventually results in cupping deformation patterns due to the non-uniform distribution of the fluid loads along the fin span. This cupping effect is more pronounced in softer rays. From this perspective, our conclusion is actually consistent with the experiment. Zhu & Bi [53] numerically examined a similar problem, where they concluded that the 'W'-shape distribution performed the best, which is also different from the present simulation. The difference is likely to be attributed to the methods used to resolve the surrounding flows: an inviscid flow model was used by Zhu & Bi, which neglected the viscous effect and vortices shed from the leading edge and the dorsal and ventral edges. These vortices are believed to significantly affect the pressure distribution across the fin surface, thereby affecting the performance [212].

5.3.3   *Near-body flow field*

The wake behind the flexible caudal fin is demonstrated in Figure 5-11. As we can see that for all stiffness distributions, the wake is composed of a sequence of vortex-rings that are comparable with the caudal fin in size. For the symmetrical deformations with respect to the centre line (uniform, cupping and W-shape), the vortex rings behind the fin are also symmetrical and resemble each other. Only subtle difference at the connection between neighbouring rings can be observed. However, for the asymmetrical deformation (heterocercal), it is evident that the vortex-rings are tilted upward compared with those from symmetrical deformations. The force component in vertical direction is thus significantly increased, which can be used for maneuvering and stabilising.
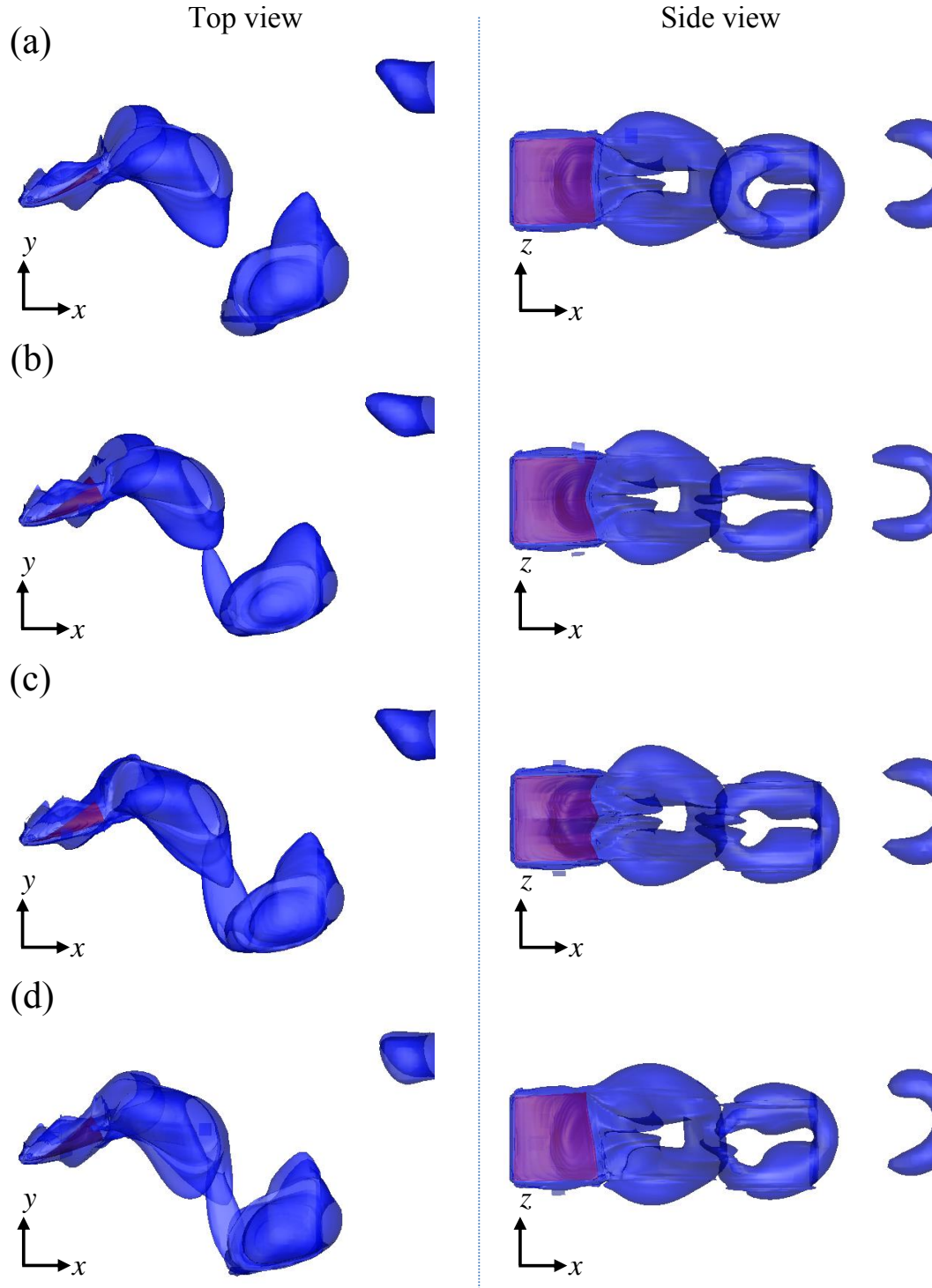
Figure 5-11 Iso-surfaces of normalised vorticity magnitude (ω_{mag}= 2) in the wake behind a fin with different stiffness distributions; (a) uniform distribution, (b) cupping distribution, (c) w-shape distribution, and (d) heterocercal distribution. $S_{t,a}$=0.4, K_b=0.5, t=T/4.

A sectional view of the wake behind the caudal fin is shown in Figure 5-12. With symmetrical stiffness distributions, the fin produces a pair of tip vortices from the

trailing edges of the dorsal (Ray 11) and ventral (Ray 1) rays. These vortices are counter-rotating and have approximately equal strength. For the fin with heterocercal stiffness distribution, there are also two counter-rotating tip vortices (with different strength) shed from the ray trailing edges.
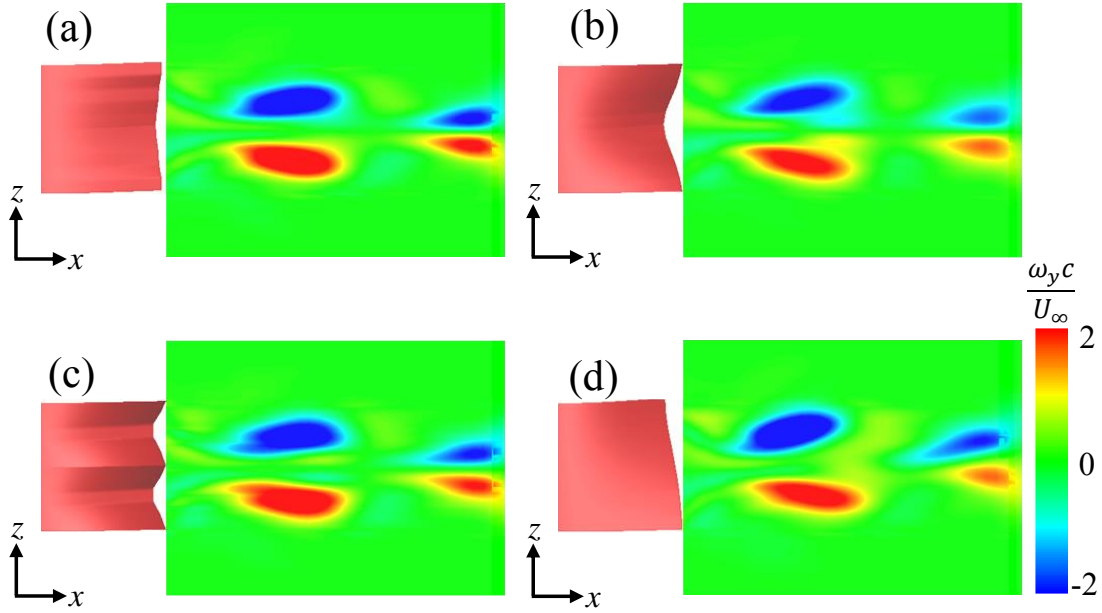
Figure 5-12 Vorticity fields behind the flexible fin with (a) uniform, (b) cupping, (c) w-shape and (d) heterocercal ray stiffness distributions. The contours display the y-component of the vorticity within y=0 plane. $S_{t,a}$=0.4, K_b=0.5, t=T/4.

5.4 Concluding remarks

In this chapter, we develop a fully coupled fluid-structure interaction model that can be used to study skeleton-strengthened fish fins. With this model, we elucidated the effects of various spanwise deformation patterns on the propulsion performance of fish fins by numerically examining a three-dimensional ray-supported caudal fin. With four spanwise stiffness distributions (uniform, cupping, W-shape and heterocercal), certain deformation patterns observed in experiments were reproduced. For all stiffness distributions, the performance of the caudal fin was enhanced over a wide range of flexibility. Both the thrust and the efficiency experienced an increase and then a decrease as the flexibility increased, indicating the existence of an optimal flexibility.

The differences between various stiffness distributions were more pronounced in softer rays. Among these stiffness distributions, uniform distribution was found to have the best overall performance in terms of thrust generation and efficiency, while the cupping distribution required the least power expenditure. This conclusion seemed to contradict previous experimental study [38]. By analysing the actual deformations, however, it was found that with a uniform bending stiffness distribution, the caudal fin produced a 'cupping' deformation as well due to the non-uniformly distributed fluid loads across the fin surface. Subsequently, both uniform and cupping stiffness distributions led to cupping deformation patterns. But the cupping distribution was more likely to be "over-cupped" (i.e. the passive ray deformations are out of phase with the swaying motions), which explained why the thrust generated by the cupping distribution dropped much more significantly than that by the uniform distribution.

The current model was concentrated on illustrating the effect of ray stiffness distribution on the hydrodynamic performance of fish-like fins with passive deformation, whereas some details of actual fish fins (e.g. the geometry) were not considered. For example, for simplicity in this model the rays were assumed to have the same length. This, together with the inclusion of viscous effect and more sophisticated vorticity shedding model, may explain the differences in the current results and those in the previous study [53]. The fins of live fish, on the other hand, rely on both passive and active control for fin shape variation. It is thus difficult to directly relate predictions from the current model with dynamics of actual fish fins.

The present study suggests that by appropriately cupping their fins, fish are able to save energy and generate more desired forces when moving against incoming surrounding fluids. This conclusion is consistent with previous observations [32,34,38]. On the other hand, unlike the fully passive fin dynamics depicted in our model, fish can actively control the curvature and flexibility of their fins, which is expected to further enhance the locomotion performance. These effects will be examined in future studies.

Chapter 6 Performance of an Actively and Passively Controlled Caudal Fin

6.1 Problem description

In the present study, the real ray-strengthened caudal fin (Figure 6-1 (a)) is geometrically and structurally simplified as a square-shaped membrane supported by N evenly distributed rays (Figure 6-1 (b)). This fin has length c in both chordwise and spanwise directions. The thickness of the fin is chosen to be $h_p = 0.004c$. Each ray is structurally represented by a nonlinear Euler-Bernoulli beam with uniform Young's modulus. The dimensionless bending stiffness for the ith ray is defined as $K_i = E_i I / \rho U_\infty^2 c^3, (i = 1, \dots, N)$, where $N = 11$, E_i is the Young's modulus of the ith ray, I is the second moment of inertia, ρ is the fluid density and U_∞ is the incoming flow velocity. The mass ratio is defined as $m_i^* = \rho_{s,i} h_p / \rho c$, where $\rho_{s,i}$ is the density of the ith ray. In the present work, two different spanwise bending stiffness distributions of the ray are studied:

1) Uniform distribution: $K_i = K_b$.

2) Cupping distribution: $K_i = K_b \Theta_i / \Theta$, where $\Theta_i = 1 + \gamma \left[1 - \sin \left(\frac{\pi(i-1)}{N-1} \right) \right]$.

Here K_b is the mean dimensionless bending stiffness of all the rays and $\Theta = \frac{1}{N} \sum_{i=1}^{N} \Theta_i$. The parameter γ is selected to be 1. The mean value of the stiffness is selected to be $K_b = 3.0$ and the mass ratios of the ray are chosen as $m_i^* = 0.2$. The two different stiffness distributions are depicted in Figure 6-2 (a).

Additionally, we assume that the bending stiffness of the membrane can be neglected, i.e., it can only sustain stretching/compression but not bending. This assumption is made based on the experimental measurement of the Young's modulus of the rays and membranes of the bluegill sunfish [62], where the rays have a Young's modulus about

1GPa while the membrane's Young's modulus is between 0.3MPa and 1MPa. Thus the fin rays are at least 1000 times stiffer than the membranes between them. This assumption is also used in some previous biomimetic studies [25,26,52]. Thus the constraints provided by the membrane are modelled as distributed linear springs between neighbouring rays. Based on numerical tests, we choose the spring constant to be $0.02\rho U_\infty^2 c$, so that the springs are sufficiently flexible to allow large spanwise deformation and yet stiff enough to prevent excessive expansion of the membrane.

(a)

(b)

(c)

(d)
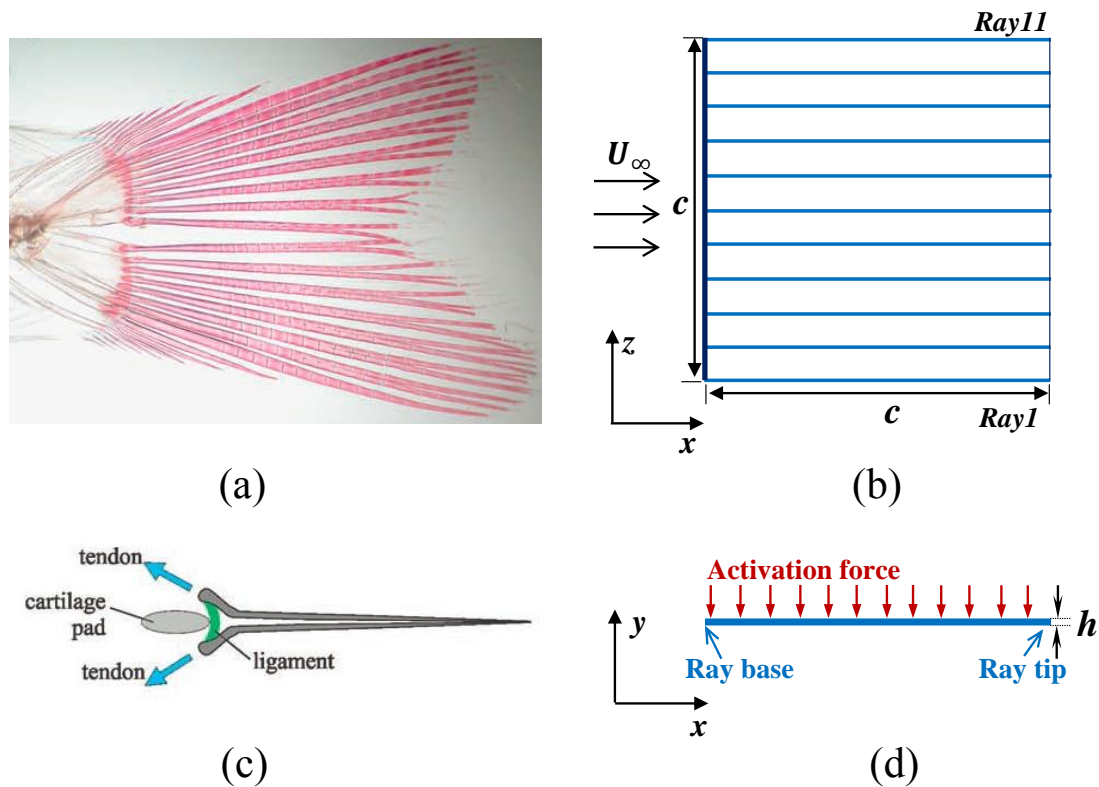
Figure 6-1 (a) Caudal fin anatomy of bluegill sunfish, Lepomis macrochirus [30]. (b) Idealised rectangular ray-supported caudal fin model. (c) Dorsal view of a fin ray with two hemitrichs [28]. (d) Dorsal view of present ray model, represented by a nonlinear Euler-Bernoulli beam. Distributed external force models the pulling effect from the tendons.

Kinematically, the basal ends of all the rays share the same sinusoidal sway motion in *y*-direction, which imitates the motion of the posterior part of the fish and is expressed as $y(t) = y_0\cos(\omega t)$, where y_0 is the sway amplitude and ω is the motion frequency. The Strouhal number based on the sway amplitude is defined as $S_{t,a} = \omega y_0/\pi U_\infty$. Here we choose $S_{t,a} = 0.4$. Besides, each ray is also actuated by independent distributed forces F_i $(i = 1, ..., N)$, mimicking the pulling effect of the tendons at the basal end of the ray (see Figure 6-1 (c), (d)). As pointed out in Chapter 2, the tendons

provide longitudinal forces at the ray base, which will induce a distributed bending moment along the ray. This distributed bending moment will further lead to a distributed force perpendicular to the ray. Therefore, pulling effect of the tendons is modelled by a uniformly distributed load along the ray as shown in Figure 6-1 (d). For each ray, the external load is applied on the discretised nodes along the beam model and the force term F_i is included in the external force term on the right-hand side of the nonlinear beam equation (see Eq. (3.51)). The external distributed loads vary with time as $F_i(t) = F_0\cos(\omega t - \varphi_i)$, where φ_i is the phase lag between the external load of ith ray and the sway motion. F_0 is assumed to be distributed uniformly along each ray and its exact value is selected via numerical tests, i.e., the desired deformation patterns are activated while maintaining the numerical stability. Here, the desired deformations are determined based on the experimentally observed conformations of live fish [35,38]. The numerical stability is defined as the achievement of a converged result, i.e., the obtained thrust force reaches a periodic oscillation. In the present work, F_0 is chosen to be $1.1\,\rho U_\infty^2 c^2$.

For such a caudal fin model, the deforming pattern is primarily determined by the exact distribution of φ_i, especially the mean phase (φ_{mean}) of the rays and the phase difference (φ_{diff}) between the maximum and minimum values of φ_i. In the present work, we examine four different phase distributions among the fin rays:

Distribution I: $\varphi_i = \varphi_{mean}$, $\varphi_{diff} = 0$.

Distribution II:

$$\varphi_i = \varphi_{mean} + \varphi_{p,i} - \varphi_0 \tag{6.1}$$

where $\varphi_0 = 180$ and $\varphi_{p,i}$ is computed as

$$\varphi_{p,i} = \varphi_0\, Q_i/Q, \tag{6.2}$$

where $Q_i = 1 + \lambda \sin\left(\frac{\pi(i-1)}{N-1}\right)$ and $Q = \frac{1}{N}\sum_{i=1}^{N} Q_i$. The parameter λ is determined by ensuring $\max\{\varphi_{p,i}\} - \min\{\varphi_{p,i}\}$ equal the designed value of φ_{diff}.

Distribution III:

$$\varphi_i = \varphi_{mean} + \frac{2i - N - 1}{2(N-1)}\varphi_{diff}. \tag{6.3}$$

Distribution IV:

$$\varphi_i = \varphi_{mean} + \varphi_{p,i} - \varphi_0, \tag{6.4}$$

where φ_0=180 and $\varphi_{p,i}$ is computed as

$$\varphi_{p,i} = \varphi_0\, Q_i/Q, \tag{6.5}$$

where $Q_i = 1 + \lambda\left|\sin\left(\frac{2\pi(i-1)}{N-1}\right)\right|$ and $Q = \frac{1}{N}\sum_{i=1}^{N} Q_i$. The parameter λ is determined by ensuring $\max\{\varphi_{p,i}\} - \min\{\varphi_{p,i}\}$ equal the designed value of φ_{diff}.

Different phase distributions are plotted in Figure 6-2 (b). These distributions are determined to reproduce certain deformation patterns similar to real fish caudal fin. It is seen that in Distribution I, the phase lag is uniform among the rays. Distribution II has the maximum phase lag achieved at the ray in the middle (Ray 6) while the rays at the dorsal and ventral edges have the minimum value. This phase distribution is expected to generate cup deformations. Distribution III is designed to achieve *H*-mode or *S*-mode (which cannot be accomplished via purely passive deformations). Distribution IV has a W-shape phase distribution, where the rays at the dorsal and ventral edges have the same phase lag as the ray at the centre. This type of phase distribution is used to activate W-shape deformations observed in live fishes.
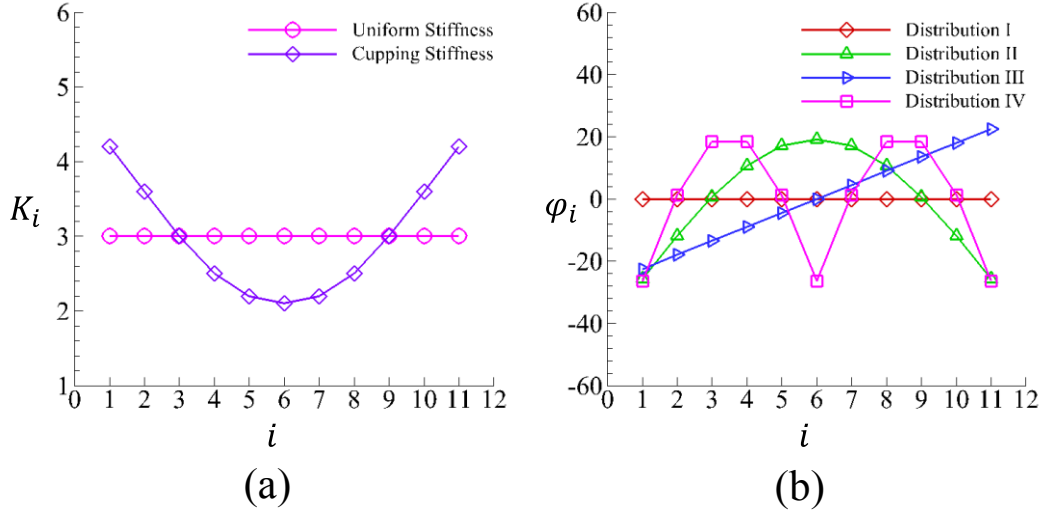
Figure 6-2   (a) Normalised bending stiffness of the ith ray in uniform and cupping stiffness distributions, $K_b = 3.0$. (b) Phase lag of the ith ray in different distributions, $\varphi_{mean} = 0$ degree and $\varphi_{diff} = 45$ degree.

The propulsion performance of the fin is characterised by the mean thrust coefficient $\overline{C_T}$, the mean vertical force coefficient $\overline{C_Z}$, the mean power expenditure coefficient $\overline{C_P}$, and the propulsion efficiency η. These mean values are evaluated by averaging the instantaneous coefficients over one motion period T. The instantaneous thrust coefficient, power expenditure coefficient and propulsion efficiency are defined in the same way as those in Chapter 5 (see Eq. (5.1), (5.2) and (5.4) respectively). It is worth pointing out that Eq. (5.3) measures the power done by the fin to the surrounding fluid. It is essentially the output power of the fin as a system. A more practical way of calculating the power consumed by the fin is to consider the input power from the sway motion at the leading edge and the uniformly distributed activation force (here noted as P_{in}). In reality, P is smaller than P_{in} due to the loss during the transmission in the caudal fin system. However, we assume there is no power loss in the caudal fin system, i.e., the input power (P_{in}) equals the output power (P). Therefore, Eq. (5.3) is a reasonable estimation of the power consumed by the caudal fin. This kind of evaluation method has also been used in previous studies [27,54,96,100].

Additionally, we have

$$C_Y(t) = \frac{F_Y(t)}{0.5\rho U_\infty^3 c^2},$$
$$C_Z(t) = \frac{F_Z(t)}{0.5\rho U_\infty^3 c^2},$$

(6.6)

where $F_Y(t)$ and $F_Z(t)$ are the components of the instantaneous hydrodynamic force $\mathbf{F}_f(t)$ in y and z directions respectively.

6.2 Self-consistency study
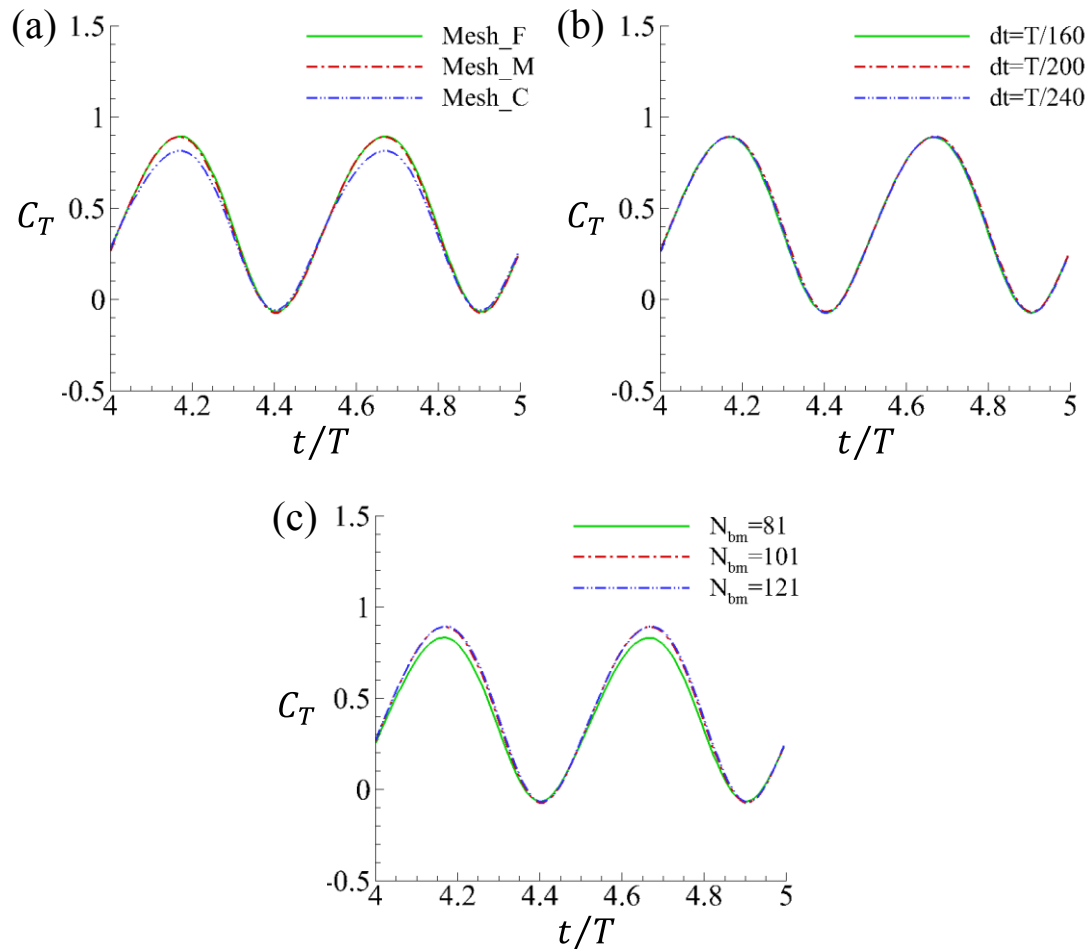
Figure 6-3 Sensitivity study of the present code to (a) CFD mesh density, (b) time step size, and (c) number of nodes along the beam. The fin has cupping stiffness distribution II with $\varphi_{diff}=45$ degree and $\varphi_{mean}= 30$ degree.

A self-consistency study is carried out to justify the fluid mesh, physical time step and number of nodes along the beam we use here. To check the sensitivity to the fluid mesh, three meshes with different densities are generated, which are termed as Mesh_F (fine mesh, 5 million grid cells), Mesh_M (medium mesh, 3.7 million grid cells) and Mesh_C (coarse mesh, 2.8 million grid cells). These meshes have the same size of those used in Section 5.2 (see Figure 5-2). Similarly, three physical time steps ($dt = T/160$, $T/200$, $T/240$) and three numbers of grids along each ray ($N_{bm} = 81, 101, 121$) are chosen for this sensitivity study.

Table 6-1 Summary of the self-consistency study results (see Figure 6-3 for physical parameters).

	dt	N_{bm}	$\overline{C_T}$	Error
Mesh_F	T/200	101	0.443	0.0%
Mesh_M	T/200	101	0.437	-1.4%
Mesh_C	T/200	101	0.412	-7.0%
Mesh_M	T/160	101	0.436	-1.6%
Mesh_M	T/240	101	0.438	-1.1%
Mesh_M	T/200	81	0.405	-8.6%
Mesh_M	T/200	121	0.439	-0.9%

Figure 6-3 (a)-(c) demonstrate the sensitivity of the present code to the fluid mesh density, time step size and number of points along the beam. The time-averaged thrust coefficients and the errors relative to the result from Mesh_F with $dt = $ T/200 and $N_{bm} = 121$ are summarised in Table 6-1. It is seen that with sufficiently high fluid/structural mesh densities and sufficiently small time step, the results are not sensitive to numerical parameters. Based on the self-consistency study, the following simulations are based on Mesh_M, $dt = $ T/200 and $N_{bm} = 101$.

6.3 Results and discussions

The ray-strengthened caudal fin problem depicted in Figure 6-1 is solved using the fluid-structure interaction solver described in Chapter 3. The computational domain used here is the same as that in Section 5.3 (see Figure 5-4) and the Reynolds number based on the length of the ray is $R_e = 1000$. The height of the first grid layer off the wall (Δy) is calculated using flat plate boundary theory for a given $y+$ value. For the present Reynolds number, $y+$ is chosen to be 0.5, resulting in $\Delta y = 0.005c$.

6.3.1 Deformation pattern of the fin

The typical deformation patterns of the caudal fin in the present study are demonstrated in Figure 6-4 and Figure 6-5. The notation 'U-I-0' stands for uniform stiffness, phase distribution I and $\varphi_{diff} = 0$. Similarly, 'C-II-45' means cupping stiffness, phase distribution II and $\varphi_{diff} = 45$ degrees. Other notations are defined in a similar way. As concluded by Shi et al. [102], the passively deformed fin with uniform stiffness (Figure 6-4 (a)) leads to a *C*-mode (in which the dorsal and ventral edges lead the sway motion whilst the central part falls behind) due to the non-uniformly distributed fluid force. Similar *C*-mode patterns are also achieved by the fin with distribution U-I (Figure 6-4 (b)). With distribution C-II, the caudal fin displays a more significant cupping pattern (Figure 6-4 (c)) at a small phase difference ($\varphi_{diff} = 45$) while a different deformation pattern, which resembles a 'W'-shape (see Figure 6-4 (d) at $t = 0$), is observed when the phase difference becomes larger ($\varphi_{diff} = 180$).
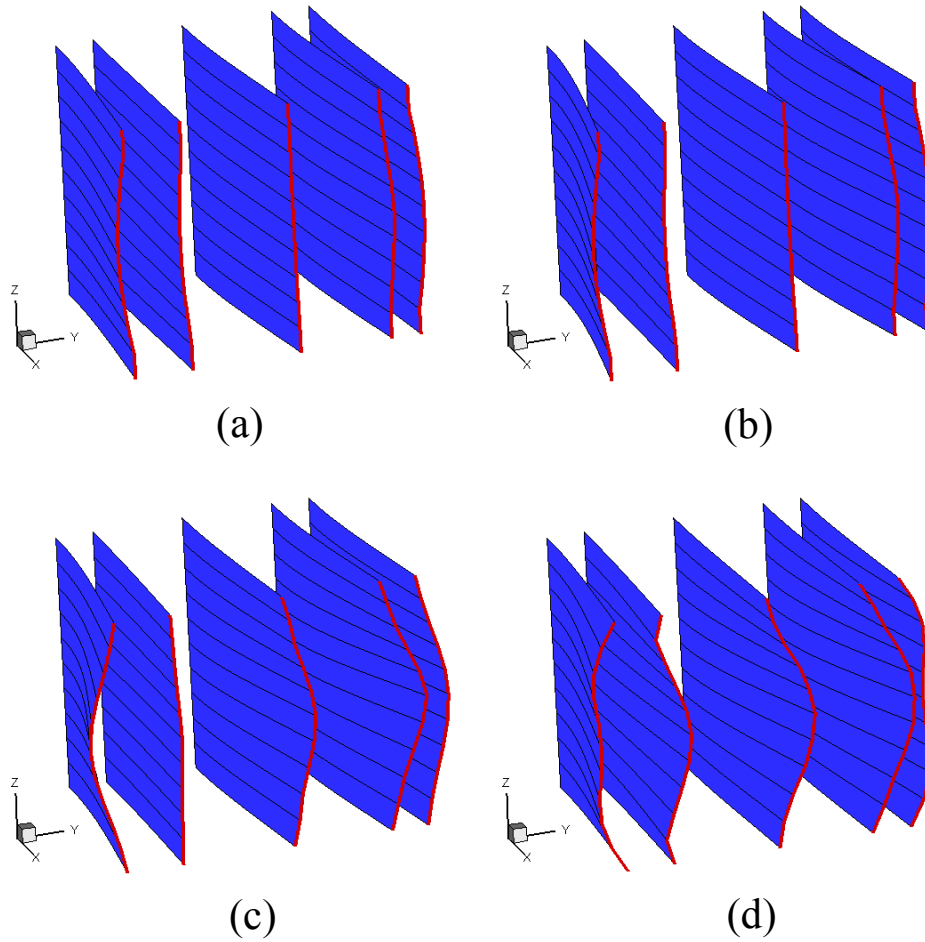
Figure 6-4 Fin deformations within half motion period. The fin moves in negative y-direction at positions t = 0, T/8, T/4, T/2. (a) U-Passive; (b) U-I-0; (c) C-II-45; (d) C-II-180. For all cases φ_{mean}= 30 degree.

For distribution U-III, the fin exhibits an asymmetrical deformation pattern. As the phase difference increases, the fin's deformation gradually transforms from *H*-mode, which is shown in Figure 6-5 (a), to *S*-mode, which is illustrated in Figure 6-5 (c). Compared with *H*-mode, *S*-mode shows a wave-like deformation pattern which is not possible to be accomplished by purely passive deformation. This mode is observed in experiments [35] to be associated with braking maneuver. Incidentally, we find that *S*-mode generates less thrust and lateral force in comparison with the *H*-mode, but still creates vertical force which may be needed for motion stabilisation, which makes the *S*-mode ideal for the braking process (see Figure 6-12 and Figure 6-13). With distribution U-IV, *W*-mode is observed as demonstrated in Figure 6-5 (d). It is noted that the *W*-mode achieved with distribution U-IV is different from that created at large

phase difference of distribution C-II. For distribution U-IV, the rays at the dorsal, ventral edges and the center of the fin have the same phase lag in terms of the activation force with respect to the sway motion.

(a)   (b)

(c)   (d)
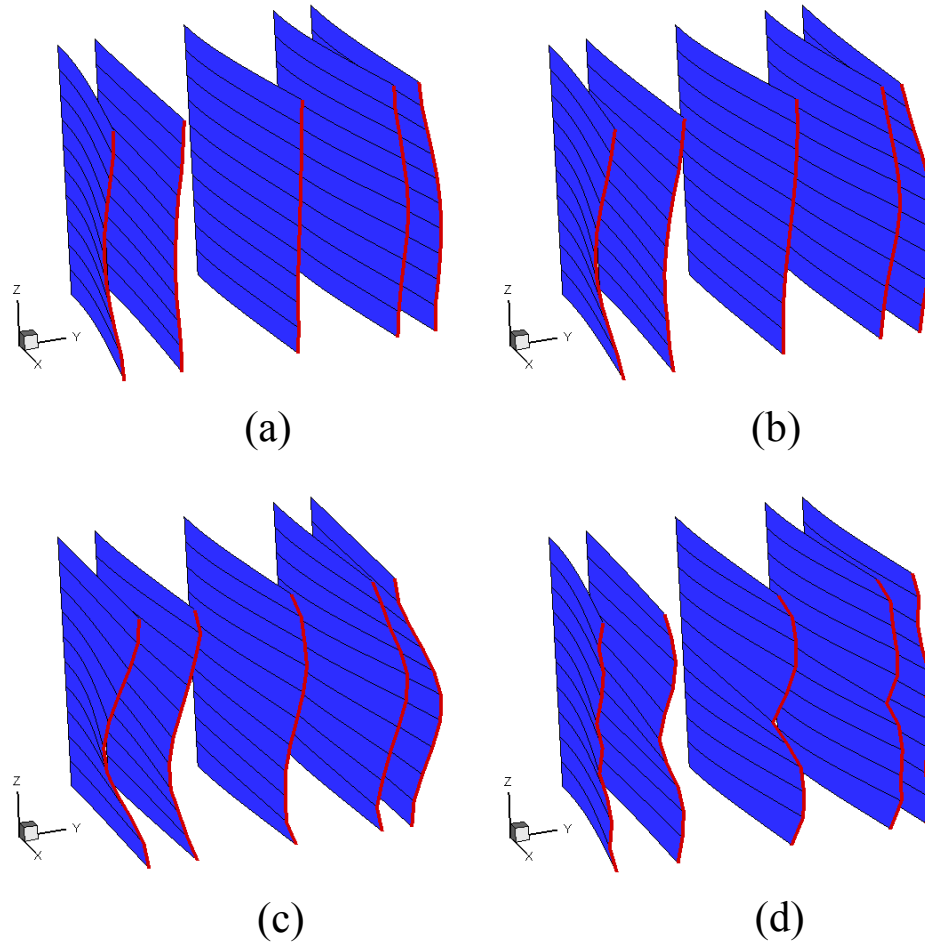
Figure 6-5 Fin deformations within half motion period. The fin moves in negative y-direction at positions t = 0, T/8, T/4, T/2. (a) U-III-90; (b) U-III-180; (c) U-III-360; (d) U-IV-90. For all cases φ_{mean}= 30 degree.

Figure 6-6 illustrates the actual deflections of Ray 1 and Ray 6 for the U-Passive case (Figure 6-6 (a)) and the C-II-45 case at $\varphi_{mean} = 30$ (Figure 6-6 (b)). It is observed that for both cases, the rays exhibit only first-order bending mode and Ray 6 has a larger lateral excursion than Ray 1. Compared with the passive case, Ray 6 of C-II-45 (with active control) creates significantly larger deformation, which may lead to better oriented forces and thus result in higher thrust.
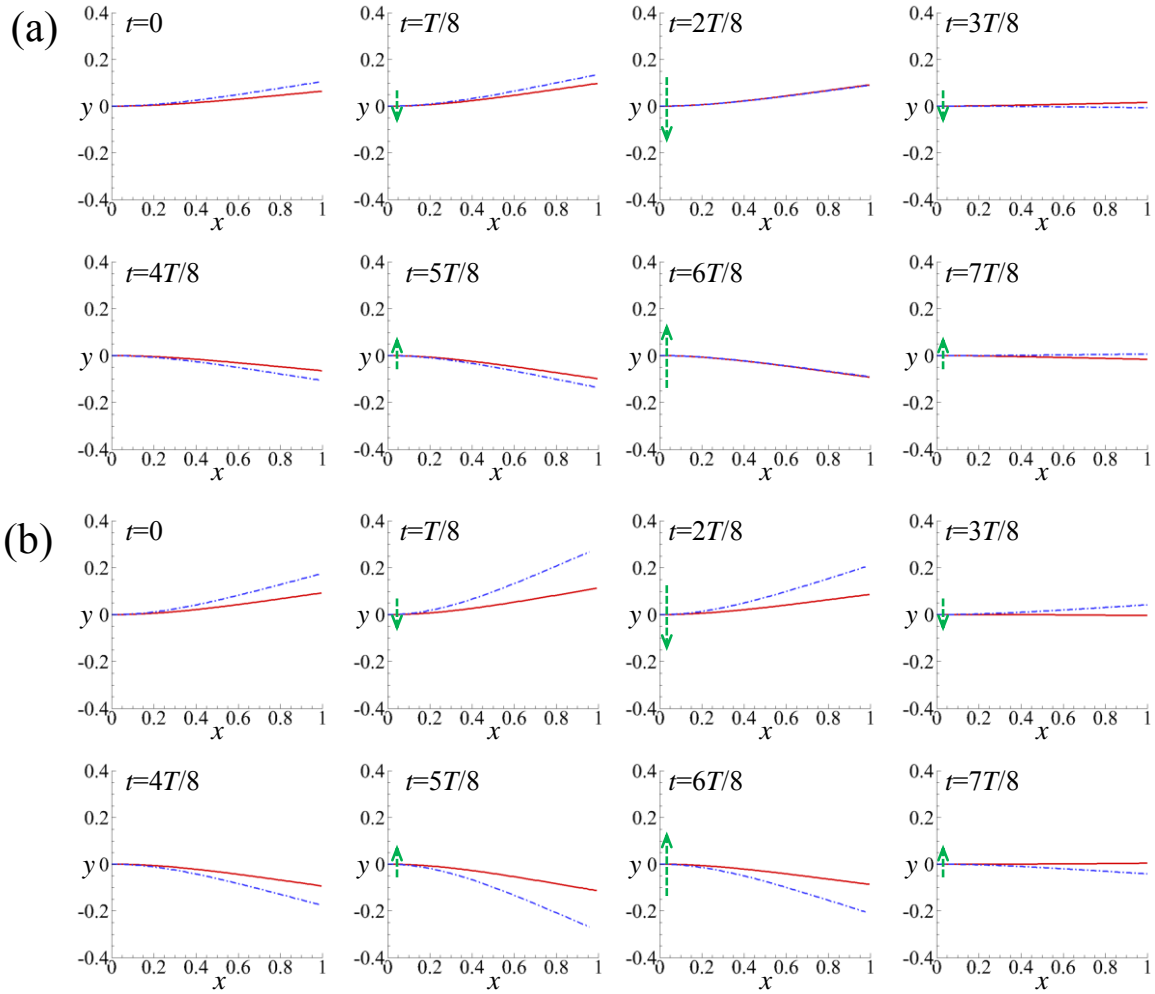
Figure 6-6 Deflections in y-direction of Ray 1 (red solid lines) and Ray 6 (blue dash-dot lines) for (a) U-Passive, and (b) C-II-45, φ_{mean}= 30 degree.

6.3.2   Force generation and propulsion efficiency of the fin

Figure 6-7 shows the instantaneous thrust and power expenditure coefficients within one motion period. It is seen that the fin with distribution U-II-45 generates significantly higher thrust peaks than the corresponding passive case with a slight increase in power expenditure (see Figure 6-7 (a) and (b)). With cupping stiffness distribution, the thrust of C-II-45 case can be further enhanced while consuming very similar input power as the U-II-45 case.
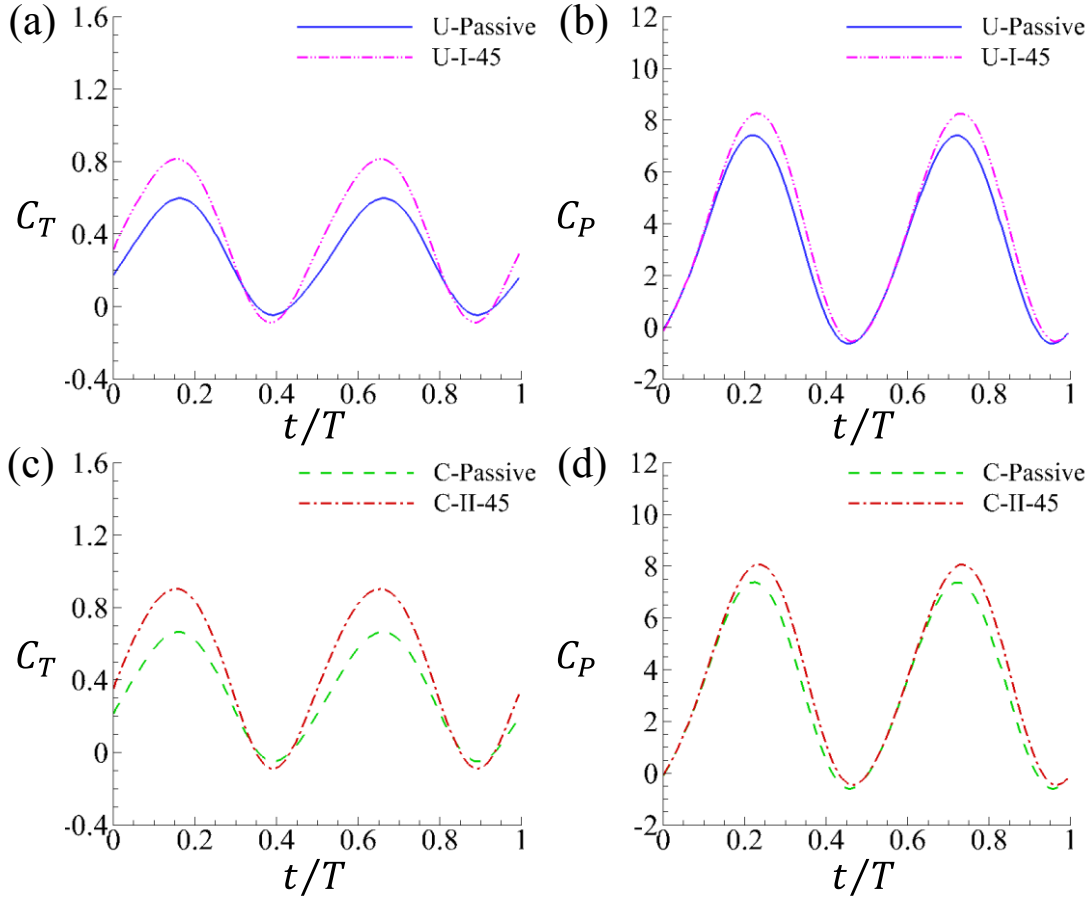
Figure 6-7 Time histories of thrust and power expenditure coefficients at various stiffness and phase distributions. φ_{mean}= 30 degree.

The time-averaged thrust coefficient and propulsion efficiency of various stiffness and phase distributions are summarised in Figure 6-8 and Figure 6-9. It is seen that for all types of phase distributions and most phase difference values, $\overline{C_T}$ and η have similar variation trends as functions of φ_{mean}. Specifically, $\overline{C_T}$ decreases monotonously as the increase of φ_{mean} while the propulsion efficiency, on the other hand, rises slightly and then declines with the increase of φ_{mean}. Besides, for all cases with active control, the thrust and propulsion efficiency of the fin are significantly enhanced when φ_{mean} is less than 90 degree. For example, the thrust and propulsion efficiency of the fin with distribution U-II-45 are improved by 43% ($\varphi_{mean} = 0$) and 35% ($\varphi_{mean} = 60$) respectively. In terms of thrust generation and propulsion efficiency, smaller phase difference values produce better performance. This is reminiscent of the experiment of Esposito et al. [38], where the cupping motion was created by imposing phase lags of 25 and 50 degree between the middle fin rays and the dorsal and ventral fin rays.

Besides, in their experiment, cupping motion generated largest thrust force compared with other motions.
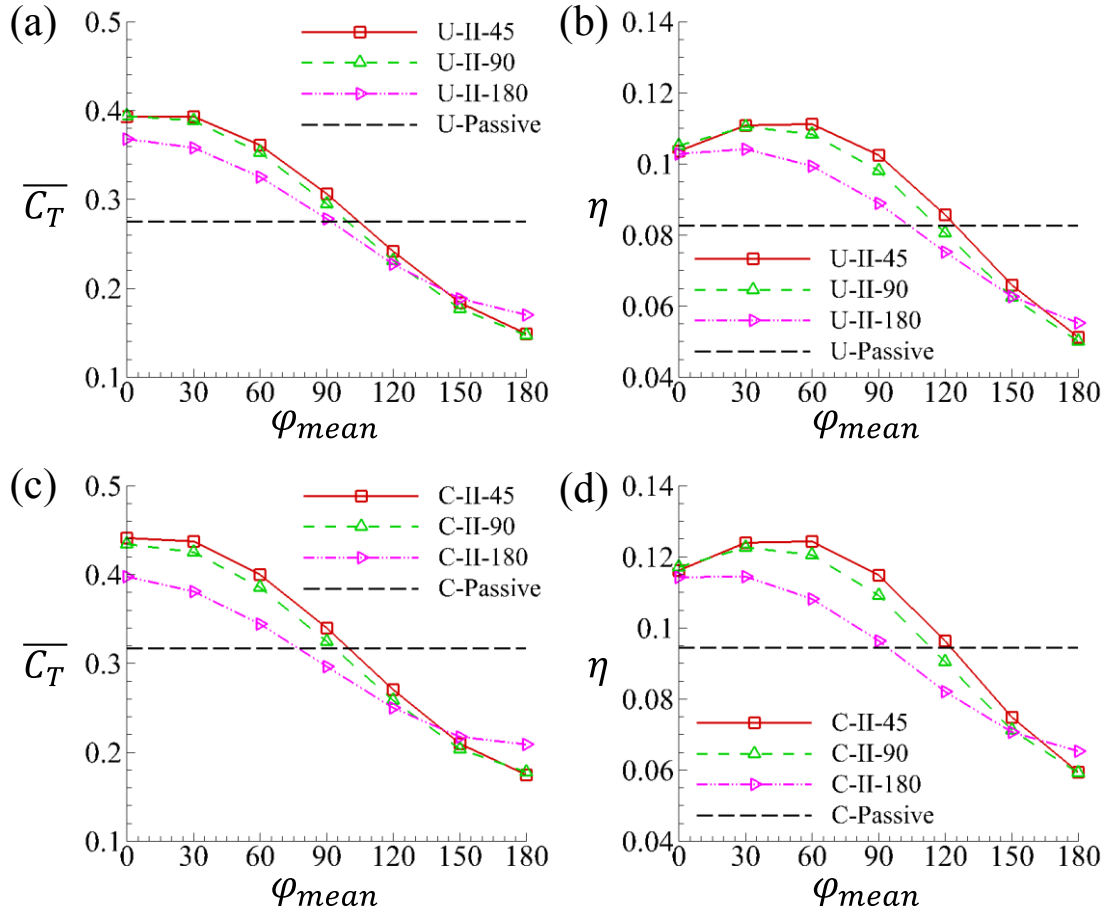
Figure 6-8 Time averaged thrust coefficient and propulsion efficiency as functions of mean phase lag φ_{mean} for U-II (a) (b), and C-II (c) (d).

Figure 6-10 compares the time-averaged thrust coefficient and propulsion efficiency between different stiffness and phase distributions at a fixed value of φ_{diff} (hereby $\varphi_{diff} = 45$, except for distribution U-I where $\varphi_{diff} = 0$). It is revealed that with uniform stiffness, for the parameters considered in the present study, the propulsion performances of the fin at different phase distributions are quite similar to each other, although they are significantly higher than the one with passive deformation only when φ_{mean} is less than 90 degree. With distribution C-II, the fin's propulsion performance is significantly augmented.
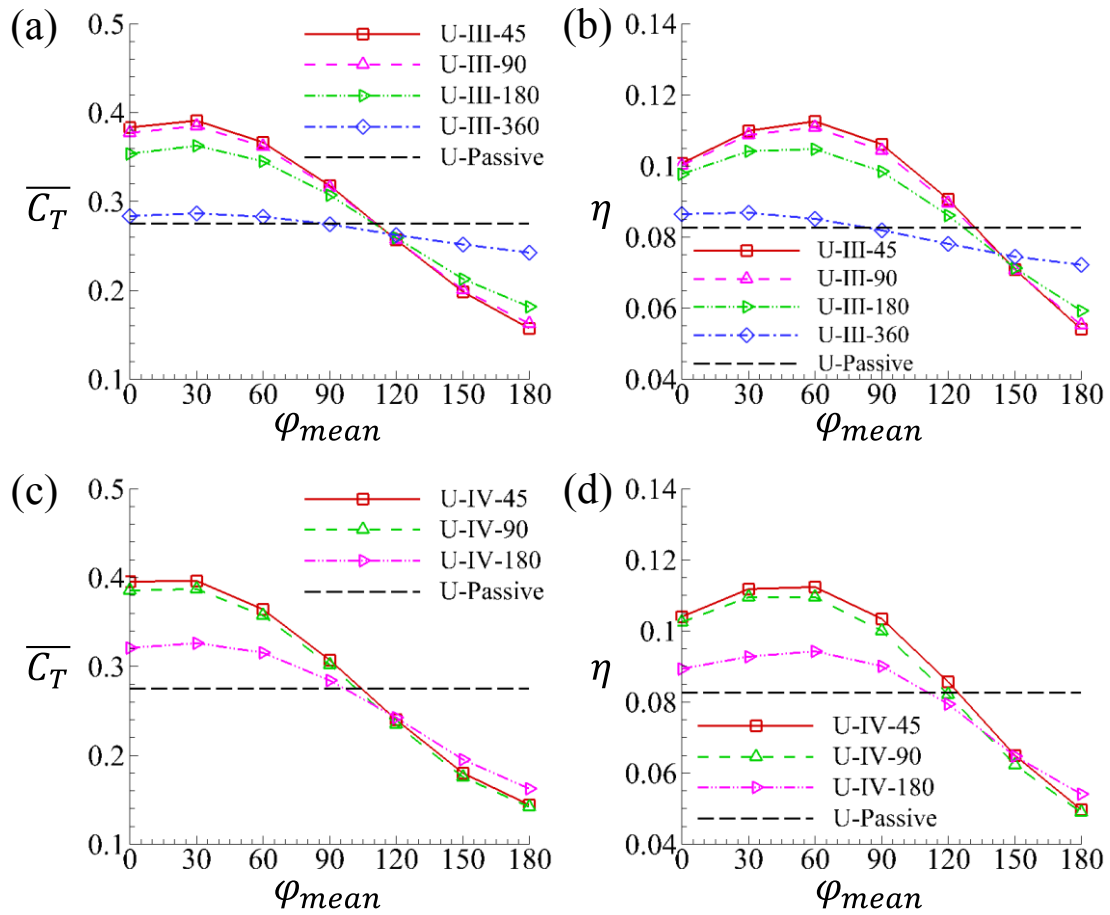
Figure 6-9 Time averaged thrust coefficient and propulsion efficiency as functions of mean phase lag φ_{mean} for U-III (a) (b), and U-IV (c) (d).
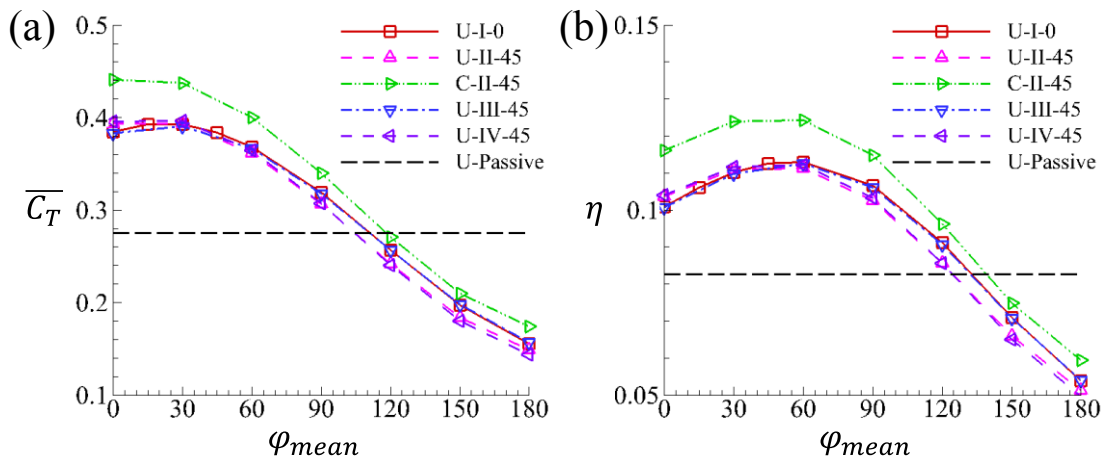
Figure 6-10 Time averaged thrust coefficient and propulsion efficiency as functions of mean phase lag φ_{mean} at various stiffness and phase distributions.
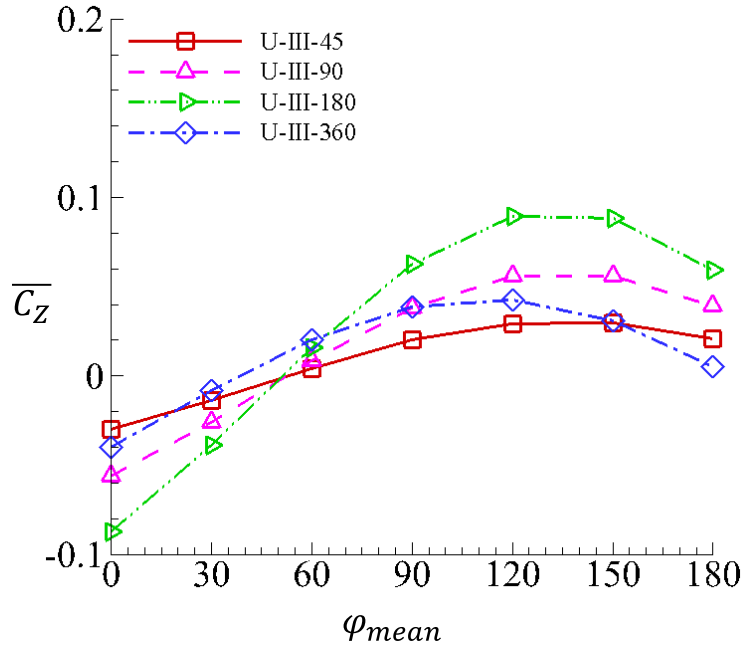
Figure 6-11 Time averaged vertical force coefficient as a function of mean phase lag φ_{mean} for U-III.

Figure 6-11 demonstrates the vertical force coefficients for distribution U-III at different values of the phase difference. For all phase difference values, two maximum vertical forces are generated at $\varphi_{mean} = 0$ (in $-z$ direction) and $\varphi_{mean} = 120$ (in $+z$ direction). It suggests that fish can control the phase distribution among the rays of its caudal fin to change both the magnitude and direction of the vertical force, which may play a significant role in body stabilisation. This vertical force can provide the lift needed to counteract the gravity force acting on the fish body and create a torque around the centre of mass of the fish to balance the torque (with opposite sign) generated by the pectoral fin.

During the braking process, the motion of the posterior part of the fish may be reduced in order to reduce the thrust generation. However, the vertical force may still be needed for stabilisation. To elucidate this, we simulate cases with no sway motion at the leading edge of the fin. The fin with distribution U-III undergoes an *H*-mode at $\varphi_{diff} = 90$ while an *S*-mode at $\varphi_{diff} = 360$ (see Figure 6-5 (a) and (c)). Figure 6-12 illustrates the time-averaged values of the thrust, vertical force and power expenditure coefficients. It is revealed that without sway motion, the fin generates no thrust in both

H-mode and *S*-mode. However, the *S*-mode creates vertical force twice as much as the *H*-mode using similar input power. This is accompanied by significant reduction in lateral force in the *S*-mode, as demonstrated in Figure 6-13. Therefore, we conclude that the *S*-mode outperforms the *H*-mode during the slowing down process. This is consistent with experimental observations.
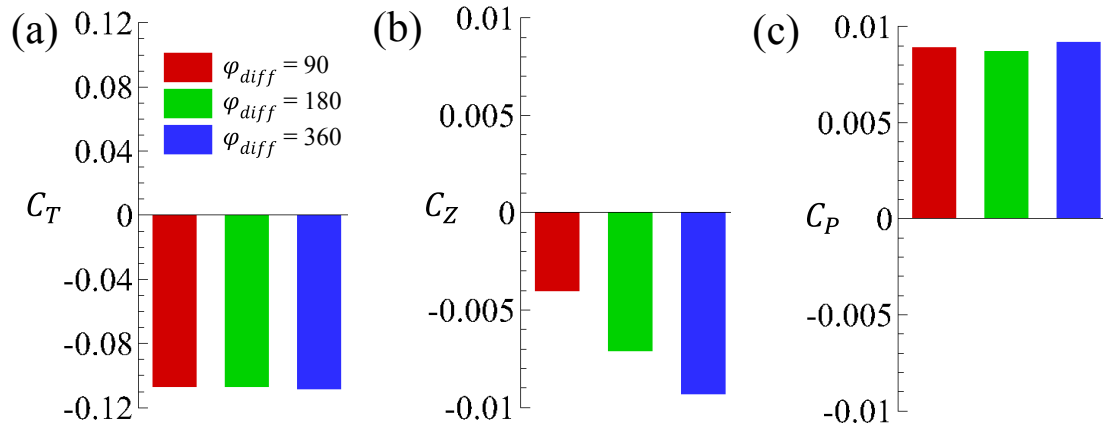
Figure 6-12 Time averaged thrust (a), vertical force (b) and power expenditure (c) coefficients of U-III without sway motion at φ_{diff}=90 (red), 180 (green) and 360 (blue).
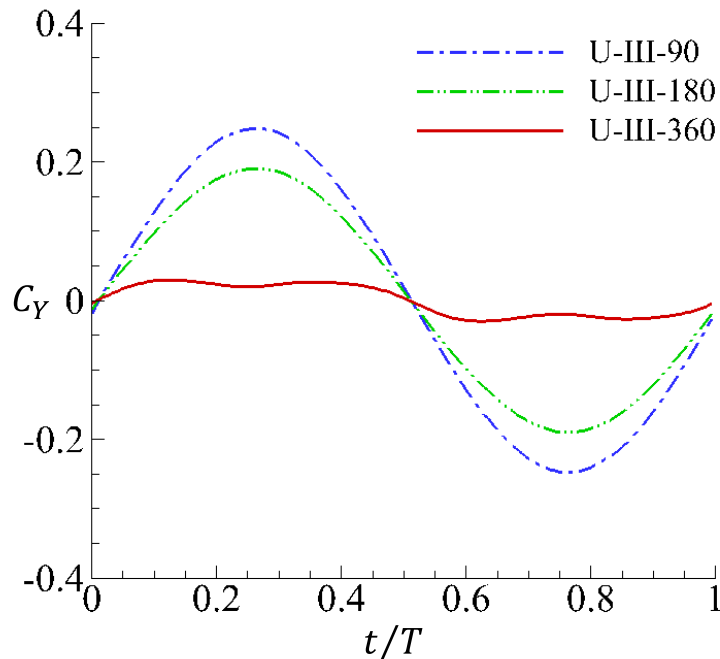
Figure 6-13 Time histories of lateral force coefficients of U-III without sway motion at different phase difference.

6.3.3   *Near-body flow field of the fin*

To further study the effect of active control over the caudal fin in sway motion and explain the physical underlying mechanisms in this fluid-structure interaction problem, we numerically visualise the near-body flow field around the fin. Figure 6-14 shows the iso-surfaces of vorticity magnitude in the wake behind the caudal fin for different deformation patterns. We can see that the wake is composed of a sequence of vortex rings (visualised using the iso-surface of the vorticity magnitude), which are similar to those observed in previous simulations [25]. These wake structures also resemble the hairpin structures proposed by Tytell [32] based on the PIV study of the flow field around a bluegill sunfish. It is observed that, in the present study, the wake structures from different deformation patterns are qualitatively similar to each other.
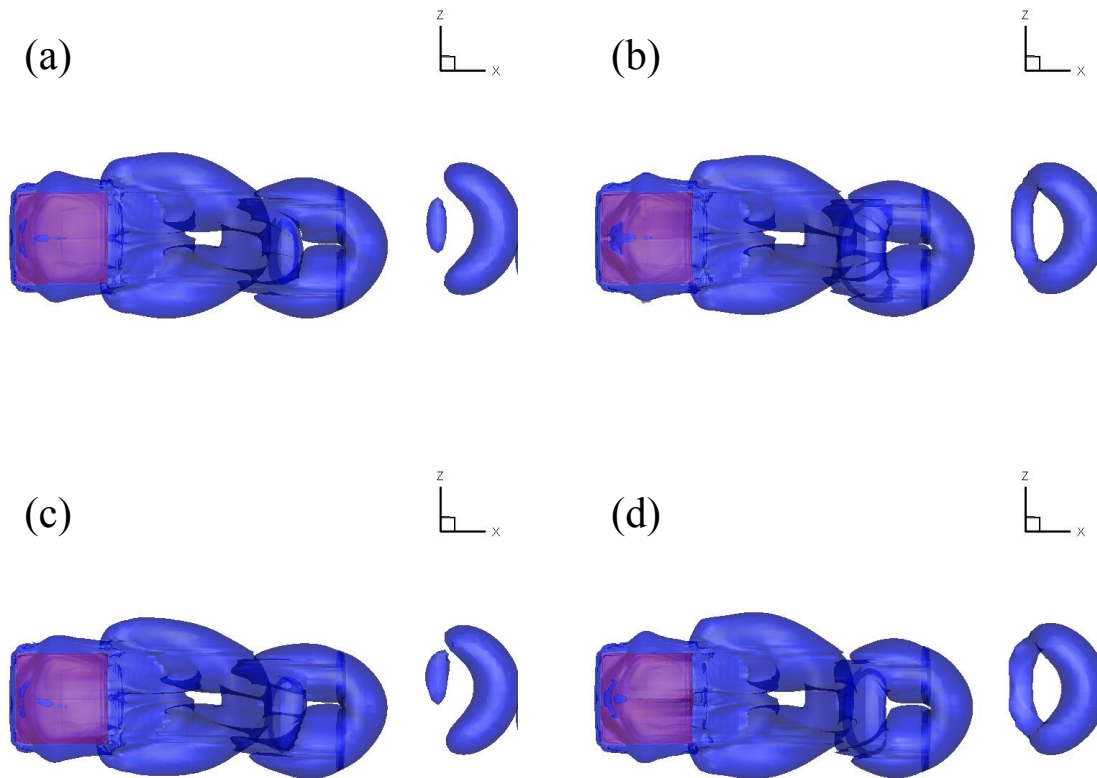
Figure 6-14 Iso-surfaces of normalised vorticity magnitude ($\omega_{mag} = 2$) in the wake behind the caudal fin for various stiffness and phase distributions at t = 0.25T. (a) U-Passive, (b) C-II-45, (c) U-III-360, (d) U-IV-90. For all cases, $\varphi_{mean} = 30$ degree.
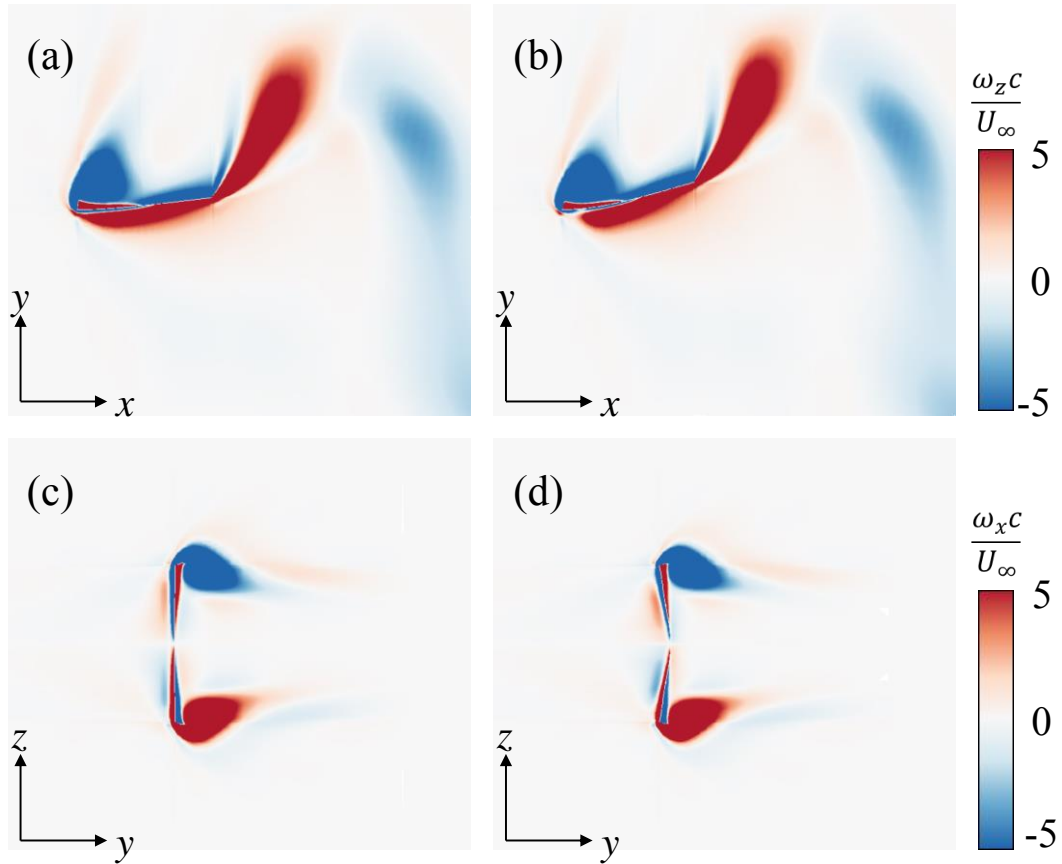
Figure 6-15 Vorticity fields for the caudal fin of U-Passive (a) (c), and C-II-45, φ_{mean}= 30 degree (b) (d). The contours show the normalised z-component of the vorticity in plane z = 0.5c (a) (b), and the normalised x-component of the vorticity in plane x = 0.7c (c) (d) at t = 0.25T.

Figure 6-15 demonstrates the sectional views of the flow vorticity within the z plane and the x plane. The vorticity of the U-Passive case (Figure 6-15 (a) (c)) and the C-II-45 case (Figure 6-15 (b) (d)) in both the x and z planes are qualitatively similar. Specifically, in the plane $z = 0.5c$, we can observe the formations of a clockwise leading edge vortex and a counter-clockwise vortex is shed at the trailing edge. It is not surprising that the vortex shedding patterns in Figure 6-15 (a) and (b) are similar to each other. As previously discussed, both the U-Passive case and the C-II-45 case have only the first bending mode excited (see Figure 6-6).

From the vorticity fields in plane $x = 0.7c$, we can see the formations of a clockwise vortex near the dorsal edge and a counter-clockwise vortex near the ventral edge and the vortices are symmetrical with respect to the mid-line (Ray 6) due to the symmetrical deformation. The C-II-45 case has more pronounced spanwise cupping deformation, so

that the fluid at the central part has a tendency to flow towards the mid-line. This makes it difficult for the fluid to move around the dorsal and ventral edges, causing an increase of the pressure in the central region. This will be further discussed later.

6.3.4   *Physical mechanism of the performance enhancement*

The parametric exploration in Section 6.3.2 indicates that the optimal performance occurs when φ_{diff} is approximately 45 degree and φ_{mean} is around 30 degree. To reveal the physical mechanism behind the performance improvement, the results will be further analysed and discussed in this section.
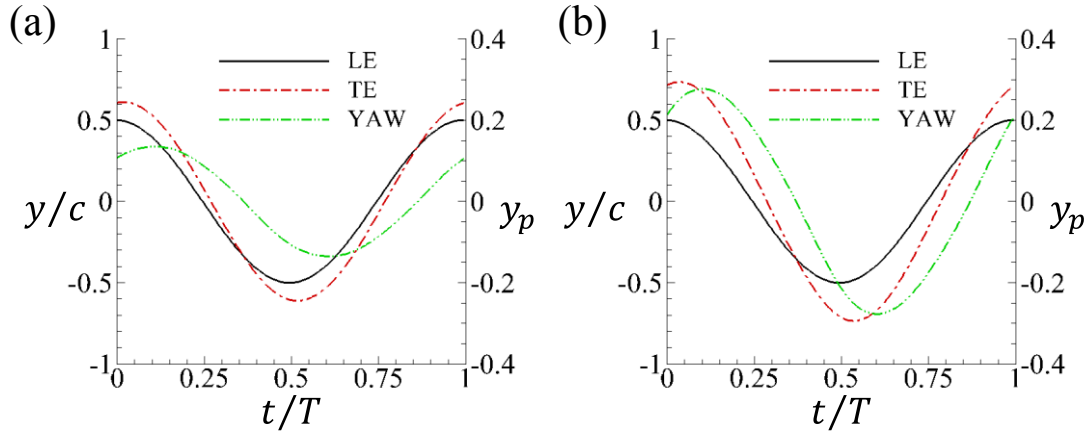
Figure 6-16 Time histories of normalised displacements of leading end y_L/c (black solid line), trailing end y_T/c (red dash-dot line) and effective yaw motion $y_p = (y_T - y_L)/c$ (green dash-dot-dot line) of Ray 6 at (a) U-Passive, and (b) C-II-45, φ_{mean}= 30 degree.

The bending deformation shown in Figure 6-6 essentially creates an effective yaw motion, as illustrated in Figure 6-16. This yaw motion can be represented as $y_p = (y_T - y_L)/c$, where y_L and y_T are the lateral deflections of the ray's leading and trailing edges, respectively. It is observed in Figure 6-16 that the yaw motion varies with time almost sinusoidally so that it can be approximated using a cosine function as $y_p(t) \sim A_p cos(\omega_p t + \psi)$, where A_p is the amplitude of the yaw motion and ψ is the phase lag between the sway motion and the yaw motion.
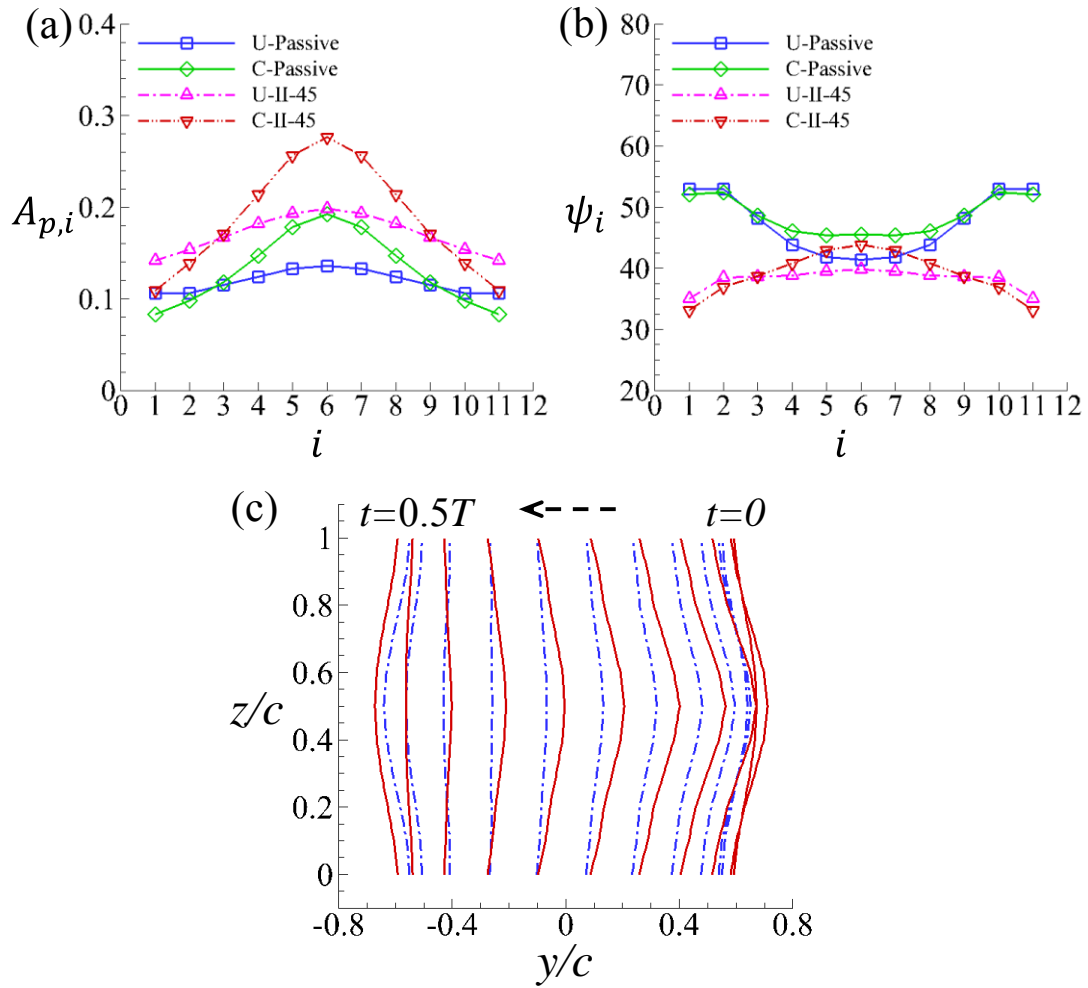
Figure 6-17 (a) The amplitudes ($A_{p,i}$) of the effective yaw motions of the rays, and (b) the actual phase lags (ψ_i) between the sway motion and the effective yaw motions of the rays. (c) Snapshots of the trailing edge of the fin within half motion period for C-Passive (blue dash-dot line) and C-II-45 (red solid line). Dash arrow represents the moving direction of the leading edge. $\varphi_{mean}= 30$ degree.

Figure 6-17 (a) demonstrates the yaw amplitudes of the rays at different stiffness distributions and phase distributions. For uniform stiffness distribution, all the rays of U-II-45 have larger yaw angles than the rays of the corresponding passive case. With a cupping stiffness distribution (C-II-45), the yaw motions of the rays in the centre of the fin are further increased while those of the rays near the dorsal and ventral edges are suppressed, leading to a deeper cupping deformation. This is believed to further enhance the thrust generation. The phase lags between the sway motion and the effective yaw motion of the rays are shown in Figure 6-17 (b). It is seen that the averaged phase lags for all these three cases are actually close to each other (within the

range of 35 degree to 45 degree). The implication is that in these high performance cases the deformation caused by the active control mechanism and that due to passive structural flexibility are almost in phase with each other (see Figure 6-17 (c)); the primary mechanism of performance enhancement through active control is that it significantly increases the effective yaw amplitude (see Figure 6-17 (a)).
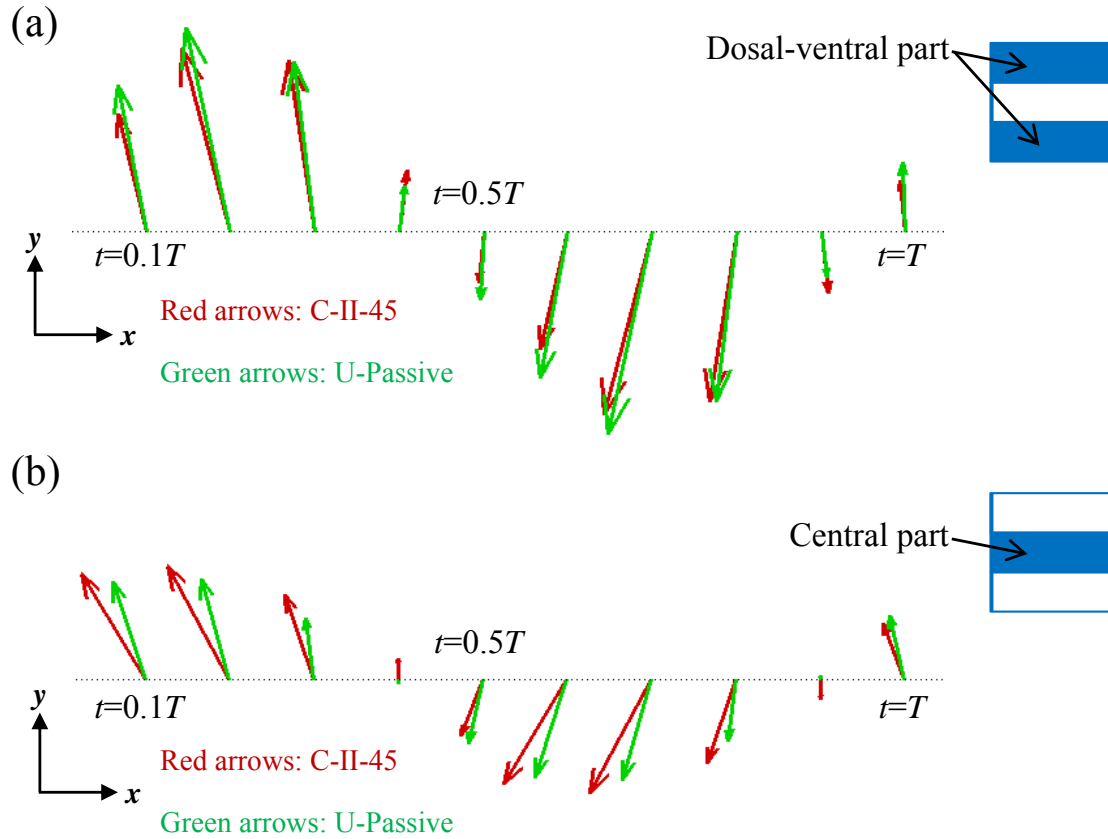
Figure 6-18 Force vectors of the dorsal-ventral part (a) and central part (b) of the fin within one motion period in x-y plane. Red arrows: C-II-45 and φ_{mean}= 30 degree, and green arrows: U-Passive.

Incidentally, we note that by carefully choosing the structural flexibility of the rays, deformation and performance enhancement of actively controlled *C*-mode motion (e.g. the C-II 45 case) are in fact within reach using purely passive fin deformations [102]. The active control mechanism, however, greatly increases the versatility and adaptability of the system by making it easier to switch from one swimming mode to another to adjust for changes in the environment. Moreover, active control enables the *S*-mode, which is particularly useful in the braking maneuver (see Section 6.3.3).
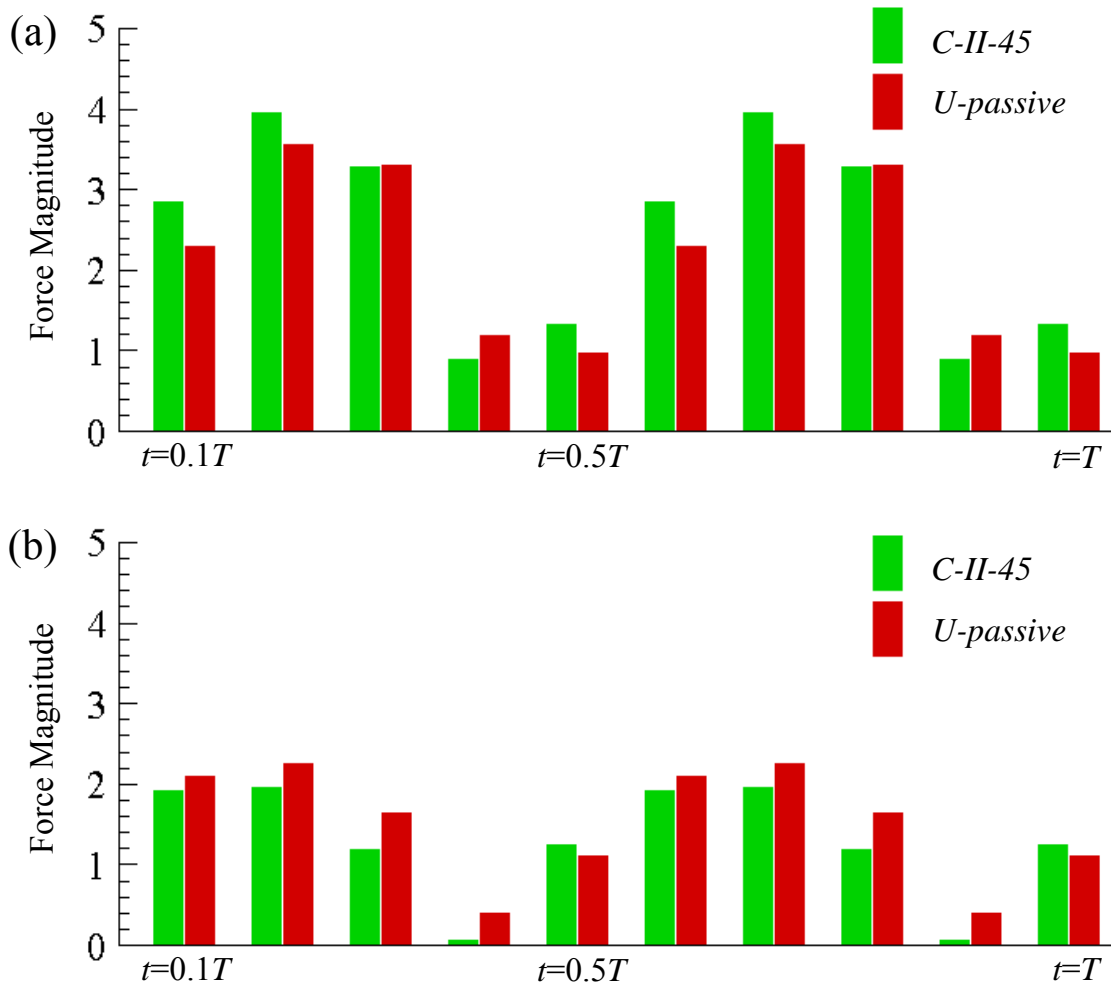
Figure 6-19 Force magnitudes of the dorsal-ventral part (a) and central part (b) of the fin within one motion period in x-y plane. Red bars: C-II-45 and φ_{mean}= 30 degree, and green bars: U-Passive.

To better understand the origin of thrust enhancement involved in the present study, the caudal fin surface is split into two parts: dorsal-ventral part and central part, as shown in Figure 6-18. For the dorsal-ventral part (Figure 6-18 (a)), the force generated by U-Passive case has larger magnitude than those of the C-II-45 case, but the forces of the C-II-45 case are better oriented in thrust direction. The advantage of active control is better illustrated in the central part (Figure 6-18 (b)), where the C-II case has both larger force magnitude and better orientation. The force magnitudes are more clearly demonstrated in Figure 6-19.
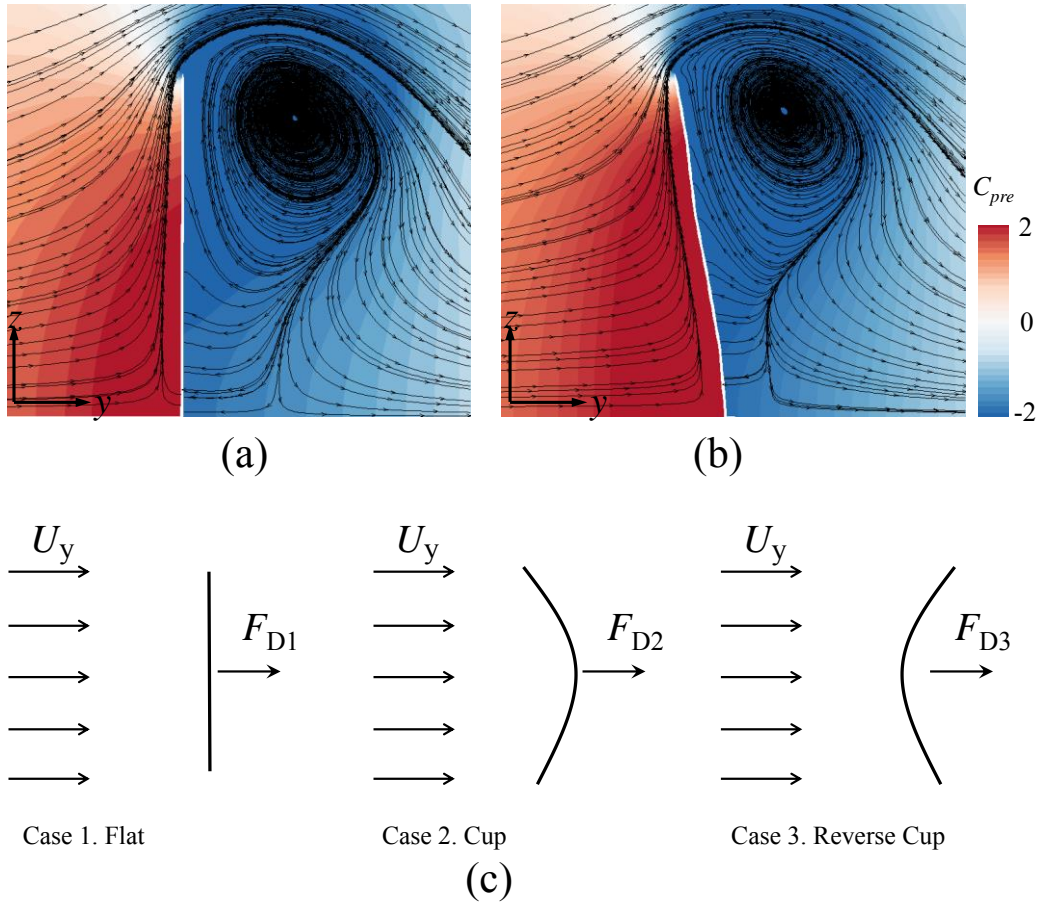
Figure 6-20 Pressure fields for the caudal fin of U-Passive (a), and C-II-45, φ_{mean}= 30 degree (b). The contours show the pressure distribution in plane x = 0.7c, and $C_{pre} = (p - p_\infty)/0.5\rho U_\infty^2$. The streamlines are drawn using in-plane flow velocity relative to the fin's leading edge at t = T/4. (c) Diagrams of three different spanwise deformations. , where U_y is the flow speed relative to the fin and F_{D1}, F_{D2}, F_{D3} are the resulting fluid forces on the fin.

As previously discussed, the cupping deformation tends to prevent the fluid from moving around the dorsal and ventral edges so that it may raise the pressure in the central area. This phenomenon can be more clearly observed in Figure 6-20 (a) and (b), where the streamlines show the relative motion of the fluid with respect to the fin. It is clearly seen that with the cup deformation, the streamlines remain horizontal very close to the surface of the fin, leading to a (slightly) wider high pressure area. Figure 6-20 (c) sketches three different spanwise deformation patterns, namely Flat, Cup and Reverse Cup. Intuitively, compared to flat deformation, the Cup deformation may hold more fluid in the central region by increasing the difficulty for the fluid to move around the upper and lower corner. Thus, the flow speed in the central area is decreased, which leads to higher pressure in that region so that the fluid dynamic force F_{D2} should be

larger than the other two cases. In contrast, the Reverse Cup deformation resembles a streamlined body (to certain extent), making it easier for the fluid to go around the upper and lower edges, thereby accelerating the flow in the central region, leading to a decrease of pressure in the central area and a reduction in the force F_{D3}. Indeed, this kind of deformation has been shown to compromise the thrust generation [53].
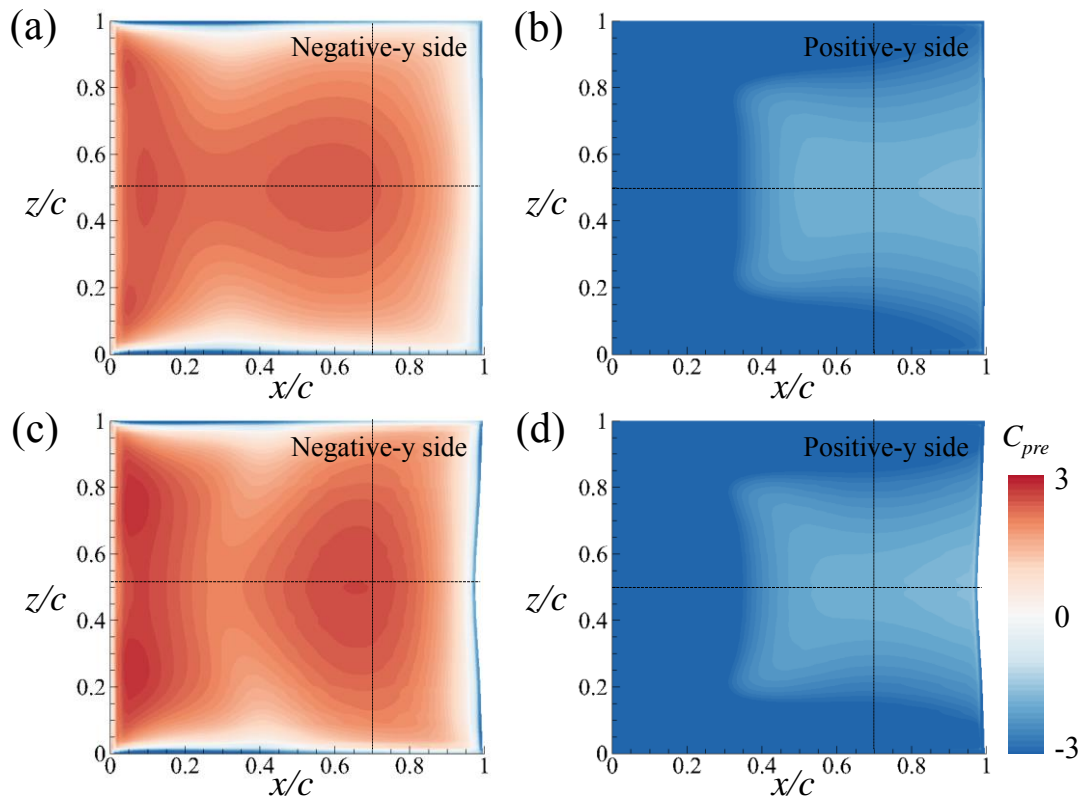
Figure 6-21 Pressure contours at the two sides of the caudal fin at t = 0.25T. (a) (b) U-Passive, and (c) (d) C-II-45, φ_{mean}= 30 degree.

Figure 6-21 illustrates the pressure distributions over the fin surface for the U-Passive case and the C-II-45 case. It is seen that in both cases, a high pressure region exists within the area of $0.4 < x/c < 0.8$ and $0.3 < z/c < 0.7$ at the negative-y side of the fin. Compared with the U-Passive case, the high pressure region of the C-II-45 case is larger and stronger, which explains why the C-II-45 case creates larger force in the central part of the fin (see Figure 6-18). The pressure increase can be quantitatively observed in Figure 6-22, where the pressure coefficients along the fin surface at $x = 0.7c$ are plotted.
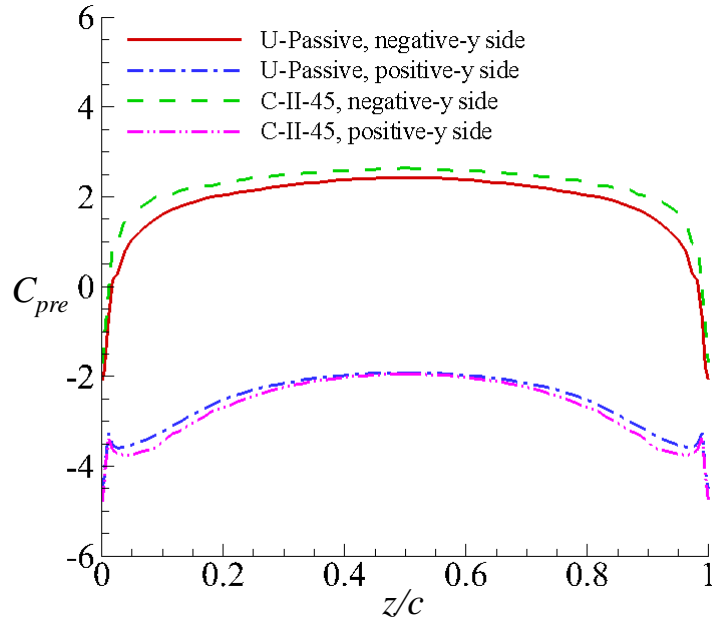
Figure 6-22 Pressure coefficients along the fin surface at x = 0.7c.

6.4 Concluding remarks

In the present chapter, we numerically examine the performance of a simplified ray-strengthened caudal fin with both active and passive control strategies. The caudal fin is activated by 1) a sway motion shared by all the leading ends of the rays, and 2) time-varying external loads distributed uniformly along each ray, which mimics the pulling effect of the tendons at the basal end of each ray. The key parameters controlling the deformation of the fin are the maximum phase difference among the rays (φ_{diff}), the mean phase lag of the rays (φ_{mean}) and the phase distribution. By changing these parameters, different deformation patterns can be accomplished.

Four different phase distributions are investigated within the $\varphi_{diff} - \varphi_{mean}$ parameter space in the present study. Several deformation modes observed in previous experiments [35,38] are reproduced, including the *C*-mode, the *W*-mode, the *H*-mode and the *S*-mode (which is not possible to be achieved with purely passive deformation). By comparing with the passive deformation case, we find that the propulsion performance of all the cases with active control is significantly enhanced

161

when φ_{mean} is less than 90 degree. For example, the thrust force and propulsion efficiency of the U-II-45 case are improved by 43% and 35% respectively.

Among these deformation patterns, the *C*-mode created by the fin with distribution C-II-45 produces the best propulsion performance. This is attributed to two reasons. First, larger deflections and curvatures are created for the rays in the central part of the fin, which lead to higher yaw angles in the induced yaw motions. The forces are therefore better aligned in the thrust direction. Second, the chordwise bending and spanwise cupping deformations result in a larger, stronger and further downstream high pressure region, which further enhances the thrust generated by the *C*-mode. In this particular mode, in terms of the performance enhancing mechanism, there is little difference between actively controlled and fully passive cases.

The *H*-mode and *S*-mode, on the other hand, both produce considerable vertical forces, which are primarily attributed to the asymmetrical deformations. Compared with the *H*-mode, the *S*-mode generates smaller thrust and vertical force while requiring less input power. This is reminiscent of the finding from previous experiment [35] that '*S*' motion is associated with braking maneuver, during which the motion of the posterior part of the fish body may be reduced to decrease the thrust force. Thus, we further demonstrate that without sway motion the *S*-mode actually generates much larger vertical force than the *H*-mode. This, together with the significant reduction in lateral force, makes *S*-mode ideal during the braking process.

The present work is focused on demonstrating the effect of active control strategy on the locomotion performance of a fish-like caudal fin instead of exactly duplicating a real fish fin. The present model captures several key characteristics possessed by real fins, e.g., anisotropic material property, individual ray activation and active curvature control of the rays. However, it is also worth pointing out the limitations of the present study. For example, for simplicity the present model is assumed to have a rectangular shape with rays of the same length. The aspect ratio of the current model is fixed at

unity while its effect is not examined. The present mass ratio is 0.2, which ensures the fin's deformation is fluid-driven. But its effect on the propulsion performance of the present caudal fin model is not studied either. Besides, the curvature changes of the rays are modelled as distributed external loads rather than explicitly modeling the bi-laminar design of the real fin rays. For simplicity the rotations at the basal ends of the rays are not considered either. The effects of fish body and other fish fins are not considered in the present study. Previous studies revealed that the vortices shed from the dorsal and ventral fins could have significant impact on the performance of the caudal fin [44]. Therefore, the interactions between the fish body and different ray-supported fins should be investigated in future research. The fins of live fish have much more complicated internal structures, musculature and nerve systems. It is thus difficult to directly relate the present results with the dynamics of actual fish fins. However, the conclusions from the present study may provide valuable inspirations and guidelines for the design of robotic fish.

Chapter 7   Performance   of   a   Bio-inspired Underwater   Robot   with   Skeleton-reinforced Undulating Pectoral Fins

7.1 Problem description

In the present chapter, a simplified bio-inspired underwater robot which is composed of a body and a pair of ray-strengthened pectoral fins (as shown in Figure 7-1 (a)) is numerically studied. The body is idealised as a rigid plate. The length, width and thickness of the body are denoted as L_{body}, W_{body} and h_p respectively, where $W_{body} = L_{body}/3$ and $h_p = 0.004L_{body}$. Each pectoral fin is modelled as a rectangular-shaped membrane supported by N evenly distributed flexible rays. The two fins are identical and have the same dimensions as the body, i.e., $L_{fin} = L_{body}$, $W_{fin} = W_{body}$ and $H_{fin} = h_p$.

It should be noted that the rays of the pectoral fins in this chapter are perpendicular to the incoming flow, which is very different from the rays of the caudal fin in Chapter 5 and 6, where the rays are align with the streamwise direction. But similar to previous two chapters, each ray is structurally represented by a nonlinear Euler-Bernoulli beam with uniform flexibility. The non-dimensional bending stiffness is defined as $K_i \equiv E_i I / \rho U_\infty^2 L_{ray}^3$, $(i = 1, \ldots, N)$, where $N = 11$, E_i is the Young's modulus of the ith ray, I is the second moment of inertia, ρ is the fluid density, U_∞ is the freestream velocity and $L_{ray} = W_{fin}$ is the length of the ray. The mass ratio is defined as $m_i^* \equiv \rho_{s,i} h_p / \rho L_{ray}$, where $\rho_{s,i}$ is the density of the ith ray. In the present work, the bending stiffness of all rays is selected to be $K_i = 3.0$ and the mass ratio of the ray are chosen as $m_i^* = 0.2$.
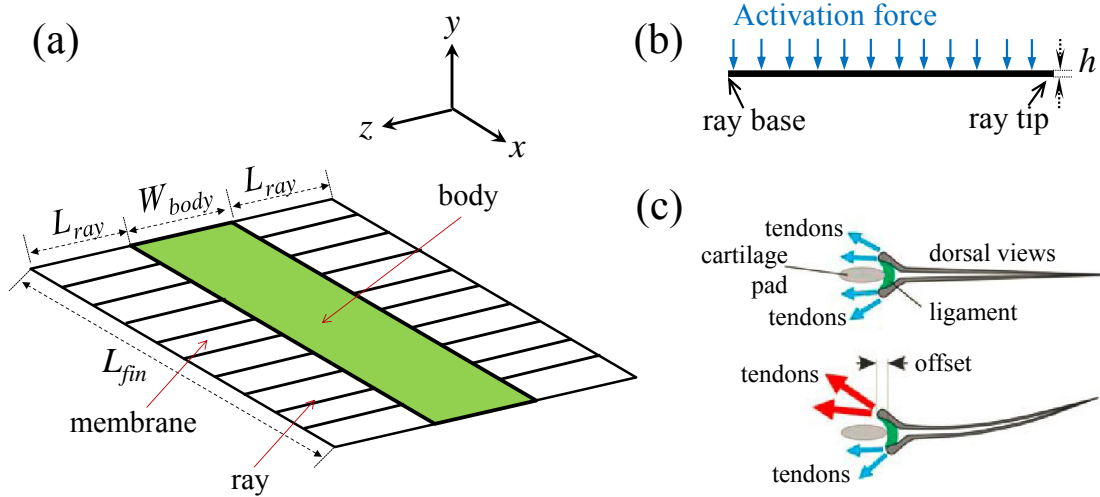
Figure 7-1 (a) Simplified underwater robot model in the present study. (b) Schematic view of the actuation of a ray, where the distributed external force models the pulling effect of the tendons. (d) Dorsal view of a fin ray with two hemitrichs [28].

Besides, the bending stiffness of the membrane is assumed to be negligible, i.e., it cannot sustain any bending but only stretching and compression. Therefore, the constraints provided by the membrane are modelled as distributed linear springs between the neighbouring rays. Based on our numerical tests, we select the spring constant to be $0.02\rho U_\infty^2 L_{fin}$, i.e., the springs are sufficiently rigid to prevent excessive expansion yet still flexible enough to allow large deformation.

Kinematically, the body is fixed in space and all the basal ends of the ray are clamped to the body. Each ray is only actuated by an independent uniformly distributed load (see Figure 7-1 (b)), which is imposed on the grid points of the beam model. This distributed force perpendicular to the beam models the pulling effect of the tendons at the basal end of the ray (see Figure 7-1 (c)). The uniformly distributed external force acting on the ith ray can be expressed as

$$F_i(t) = F_0 sin(2\pi f t - \varphi_i) \tag{7.1}$$

where F_0 is the magnitude of the external force, f is the frequency, φ_i is the phase and t is the time. In this study, we choose $\varphi_1 = 0$ and $\varphi_i = \varphi_d(i-1)/(N-1)$,

where φ_d is the phase lag between the leading edge ray and trailing edge ray. F_0 is assumed to be uniform along the ray and its value is chosen based on numerical tests. Here, F_0 is selected to be $2\rho U_\infty^2 L_{fin}^2$. The reduced frequency based on the fin length L_{fin}, frequency f and incoming flow velocity U_∞ is defined as $f_r \equiv fL_{fin}/U_\infty$. The actuation method here is similar with that used in Chapter 6. But it should be noted that in the present chapter, the pectoral fins are only activated by distributed external loads while the caudal fin model in Chapter 6 is also imposed a sway motion at its leading edge. Another difference is the rays here is in perpendicular to the incoming flow whereas the rays of caudal fin are aligned with the freestream.

The propulsion performance of the pectoral fin is characterised by the mean thrust coefficient $\overline{C_T}$, the mean vertical force coefficient $\overline{C_Y}$, the mean lateral force coefficient $\overline{C_Z}$, the mean moment coefficient $\overline{C_M}$, the mean power expenditure coefficient $\overline{C_P}$, and the propulsion efficiency η. These mean values are evaluated by averaging the instantaneous coefficients over one motion period T. The instantaneous coefficients $C_T(t)$, $C_Y(t)$, $C_Z(t)$ and $C_P(t)$ are defined in the same way as those in Chapter 5 and 6. Here, the propulsion efficiency also has the same definition as Eq. (5.4). The moment coefficient is defined as

$$C_M(t) = \frac{M_Y(t)}{0.5\rho U_\infty^2 L_{fin}^3},\tag{7.2}$$

where $M_Y(t)$ is the moment about the axis parallel to y-axis and through the centre of the body.

7.2 Results and discussions

The problem depicted in Figure 7-1 (a) is solved using the fluid-structure interaction solver described in Chapter 3. The computational domain used here is the same as that in Section 5.3. The Reynolds number based on the length of the fin is $R_e = 6000$

unless specified. The height of the first grid layer off the wall (Δy) is calculated using flat plate boundary theory for a given y+ value. For the present Reynolds number, y+ is chosen to be 0.5, resulting in $\Delta y = 0.001L_{fin}$. The current Reynolds number is selected according to the study of Bozkurttas et al. [101], where the measured Reynolds number based on the pectoral fin of bluegill sunfish was approximately 6300. It is acknowledged that the turbulence may play a role at this Reynolds number. However, it is believed that the turbulence effect is marginal for the Reynolds number considered here. For example, Dong et al. [43] studied the hydrodynamics of a highly flexible pectoral fin of bluegill sunfish using an immersed boundary method at $R_e = 6300$. Their simulating result achieved good comparison with experimental data although only a laminar model was used. Chang et al. [47] numerically investigated the hydrodynamics of a tuna-like swimmer with different turbulence models. It was found that the influence of turbulence models was tiny at $R_e = 7100$.

7.2.1   *Fin deformation and near-body flow field of symmetric fin kinematics*

Typical deformations of the undulating pectoral fins within one motion period are demonstrated in Figure 7-2. The two fins are labelled as Fin-L (left fin) and Fin-R (right fin) respectively. It is seen that with symmetric fin kinematics, the fin deformation patterns are also symmetrical against the middle line of the body. For small phase difference value (φ_d=90 degree), the pectoral fins actually undergo flapping motions rather than undulating motions. As the increase of the phase difference, the undulating motions of the fins are more pronounced, particularly when φ_d=360 degree. The undulating patterns of the fins can be better seen from the lateral views of the robot, which are demonstrated in Figure 7-3. As seen from this figure, there exists a clear traveling wave along the pectoral fin at φ_d=360 degree.

(a)

Fin-R

Fin-L

(b)

(c)

$t=0$ $t=T/4$ $t=2T/4$ $t=3T/4$
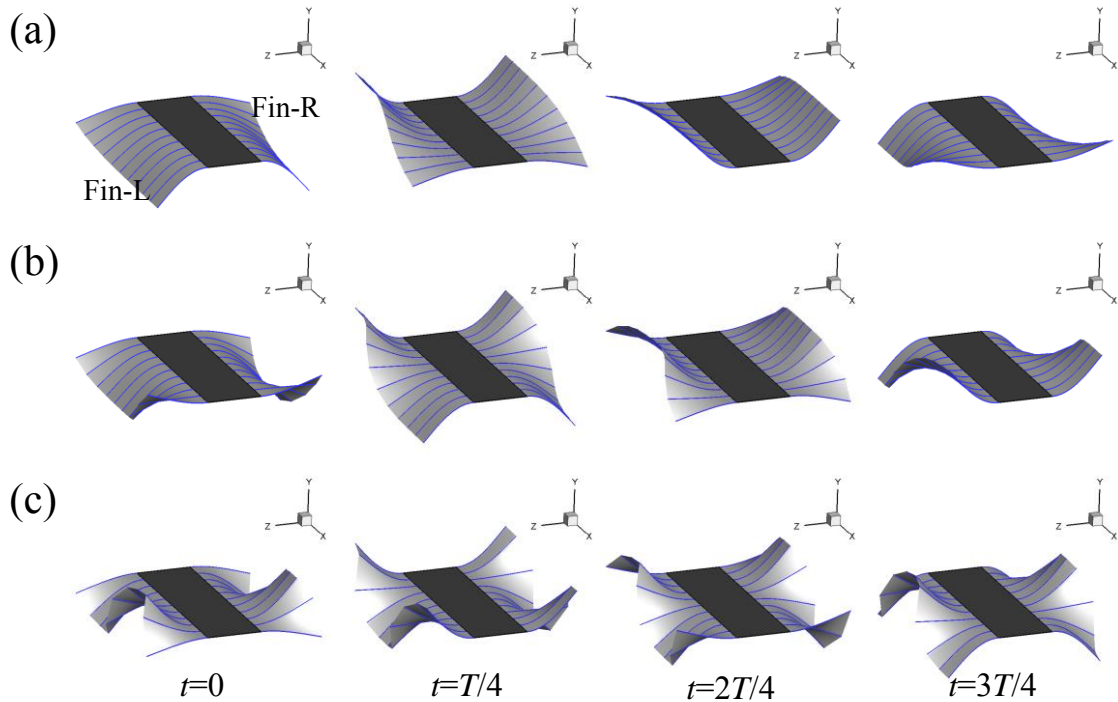
Figure 7-2 Typical 3D fin deformations within one motion period, (a) $\varphi_d=90$, (b) $\varphi_d=180$, (c) $\varphi_d=360$. $f_r=1.2$.

y

x

(a) (b) (c)
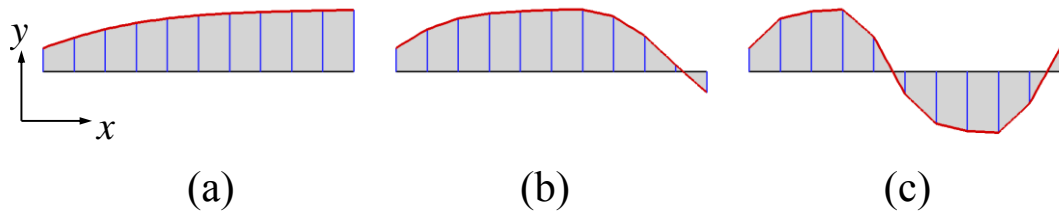
Figure 7-3 Lateral veiw of the undulating fin's deformation pattern at t = T/2, (a) $\varphi_d=90$, (b) $\varphi_d=180$, (c) $\varphi_d=360$. $f_r=1.2$.

Figure 7-4 illustrates the difference between the flexible ray in the present work and a rotational rigid ray. The present flexible ray is actuated by a distributed external force which imitates the pulling effects of the muscles. This kind of activation leads to an actively-controlled curvature along the ray, i.e., the slope of the ray varies significantly from the ray base to the ray tip. However, for a rigid ray with the same effective rotational angle, the slope along the ray remains unchanged. The difference between the flexible and rigid rays can be clearly observed from Figure 7-4. In addition, the actively-controlled ray is curved into the direction of motion, thus is also different from the case of purely passive bending in response to the surrounding fluid.

This type of curvature changing is also observed in previous study of a live knifefish [65].
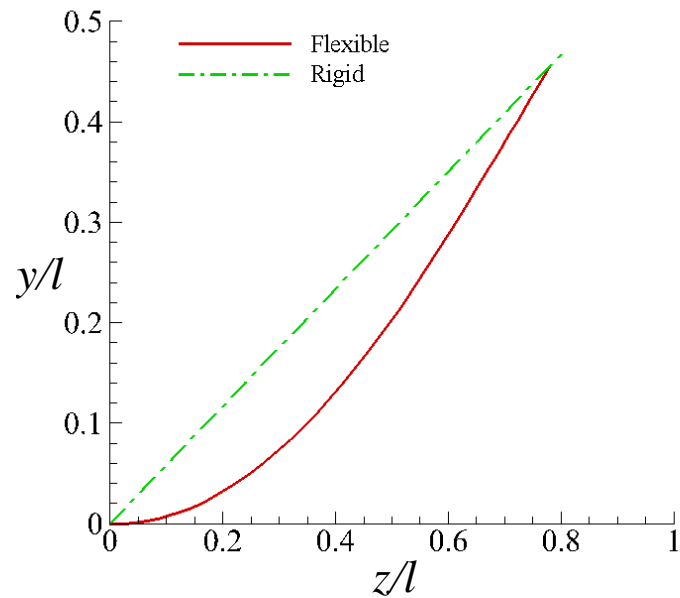
Figure 7-4 Schematic view of the deformations of the present flexible ray with actively controlled curvature and a rotational rigid ray.
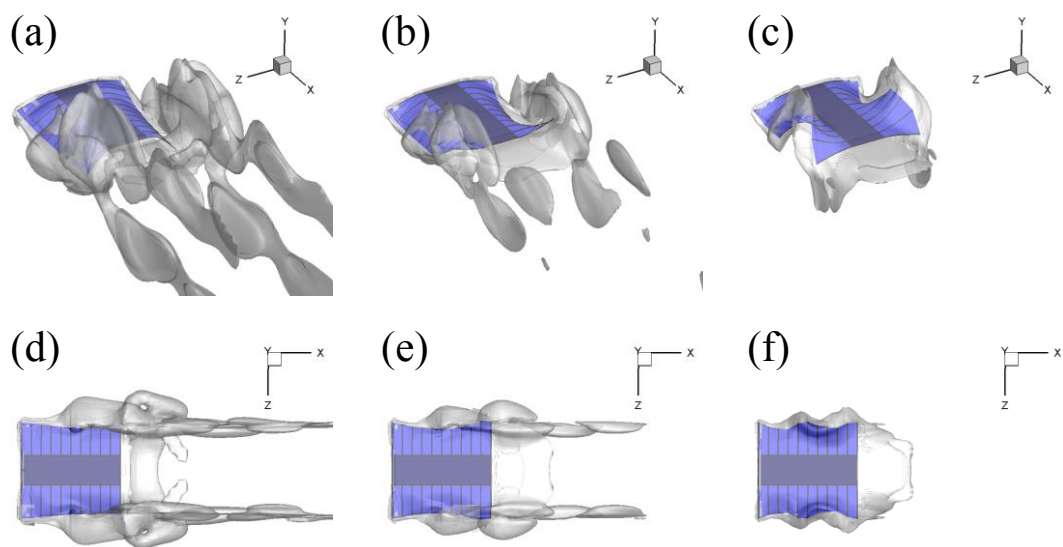
Figure 7-5 Different views of the flow wake behind the robot at t = 0. 3D view: (a), (b), (c), and top view: (d), (e), (f). (a), (d) $\varphi_d=90$; (b), (e) $\varphi_d=180$; (c), (f) $\varphi_d=360$. $f_r=1.2$. The wake is visualised using the iso-surface of the normalised vorticity magnitude ($\omega_{mag}= 2$).
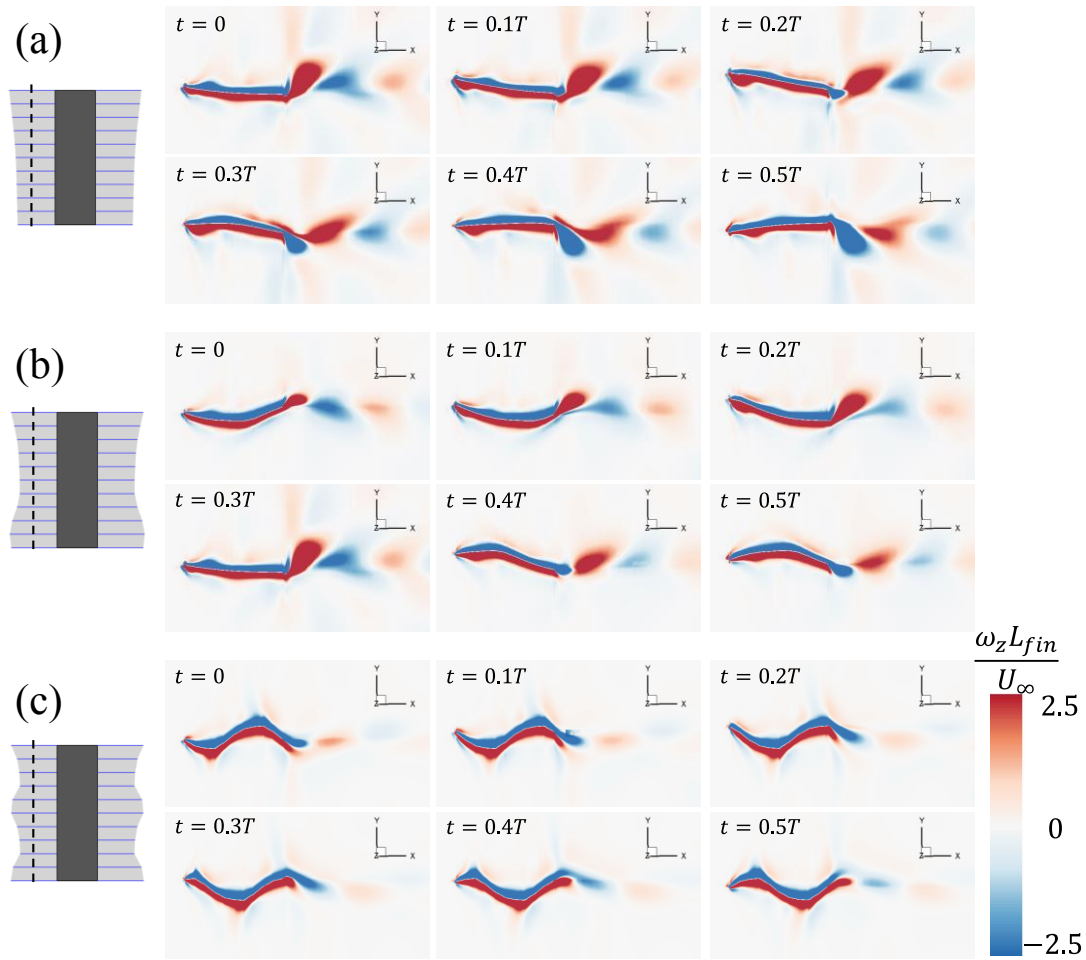
Figure 7-6 Flow vorticity of slice z = 0.6L$_{ray}$ of Fin-L within half motion period. f$_r$=1.2.

The iso-surfaces of the flow vorticity magnitude behind the bio-inspired robot are demonstrated in Figure 7-5. It is seen that the strongest wake is generated by the flapping motion at φ_d=90 degree while the undulating motion at φ_d=360 degree produces the weakest flow wake, which indicates the flapping motion will generate larger thrust force. The vortex shedding behind the pectoral fin can be more clearly observed in Figure 7-6. At φ_d=90 degree, stronger counter-clockwise and clockwise trailing edge vortices are generated and shed into the wake alternatively, whist the trailing edge vortices become weaker at φ_d=180 degree. When the phase difference value reaches 360 degree, where the pectoral fin forms a complete trailing wave (the wave length equals one fin length), no clear trailing edge vortex is observed, which also implies less thrust force will be created in this case, which will be discussed in later section. At φ_d=90 degree, obvious clockwise and counter-clockwise leading edge vortices are created and traveling along the fin surface while no apparent leading

edge vortex is generated at φ_d=360 degree. The leading edge vortex will create a low pressure region on one side of the fin, thus leads to larger pressure difference between the two sides of the pectoral fin. Figure 7-7 shows the pressure coefficient ($C_{pre} \equiv \frac{p-p_\infty}{0.5\rho U_\infty^2}$) distributions at both sides of the robot at φ_d=90 and 360 degrees. It is clearly seen that the flapping motion (φ_d=90) creates significantly larger pressure difference, which may contribute to the thrust generation if appropriately reoriented (see Figure 7-9 (a)). On the other hand, the larger pressure difference also requires more power input (see Figure 7-9 (b)).
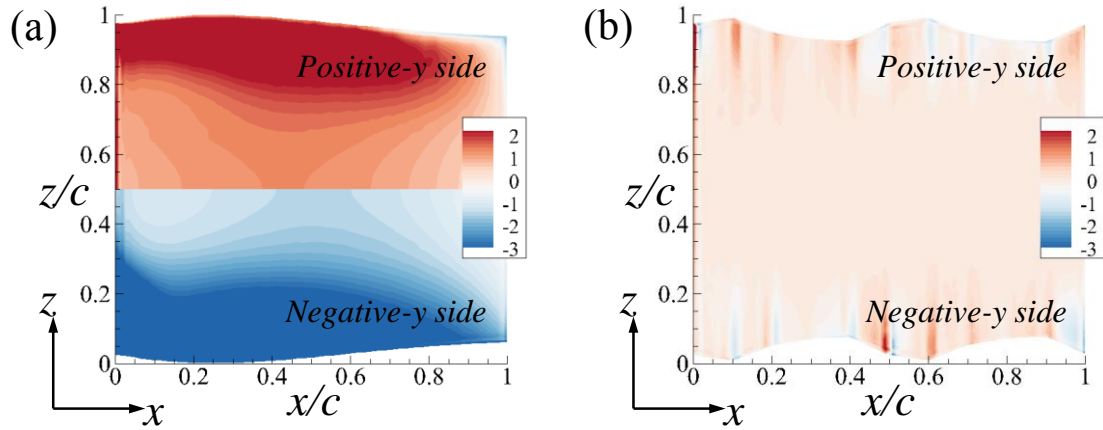
Figure 7-7 Pressure coefficients (C_{pre}) distributions at both sides of the robot for φ_d=90 (a) and 360 degrees (b) at t=0.2T, f_r=1.2.

7.2.2 *Force generation and propulsion efficiency of symmetric fin kinematics*

Time averaged thrust coefficient C_T, power expenditure coefficient C_P and propulsion efficiency η as functions of φ_d at different reduced frequencies are summarised in Figure 7-8. The three reduced frequencies are selected to be large enough to generate positive net thrust force, yet not too high to cause numerical instabilities. For all three motion frequencies considered here, the thrust force rises first and then decreases with the increase of the phase difference between the leading and trailing edge rays and the peak value is achieved at φ_d=90 degree, which corresponds to a wave length of $4L_{fin}$. The power expenditure coefficient descends monotonously as φ_d increases from 0 to 360 degree. The propulsion efficiency

undergoes a similar trend as the thrust, however, with the peak values accomplished at different φ_d for different reduced frequencies. Specifically, the highest propulsion efficiencies are reached at φ_d=90, 135 and 180 degrees for f_r = 0.8, 1.0 and 1.2 respectively. Previous experimental study of an undulating fin [21] found that the largest thrust force is produced when the wave length is half of the fin's length, which is different from the present study. This difference may be attributed to various reasons. First, the fin in the present study has an aspect ratio of 0.33 while the aspect ratio of the fin used in the experiment of Curet et al. [21] is around 0.1. Another probable reason is that in the experiment, they used a self-propelled device while the robot is fixed in space in the present study. Despite of the lowest thrust force produced by the undulating motion at φ_d=360 degree, it requires the least power input as well, which may be advantageous under certain circumstances.
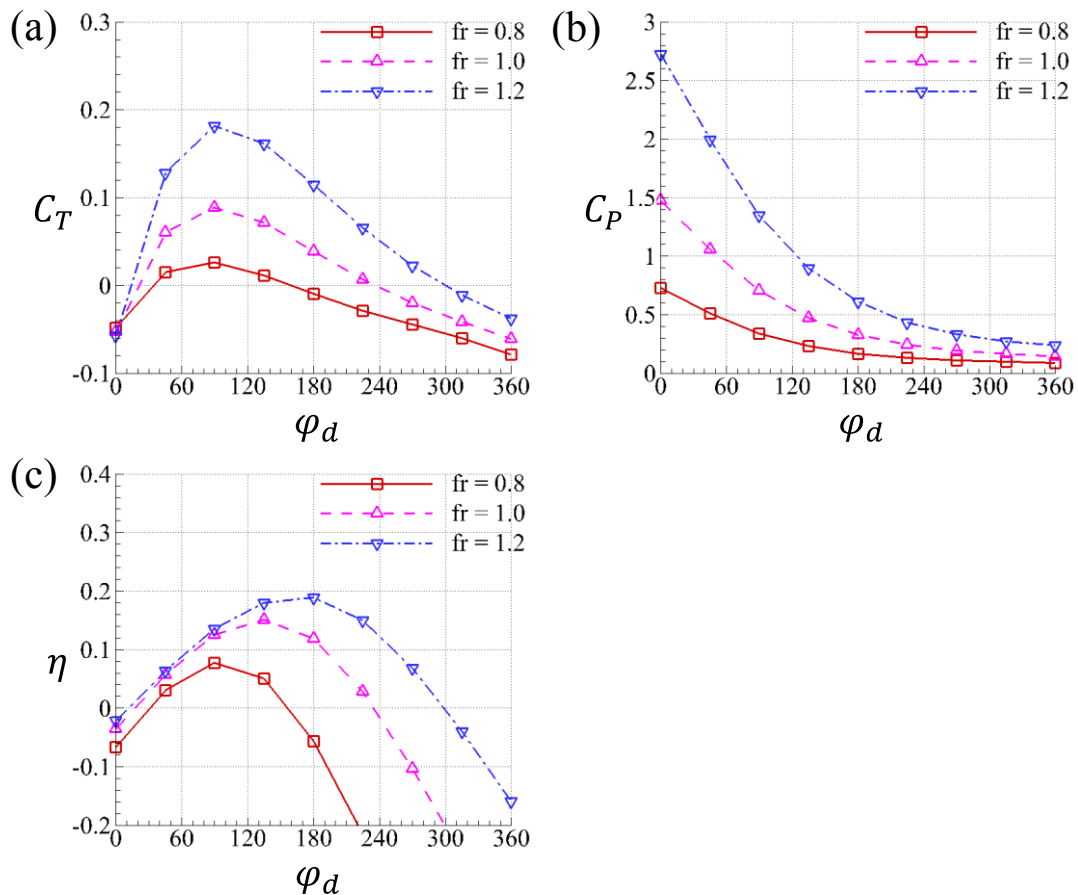
Figure 7-8 Time averaged thrust, power expenditure coefficients and propulsion efficiency as functions of the phase difference φ_d at different reduced frequencies.

(a)

(b)

(c)
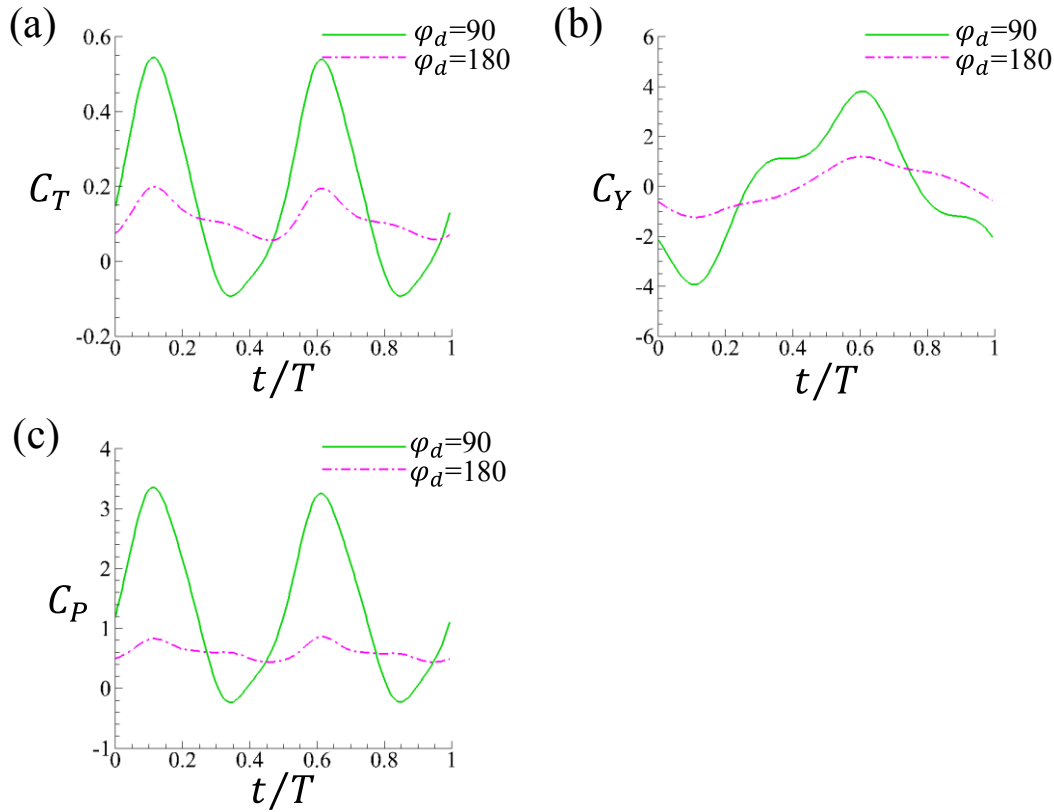
Figure 7-9 Instantaneous C_T, C_Y and C_P within one motion period at two different phase difference values. $f_r=1.2$.

The time histories of C_T, C_Y and C_P for $\varphi_d= 90$ and 180 degrees at $f_r = 1.2$ are demonstrated in Figure 7-9. One obvious effect of increasing φ_d from 90 degree to 180 degree is the reduction in the generation of thrust peaks. It is seen that two much higher thrust peaks are produced within one motion period at $\varphi_d=90$ degree compared with the case of $\varphi_d=360$ degree. Another effect is the significant reduction in the vertical force generation (force in *y*-direction), as shown in Figure 7-9 (b). This leads to a substantial decrease in power expenditure coefficient. The decreasing rate of the power expenditure is higher than that of the thrust force, leading to an increase in propulsion efficiency, as observed in Figure 7-8 (c).

7.2.3   *Effect of non-symmetric kinematics*

To examine the effects of non-symmetrical kinematics on the performance of this bio-inspired robot, two additional simulation cases are performed. In the first case (Case I), the phase difference value of Fin-R is 90 degree (φ_d=90) while for Fin-L,

the phase difference is 180 degree (φ_d=180). In the second case (Case II), the phase differences of both Fin-R and Fin-L are 90 degree, but the phase distribution of Fin-L is reversed while the phase distribution of Fin-R is the same as that of symmetric kinematics case. For both Case I and Case II, the reduced frequency is f_r = 1.2 and Reynolds number is R_e = 6000.
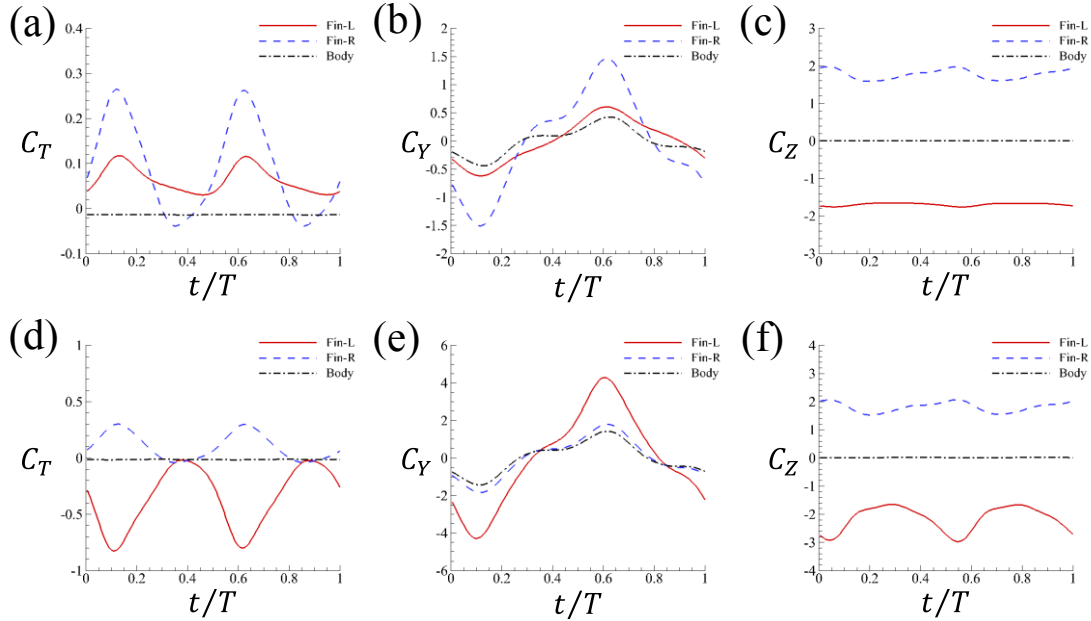
Figure 7-10 Instantaneous C_T, C_Y and C_Z within one motion period for Case I (a) (b) (c), and Case II (d) (e) (f).

Figure 7-10 demonstrates the time histories of C_T, C_Y and C_Z of Fin-L, Fin-R and body for Case I and II. It is seen that non-symmetrical kinematics leads to more complicated force generations on the pectoral fins. Specifically, the thrust forces generated by Fin-L and Fin-R are no longer symmetrical. This non-symmetry will create a moment in *y*-direction (see Figure 7-11), which may be useful during turning maneuvering. For symmetrical fin kinematics, the total force along *z*-axis is zero because the two fins generate forces of the same magnitude but in opposite directions. Due to the non-symmetrical kinematics, the forces in z-axis have different magnitudes, which lead to a net force in z-direction. Compared with Case I, Case II not only creates non-equal thrust forces, but also in opposite directions. In particular, Fin-R generates net thrust while Fin-L creates net drag with larger magnitude. This leads to

a larger rotational moment along *y*-direction, as shown in Figure 7-11, indicating faster turning maneuvering will be achieved compared with Case I.
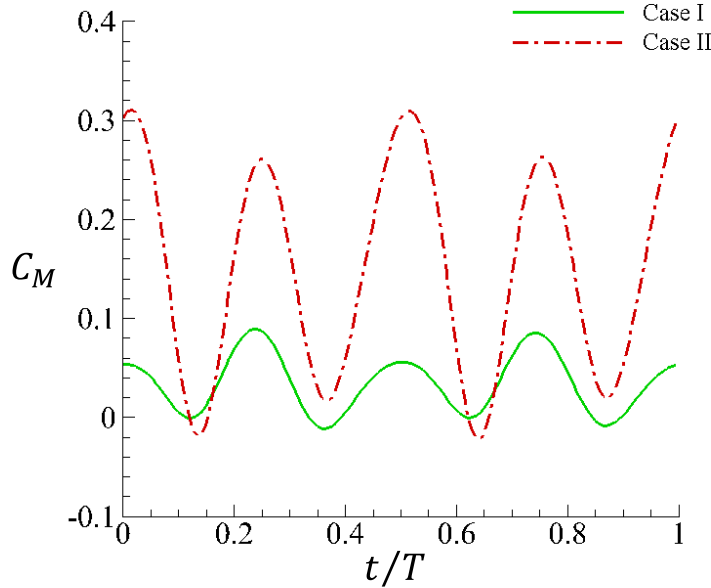
Figure 7-11 Time histroies of y-moment coefficients for Case I and Case II.

7.2.4   Effect of Reynolds number

Up to this point, our simulations are carried out at a fixed Reynolds number (R_e = 6000). The effect of Reynolds number on the performance of the underwater robot is examined by performing the simulations at two additional Reynolds numbers (R_e = 300, 1000). In order to avoid significant turbulence effects, two lower Reynolds numbers are chosen here. Similar numbers were also chosen by Bozkurttas et al. [101] to examine the Reynolds number effect on a pectoral fin of bluegill sunfish (R_e = 1440 and 540). The two pectoral fins have symmetrical kinematics and the reduced frequency f_r is fixed at 1.2. The time averaged values of thrust, power expenditure coefficients and propulsion efficiency as functions of φ_d are demonstrated in Figure 7-12. It is observed that for the Reynolds numbers considered here, both the thrust and propulsion efficiency have been seen significant enhancements as the increase of Reynolds number. It is also seen that the differences of the power expenditure

175

coefficients between various Reynolds numbers are marginal, especially when compared with those of thrust force.
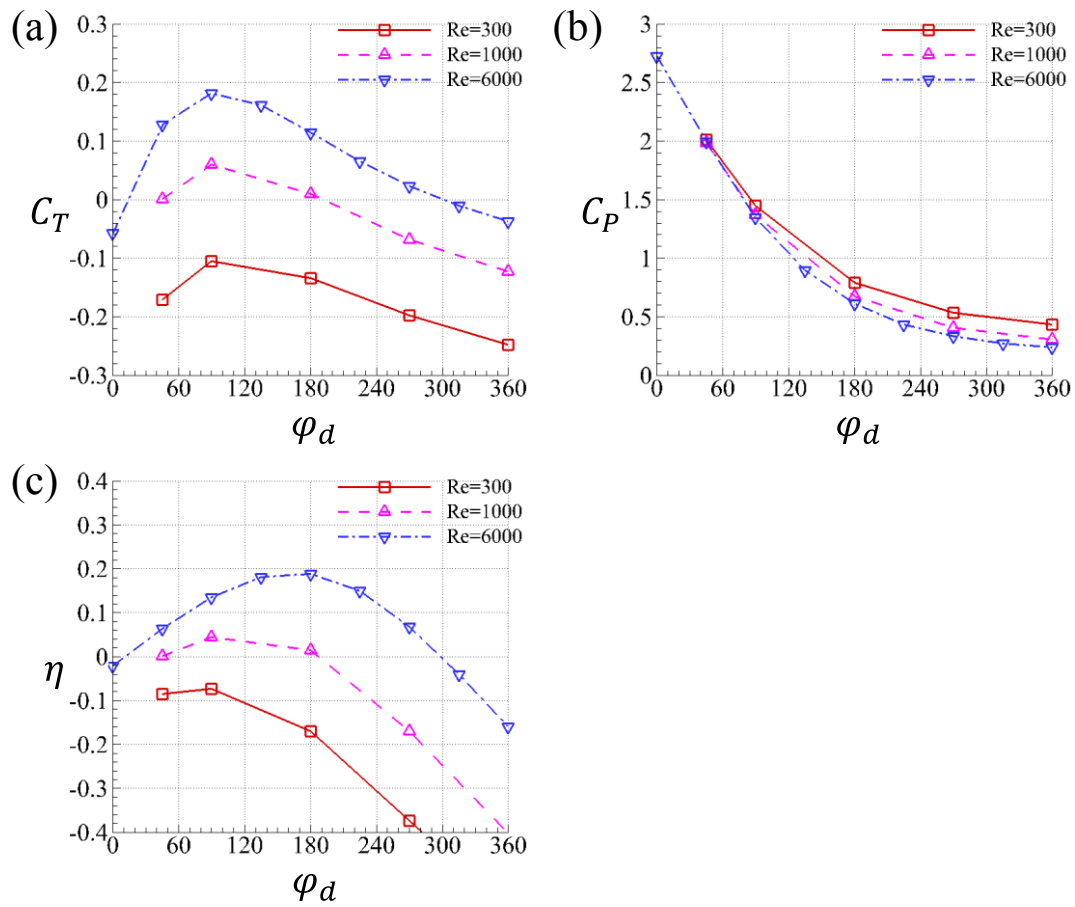
Figure 7-12 Time averaged thrust, power expenditure coefficients and propulsion efficiency as functions of the phase difference φ_d at different Reynolds numbers. $f_r=1.2$.
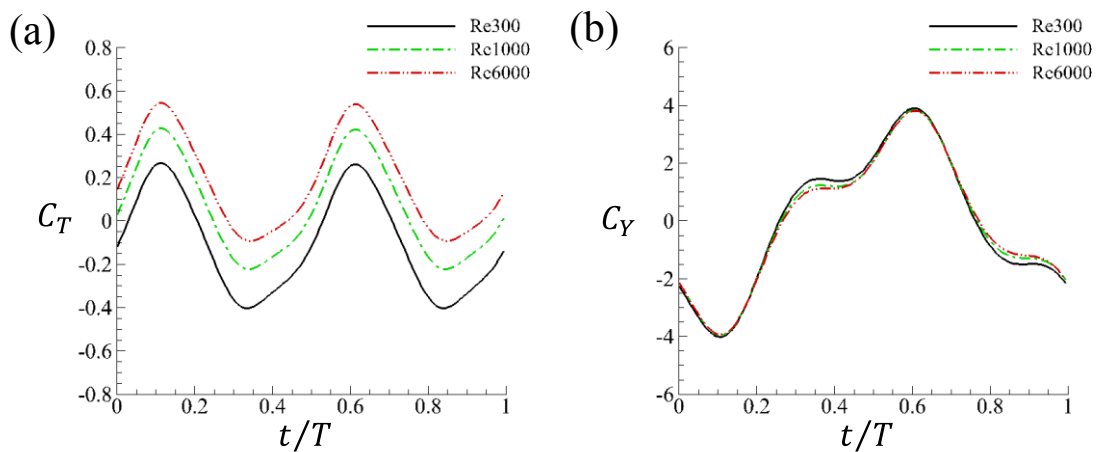
Figure 7-13 Instantaneous C_T and C_Y within one motion period at different Reynolds numbers. $f_r=1.2$ and $\varphi_d=90$ degree.

The time histories of C_T and C_Y within one motion period at different Reynolds numbers are shown in Figure 7-13. All cases at different Reynolds numbers produce both thrust and drag within one motion period. The drag accounts for higher percentage than the thrust at low Reynolds number ($R_e = 300$) while larger thrust force is produced at higher Reynolds number ($R_e = 6000$). However, since no turbulence model is used in the present simulation, the present results may have limited accuracy in the prediction of flow separation, especially at $R_e = 6000$, which is believed to be in turbulent regime. Therefore, it should be acknowledged that the present data may only give some indications of the general trends while a more accurate study using high-fidelity turbulence models is needed in the future.
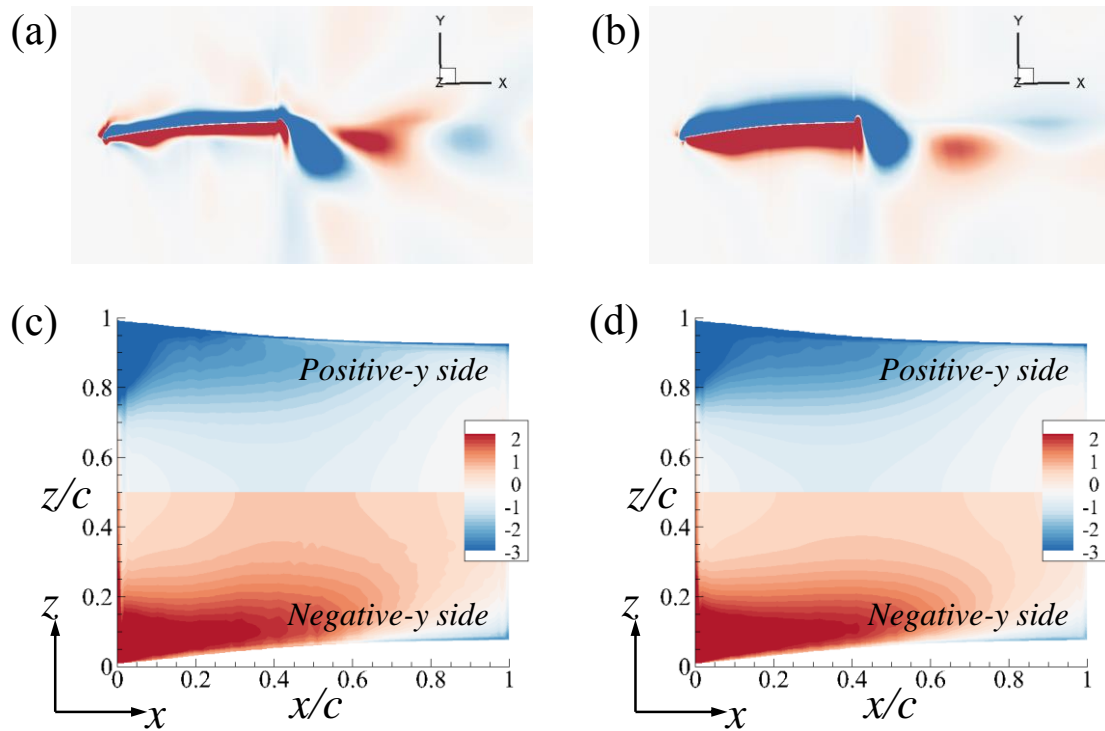
Figure 7-14 Flow vorticity of slice $z = 0.6L_{ray}$ of Fin-L (a) (b), and pressure coefficient distributions at both sides of the robot at t=0.5T (c) (d). (a) (c) R_e=6000, and (b) (d) R_e=300. f_r=1.2 and φ_d=90 degree.

Flow vorticity of slice $z = 0.6L_{ray}$ of Fin-L at $t = 0.5T$ for different Reynolds numbers are shown in Figure 7-14 (a) and (b). It is observed that stronger trailing edge vortex is generated in the higher Reynolds number case, while the lower Reynolds number case has significantly thicker shear layer, which may be attributed to the more

dominated effect of the viscosity. The pressure distributions at both sides of the robot at $t = 0.5T$ are demonstrated in Figure 7-14 (c) and (d), from which we can see that only subtle differences can be observed, which may explain why the power expenditures for the two cases are very similar to each other (see Figure 7-13 (b)). This also indicates that the larger shear stress in the lower Reynolds number case may be the primary reason for the increase of the drag force (see Figure 7-13 (a)).

7.3 Concluding remarks

In the present chapter, we numerically examined the propulsion performance of a biomimetic robot with two sided pectoral fins, which were supported by flexible rays with actively controlled curvatures. The fin rays were activated individually by time-varying distributed forces along each ray, which imitated the pulling effect from the tendons attached at the basal end of each ray. By controlling the phase difference (φ_d) between the leading edge and trailing edge rays, the pectoral fins could achieve a flapping motion (smaller phase difference) as well as an undulating motion (larger phase difference). The present results demonstrated that for all three motion frequencies considered in this work, the largest thrust was generated when φ_d=90 degree (corresponding to a wave length of $4L_{fin}$), where the pectoral fins were undergoing flapping motions. The maximum propulsion efficiency, on the contrary, was accomplished at different φ_d values for various motion frequencies. Specifically, the peaks of propulsion efficiency were achieved at smaller φ_d values for lower frequencies. Additionally, undulating motion created significantly smaller pressure differences between the upper and lower sides of the fin, thereby leading to a significant decrease in power expenditure. With non-symmetrical kinematics, the force generation on the pectoral fin became more complicated. Non-equal thrust forces were created by the left and right fins, which creates a non-zero moment along y-direction. The non-symmetrical kinematics also led to a non-zero lateral force in z-direction, which, together with the y-moment, may contribute to the turning maneuvering of the robot.

It is acknowledged that the Reynolds number used in the present study (6000) is in the turbulence regime. Thus, the laminar flow model used here may not accurately predict the flow separation and capture the true shedding vortices. Therefore, the numerical results in this chapter only provide some general indications of the flow behaviour. Further investigations using high-fidelity turbulent flow solvers are needed in future research.

Generally, the motion of the ray-supported fin can be categorised into flapping mode and undulating mode, according to the wave number existing along the fin. The present study suggests that the largest thrust force is produced by flapping mode (corresponding wave number is 0.25). However, this may not be a general conclusion for all different morphologies. An experimental study of Curet et al. [21] using a robotic knifefish found that the highest thrust was achieved at a wave number of two. As discussed in section 4.2, the difference may be caused by the aspect ratio of the fin. In the present work ,the aspect ratio of the fin is 0.33 while the aspect ratio of Curet et al. [21] is 0.1. Therefore, we anticipate that for ray-strengthened fins with larger aspect ratios, flapping mode may produce better propulsion performance, but for fins with smaller aspect ratios, better performance may be achieved by undulating mode. Besides, undulating mode may require more rays for actuation, e.g., the anal fin of the weakly electric ghost knifefish (*Apteronotus albifrons*) is composed of approximately 150 individual rays [65], which enables the existence of multiple traveling waves along its fin. The present study also suggests that undulating mode needs much less power expenditure than flapping motion, which may be a significant advantage of undulating mode.

Another important feature of fish fin is the ability of actively controlling the curvature and bending stiffness of the rays [28–30,65]. The actively controlled ray is able to curve into the flow, i.e., the bending direction of the ray is the same as its moving direction.

This is significantly different with the rigid and passively deformed rays. The rigid ray does not change its curvature while the passively deformed ray bends in the direction opposite to the moving direction. Such a curvature change is supposed to have significant impact on the fins' performance. Tangorra et al. [87] designed and tested a biomimetic pectoral fin with a novel actuation mechanism inspired by bluegill sunfish. However, the effects of active control over the curvature as well as the bending stiffness are not fully studied and understood, which requires more work in the future research.

Chapter 8   Conclusions and Recommendations

In this chapter, the conclusions drawn from the studies of the present thesis are given in subsection 8.1 and the recommendations for future work are suggested in subsection 8.2.

8.1 Conclusions

Inspired by previous experimental and numerical studies on ray-finned fish that these species possess fins with unique features (anisotropic bending stiffness, individual actuation of fin rays and ability of active curvature control over the rays), we propose four objectives in subsection 1.3 in order to investigate the effects of these characteristics on the performance and hydrodynamics of some bio-inspired propulsive systems within the scope of the present thesis (subsection 1.2.2). All the objectives are fulfilled and the main outcomes and contributions from these studies are summarised as follows:

8.1.1   *An overset grid based method for rigid and flexible fluid-structure interaction modelling (Chapter 3 & Chapter 4)*

The first objective of this thesis was developing a fluid-structure interaction solver that can be applied to investigate a range of scientific problems, including the biomimetic problems we are particularly interested here. Based on the in-house CFD solver of our research group, several new modules (including a nonlinear beam model, an overset grid assembler and a fluid-structure coupling procedure) were successfully integrated into our in-house code. The main conclusions from this work are:

(1) A FSI solver was successfully developed by coupling a finite-volume flow solver based on an overset, multi-block, structured grid system and a nonlinear Euler-Bernoulli beam model.

(2) The flow solver, structural solver and the coupled FSI solver were validated separately against available benchmarks in literature and the results showed that the present code is of adequate accuracy and reliability.

(3) The established FSI solver is able to deal with a series of fluid-structure coupling problems, in particular, the skeleton-reinforced bio-membrane problems (e.g., fish fins and insect wings).

As noted in Chapter 3, no turbulence model was included in the current flow solver. Considering most flows of real biological systems are fully turbulent, the results of the present laminar flow model may be different from the turbulent ones. However, according to Chang et al. [47], where the hydrodynamics of a tuna-like swimmer was numerically investigated, the difference between the laminar and the turbulent (SA and SST models) simulations was marginal at R_e = 7,100. At higher Reynolds numbers (Re = 71,000 and 710,000), the inclusion of turbulent models led to a slight increase of thrust force whereas the power consumptions were almost identical. As the highest Reynolds number studied in the present thesis was 6,000, the deviation due to the laminar flow assumption is believed to be small. Another factor that can possibly have significant effects on the accuracy of the present compressible flow solver is the lack of low-speed preconditioning (LSP). The LSP may have considerable impact on the flow separation of wind turbines at high Reynolds numbers [157], however, its influence on the force generation is small according to the validation cases in Chapter 4 and the previous publications of the research group [145,147,159,160,197].

8.1.2   *Effects of spanwise deformations on the performance of a ray-strengthened caudal fin (Chapter 5)*

The second objective of the present thesis was investigating the effects of different spanwise deformations on the propulsion performance of a 3D ray-supported caudal fin. Four deformation patterns were considered in this study, which were

accomplished via four different stiffness distributions (uniform, cupping, W-shape and heterocercal) among the rays. The main outcomes from this study can be summarised as:

(1) Compared with rigid caudal fin, the flexible caudal fin had an enhanced propulsion performance over a wide range of ray stiffness. Besides, there was an optimal flexibility maximising the thrust and propulsion efficiency.

(2) Both the uniform and the cupping stiffness distributions produced 'cupping' deformation. However, the deformation of the fin with cupping stiffness distribution seemed to be 'over-cupped', leading to a degraded propulsion performance compared with the uniform stiffness case.

(3) Among all the four stiffness distributions, the uniform stiffness distribution produced the best propulsion performance in terms of thrust generation and efficiency. The heterocercal stiffness distribution created a vertical force which can be used for stabilising and maneuvering.

(4) By appropriately cupping the fins, fish are able to save energy and generate larger thrust and propulsion efficiency.

8.1.3   *Performance of an actively and passively controlled caudal fin (Chapter 6)*

Our third objective was studying the effect of active curvature control of the rays on the performance of a simplified skeleton-strengthened caudal fin. This research was inspired by an important feature of fish fin that the curvatures of the rays are actively controlled. In the present model, the curvatures of the rays were actively changed by distributed external loads which imitated the pulling effects of tendons at the basal ends of the rays. The main conclusions drawn from this study are:

(1) The performance of the caudal fin was controlled by three main factors, namely, the phase between the leading edge sway motion and the external force (φ_{mean}), the phase difference between the dorsal edge and ventral edge (φ_{iff}), the phase distribution among the rays. By carefully combining these parameters, various

deformation patterns (the *C*-mode, the *W*-mode, the *H*-mode and the *S*-mode) observed in experiments had been reproduced.

(2) The propulsion performance of all the cases with active curvature control were significantly improved when φ_{mean} is less than 90 degree. The thrust and propulsion efficiency could be improved by up to 43% and 35% respectively.

(3) The *C*-mode produced the best performance in terms of thrust generation and propulsion performance, which was attributed to larger deflections of rays in the central part of the fin and the resulting larger, stronger and further downstream high pressure region.

(4) The *H*-mode and *S*-mode both created considerable vertical forces. Compared with the *H*-mode, the *S*-mode could produce smaller thrust and larger vertical force when the swaying motion was reduced to zero. This, together with the reduction in lateral force, makes *S*-mode ideal for braking maneuvering.

(5) The present model captured several key features of real caudal fin, whereas some details were not considered. For example, the present caudal fin model was simplified as a rectangular shape and the bi-laminar design of real fin rays was not explicitly modelled. Besides, the complicated internal structures, musculature and nerve systems were not considered either. However, the conclusions from this study can provide useful inspirations and guidelines for the design of robotic fish.

8.1.4 *Performance of a bio-inspired underwater robot with skeleton-reinforced undulating pectoral fins (Chapter 7)*

The final objective of the present thesis was investigating the propulsion performance of a bio-inspired underwater robot with two sided undulating pectoral fins. The fins were supported by several flexible rays with actively controlled curvatures and independent actuations. The robot was fixed in space with a uniform incoming flow. The key findings from this study can be concluded as follows:

(1) By controlling the phase difference (φ_d) between the leading edge ray and trailing edge ray, both flapping motion (smaller φ_d) and undulating motion (larger φ_d) could be achieved by the pectoral fins. Higher thrust and efficiency were accomplished by flapping motion while the undulating motion required much less energy expenditure.

(2) With non-symmetric kinematics, non-equal thrust forces were generated on the pectoral fins, which created a non-zero moment along vertical axis. This also generated a non-zero force along lateral direction, which, together with the non-zero moment, may contribute to the turning maneuvering of the robot.

(3) With an incoming flow, the in-place rotation of the robot could not be accomplished by simply reversing the direction of the travelling wave along one of the pectoral fins. It may require more complicated control strategies to achieve this.

(4) The propulsion performance of an underwater robot with undulating fins may also be significantly influenced by the aspect ratio of the fin. It is anticipated that with a larger aspect ratio, the flapping motion creates higher thrust whereas for smaller aspect ratio, the undulating motion may produce better performance.

8.1.5   *Efficiencies of various biomimetic propulsive systems*

Table 8-1 summarises the maximum propulsion efficiencies of biomimetic systems reported in previous publications. It is seen that for most biomimetic systems listed here (including the two studied in this thesis), the highest propulsive efficiency falls between 0.2 and 0.4. Bozkurttas et al [101] reported an efficiency as high as 60% for a highly flexible pectoral fin. The fin's conformation was reconstructed from experimental measurement, indicating that the real biological systems can achieve much higher efficiency by more complicated kinematics control. Therefore, more research effort should be made to understand the mechanism in order to design more efficient biomimetic propulsion devices.

Table 8-1 Summary of the propulsive efficiency of various biomimetic systems

Fin Type	Approach	Reynolds Number	Strouhal Number	Maximum Efficiency
Flexible caudal fin (present)	Numerical	1,000	0.4	0.21
Flexible Pitching Panel [100]	Numerical	640	0.58	0.21
Flexible caudal fin [213]	Numerical	2,500	0.47	0.23
Flexible caudal fin [25]	Numerical	Inviscid flow	0.3	0.22
Rigid flapping foil [214]	Numerical	200	0.46	0.26
Flexible pectoral fin [101]	Numerical	6,300	0.54	0.60
Flexible pectoral fin [52]	Numerical	Inviscid flow	0.31	0.32
Flexible pectoral fin [27]	Numerical	400	0.45	0.36
Flexible pitching panel [215]	Experimental	7,200	0.3	0.37
Flexible heaving panel [85]	Experimental	21,000–115,000	-	0.45
Flexible tuna-like foil [216]	Experimental	27,750	-	0.21
Undulating pectoral fin (present)	Numerical	6,000	-	0.18
Undulating pectoral fin [217]	Numerical	10,000	-	0.21
Undulating anal fin [92]	Experimental	-	-	0.17

8.1.6 *Practical guidelines for the design of fin-inspired underwater propellers*

The conclusions from the present thesis also provide some general guidelines for the practical design of bio-inspired underwater propellers.

(1) Ray-supported membrane architecture. Such a structure allows rays to have different material properties, making non-uniform stiffness distribution over the propeller relatively easier for manufacturing. The flexibility distribution may be optimised to enhance the propeller's performance.

(2) Individual ray activation. The separate actuation of each ray enables the propeller to achieve various conformations (e.g., *C*-mode, *S*-mode and *H*-mode) according to different needs, which gives the propeller more DOFs for control.

(3) Active curvature control. Our study reveals that active curvature control over the fin rays can further increase the thrust production. Novel mechanical designs of fin rays able to actively change the bending curvature may be needed in the future.

8.2 Recommendations for future research

The present thesis is concentrated on numerically investigating the effects of several key features of ray-finned fish on the propulsion performance of simplified bio-inspired propulsive systems. However, these systems are very complicated and involve multiple disciplines. Due to the limited research time and computing resources, the present studies inevitably have some limitations and cannot cover all those details involved in the biological locomotion systems. In the field of numerical modelling of bio-inspired locomotion, there are still many interesting topics worth further investigation. The suggestions based on available studies for the future research are outlined as follows:

(1) In the present FSI tool, the structural dynamics is resolved by a nonlinear beam model, which can only represent simple geometries. To study the dynamics of more realistic biomimetic problems, more sophisticated structural models should be used. Some open source codes such as Calculix (http://www.calculix.de/), deal.II (https://www.dealii.org/) and FEniCS (https://fenicsproject.org/) may be good options.

(2) Most biomimetic problems involve large structural deformations, which pose a great challenge for CFD mesh manipulation. Overset grid methods may enhance the capability of flow solvers dealing with complex geometries and/or multiple bodies with relative motion, but it has limited use when handling large local mesh deformation. Two approaches may be utilised to solve this problem: 1) overset grid plus local re-meshing; 2) immersed boundary method with adaptive grid.

(3) In nature, most aquatic animals swim at moderately high Reynolds numbers, where turbulence may play an important role. However, most numerical simulations on biomimetic locomotion systems use laminar flow models by

reducing the Reynolds number to an acceptable regime. This is not only because of the complexity for high-fidelity turbulence modelling itself, but also because of the large amount of computational time required. The development of advanced reduced order models for complicated turbulence flows may provide a solution for this kind of problem.

(4) The bio-inspired propulsion is a multi-disciplinary subject. It not only involves strong fluid-structure interaction, but also needs multi-body dynamics in order to achieve self-propelled motion. However, the coupling of multi-physics is very challenging in terms of convergence and numerical stability. The recently released open source multi-physics coupling tool named preCICE (https://www.precice.org/), which adopts the most advanced coupling algorithms, may be very helpful for developing more powerful biomimetic simulation tools.

(5) The CFD (including multi-physics coupling) can also be integrated with advanced control strategies, which will greatly enhance the capability and applicability of numerical tools in the area of biomimetics.

References

[1]   Yuh, J. "Design and Control of Autonomous Underwater Robots: A Survey."
Autonomous Robots, Vol. 8, No. 1, 2000, pp. 7–24.
doi:10.1023/A:1008984701078.

[2]   Raj, A., and Thakur, A. "Fish-Inspired Robots: Design, Sensing, Actuation, and
Autonomy—a Review of Research." *Bioinspiration and Biomimetics*, Vol. 11,
No. 3, 2016, p. 031001.

[3]   Scaradozzi, D., Palmieri, G., Costa, D., and Pinelli, A. "BCF Swimming
Locomotion for Autonomous Underwater Robots: A Review and a Novel
Solution to Improve Control and Efficiency." *Ocean Engineering*, Vol. 130, No.
March 2016, 2017, pp. 437–453. doi:10.1016/j.oceaneng.2016.11.055.

[4]   Salazar, R., Fuentes, V., and Abdelkefi, A. "Classification of Biological and
Bioinspired Aquatic Systems: A Review." *Ocean Engineering*, Vol. 148, 2018,
pp. 75–114. doi:10.1016/j.oceaneng.2017.11.012.

[5]   Najem, J., Sarles, S. A., Akle, B., and Leo, D. J. "Biomimetic Jellyfish-Inspired
Underwater Vehicle Actuated by Ionic Polymer Metal Composite Actuators."
Smart Materials and Structures, Vol. 21, No. 9, 2012.
doi:10.1088/0964-1726/21/9/094026.

[6]   Sfakiotakis, M., Lane, D. M., and Davies, J. B. C. "Review of Fish Swimming
Modes for Aquatic Locomotion." *IEEE Journal of Oceanic Engineering*, Vol.
24, No. 2, 1999, pp. 237–252.

[7]   Korsmeyer, K. E., Steffensen, J. F., and Herskin, J. "Energetics of Median and
Paired Fin Swimming, Body and Caudal Fin Swimming, and Gait Transition in
Parrotfish (Scarus Schlegeli) and Triggerfish (Rhinecanthus Aculeatus)."
Journal of Experimental Biology, Vol. 205, No. 9, 2002, pp. 1253 LP – 1263.

[8]   Bluespotted Ribbontail Ray.
https://commons.wikimedia.org/wiki/File:Bluespotted_Ribbontail_Ray,_Taeni

ura_lymma_at_Sataya_Reef,_Red_Sea,_Egypt_-SCUBA_(6395392561).jpg. Accessed Mar. 26, 2020.

[9] Black Ghost Kinfefish. https://www.indiamart.com/proddetail/black-ghost-knife-fish-11001818812.ht ml. Accessed Mar. 26, 2020.

[10] Australian Box Jellyfish. https://www.worldatlas.com/articles/australian-box-jellyfish-animals-of-oceani a.html. Accessed Mar. 26, 2020.

[11] Juvenile Octopus. https://www.discoveranimals.co.uk/news/visit-pumpkin-baby-octopus-brighton -sealife/. Accessed Mar. 26, 2020.

[12] Spotted Porcupinefish. https://oceana.org/marine-life/ocean-fishes/spotted-porcupinefish. Accessed Mar. 26, 2020.

[13] Common Cuttlefish. https://images.app.goo.gl/vshn8QabeQuibdDA8. Accessed Mar. 26, 2020.

[14] Tolkoff, S. W. *Robotics and Power Measurments of the RoboTuna*. Master of Science Dissertation. Massachusetts Institute of Technology, 1999.

[15] Techet, A. H., Hover, F. S., and Triantafyllou, M. S. "Separation and Turbulence Control in Biomimetic Flows." *Flow, Turbulence and Combustion*, Vol. 71, No. 1–4, 2003, pp. 105–118. doi:10.1023/B:APPL.0000014923.28324.87.

[16] Crespi, A., Badertscher, A., Guignard, A., and Ijspeert, A. J. "AmphiBot I: An Amphibious Snake-like Robot." *Robotics and Autonomous Systems*, Vol. 50, No. 4, 2005, pp. 163–175. doi:10.1016/j.robot.2004.09.015.

[17] Crespi, A., Karakasiliotis, K., Guignard, A., and Ijspeert, A. J. "Salamandra Robotica II: An Amphibious Robot to Study Salamander-like Swimming and Walking Gaits." *IEEE Transactions on Robotics*, Vol. 29, No. 2, 2013, pp. 308–320. doi:10.1109/TRO.2012.2234311.

[18] Hu, H., Liu, J., Dukes, I., and Francis, G. "Design of 3D Swim Patterns for Autonomous Robotic Fish." *IEEE International Conference on Intelligent Robots and Systems*, 2006, pp. 2406–2411. doi:10.1109/IROS.2006.281680.

[19] Zhou, C., and Low, K. H. "Design and Locomotion Control of a Biomimetic Underwater Vehicle with Fin Propulsion." *IEEE/ASME Transactions on Mechatronics*, Vol. 17, No. 1, 2012, pp. 25–35. doi:10.1109/TMECH.2011.2175004.

[20] Low, K. H., Zhou, C., Seet, G., Bi, S., and Cai, Y. "Improvement and Testing of a Robotic Manta Ray (RoMan-III)." *2011 IEEE International Conference on Robotics and Biomimetics, ROBIO 2011*, 2011, pp. 1730–1735. doi:10.1109/ROBIO.2011.6181539.

[21] Curet, O. M., Patankar, N. A., Lauder, G. V., and MacIver, M. A. "Mechanical Properties of a Bio-Inspired Robotic Knifefish with an Undulatory Propulsor." *Bioinspiration and Biomimetics*, Vol. 6, No. 2, 2011, p. 026004. doi:10.1088/1748-3182/6/2/026004.

[22] Villanueva, A., Smith, C., and Priya, S. "A Biomimetic Robotic Jellyfish (Robojelly) Actuated by Shape Memory Alloy Composite Actuators." *Bioinspiration and Biomimetics*, Vol. 6, No. 3, 2011, p. 036004. doi:10.1088/1748-3182/6/3/036004.

[23] Sfakiotakis, M., Kazakidi, A., and Tsakiris, D. P. "Octopus-Inspired Multi-Arm Robotic Swimming." *Bioinspiration and Biomimetics*, Vol. 10, No. 3, 2015, p. 035005. doi:10.1088/1748-3190/10/3/035005.

[24] Lauder, G. V, and Drucker, E. G. "Morphology and Experimental Hydrodynamics of Fish Fin Control Surfaces." *IEEE Journal of Oceanic Engineering*, Vol. 29, No. 3, 2004, pp. 556–571. doi:10.1109/JOE.2004.833219.

[25] Zhu, Q., and Shoele, K. "Propulsion Performance of a Skeleton-Strengthened Fin." *The Journal of experimental biology*, Vol. 211, 2008, pp. 2087–2100. doi:10.1242/jeb.016279.

[26]   Shoele, K., and Zhu, Q. "Fluid-Structure Interactions of Skeleton-Reinforced Fins: Performance Analysis of a Paired Fin in Lift-Based Propulsion." *The Journal of experimental biology*, Vol. 212, 2009, pp. 2679–2690. doi:10.1242/jeb.030023.

[27]   Shoele, K., and Zhu, Q. "Leading Edge Strengthening and the Propulsion Performance of Flexible Ray Fins." *Journal of Fluid Mechanics*, Vol. 693, 2012, pp. 402–432. doi:10.1017/jfm.2011.538.

[28]   Alben, S., Madden, P. G., and Lauder, G. V. "The Mechanics of Active Fin-Shape Control in Ray-Finned Fishes." *Journal of the Royal Society, Interface / the Royal Society*, Vol. 4, No. 13, 2007, pp. 243–56. doi:10.1098/rsif.2006.0181.

[29]   Lauder, G. V., and Madden, P. G. A. "Fish Locomotion: Kinematics and Hydrodynamics of Flexible Foil-like Fins." *Experiments in Fluids*, Vol. 43, No. 5, 2007, pp. 641–653. doi:10.1007/s00348-007-0357-4.

[30]   Lauder, G. V., Madden, P. G. A., Tangorra, J. L., Anderson, E., and Baker, T. V. "Bioinspiration from Fish for Smart Material Design and Function." *Smart Materials and Structures*, Vol. 20, No. 9, 2011. doi:10.1088/0964-1726/20/9/094014.

[31]   Lauder, G. V. "Function of the Caudal Fin during Locomotion in Fishes: Kinematics, Flow Visualization, and Evolutionary Patterns." *Integrative and Comparative Biology*, Vol. 40, No. 1, 2000, pp. 101–122.

[32]   Tytell, E. D. "Median Fin Function in Bluegill Sunfish Lepomis Macrochirus: Streamwise Vortex Structure during Steady Swimming." *J. Exp. Biol.*, Vol. 209, 2006, pp. 1516–1534. doi:https://doi.org/10.1242/jeb.02154.

[33]   Tytell, E. D., Standen, E. M., and Lauder, G. V. "Escaping Flatland: Three-Dimensional Kinematics and Hydrodynamics of Median Fins in Fishes." *Journal of Experimental Biology*, Vol. 211, No. 2, 2008, pp. 187–195. doi:10.1242/jeb.008128.

[34]   Flammang, B. E., and Lauder, G. V. "Speed-Dependent Intrinsic Caudal Fin Muscle Recruitment during Steady Swimming in Bluegill Sunfish, Lepomis

Macrochirus." *The Journal of experimental biology*, Vol. 211, No. 4, 2008, p. 587. doi:10.1242/jeb.012096.

[35]   Flammang, B. E., and Lauder, G. V. "Caudal Fin Shape Modulation and Control during Acceleration, Braking and Backing Maneuvers in Bluegill Sunfish, Lepomis Macrochirus." *The Journal of experimental biology*, Vol. 212, No. 2, 2009, p. 277. doi:10.1242/jeb.021360.

[36]   Park, Y. J., Jeong, U., Lee, J., Kwon, S. R., Kim, H. Y., and Cho, K. J. "Kinematic Condition for Maximizing the Thrust of a Robotic Fish Using a Compliant Caudal Fin." *IEEE Transactions on Robotics*, Vol. 28, No. 6, 2012, pp. 1216–1227. doi:10.1109/TRO.2012.2205490.

[37]   Feilich, K. L., and Lauder, G. V. "Passive Mechanical Models of Fish Caudal Fins: Effects of Shape and Stiffness on Self-Propulsion." *Bioinspiration and Biomimetics*, Vol. 10, No. 3, 2015, p. 36002. doi:10.1088/1748-3190/10/3/036002.

[38]   Esposito, C. J., Tangorra, J. L., Flammang, B. E., and Lauder, G. V. "A Robotic Fish Caudal Fin: Effects of Stiffness and Motor Program on Locomotor Performance." *Journal of Experimental Biology*, Vol. 215, No. 1, 2012, pp. 56–67. doi:10.1242/jeb.062711.

[39]   Ren, Z., Yang, X., Wang, T., and Wen, L. "Hydrodynamics of a Robotic Fish Tail: Effects of the Caudal Peduncle, Fin Ray Motions and the Flow Speed." *Bioinspiration and Biomimetics*, Vol. 11, No. 1, 2016, p. 016008. doi:10.1088/1748-3190/11/1/016008.

[40]   Lauder, G. V. "Fish Locomotion: Recent Advances and New Directions." *Annual Review of Marine Science*, Vol. 7, No. 1, 2015, pp. 521–545. doi:10.1146/annurev-marine-010814-015614.

[41]   Mittal, R. "Computational Modeling in Biohydrodynamics: Trends, Challenges, and Recent Advances." *IEEE Journal of Oceanic Engineering*, Vol. 29, No. 3, 2004, pp. 595–604. doi:10.1109/JOE.2004.833215.

[42] Mittal, R., Dong, H., Bozkurttas, M., Lauder, G. V., and Madden, P. "Locomotion with Flexible Propulsors: II. Computational Modeling of Pectoral Fin Swimming in Sunfish." *Bioinspiration and Biomimetics*, Vol. 1, No. 4, 2006, p. S35. doi:10.1088/1748-3182/1/4/S05.

[43] Dong, H., Bozkurttas, M., Mittal, R., Madden, P., and Lauder, G. V. "Computational Modelling and Analysis of the Hydrodynamics of a Highly Deformable Fish Pectoral Fin." *Journal of Fluid Mechanics*, Vol. 645, 2010, pp. 345–373. doi:10.1017/S0022112009992941.

[44] Liu, G., Ren, Y., Dong, H., Akanyeti, O., Liao, J. C., and Lauder, G. V. "Computational Analysis of Vortex Dynamics and Performance Enhancement Due to Body-Fin and Fin-Fin Interactions in Fish-like Locomotion." *Journal of Fluid Mechanics*, Vol. 829, 2017, pp. 65–88. doi:10.1017/jfm.2017.533.

[45] Dai, L., He, G., Zhang, X., and Zhang, X. "Intermittent Locomotion of a Fish-like Swimmer Driven by Passive Elastic Mechanism." *Bioinspiration and Biomimetics*, Vol. 13, No. 5, 2018. doi:10.1088/1748-3190/aad419.

[46] Hua, R.-N., Zhu, L., and Lu, X.-Y. "Locomotion of a Flapping Flexible Plate." *Physics of Fluids*, Vol. 25, No. 25, 2013, pp. 121901–111902. doi:10.1063/1.3499739.

[47] Chang, X., Zhang, L., and He, X. "Numerical Study of the Thunniform Mode of Fish Swimming with Different Reynolds Number and Caudal Fin Shape." *Computers & Fluids*, Vol. 68, 2012, pp. 54–70. doi:10.1016/j.compfluid.2012.08.004.

[48] Li, G., Müller, U. K., Leeuwen, J. L. Van, and Liu, H. "Body Dynamics and Hydrodynamics of Swimming Fish Larvae: A Computational Study." *The Journal of Experimental Biology*, 2012, pp. 4015–4033. doi:10.1242/jeb.071837.

[49] Kern, S., and Koumoutsakos, P. "Simulations of Optimized Anguilliform Swimming." *Journal of Experimental Biology*, Vol. 209, No. 24, 2006, pp. 4841–4857. doi:10.1242/jeb.02526.

[50] Li, R., Xiao, Q., Liu, Y., Hu, J., Li, L., Li, G., Liu, H., Hu, K., and Wen, L. "A Multi-Body Dynamics Based Numerical Modelling Tool for Solving Aquatic Biomimetic Problems." *Bioinspiration and Biomimetics*, Vol. 13, No. 5, 2018, p. 056001. doi:10.1088/1748-3190/aacd60.

[51] Yeh, P. D., and Alexeev, A. "Free Swimming of an Elastic Plate Plunging at Low Reynolds Number." *Physics of Fluids*, Vol. 26, No. 5, 2014, p. 053604. doi:10.1063/1.4876231.

[52] Shoele, K., and Zhu, Q. "Numerical Simulation of a Pectoral Fin during Labriform Swimming." *The Journal of Experimental Biology*, Vol. 213, 2010, pp. 2038–2047. doi:10.1242/jeb.040162.

[53] Zhu, Q., and Bi, X. "Effects of Stiffness Distribution and Spanwise Deformation on the Dynamics of a Ray-Supported Caudal Fin." *Bioinspiration & Biomimetics*, Vol. 12, No. 2, 2017, p. 26011. doi:https://doi.org/10.1088/1748-3190/aa5d3f.

[54] Shoele, K., and Zhu, Q. "Performance of Synchronized Fins in Biomimetic Propulsion." *Bioinspiration and Biomimetics*, Vol. 10, No. 2, 2015, pp. 1–20. doi:10.1088/1748-3190/10/2/026008.

[55] Van Buren, T., Floryan, D., Wei, N., and Smits, A. J. "Flow Speed Has Little Impact on Propulsive Characteristics of Oscillating Foils." *Physical Review Fluids*, Vol. 3, No. 1, 2018, pp. 1–13. doi:10.1103/PhysRevFluids.3.013103.

[56] Triantafyllou, M. S., Triantafyllou, G. S., and Yue, D. K. P. "Hydrodynamics of Fishlike Swimming." *Annual Review of Fluid Mechanics*, 2000, pp. 33–53.

[57] Lauder, G. V. "Caudal Fin Locomotion in Ray-Finned Fishes Historical and Functional Analyses." *American Zoologist*, Vol. 29, 1989, pp. 85–102.

[58] Nauen, J. C., and Lauder, G. V. "Hydrodynamics of Caudal Fin Locomotion by Chub Mackerel, Scomber Japonicus (Scombridae)." *The Journal of experimental biology*, Vol. 205, 2002, pp. 1709–1724.

[59] Wilga, C. D., and Lauder, G. V. "Function of the Heterocercal Tail in Sharks: Quantitative Wake Dynamics during Steady Horizontal Swimming and Vertical Maneuvering." *J. Exp. Biol.*, Vol. 205, 2002, pp. 2365–2374.

[60] Drucker, E. G., and Lauder, G. V. "A Hydrodynamic Analysis of Fish Swimming Speed: Wake Structure and Locomotor Force in Slow and Fast Labriform Swimmers." *Journal of Experimental Biology*, Vol. 203, No. 16, 2000, pp. 2379–2393.

[61] Drucker, E. G., and Lauder, G. V. "Function of Pectoral Fins in Rainbow Trout: Behavioral Repertoire and Hydrodynamic Forces." *Journal of Experimental Biology*, Vol. 206, 2003, pp. 813–826. doi:10.1242/jeb.01922.

[62] Lauder, G. V., Madden, P. G. A., Mittal, R., Dong, H., and Bozkurttas, M. "Locomotion with Flexible Propulsors: I. Experimental Analysis of Pectoral Fin Swimming in Sunfish." *Bioinspiration and Biomimetics*, Vol. 1, No. 4, 2006. doi:10.1088/1748-3182/1/4/S04.

[63] Standen, E. M., and Lauder, G. V. "Hydrodynamic Function of Dorsal and Anal Fins in Brook Trout (Salvelinus Fontinalis)." *The Journal of experimental biology*, 2007, pp. 325–339. doi:10.1242/jeb.02661.

[64] Hu, T., Shen, L., Lin, L., and Xu, H. "Biological Inspirations, Kinematics Modeling, Mechanism Design and Experiments on an Undulating Robotic Fin Inspired by Gymnarchus Niloticus." *Mechanism and Machine Theory*, Vol. 44, No. 3, 2009, pp. 633–645. doi:10.1016/j.mechmachtheory.2008.08.013.

[65] Youngerman, E. D., Flammang, B. E., and Lauder, G. V. "Locomotion of Free-Swimming Ghost Knifefish: Anal Fin Kinematics during Four Behaviors." *Zoology*, Vol. 117, No. 5, 2014, pp. 337–348. doi:10.1016/j.zool.2014.04.004.

[66] Standen, E. M. "Pelvic Fin Locomotor Function in Fishes: Three-Dimensional Kinematics in Rainbow Trout (Oncorhynchus Mykiss)." *Journal of Experimental Biology*, Vol. 211, No. 18, 2008, pp. 2931–2942. doi:10.1242/jeb.018572.

[67] Chadwell, B. A., Standen, E. M., Lauder, G. V., and Ashley-Ross, M. A. "Median Fin Function during the Escape Response of Bluegill Sunfish

(Lepomis Macrochirus). I: Fin-Ray Orientation and Movement." *Journal of Experimental Biology*, Vol. 215, No. 16, 2012, pp. 2869–2880. doi:10.1242/jeb.068585.

[68]   Chadwell, B. A., Standen, E. M., Lauder, G. V., and Ashley-Ross, M. A. "Median Fin Function during the Escape Response of Bluegill Sunfish (Lepomis Macrochirus). II: Fin-Ray Curvature." *Journal of Experimental Biology*, Vol. 215, No. 16, 2012, pp. 2881–2890. doi:10.1242/jeb.068593.

[69]   Flammang, B. E., and Lauder, G. V. "Functional Morphology and Hydrodynamics of Backward Swimming in Bluegill Sunfish, Lepomis Macrochirus." *Zoology*, Vol. 119, No. 5, 2016, pp. 414–420. doi:10.1016/j.zool.2016.05.002.

[70]   Sfakiotakis, M., Fasoulas, J., Kavoussanos, M. M., and Arapis, M. "Experimental Investigation and Propulsion Control for a Bio-Inspired Robotic Undulatory Fin." *Robotica*, Vol. 33, No. 5, 2015, pp. 1062–1084. doi:10.1017/s0263574714002926.

[71]   Gliva, R., Mountoufaris, M., Spyridakis, N., and Sfakiotakis, M. "Development of a Bio-Inspired Underwater Robot Prototype with Undulatory Fin Propulsion." *Proc. NHIBE*, No. August, 2015, pp. 81–86.

[72]   Wang, R., Wang, S., Wang, Y., Tan, M., and Yu, J. "A Paradigm for Path Following Control of a Ribbon-Fin Propelled Biomimetic Underwater Vehicle." *IEEE Transactions on Systems, Man, and Cybernetics: Systems*, Vol. 49, No. 3, 2019, pp. 482–493. doi:10.1109/TSMC.2017.2705340.

[73]   Blevins, E. L., and Lauder, G. V. "Rajiform Locomotion: Three-Dimensional Kinematics of the Pectoral Fin Surface during Swimming in the Freshwater Stingray Potamotrygon Orbignyi." *Journal of Experimental Biology*, Vol. 215, No. 18, 2012, pp. 3231–3241. doi:10.1242/jeb.068981.

[74]   Di Santo, V., Blevins, E. L., and Lauder, G. V. " Batoid Locomotion: Effects of Speed on Pectoral Fin Deformation in the Little Skate, Leucoraja Erinacea ."

The Journal of Experimental Biology, Vol. 220, No. 4, 2017, pp. 705–712. doi:10.1242/jeb.148767.

[75]   Drucker, E. G., and Lauder, G. V. "Locomotor Function of the Dorsal Fin in Teleost Fishes: Experimental Analysis of Wake Forces in Sunfish." *Journal of Experimental Biology*, Vol. 204, No. 17, 2001, pp. 2943–2958.

[76]   Drucker, E. G., and Lauder, G. V. "Locomotor Function of the Dorsal Fin in Rainbow Trout: Kinematic Patterns and Hydrodynamic Forces." *Journal of Experimental Biology*, Vol. 208, No. 23, 2005, pp. 4479–4494. doi:10.1242/jeb.01922.

[77]   Triantafyllou, M. S., Techet, A. H., and Hover, F. S. "Review of Experimental Work in Biomimetic Foils." *IEEE Journal of Oceanic Engineering*, Vol. 29, No. 3, 2004, pp. 585–594. doi:10.1109/JOE.2004.833216.

[78]   Platzer, M. F., Jones, K. D., Young, J., and S. Lai, J. C. "Flapping Wing Aerodynamics: Progress and Challenges." *AIAA Journal*, Vol. 46, No. 9, 2008, pp. 2136–2149. doi:10.2514/1.29263.

[79]   Gursul, I., Cleaver, D. J., and Wang, Z. "Control of Low Reynolds Number Flows by Means of Fluid–Structure Interactions." *Progress in Aerospace Sciences*, Vol. 64, 2014, pp. 17–55. doi:10.1016/j.paerosci.2013.07.004.

[80]   Gursul, I., and Cleaver, D. "Plunging Oscillations of Airfoils and Wings: Progress, Opportunities, and Challenges." *AIAA Journal*, 2018, pp. 1–18. doi:10.2514/1.J056655.

[81]   Fish, F. E., and Lauder, G. V. "Passive and Active Flow Control By Swimming Fishes and Mammals." *Annual Review of Fluid Mechanics*, Vol. 38, No. 1, 2006, pp. 193–224. doi:10.1146/annurev.fluid.38.050304.092201.

[82]   Heathcote, S., Martin, D., and Gursul, I. "Flexible Flapping Airfoil Propulsion at Zero Freestream Velocity." *AIAA Journal*, Vol. 42, No. 11, 2004, pp. 2196–2204. doi:10.2514/1.5299.

[83]   Heathcote, S., and Gursul, I. "Flexible Flapping Airfoil Propulsion at Low Reynolds Numbers." *AIAA Journal*, Vol. 45, No. 5, 2007, pp. 1066–1079. doi:10.2514/1.25431.

[84]   Quinn, D. B., Lauder, G. V., and Smits, A. J. "Flexible Propulsors in Ground Effect." *Bioinspiration and Biomimetics*, Vol. 9, No. 3, 2014. doi:10.1088/1748-3182/9/3/036008.

[85]   Lucas, K. N., Thornycroft, P. J. M., Gemmell, B. J., Colin, S. P., Costello, J. H., and Lauder, G. V. "Effects of Non-Uniform Stiffness on the Swimming Performance of a Passively- Flexing , Fish-like Foil Model." *Bioinspiration & Biomimetics*, Vol. 10, No. 5, 2015, p. 056019. doi:10.1088/1748-3190/10/5/056019.

[86]   Kancharala, A. K., and Philen, M. K. "Optimal Chordwise Stiffness Profiles of Self-Propelled Flapping Fins." *Bioinspiration and Biomimetics*, Vol. 11, No. 5, 2016, p. 056016. doi:10.1088/1748-3190/11/5/056016.

[87]   Tangorra, J. L., Davidson, S. N., Hunter, I. W., Madden, P. G. A., Lauder, G. V., Dong, H., Bozkurttas, M., and Mittal, R. "The Development of a Biologically Inspired Propulsor for Unmanned Underwater Vehicles." *IEEE Journal of Oceanic Engineering*, Vol. 32, No. 3, 2007, pp. 533–550. doi:10.1109/JOE.2007.903362.

[88]   Wen, L., Ren, Z., Di Santo, V., Hu, K., Yuan, T., Wang, T., and Lauder, G. V. "Understanding Fish Linear Acceleration Using an Undulatory Biorobotic Model with Soft Fluidic Elastomer Actuated Morphing Median Fins." *Soft Robotics*, Vol. 5, No. 4, 2018, pp. 375–388. doi:10.1089/soro.2017.0085.

[89]   Liu, H., and Curet, O. "Swimming Performance of a Bio-Inspired Robotic Vessel with Undulating Fin Propulsion." *Bioinspiration and Biomimetics*, Vol. 13, No. 5, 2018. doi:10.1088/1748-3190/aacd26.

[90]   Tangorra, J. L., Lauder, G. V, Hunter, I. W., Mittal, R., Madden, P. G. a, and Bozkurttas, M. "The Effect of Fin Ray Flexural Rigidity on the Propulsive Forces Generated by a Biorobotic Fish Pectoral Fin." *J. Exp. Biol.*, Vol. 213, No. 23, 2010, pp. 4043–4054. doi:10.1242/jeb.048017.

[91]   Shirgaonkar, A. A., Curet, O. M., Patankar, N. A., and MacIver, M. A. "The Hydrodynamics of Ribbon-Fin Propulsion during Impulsive Motion." *Journal*

of Experimental Biology, Vol. 211, No. 21, 2008, pp. 3490–3503. doi:10.1242/jeb.019224.

[92] Liu, H., and Curet, O. M. "Propulsive Performance of an Under-Actuated Robotic Ribbon Fin." *Bioinspiration & biomimetics*, Vol. 12, No. 3, 2017, p. 36015. doi:10.1088/1748-3190/aa7184.

[93] Liu, H., Taylor, B., and Curet, O. M. "Fin Ray Stiffness and Fin Morphology Control Ribbon-Fin-Based Propulsion." *Soft Robotics*, Vol. 4, No. 2, 2017, pp. 103–116. doi:10.1089/soro.2016.0040.

[94] Anderson, J. M., Streitlien, K., Barrett, D. S., and Triantafyllou, M. S. "Oscillating Foils of High Propulsive Efficiency." *Journal of Fluid Mechanics*, Vol. 360, 1998, pp. 41–72. doi:10.1017/S0022112097008392.

[95] Zhu, Q. "Numerical Simulation of a Flapping Foil with Chordwise or Spanwise Flexibility." *AIAA J.*, Vol. 45, No. 10, 2007, pp. 2448–2457. doi:10.2514/1.28565.

[96] Lewin, G. C., and Haj-Hariri, H. "Modelling Thrust Generation of a Two-Dimensional Heaving Airfoil in a Viscous Flow." *Journal of Fluid Mechanics*, Vol. 492, No. 492, 2003, pp. 339–362. doi:10.1017/S0022112003005743.

[97] Young, J., and Lai, J. C. S. "Mechanisms Influencing the Efficiency of Oscillating Airfoil Propulsion." *AIAA Journal*, Vol. 45, No. 7, 2007, pp. 1695–1702. doi:10.2514/1.27628.

[98] Blondeaux, P., Fornarelli, F., Guglielmini, L., Triantafyllou, M. S., and Verzicco, R. "Numerical Experiments on Flapping Foils Mimicking Fish-like Locomotion." *Physics of Fluids*, Vol. 17, No. 11, 2005, pp. 1–12. doi:10.1063/1.2131923.

[99] Olivier, M., and Dumas, G. "A Parametric Investigation of the Propulsion of 2D Chordwise-Flexible Flapping Wings at Low Reynolds Number Using Numerical Simulations." *Journal of Fluids and Structures*, Vol. 63, 2016, pp. 210–237. doi:10.1016/j.jfluidstructs.2016.03.010.

[100] Dai, H., Luo, H., de Sousa, P. J. S. A. F., and Doyle, J. F. "Thrust Performance of a Flexible Low-Aspect-Ratio Pitching Plate." *Physics of Fluids*, Vol. 24, No. 10, 2012, pp. 1–9. doi:10.1063/1.4764047.

[101] Bozkurttas, M., Mittal, R., Dong, H., Lauder, G. V., and Madden, P. "Low-Dimensional Models and Performance Scaling of a Highly Deformable Fish Pectoral Fin." *Journal of Fluid Mechanics*, Vol. 631, 2009, pp. 311–342. doi:10.1017/S0022112009007046.

[102] Shi, G., Xiao, Q., Zhu, Q., and Liao, W. "Fluid-Structure Interaction Modeling on a 3D Ray-Strengthened Caudal Fin." *Bioinspiration & Biomimetics*, Vol. 14, 2019, p. 036012. doi:https://doi.org/10.1088/1748-3190/ab0fbe.

[103] Neveln, I. D., Bale, R., Bhalla, A. P. S., Curet, O. M., Patankar, N. A., and MacIver, M. A. "Undulating Fins Produce Off-Axis Thrust and Flow Structures." *Journal of Experimental Biology*, Vol. 217, No. 2, 2014, pp. 201–213. doi:10.1242/jeb.091520.

[104] Flammang, B. E., Lauder, G. V., Troolin, D. R., and Strand, T. E. "Volumetric Imaging of Fish Locomotion." *Biology Letters*, Vol. 7, No. 5, 2011, pp. 695–698. doi:10.1098/rsbl.2011.0282.

[105] Liu, G., Geng, B., Zheng, X., Xue, Q., Dong, H., and Lauder, G. V. "An Image-Guided Computational Approach to Inversely Determine in Vivo Material Properties and Model Flow-Structure Interactions of Fish Fins." *Journal of Computational Physics*, Vol. 392, 2019, pp. 578–593. doi:10.1016/j.jcp.2019.04.062.

[106] Zhao, Z., and Dou, L. "Computational Research on a Combined Undulating-Motion Pattern Considering Undulations of Both the Ribbon Fin and Fish Body." *Ocean Engineering*, Vol. 183, No. April, 2019, pp. 1–10. doi:10.1016/j.oceaneng.2019.04.094.

[107] Zhang, J., Bai, Y., Zhai, S., and Gao, D. "Numerical Study on Vortex Structure of Undulating Fins in Stationary Water." *Ocean Engineering*, Vol. 187, No. June, 2019, p. 106166. doi:10.1016/j.oceaneng.2019.106166.

[108] Curet, O. M., Patankar, N. A., Lauder, G. V, and Maciver, M. A. "Aquatic Manoeuvering with Counter-Propagating Waves : A Novel Locomotive Strategy." *Journal of the Royal Society, Interface*, Vol. 8, 2011, pp. 1041–1050.

[109] Jeong, J., and Hussain, F. "On the Identification of a Vortex." *Journal of Fluid Mechanics*, Vol. 285, 1995, pp. 69–94. doi:DOI: 10.1017/S0022112095000462.

[110] Kazakidi, A., Tsakiris, D. P., Angelidis, D., Sotiropoulos, F., and Ekaterinaris, J. A. "CFD Study of Aquatic Thrust Generation by an Octopus-like Arm under Intense Prescribed Deformations." *Computers and Fluids*, Vol. 115, 2015, pp. 54–65. doi:10.1016/j.compfluid.2015.03.009.

[111] Maertens, A. P., Gao, A., and Triantafyllou, M. S. "Optimal Undulatory Swimming for a Single Fish-like Body and for a Pair of InteractingÂ Swimmers." *Journal of Fluid Mechanics*, Vol. 813, 2017, pp. 301–345. doi:10.1017/jfm.2016.845.

[112] Soria, J., and Cantwell, B. J. Identification and Classification of Topological Structures in Free Shear Flows BT - Eddy Structure Identification in Free Turbulent Shear Flows: Selected Papers from the IUTAM Symposium Entitled: "Eddy Structures Identification in Free Turbulent Shear F. In (J. P. Bonnet and M. N. Glauser, eds.), Springer Netherlands, Dordrecht, pp. 379–390.

[113] Mittal, R., and Balachandar, S. "Generation of Streamwise Vortical Structures in Bluff Body Wakes." *Physical Review Letters*, Vol. 75, No. 7, 1995, pp. 1300–1303. doi:10.1103/PhysRevLett.75.1300.

[114] Hunt, J. C. R., Wray, A. A., and Moin, P. Eddies, Streams, and Convergence Zones in Turbulent Flows. 1988.

[115] Li, G., Müller, U. K., Leeuwen, J. L. Van, and Liu, H. "Escape Trajectories Are Deflected When Fish Larvae Intercept Their Own C-Start Wake." *Journal of the Royal Society, Interface*, 2014.

[116] Borazjani, I. "The Functional Role of Caudal and Anal/Dorsal Fins during the C-Start of a Bluegill Sunfish." *Journal of Experimental Biology*, Vol. 216, No. 9, 2013, pp. 1658–1669. doi:10.1242/jeb.079434.

[117] Borazjani, I., Sotiropoulos, F., Tytell, E. D., and Lauder, G. V. "Hydrodynamics of the Bluegill Sunfish C-Start Escape Response: Three-Dimensional Simulations and Comparison with Experimental Data." *Journal of Experimental Biology*, Vol. 215, No. 4, 2012, pp. 671–684. doi:10.1242/jeb.063016.

[118] Kazakidi, A., Tsakiris, D. P., and Ekaterinaris, J. A. "Propulsive Efficiency in Drag-Based Locomotion of a Reduced-Size Swimmer with Various Types of Appendages." *Computers and Fluids*, Vol. 167, 2018, pp. 241–248. doi:10.1016/j.compfluid.2018.03.002.

[119] Katz, J., and Weihs, D. "Hydrodynamic Propulsion by Large Amplitude Oscillation of an Airfoil with Chordwise Flexibility." *Journal of Fluid Mechanics*, Vol. 88, No. 3, 1978, pp. 485–497. doi:DOI: 10.1017/S0022112078002220.

[120] Jones, K., Castro, B., Mahmoud, O., and Platzer, M. A Numerical and Experimental Investigation of Flapping-Wing Propulsion in Ground Effect. In *Proceedings of 40th AIAA Aerospace Sciences Meeting & Exhibit, Reno, USA, January,* 2002.

[121] Ramamurti, R., and Sandberg, W. C. "A Three-Dimensional Computational Study of the Aerodynamic Mechanisms of Insect Flight." *Journal of Experimental Biology*, Vol. 205, No. 10, 2002, pp. 1507 LP – 1518.

[122] Zhu, Q., Wolfgang, M. J., Yue, D. K. P., and Triantafyllou, M. S. "Three-Dimensional Flow Structures and Vorticity Control in Fish-like Swimming." *J. Fluid Mech.*, Vol. 468, No. 2002, 2002, p. 1. doi:10.1017/S002211200200143X.

[123] Buchholz, James H J and Smits, A. J. "On the Evolution of the Wake Structure Produced by a Low-Aspect-Ratio Pitching Panel." *J. Fluid Mech*, Vol. 546, 2006, pp. 433–443. doi:10.1017/S0022112005006865.

[124] Li, G., Müller, U. K., Leeuwen, J. L. Van, and Liu, H. "Fish Larvae Exploit Edge Vortices along Their Dorsal and Ventral Fin Folds to Propel Themselves." *Journal of the Royal Society, Interface*, 2016.

[125] Nakata, T., and Liu, H. "A Fluid-Structure Interaction Model of Insect Flight with Flexible Wings." *Journal of Computational Physics*, Vol. 231, No. 4, 2012, pp. 1822–1847. doi:10.1016/j.jcp.2011.11.005.

[126] Fish, F. E. "Comparative Kinematics and Hydrodynamics of Odontocete Cetaceans: Morphological and Ecological Correlates with Swimming Performance." *The Journal of Experimental Biology*, Vol. 201, No. 20, 1998, pp. 2867 LP – 2877.

[127] Rohr, J. J., and Fish, F. E. "Strouhal Numbers and Optimization of Swimming by Odontocete Cetaceans." *Journal of Experimental Biology*, Vol. 207, No. 10, 2004, pp. 1633 LP – 1642. doi:10.1242/jeb.00948.

[128] Webb, P. W., and Keyes, R. S. "Swimming Kinematics of Sharks." *Fishery Bulletin*, Vol. 80, 1982, pp. 803–812.

[129] Dewar, H., and Graham, J. "Studies of Tropical Tuna Swimming Performance in a Large Water Tunnel - Kinematics." *The Journal of Experimental Biology*, Vol. 192, No. 1, 1994, pp. 45 LP – 59.

[130] Dickson, K. A., Donley, J. M., Sepulveda, C., and Bhoopat, L. "Effects of Temperature on Sustained Swimming Performance and Swimming Kinematics of the Chub Mackerel Scomber Japonicus." *Journal of Experimental Biology*, Vol. 205, No. 7, 2002, pp. 969 LP – 980.

[131] Webb, P. W. "Effects of Partial Caudal-Fin Amputation on the Kinematics and Metabolic Rate of Underyearling Sockeye Salmon (Oncorhynchus Nerka) At Steady Swimming Speeds." *Journal of Experimental Biology*, Vol. 59, No. 3, 1973, pp. 565 LP – 582.

[132] Webb, P. W., Kostecki, P. T., and Stevens, E. D. O. N. "The Effect of Size and Swimming Speed on Locomotor Kinematics of Rainbow Trout." *Journal of Experimental Biology*, Vol. 109, No. 1, 1984, pp. 77 LP – 95.

[133] Blake, R. W., Li, J., and Chan, K. H. S. "Swimming in Four Goldfish Carassius Auratus Morphotypes: Understanding Functional Design and Performance Employing Artificially Selected Forms." *Journal of Fish Biology*, Vol. 75, No. 3, 2009, pp. 591–617. doi:10.1111/j.1095-8649.2009.02309.x.

[134] Shi, G., Xiao, Q., and Zhu, Q. A Study of 3D Flexible Caudal Fin for Fish Propulsion. In *Proceedings of the 36th International Conference on Offshore Mechanics and Arctic Engineering, Trondheim, Norway,June,* 2017.

[135] Xiao, T., Qin, N., Luo, D., and Deng, S. "Deformable Overset Grid for Multibody Unsteady Flow Simulation." *AIAA Journal*, Vol. 54, No. 8, 2016, pp. 2392–2406. doi:10.2514/1.J054861.

[136] Peskin, C. S. "Flow Patterns around Heart Valves: A Numerical Method." *Journal of Computational Physics*, Vol. 10, No. 2, 1972, pp. 252–271. doi:10.1016/0021-9991(72)90065-4.

[137] Peskin, C. S. "The Immersed Boundary Method." *Acta Numerica*, Vol. 11, 2002, pp. 479–517. doi:DOI: 10.1017/S0962492902000077.

[138] Mittal, R., and Iaccarino, G. "IMMERSED BOUNDARYMETHODS." *Annual Review of Fluid Mechanics*, Vol. 37, No. 1, 2005, pp. 239–261. doi:10.1146/annurev.fluid.37.061903.175743.

[139] Sadeghi, M. *Parallel Computation of Three Dimensional Aeroelastic Fluid-Structure Interaction*. PhD Thesis, University of California, Irvine, 2004.

[140] Jameson, A., Schmidt, W., and Turkel, E. L. I. "Numerical Solution of the Euler Equations by Finite Volume Methods Using Runge Kutta Time Stepping Schemes." In *Proceedings of 14th Fluid and Plasma Dynamics Conference*, Palo Alto, USA, June, 1981. doi:doi:10.2514/6.1981-1259.

[141] Jameson, A. "Time Dependent Calculations Using Multigrid, with Applications to Unsteady Flows Past Airfoils and Wings." In *Proceedings of AIAA 10th*

Computational Fluid Dynamics Conference, Honolulu, USA, June, 1991. doi:10.2514/6.1991-1596.

[142] Liu, F., and Ji, S. "Unsteady Flow Calculations with a Multigrid Navier-Stokes Method." *AIAA Journal*, Vol. 34, No. 10, 1996, pp. 2047–2053. doi:10.2514/3.13351.

[143] Liu, F., and Zheng, X. "A Strongly Coupled Time-Marching Method for Solving the Navier–Stokes and k-w Turbulence Model Equations with Multigrid." *Journal of Computational Physics*, Vol. 128, 1996, pp. 289–300. doi:10.1006/jcph.1996.0211.

[144] Sadeghi, M., Yang, S., Liu, F., and Tsai, H. Parallel Computation of Wing Flutter with a Coupled Navier-Stokes/CSD Method. In *Proceedings of 41st Aerospace Sciences Meeting and Exhibit*, Reno, USA, January, 2003.

[145] Xiao, Q., and Liao, W. "Numerical Investigation of Angle of Attack Profile on Propulsion Performance of an Oscillating Foil." *Computers and Fluids*, Vol. 39, No. 8, 2010, pp. 1366–1380. doi:10.1016/j.compfluid.2010.04.006.

[146] LIU, Q., QU, K., CAI, J., and XU, J. "An Automated Chimera Method Based on a Hierarchical Overset Grid Strategy and the Implicit Hole Cutting Technique." *Scientia Sinica Physica, Mechanica & Astronomica*, Vol. 43, No. 2, 2013, p. 186. doi:10.1360/132012-631.

[147] Liu, W., Xiao, Q., and Zhu, Q. "Passive Flexibility Effect on Oscillating Foil Energy Harvester." *AIAA Journal*, Vol. 54, No. 4, 2016, pp. 1172–1187. doi:10.2514/1.J054205.

[148] Turkel, E., Radespiel, R., and Kroll, N. "Assessment of Preconditioning Methods for Multidimensional Aerodynamics." *Computers and Fluids*, Vol. 26, No. 6, 1997, pp. 613–634. doi:10.1016/S0045-7930(97)00013-3.

[149] Vatsa, V., and Turkel, E. Assessment of Local Preconditioners for Steady State and Time Dependent Flows. In *Proceedings of 34th AIAA Fluid Dynamics Conference and Exhibit*, Portland, Oregon, USA, June, 2004.

[150] Turkel, E., and Vatsa, V. N. "Local Preconditioners for Steady and Unsteady Flow Applications." *ESAIM: Mathematical Modelling and Numerical Analysis*, Vol. 39, No. 3, 2005, pp. 515–535. doi:DOI: 10.1051/m2an:2005021.

[151] Weiss, J. M., and Smith, W. A. "Preconditioning Applied to Variable and Constant Density Flows." *AIAA J.*, Vol. 33, No. 11, 1995. doi:10.2514/6.1994-2209.

[152] Weiss, J. M., Maruszewski, J. P., and Smith, W. A. "Implicit Solution of Preconditioned Navier-Stokes Equations Using Algebraic Multigrid." *AIAA Journal*, Vol. 37, No. 1, 1999, pp. 29–36. doi:10.2514/2.689.

[153] Choi, Y. H., and Merkle, C. L. The Application of Preconditioning in Viscous Flows. *Journal of Computational Physics*. 2. Volume 105, 207–223.

[154] Venkateswaran, S., and Merkle, C. Dual Time-Stepping and Preconditioning for Unsteady Computations. In *Proceedings of 33rd Aerospace Sciences Meeting and Exhibit*, Reno, USA, January, 1995.

[155] Pandya, S., Venkateswaran, S., and Pulliam, T. Implementation of Preconditioned Dual-Time Procedures in OVERFLOW. In *Proceedings of 41st Aerospace Sciences Meeting and Exhibit*, Reno, USA, January, 2003.

[156] Dailey, L. D., and Pletcher, R. H. "Evaluation of Multigrid Acceleration for Preconditioned Time-Accurate Navier-Stokes Algorithms." *Computers & Fluids*, Vol. 25, No. 8, 1996, pp. 791–811. doi:10.2514/6.1995-1668.

[157] Campobasso, M. S., and Drofelnik, J. "Compressible Navier-Stokes Analysis of an Oscillating Wing in a Power-Extraction Regime Using Efficient Low-Speed Preconditioning." *Computers and Fluids*, Vol. 67, 2012, pp. 26–40. doi:10.1016/j.compfluid.2012.07.002.

[158] Colin, Y., Deniau, H., and Boussuge, J. F. "A Robust Low Speed Preconditioning Formulation for Viscous Flow Computations." *Computers and Fluids*, Vol. 47, No. 1, 2011, pp. 1–15. doi:10.1016/j.compfluid.2011.01.015.

[159] Xiao, Q., Liao, W., Yang, S., and Peng, Y. "How Motion Trajectory Affects Energy Extraction Performance of a Biomimic Energy Generator with an

Oscillating Foil?" *Renewable Energy*, Vol. 37, No. 1, 2012, pp. 61–75. doi:10.1016/j.renene.2011.05.029.

[160] Liu, W., Xiao, Q., and Cheng, F. "A Bio-Inspired Study on Tidal Energy Extraction with Flexible Flapping Wings." *Bioinspir. Biomim*, Vol. 8, No. 3, 2013, pp. 36011–16. doi:10.1088/1748-3182/8/3/036011.

[161] Connell, B. S. H., and Yue, D. K. P. "Flapping Dynamics of a Flag in a Uniform Stream." *Journal of Fluid Mechanics*, Vol. 581, 2007, pp. 33–67. doi:DOI: 10.1017/S0022112007005307.

[162] Connell, B. S. H. *Numerical Investigation of the Flow-Body Interaction of Thin Flexible Foils and Ambient Flow*. PhD Thesis, Massachusetts Institute of Technology, 2006.

[163] Hübner, B., Walhorn, E., and Dinkler, D. "A Monolithic Approach to Fluid-Structure Interaction Using Space-Time Finite Elements." *Computer Methods in Applied Mechanics and Engineering*, Vol. 193, 2004, pp. 2087–2104. doi:10.1016/j.cma.2004.01.024.

[164] Walhorn, E., Kölke, A., Hübner, B., and Dinkler, D. "Fluid-Structure Coupling within a Monolithic Model Involving Free Surface Flows." *Computers and Structures*, Vol. 83, 2005, pp. 2100–2111. doi:10.1016/B978-008044046-0.50381-X.

[165] Tezduyar, T. E., Sathe, S., Keedy, R., and Stein, K. "Space-Time Finite Element Techniques for Computation of Fluid-Structure Interactions." *Computer Methods in Applied Mechanics and Engineering*, Vol. 195, 2006, pp. 2002–2027. doi:10.1016/j.cma.2004.09.014.

[166] Hron, S., and Turek, J. *A Monolithic FEM/Multigrid Solver for an ALE Formulation of Fluid-Structure Interaction with Applications in Biomechanics. In Fluid-Structure Interaction Modelling, Simulation, Optimisation, pp 146-170, the Lecture Notes in Computational Science and Engineering book series (LNCSE, volume 53,)* 2006.

[167] Michler, C., Hulshoff, S. J., van Brummelen, E. H., and de Borst, R. "A Monolithic Approach to Fluid-Structure Interaction." *Computers and Fluids*, Vol. 33, No. 5–6, 2004, pp. 839–848. doi:10.1016/j.compfluid.2003.06.006.

[168] Idelsohn, S. R., Marti, J., Limache, A., and Oñate, E. "Unified Lagrangian Formulation for Elastic Solids and Incompressible Fluids: Application to Fluid-Structure Interaction Problems via the PFEM." *Computer Methods in Applied Mechanics and Engineering*, Vol. 197, No. 19–20, 2008, pp. 1762–1776. doi:10.1016/j.cma.2007.06.004.

[169] Greenshields, C. J., and Weller, H. G. "A Unified Formulation for Continuum Mechanics Applied to Fluid-Structure Interaction in Flexible Tubes." *International Journal for Numerical Methods in Engineering*, Vol. 64, 2005, pp. 1575–1593. doi:10.1002/nme.1409.

[170] Papadakis, G. "A Novel Pressure-Velocity Formulation and Solution Method for Fluid-Structure Interaction Problems." *Journal of Computational Physics*, Vol. 227, No. 6, 2008, pp. 3383–3404. doi:10.1016/j.jcp.2007.12.004.

[171] Farhat, C., and Lesoinne, M. "Two Efficient Staggered Algorithms for the Serial and Parallel Solution of Three-Dimensional Nonlinear Transient Aeroelastic Problems." *Computer Methods in Applied Mechanics and Engineering*, Vol. 182, No. 3–4, 2000, pp. 499–515. doi:10.1016/S0045-7825(99)00206-6.

[172] Jaiman, R. K., Jiao, X., Geubelle, P. H., and Loth, E. "Conservative Load Transfer along Curved Fluid-Solid Interface with Non-Matching Meshes." *Journal of Computational Physics*, Vol. 218, No. 1, 2006, pp. 372–397. doi:10.1016/j.jcp.2006.02.016.

[173] Causin, P., Gerbeau, J. F., and Nobile, F. "Added-Mass Effect in the Design of Partitioned Algorithms for Fluid-Structure Problems." *Computer Methods in Applied Mechanics and Engineering*, Vol. 194, No. 42–44, 2005, pp. 4506–4527. doi:10.1016/j.cma.2004.12.005.

[174] Piperno, S., Farhat, C., and Larrouturou, B. "Partitioned Procedures for the Transient Solution of Coupled Aroelastic Problems Part I: Model Problem, Theory and Two-Dimensional Application." *Computer methods in applied mechanics and engineering*, Vol. 124, No. 1–2, 1995, pp. 79–112. doi:http://dx.doi.org/10.1016/0045-7825(95)92707-9.

[175] Piperno, S., and Farhat, C. "Partitioned Procedures for the Transient Solution of Coupled Aeroelastic Problems - Part II: Energy Transfer Analysis and Three-Dimensional Applications." *Computer Methods in Applied Mechanics and Engineering*, Vol. 190, No. 24–25, 2001, pp. 3147–3170. doi:10.1016/S0045-7825(00)00386-8.

[176] Förster, C., Wall, W. A., and Ramm, E. "Artificial Added Mass Instabilities in Sequential Staggered Coupling of Nonlinear Structures and Incompressible Viscous Flows." *Computer Methods in Applied Mechanics and Engineering*, Vol. 196, No. 7, 2007, pp. 1278–1293. doi:10.1016/j.cma.2006.09.002.

[177] Degroote, J., Bathe, K. J., and Vierendeels, J. "Performance of a New Partitioned Procedure versus a Monolithic Procedure in Fluid-Structure Interaction." *Computers and Structures*, Vol. 87, No. 11–12, 2009, pp. 793–801. doi:10.1016/j.compstruc.2008.11.013.

[178] Degroote, J., Bruggeman, P., Haelterman, R., and Vierendeels, J. "Stability of a Coupling Technique for Partitioned Solvers in FSI Applications." *Computers and Structures*, Vol. 86, No. 23–24, 2008, pp. 2224–2234. doi:10.1016/j.compstruc.2008.05.005.

[179] Degroote, J., Annerel, S., and Vierendeels, J. "Stability Analysis of Gauss-Seidel Iterations in a Partitioned Simulation of Fluid-Structure Interaction." *Computers and Structures*, Vol. 88, No. 5–6, 2010, pp. 263–271. doi:10.1016/j.compstruc.2009.09.003.

[180] Degroote, J., Swillens, A., Bruggeman, P., Haelterman, R., Segers, P., and Vierendeels, J. "Simulation of Fluid–Structure Interaction with the Interface Artificial Compressibility Method." *International Journal for Numerical Methods in Engineering*, Vol. 26, 2010, pp. 276–289. doi:10.1002/cnm.

[181] Degroote, J. "On the Similarity between Dirichlet–Neumann with Interface Artificial Compressibility and Robin–Neumann Schemes for the Solution of Fluid-Structure Interaction Problems." *Journal of Computational Physics*, Vol. 230, No. 17, 2011, pp. 6399–6403. doi:10.1016/j.jcp.2011.05.012.

[182] Vierendeels, J., Lanoye, L., Degroote, J., and Verdonck, P. "Implicit Coupling of Partitioned Fluid-Structure Interaction Problems with Reduced Order Models." *Computers and Structures*, Vol. 85, No. 11–14, 2007, pp. 970–976. doi:10.1016/j.compstruc.2006.11.006.

[183] Küttler, U., and Wall, W. A. "Fixed-Point Fluid-Structure Interaction Solvers with Dynamic Relaxation." *Computational Mechanics*, Vol. 43, No. 1, 2008, pp. 61–72. doi:10.1007/s00466-008-0255-5.

[184] Gerbeau, J. F., and Vidrascu, M. "A Quasi-Newton Algorithm Based on a Reduced Model for Fluid-Structure Interaction Problems in Blood Flows." *ESAIM: Mathematical Modelling and Numerical Analysis*, Vol. 37, 2003, pp. 631–647. doi:10.1051/m2an.

[185] Gerbeau, J. F., Vidrascu, M., and Frey, P. "Fluid-Structure Interaction in Blood Flows on Geometries Based on Medical Imaging." *Computers and Structures*, Vol. 83, No. 2–3, 2005, pp. 155–165. doi:10.1016/j.compstruc.2004.03.083.

[186] Michler, C., Brummelen, E. H. Van, and Borst, R. De. "An Interface Newton–Krylov Solver for Fluid–Structure Interaction." *International Journal for Numerical Methods in Fluids*, Vol. 47, 2005, pp. 1189–1195.

[187] Michler, C., van Brummelen, E. H., and de Borst, R. "Error-Amplification Analysis of Subiteration-Preconditioned GMRES for Fluid-Structure Interaction." *Computer Methods in Applied Mechanics and Engineering*, Vol. 195, No. 17–18, 2006, pp. 2124–2148. doi:10.1016/j.cma.2005.01.018.

[188] Degroote, J., Haelterman, R., Annerel, S., Bruggeman, P., and Vierendeels, J. "Performance of Partitioned Procedures in Fluid-Structure Interaction." *Computers and Structures*, Vol. 88, No. 7–8, 2010, pp. 446–457. doi:10.1016/j.compstruc.2009.12.006.

[189] Goura, G. S. L., Badcock, K. J., Woodgate, M. A., and Richards, B. E. "A Data Exchange Method for Fluid-Structure Interaction Problems." *The Aeronautical Journal*, Vol. 105, No. 1046, 2001, pp. 215–221. doi:10.1017/S0001924000025458.

[190] Sadeghi, M., Liu, F., Lai, K. L., and Tsai, H. M. "Application of Three-Dimensional Interfaces for Data Transfer in Aeroelastic Computations." In *Proceedings of 22nd Applied Aerodynamics Conference and Exhibit*, Providence, Rhode Island, USA, August, 2004, doi:doi:10.2514/6.2004-5376.

[191] Batina, J. T. "Unsteady Euler Airfoil Solutions Using Unstructured Dynamic Meshes." *AIAA Journal*, Vol. 28, No. 8, 1990, pp. 1381–1388. doi:10.2514/3.25229.

[192] Lee, Y., and Baeder, J. "High-Order Overset Method for Blade Vortex Interaction." In *Proceedings of 40th AIAA Aerospace Sciences Meeting & Exhibit* , Reno, USA, January, 2002. doi:10.2514/6.2002-559.

[193] Lee, Y., and Baeder, J. Implicit Hole Cutting - A New Approach to Overset Grid Connectivity. In Proceedings of *16th AIAA Computational Fluid Dynamics Conference*, Orlando, USA, June, 2003.

[194] Liao, W., Cai, J., and Tsai, H. M. "A Multigrid Overset Grid Flow Solver with Implicit Hole Cutting Method." *Computer Methods in Applied Mechanics and Engineering*, Vol. 196, No. 9–12, 2007, pp. 1701–1715. doi:10.1016/j.cma.2006.09.012.

[195] Liu, Q., Qu, K., and Cai, J. "An Automated Multi-Grid Chimera Method Based on the Implicit Hole Technique." *Proceedings of the Institution of Mechanical Engineers, Part G: Journal of Aerospace Engineering*, Vol. 231, No. 2, 2016, pp. 279–293. doi:10.1177/0954410016636162.

[196] Tsai, H. M., F. Wong, A. S., Cai, J., Zhu, Y., and Liu, F. "Unsteady Flow Calculations with a Parallel Multiblock Moving Mesh Algorithm." *AIAA Journal*, Vol. 39, No. 6, 2001, pp. 1021–1029. doi:10.2514/2.1442.

[197] Liu, W., and Xiao, Q. "Investigation on Darrieus Type Straight Blade Vertical Axis Wind Turbine with Flexible Blade." *Ocean Engineering*, Vol. 110, 2015, pp. 339–356. doi:10.1016/j.oceaneng.2015.10.027.

[198] Guilmineau, E., and Queutey, P. "A Numerical Simulation of Vortex Shedding from an Oscillating Circular Cylinder" *Journal of Fluids and Structures*, Vol. 16, No. 6, 2002, pp. 773–794. doi:10.1006/jfls.449.

[199] Lu, X. Y., and Dalton, C. "Calculation of the Timing of Vortex Formation from an Oscillating Cylinder." *Journal of Fluids and Structures*, Vol. 10, No. 5, 1996, pp. 527–541. doi:10.1006/jfls.1996.0035.

[200] Williamson, C. H. K. "Defining a Universal and Continuous Strouhal–Reynolds Number Relationship for the Laminar Vortex Shedding of a Circular Cylinder." *Physics of Fluids*, Vol. 31, No. 10, 1988, p. 2742. doi:10.1063/1.866978.

[201] Rajani, B. N., Kandasamy, A., and Majumdar, S. "Numerical Simulation of Laminar Flow Past a Circular Cylinder." *Applied Mathematical Modelling*, Vol. 33, No. 3, 2009, pp. 1228–1247. doi:10.1016/j.apm.2008.01.017.

[202] Constant, E., Favier, J., Meldi, M., Meliga, P., and Serre, E. "An Immersed Boundary Method in OpenFOAM : Verification and Validation." *Computers & Fluids*, Vol. 157, 2017, pp. 55–72. doi:10.1016/j.compfluid.2017.08.001.

[203] Gordnier, R. E., Kumar Chimakurthi, S., Cesnik, C. E. S., and Attar, P. J. "High-Fidelity Aeroelastic Computations of a Flapping Wing with Spanwise Flexibility." *Journal of Fluids and Structures*, Vol. 40, 2013, pp. 86–104. doi:10.1016/j.jfluidstructs.2013.03.009.

[204] Heathcote, S., Wang, Z., and Gursul, I. "Effect of Spanwise Flexibility on Flapping Wing Propulsion." *Journal of Fluids and Structures*, Vol. 24, No. 2, 2008, pp. 183–199. doi:10.1016/j.jfluidstructs.2007.08.003.

[205] Volterra, E., and Zachmanoglou, E. C. *Dynamics of Vibrations*. CE Merrill, Columbus, 1965.

[206] Wood, C., Gil, A. J., Hassan, O., and Bonet, J. "Partitioned Block-Gauss-Seidel Coupling for Dynamic Fluid-Structure Interaction." *Computers and Structures*, Vol. 88, No. 23–24, 2010, pp. 1367–1382. doi:10.1016/j.compstruc.2008.08.005.

[207] Kassiotis, C., Ibrahimbegovic, A., Niekamp, R., and Matthies, H. G. "Nonlinear Fluid-Structure Interaction Problem. Part I: Implicit Partitioned Algorithm, Nonlinear Stability Proof and Validation Examples." *Computational Mechanics*, Vol. 47, No. 3, 2011, pp. 305–323. doi:10.1007/s00466-010-0545-6.

[208] Habchi, C., Russeil, S., Bougeard, D., Harion, J. L., Lemenand, T., Ghanem, A., Valle, D. Della, and Peerhossaini, H. "Partitioned Solver for Strongly Coupled Fluid-Structure Interaction." *Computers and Fluids*, Vol. 71, 2013, pp. 306–319. doi:10.1016/j.compfluid.2012.11.004.

[209] Matthies, H. G., and Steindorf, J. "Partitioned Strong Coupling Algorithms for Fluid–Structure Interaction." *Computers & Structures*, Vol. 81, No. 8–11, 2003, pp. 805–812. doi:http://dx.doi.org/10.1016/S0045-7949(02)00409-1.

[210] Dettmer, W., and Perić, D. "A Computational Framework for Fluid-Structure Interaction: Finite Element Formulation and Applications." *Computer Methods in Applied Mechanics and Engineering*, Vol. 195, No. 41–43, 2006, pp. 5754–5779. doi:10.1016/j.cma.2005.10.019.

[211] Paraz, F., Eloy, C., and Schouveiler, L. "Experimental Study of the Response of a Flexible Plate to a Harmonic Forcing in a Flow." *Comptes Rendus - Mecanique*, Vol. 342, No. 9, 2014, pp. 532–538. doi:10.1016/j.crme.2014.06.004.

[212] Dong, H., Mittal, R., Bozkurttas, M., and Najjar, F. "Wake Structure and Performance of Finite Aspect-Ratio Flapping Foils." In *Proceedings of 43rd AIAA Aerospace Sciences Meeting and Exhibit*, Reno, USA, January, 2005. doi:10.2514/6.2005-81.

[213] Luo, Y., Xiao, Q., Shi, G., Wen, L., Chen, D., and Pan, G. "A Fluid–Structure Interaction Solver for the Study on a Passively Deformed Fish Fin with

Non-Uniformly Distributed Stiffness." *Journal of Fluids and Structures*, Vol. 92, 2020, p. 102778. doi:10.1016/j.jfluidstructs.2019.102778.

[214] Dong, H., Mittal, R., and Najjar, F. M. *Wake Topology and Hydrodynamic Performance of Low-Aspect-Ratio Flapping Foils*. Journal of Fluid Mechanics, Vol. 566, 2006, pp. 309–343. https://doi.org/10.1017/S002211200600190X.

[215] Dewey, P. A., Boschitsch, B. M., Moored, K. W., Stone, H. A., and Smits, A. J. "Scaling Laws for the Thrust Production of Flexible Pitching Panels." *Journal of Fluid Mechanics*, Vol. 732, 2013, pp. 29–46. doi:10.1017/jfm.2013.384.

[216] Rosic, M. L. N., Thornycroft, P. J. M., Feilich, K. L., Lucas, K. N., and Lauder, G. V. "Performance Variation Due to Stiffness in a Tuna-Inspired Flexible Foil Model." *Bioinspiration and Biomimetics*, Vol. 12, No. 1, 2017, p. aa5113. doi:10.1088/1748-3190/aa5113.

[217] Rahman, M. M., Toda, Y., and Miki, H. "Computational Study on a Squid-Like Underwater Robot with Two Undulating Side Fins." *Journal of Bionic Engineering*, Vol. 8, No. 1, 2011, pp. 25–32. doi:10.1016/S1672-6529(11)60003-6.

[218] Ghia, U., Ghia, K. N., and Shin, C. T. "High-Re Solutions for Incompressible Flow Using the Navier-Stokes Equations and a Multigrid Method." *Journal of Computational Physics*, Vol. 48, No. 3, 1982, pp. 387–411. doi:https://doi.org/10.1016/0021-9991(82)90058-4.

Appendix: Preconditioning Methods for Compressible Navier-Stokes Equations

A.1   Preconditioned Navier-Stokes equations

The original integral form of Navier-Stoke equations for compressible flow is given in Eq. (3.1). With preconditioning, the equations are formulated as follows:

$$\frac{\partial}{\partial t} \iiint_V \boldsymbol{U} dV + \boldsymbol{P}\boldsymbol{\Gamma}^{-1} \iint_S (\boldsymbol{F}_c - \boldsymbol{F}_d) \cdot \boldsymbol{n} dS = \boldsymbol{0}, \tag{A.1}$$

where $\boldsymbol{P}$ and $\boldsymbol{\Gamma}$ are the transformation and preconditioning matrices respectively. The transformation matrix is needed if conservative flow variables are used in computation. Here, the primitive variables are selected as

$$\boldsymbol{U_p} = \{p, u, v, w, T_e\}, \tag{A.2}$$

For perfect gas, the transformation matrix from primitive to conservative variables $\boldsymbol{P} = \partial \boldsymbol{U}/\partial \boldsymbol{U_p}$ reads

$$\boldsymbol{P} = \begin{bmatrix} \rho/p & 0 & 0 & 0 & -\rho/T_e \\ \rho u/p & \rho & 0 & 0 & -\rho u/T_e \\ \rho v/p & 0 & \rho & 0 & -\rho v/T_e \\ \rho w/p & 0 & 0 & \rho & -\rho w/T_e \\ \rho\bar{E}/p & \rho u & \rho v & \rho w & -\rho q^2/2T_e \end{bmatrix}. \tag{A.3}$$

where $q^2 = \|\boldsymbol{u}\|_2^2 = u^2 + v^2 + w^2$.

The Weiss-Smith preconditioning matrix is used in the present implementation, which can be expressed as [151,152]

$$\mathbf{\Gamma} = \begin{bmatrix} \Theta & 0 & 0 & 0 & -\rho/T_e \\ \Theta u & \rho & 0 & 0 & -\rho u/T_e \\ \Theta v & 0 & \rho & 0 & -\rho v/T_e \\ \Theta w & 0 & 0 & \rho & -\rho w/T_e \\ \Theta \bar{H} - 1 & \rho u & \rho v & \rho w & -\rho q^2/2T_e \end{bmatrix}. \tag{A.4}$$

where $\Theta = 1/\beta c^2$ for perfect gas. β is defined as

$$\beta = \frac{M_r^2}{1 + (\gamma - 1)M_r^2}, \tag{A.5}$$

where M_r^2 is the square of the reference Mach number, which is computed as $M_r^2 = \min\left(\max\left(M_a^2, M_{vis}^2, M_{pd}^2, \kappa_1 M_{a,\infty}^2\right), 1\right)$ [152,155], where $\kappa_1 \sim O(1)$ and is selected to be 5 here. M_{vis}^2 and M_{pd}^2 are cut-off values based on the local diffusion velocity and local pressure difference, which are defined as [152]

$$M_{vis}^2 = \left(\frac{\nu}{\Delta x'}\right)^2 \frac{1}{a^2},$$
$$M_{pd}^2 = \varepsilon \frac{\Delta p'}{\rho} \frac{1}{a^2}, \tag{A.6}$$

where $\Delta x' = \min\left(\Delta x_\xi, \Delta x_\eta, \Delta x_\zeta\right)$, $\Delta p' = \max\left(\Delta p_\xi, \Delta p_\eta, \Delta p_\zeta\right)$ and $\varepsilon \sim O(10^{-6})$.

The eigenvalue matrix of the convective flux Jacobian of the preconditioned system $\mathbf{P}\mathbf{\Gamma}^{-1}\mathbf{J}$ is given by

$$\widetilde{\mathbf{\Lambda}}_p = \begin{bmatrix} V & 0 & 0 & 0 & 0 \\ 0 & V & 0 & 0 & 0 \\ 0 & 0 & V & 0 & 0 \\ 0 & 0 & 0 & V' + a' & 0 \\ 0 & 0 & 0 & 0 & V' - a' \end{bmatrix}. \tag{A.7}$$

where $V = \boldsymbol{u} \cdot \boldsymbol{n}$ is the contravariant velocity, and V' and a' denote the modified contravariant velocity and modified speed of sound respectively. The two modified terms are calculated as

$$V' = \frac{1}{2}(1 + M_r^2)V,$$

$$a' = \frac{1}{2}\sqrt{(1 - M_r^2)^2 V^2 + 4M_r^2 a^2},$$

(A.8)

The spectral radii used in the calculations of the artificial dissipation and local time step should be replaced by the following modified formula

$$\Lambda_p = (|V'| + a')\Delta S.$$

(A.9)

Since the preconditioning matrix has been included when calculating spectral radii (in different forms with Eq. (A.4)), the artificial dissipation term should not be multiplied by $\boldsymbol{P\Gamma}^{-1}$. Therefore, the formula used to compute the artificial dissipation (Eq. (3.21)) should be modified as

$$D_{i+\frac{1}{2},j,k} = \widehat{\Lambda}_{I,i+\frac{1}{2},j,k}\left(\boldsymbol{\Gamma P}^{-1}\right)_{I,i+\frac{1}{2},j,k}\left[\epsilon^{(2)}_{I,i+\frac{1}{2},j,k}\left(\widehat{U}_{i+1,j,k} - \widehat{U}_{i,j,k}\right)\right.$$
$$\left. - \epsilon^{(4)}_{I,i+\frac{1}{2},j,k}\left(\widehat{U}_{i+2,j,k} - 3\widehat{U}_{i+1,j,k} + 3\widehat{U}_{i+1,j,k} + \widehat{U}_{i-1,j,k}\right)\right]$$

(A.10)

The far-field boundary condition (Subsection 3.1.4.2) is based on the flow characteristic variables, and should also be modified as the convective flux Jacobian has been changed. In the present implementation, the following simplified non-characteristic far-field boundary condition [148] is used for preconditioned computation. For inflow condition, the flow velocity and temperature at the boundary are obtained from freestream flow, and the pressure at the boundary is given by the interior cell adjacent to the boundary:

$$\boldsymbol{u}_b = \boldsymbol{u}_\infty, T_b = T_\infty, p_b = p_{int}.$$

(A.11)

For outflow condition, the flow velocity and temperature at the boundary are obtained from the interior cell adjacent to the boundary, and the pressure at the boundary is given by freestream pressure:

$$\boldsymbol{u}_b = \boldsymbol{u}_{int}, T_b = T_{int}, p_b = p_\infty. \tag{A.12}$$

The flow density at the boundary is computed using the gas state equation.

A.2 Test cases

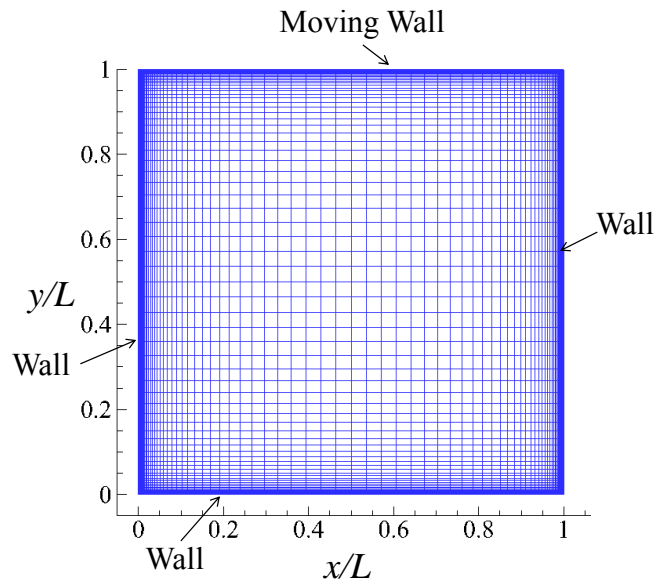**Test 1: Steady flow in a lid-driven cavity**

Figure A-1 The computational mesh and boundary conditions for lid-driven cavity flow.

The lid-driven cavity flow is used to test the accuracy of the present implementation of the above preconditioning method. As shown in Figure A-1, both the length and the height of the cavity is L. The upper wall is moving at a constant speed of U_0, and the other walls are fixed. The Reynolds numbers based on L and U_0 are selected to be R_e=100 and 1000. The computational mesh is composed of 80x80 hexahedral cells and is refined near the walls as demonstrated in Figure A-1.

Figure A-2 illustrates the u-velocity profiles along the vertical middle line and the v-velocity profiles along the horizontal middle line obtained using different Mach numbers. At R_e=100 and M_a=0.06 (Figure A-2 (a), (b)), both preconditioned and non-preconditioned results match very well with the reference data. The preconditioned code can also produce the same result at an extremely low Mach number (M_a=0.001), indicating the converged result is independent of the Mach number when preconditioning technique is used. At a higher Reynolds number (R_e=1000), the preconditioned results are slightly closer to the reference data.
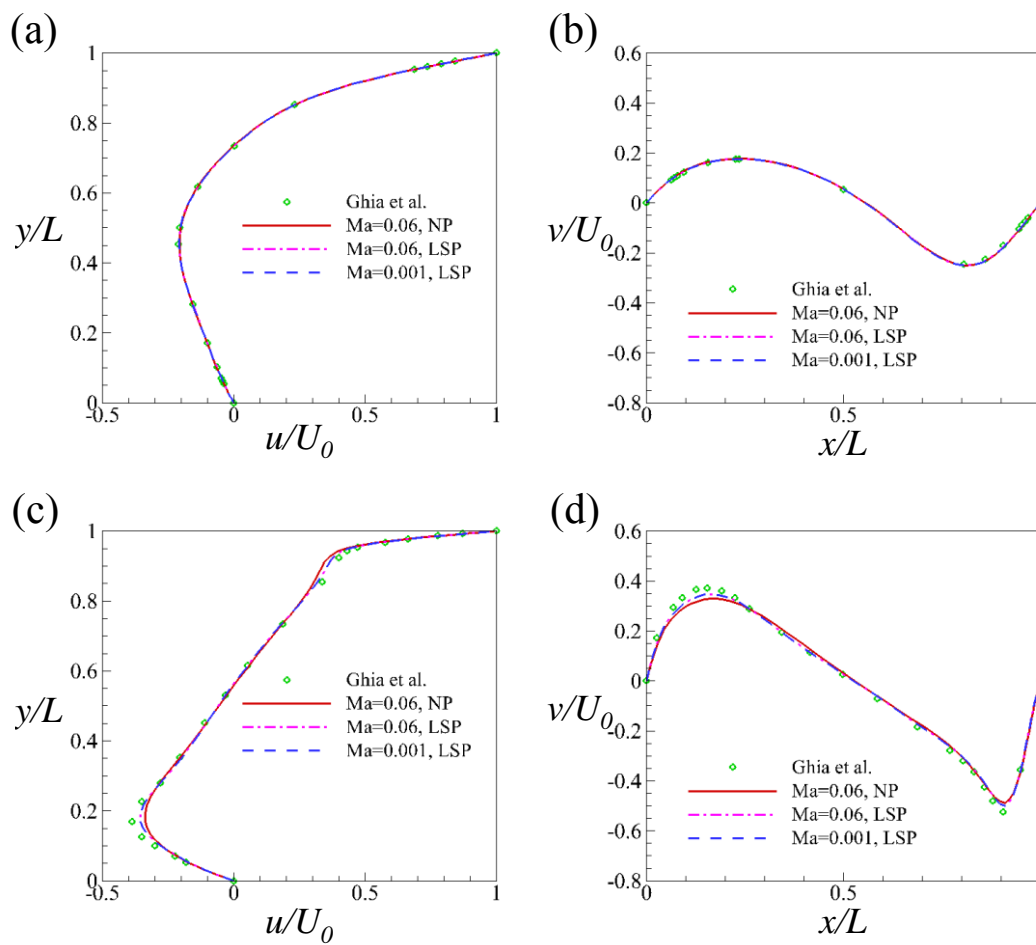

Figure A-2 U-velocity profiles (a), (c) and V-velocity profiles (b), (d) at R_e=100 (a), (b) and R_e=1000 (c), (d). Reference data is from [218].

Figure A-3 demonstrates the convergence histories of the normalised flow density change rate r/r_0 (the value is averaged within the entire computational domain). It is observed that preconditioning significantly improves the convergence rate at R_e=100.

Despite of the slower convergence of preconditioned case at R_e=1000, preconditioned simulation produces more accuracy results (see Figure A-2 (c), (d)).
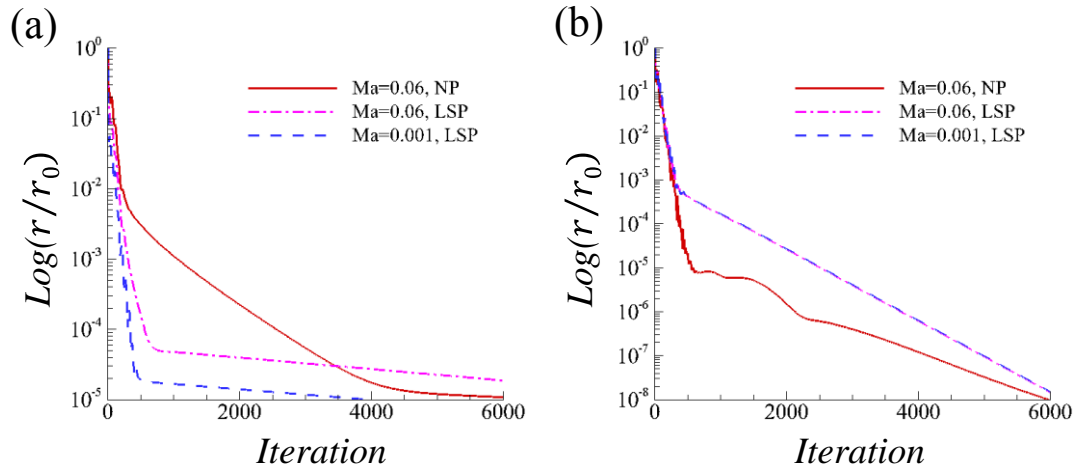

Figure A-3 Flow convergence histories at R_e=100 (a) and 1000 (b).

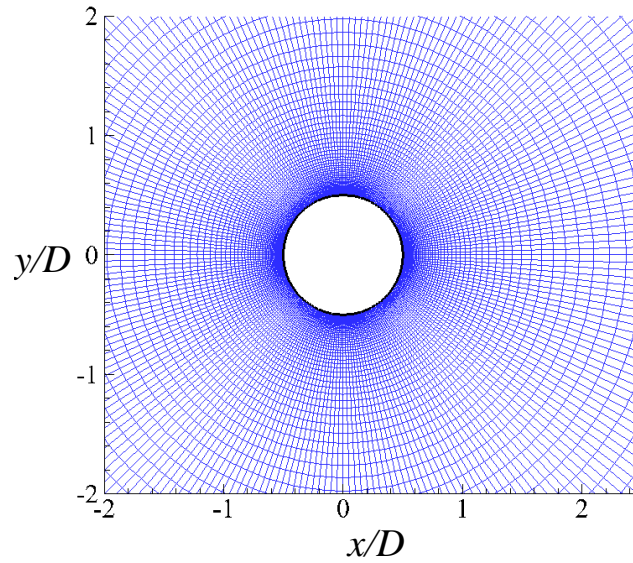**Test 2: Steady flow past a circular cylinder at R_e=40**

Figure A-4 The computational mesh for steady flow past a circular cylinder.

The steady flow past a circular cylinder at R_e=40 is simulated in order to test the external flows. Figure A-4 shows the computational mesh and the Reynolds number is based on the incoming flow velocity and the diameter (D) of the cylinder. The

far-field boundary is located at 100*D* away from the cylinder in order to mitigate the possible negative effect of non-characteristic far-field boundary condition.
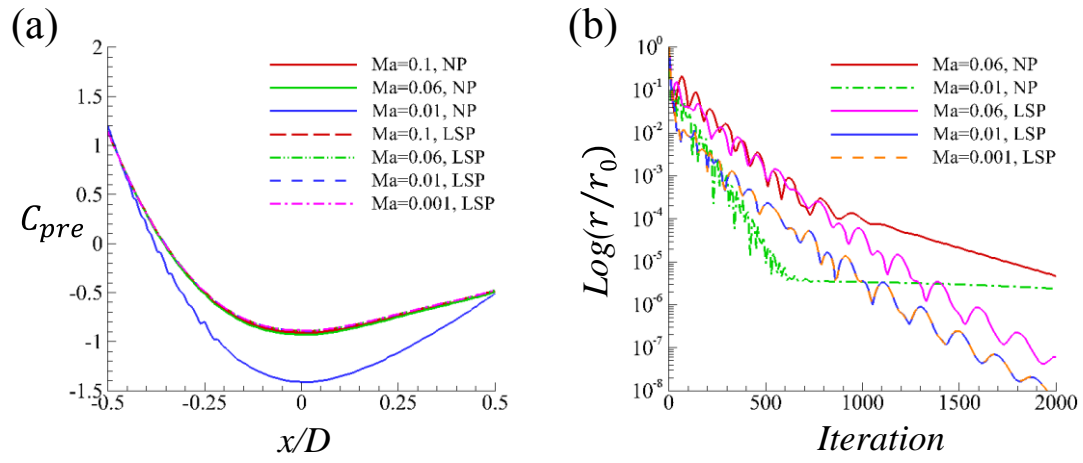

Figure A-5 (a) Pressure coefficient distribution along the surface of the cylinder. (b) Flow convergence histories.
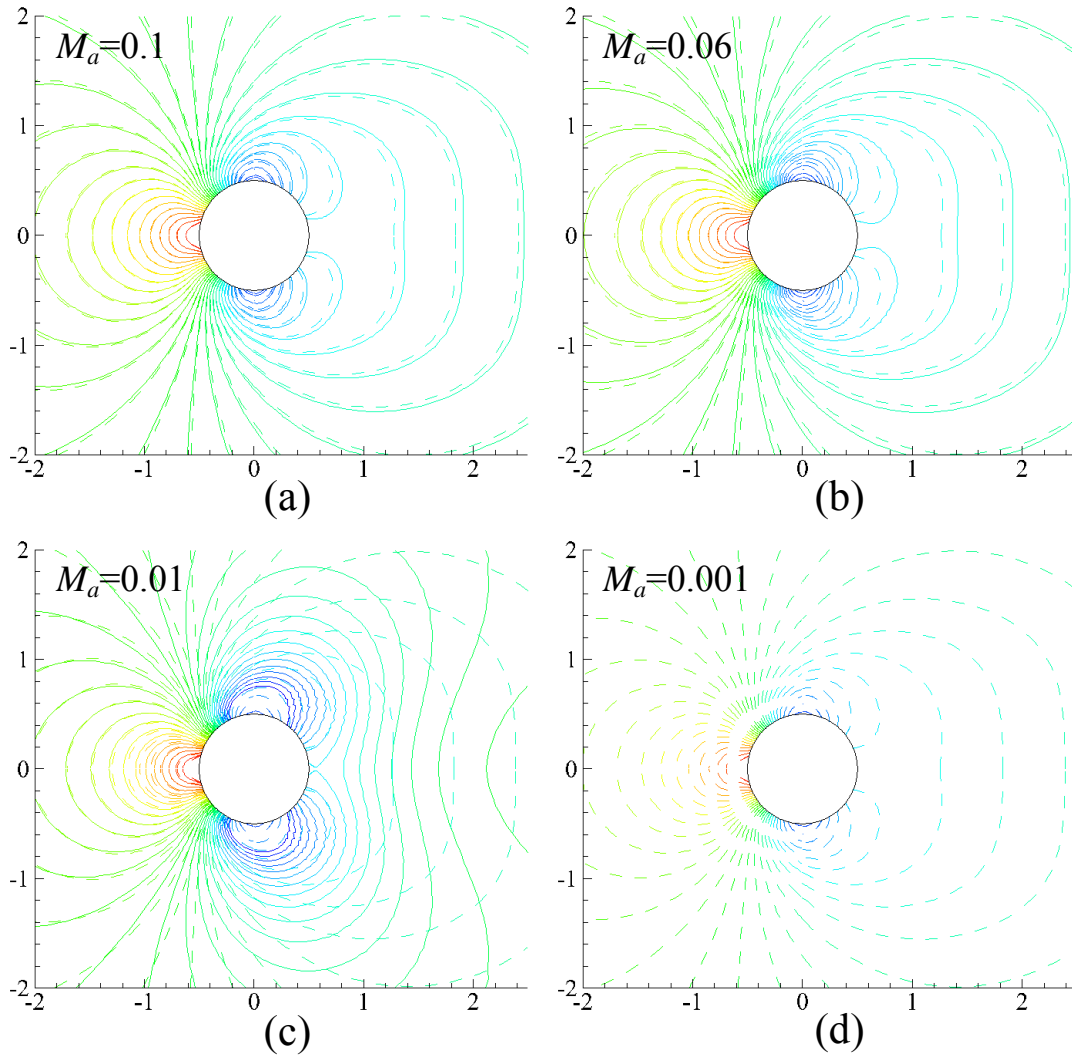
Figure A-6 Contours of pressure coefficient. Solid-lines: non-preconditioned results, and dash-lines: preconditioned results.

Figure A-5 (a) shows the distribution of pressure coefficient along the upper surface of the cylinder, it is seen that at higher Mach numbers (M_a=0.1 and 0.06), the preconditioned and non-preconditioned distributions are very close to each other. However, at a lower Mach number (M_a=0.01), the non-preconditioned code gives incorrect result while the preconditioned solver still produces accurate data even at M_a=0.001. Figure A-5 (b) compares the convergence histories of preconditioned and non-preconditioned codes at different Mach numbers. It is observed that the convergence performance is improved by preconditioning. Therefore, preconditioning not only maintains the accuracy for very low speed flows (e.g., M_a<0.01), but also accelerates the convergence. The pressure contours are illustrated in Figure A-6.

Similar to the pressure distribution along the cylinder, the preconditioned code gives the same contours at all Mach numbers considered here. In contrast, the non-preconditioned code only produces accurate results at higher Mach numbers (M_a=0.1 and 0.06).

Test 3: Steady flow past a NACA0012 foil at R_e=1000
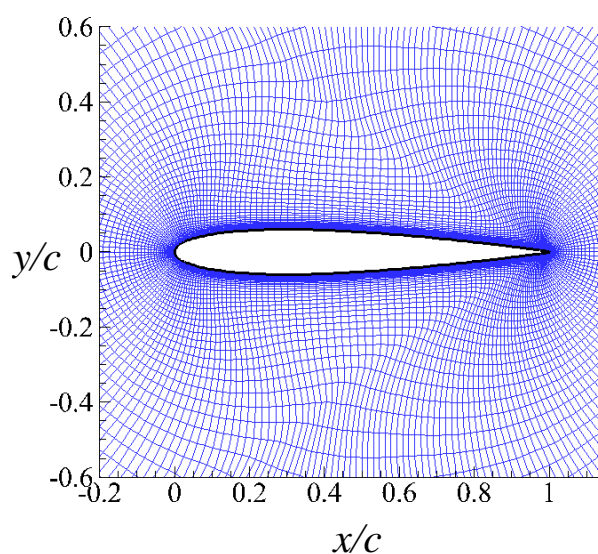

Figure A-7 The computational mesh for steady flow past a NACA0012 foil.

The third case used to test the present implementation of preconditioning is the steady flow past a NACA0012 foil at two different angle of attack (AOA=0 and 10 degree). The chord length of the airfoil is c and the Reynolds number based on the incoming flow velocity and the foil length is R_e=1000. Figure A-7 shows the O-grid used for flow computation and the far-field boundary is located at $100c$ away from the airfoil.
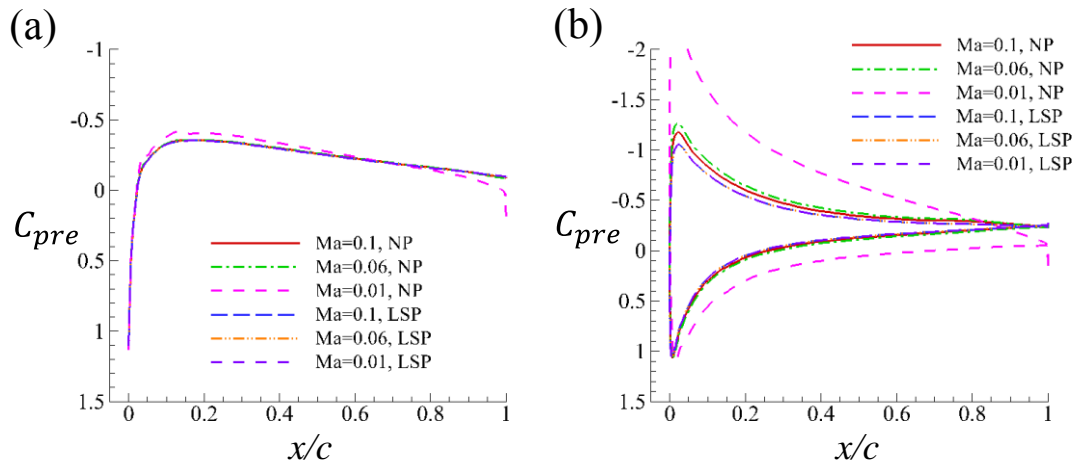
Figure A-8 Pressure coefficient distributions along the surface of the foil. (a) AOA=0 degree, and (b) AOA=10 degree.
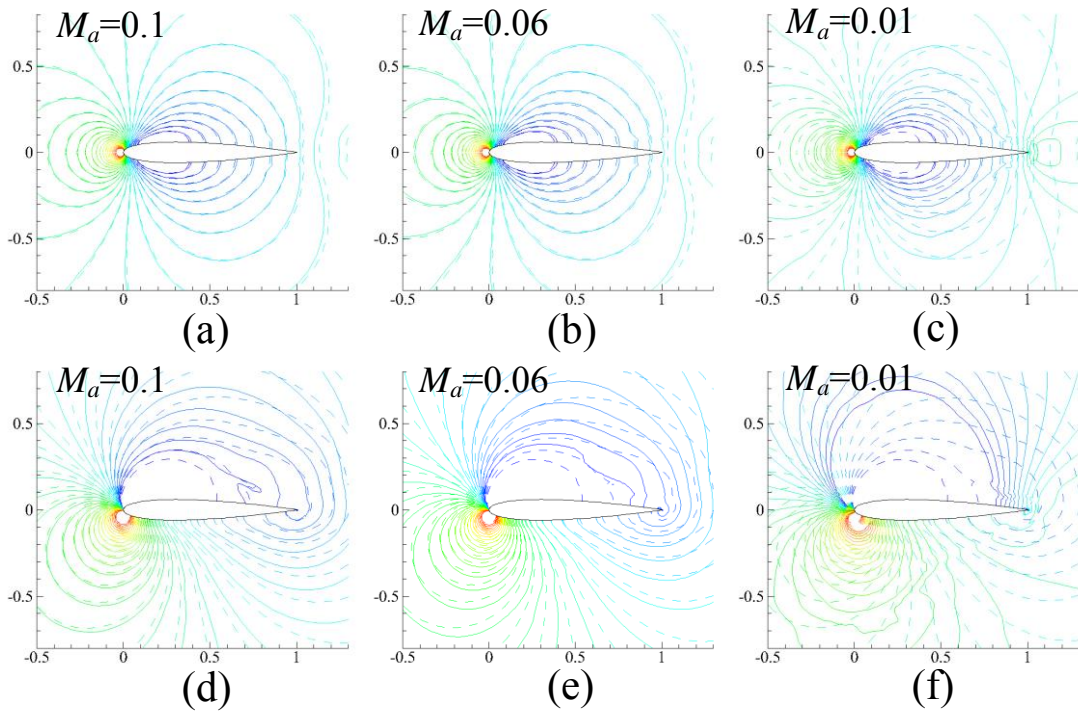

Figure A-9 Contours of pressure coefficient. Solid-lines: non-preconditioned results, and dash-lines: preconditioned results. (a)-(c) AOA=0 degree, and (d)-(f) AOA=10 degree.

Figure A-8 shows the pressure distribution along the surface of the airfoil. It is seen that for both values of AOA, the pressure distributions from preconditioned code are the same independent of the Mach numbers. For non-preconditioned code, however, the results are dependent on the Mach numbers. When M_a decreases to 0.01, the non-preconditioned solver is not able to produce accurate results. Similar conclusions can be drawn from the pressure contours demonstrated in Figure A-9.

The convergence histories of flow density residuals and drag coefficients are demonstrated in Figure A-10. It is seen that the convergence is significantly accelerated. For example, the preconditioned code takes only 1000 iterations to reach a convergence of drag coefficient while the non-preconditioned requires at least 3000 iterations. Considering the preconditioned code consumes more computational time per iteration, the computational efficiency is briefly summarised in Table A-1. It can be observed that the time required for convergence of the precondition solver is approximately half of that required by the non-preconditioned code.
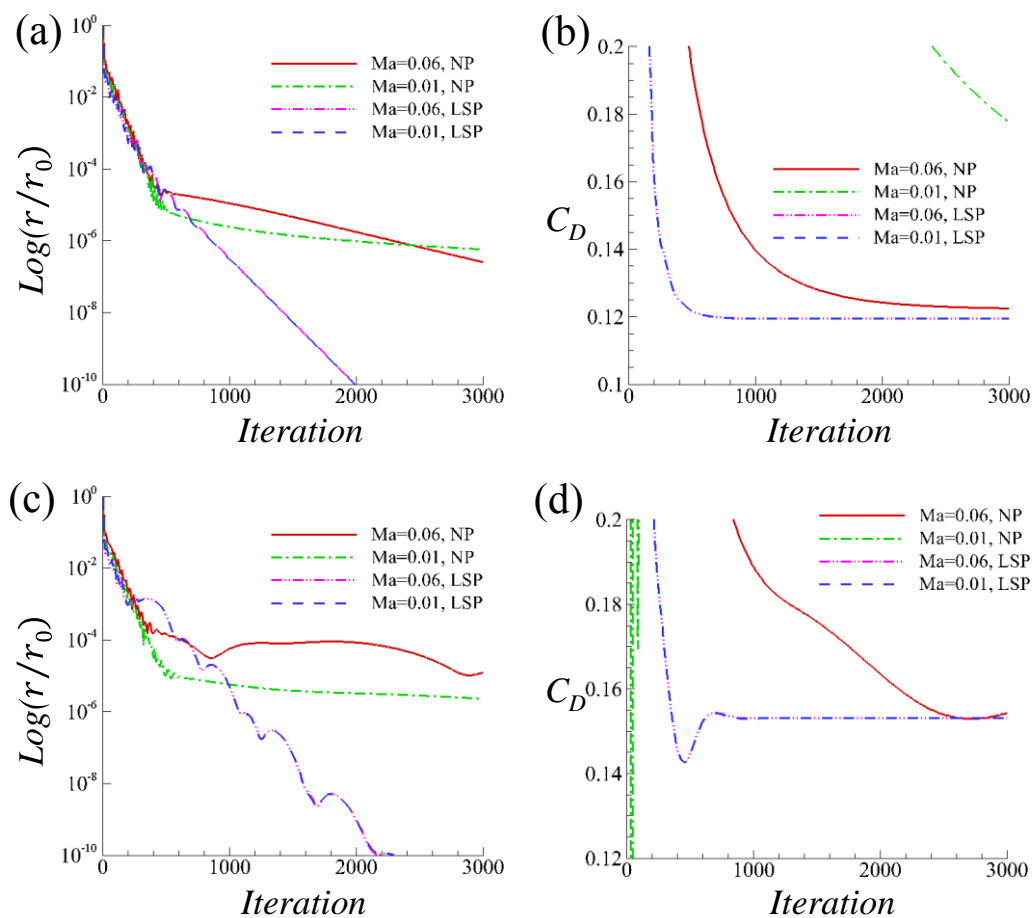

Figure A-10 Flow and drag coefficient convergence histories. (a), (b) AOA=0 degree, and (c), (d) AOA=10 degree.

Table A-1 Summary of computational time used for the case at AOA=10 degree, M_a=0.06.

	Total iterations	Total time (s)	Time per iteration (s)	Least time used to converge (s)
Non-preconditioned code	3000	645	0.215	0.215×3000=645
Preconditioned code	3000	1113	0.371	0.371×1000=371

Test 4: Unsteady flow past a circular cylinder at R_e=185

In this test, we extend the above preconditioning to a time-dependent problem: the vortex shedding behind a cylinder at R_e=185, which is also used as a validation case in Subsection 4.1.1. The computational mesh is the same with the one shown in Figure A-4 and the time step is $0.04D/U_\infty$. Figure A-11 (a) shows the instantaneous lift coefficient, from which we can see that the non-preconditioned code produces a periodical vortex shedding after a starting period while the preconditioned code has lost its time accuracy. The convergence histories within ten physical time steps are demonstrated in Figure A-11 (b). It is seen that the residual of non-preconditioned code drops more than four orders of magnitude whereas the preconditioned residual reduces less than three orders, implying the convergence rate of preconditioned code is deteriorated for unsteady flow computations.
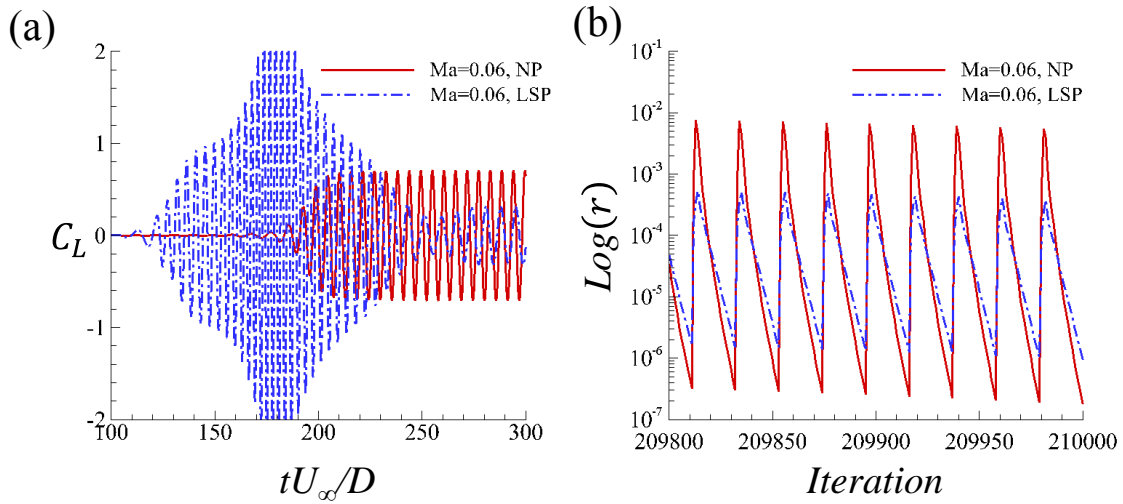

Figure A-11 (a) Lift coefficient histories of preconditioned and non-preconditioned solutions at M_a=0.06. (b) Convergence histories within 10 physical time steps.

Various reasons can lead to such an inaccuracy. First, a fully-explicit multiple stage Runge-Kutta stepping scheme (Eq. (3.32)) is used for temporal integration in the present implementation. Compared with semi-explicit Runge-Kutta stepping methods [151,157] and implicit lower-upper symmetric-Gauss-Seidel (LU-SGS) methods [135,156], the fully-explicit Runge-Kutta scheme is more prone to stability issues. A

second reason may be the definition of M_r in Eq. (A.5). It is suggested that a new cut-off value considering the effect of physical time step should be included [154,155]. Campobasso and Drofelnik [157] developed a *mixed* preconditioning method to further enhance the stability and robustness of the preconditioned code and great accuracy was obtained in their study. A third reason may be the simplified non-characteristic far-field boundary condition, which is no longer effective for unsteady flow problems, as pointed out by Vatsa and Turkel [149]. Further rigorous tests of these possible solutions are needed in the future.

A.3   Summary

In the current appendix, the implementation of preconditioning technique for compressible Navier-Stokes equations is presented. Conservative variables and Weiss-Smith preconditioning matrix are used in the preconditioned flow equations. A simplified far-field boundary condition is used in replacement of the characteristic-based boundary condition. The performance of the preconditioned code is evaluated using three steady flow cases and one unsteady flow case. It is observed that for steady flows, preconditioning can increase the convergence rate and the preconditioned solution is independent of the Mach numbers. Therefore, the present implementation of preconditioning is successful for steady flow problems. However, for time-dependent flows, the present preconditioning cannot produce time-accurate results, which may be attributed to the temporal integration scheme, the definition of the cut-off values in preconditioning matrix, and the non-characteristic far-field boundary condition. Therefore, the preconditioning method introduced in this appendix is not used for the investigation of the biomimetic problems in the present thesis. The examinations of these issues are subject to the future work.